

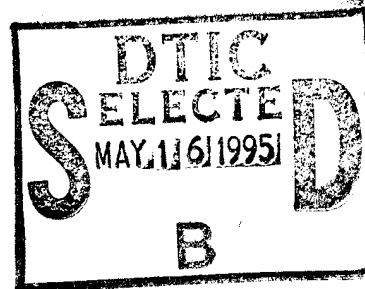
NASA  
Technical Memorandum 106518

Army Research Laboratory  
Technical Report ARL-TR-403

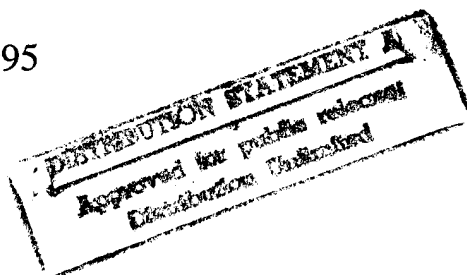
## Thermal Behavior of Spiral Bevel Gears

Robert F. Handschuh  
*Vehicle Propulsion Directorate*  
*U.S. Army Research Laboratory*  
*Lewis Research Center*  
*Cleveland, Ohio*

Original contains color  
plates. All DTIC reproductions  
will be in black and  
white.



January 1995



DTIC QUALITY INSPECTED 5

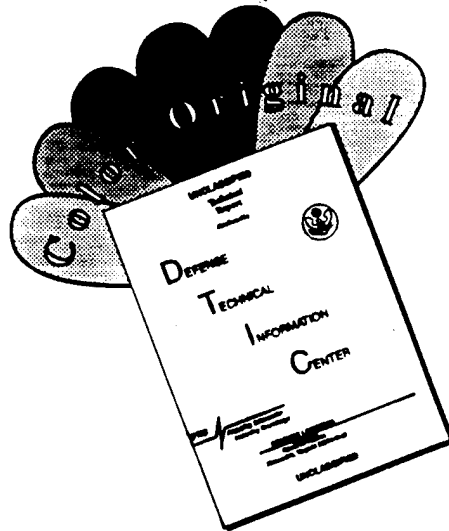


National Aeronautics and  
Space Administration



19950515 105

# DISCLAIMER NOTICE



THIS DOCUMENT IS BEST QUALITY AVAILABLE. THE COPY FURNISHED TO DTIC CONTAINED A SIGNIFICANT NUMBER OF COLOR PAGES WHICH DO NOT REPRODUCE LEGIBLY ON BLACK AND WHITE MICROFICHE.

## TABLE OF CONTENTS

	Page
SUMMARY .....	1
CHAPTER 1: BACKGROUND	
1.1 Introduction .....	2
1.2 Heat Generation in Gear Systems .....	2
1.3 Lubrication of Gears and Gear Scoring .....	3
1.4 Spiral Bevel Gear Geometry .....	5
1.5 Experimental Measurement of Gear Tooth Temperatures .....	6
1.6 Objective of Current Research .....	7
CHAPTER 2: FLASH TEMPERATURE EVALUATION	
2.1 Introduction .....	14
2.2 Historical Perspective of the Flash Temperature Calculation .....	14
2.3 Flash Temperature Calculation for Spiral Bevel Gears .....	16
2.4 Experimental Measurement of Flash Temperature .....	16
2.5 Improvements Needed in the Flash Temperature Methodology for Spiral Bevel Gear .....	17
CHAPTER 3: TEST FACILITY AND EXPERIMENTAL RESULTS	
3.1 Introduction .....	27
3.2 Description of Test Facility .....	27
3.3 Description of Test Instrumentation .....	27
3.4 Description of Test Hardware .....	28
3.5 Calibration of Test Instrumentation .....	29
3.6 Calibration of Test Hardware .....	31
3.7 Rotating Thermocouples and Slip Rings .....	31

	Page
3.8 Experimental Results From Thermocoupled Pinions .....	32
3.9 Experimental Results Using an Infrared Microscope .....	35
 CHAPTER 4: SPIRAL BEVEL GEAR GEOMETRY AND CONTACT MODELING	
4.1 Introduction .....	70
4.2 Spiral Bevel Gear Geometrical Approach .....	70
4.3 Description of Spiral Bevel Gear Manufacture .....	71
4.4 Analytical Development of Gear Surface Geometry .....	71
4.5 Three-Dimensional Contact Methodology for Application to Spiral Bevel Gears .....	75
 CHAPTER 5: HEAT GENERATION AND HEAT TRANSFER	
5.1 Introduction .....	93
5.2 Two-Dimensional Simulation of Time and Position Variable Heat Transfer Analysis .....	93
5.3 Time-Averaged Boundary Conditions .....	96
5.4 Comparison of Finite Element and Finite Difference Results on Two-Dimensional Model .....	96
5.5 Friction Coefficient in Meshing Gear Systems .....	97
5.6 Load Sharing in Meshing Gear Systems .....	99
5.7 Convection Heat Transfer Coefficients for Rotating Gears .....	100
 CHAPTER 6: THREE-DIMENSIONAL SPIRAL BEVEL GEAR MODEL AND RESULTS	
6.1 Introduction .....	121
6.2 Relationship Between Hertzian Analysis and Three-Dimensional Finite Element Spiral Bevel Gear Model .....	122
6.3 Heat Flux Distribution on the Three-Dimensional Gear Model .....	123
6.4 Three-Dimensional Finite Element Model and Application of Steady State and Transient Boundary Conditions .....	124
6.5 Time-Averaged and Time-Transient Analytical Results .....	126

## CHAPTER 7: COMPARISON OF EXPERIMENTAL AND ANALYTICAL RESULTS

7.1 Introduction .....	160
7.2 Comparison of Measured and Calculated Results .....	160
7.3 Comparison of Flash Temperature Calculation and Results of Other Studies .....	162
7.4 Recommendations .....	163

CHAPTER 8: CONCLUSIONS .....	170
------------------------------	-----

## APPENDICES

A CURRENT FLASH TEMPERATURE CALCULATION .....	172
B SOLID MODEL GENERATION DESCRIPTION .....	176
C USER SUBROUTINES .....	184

Accession For	
NTIS GRA&I	<input checked="" type="checkbox"/>
DTIC TAB	<input type="checkbox"/>
Unannounced	<input type="checkbox"/>
Justification	
By	
Distribution/	
Availability Codes	
Dist	Avail and/or Special
A-1	

# THERMAL BEHAVIOR OF SPIRAL BEVEL GEARS

Robert F. Handschuh  
National Aeronautics and Space Administration  
Lewis Research Center  
Cleveland, Ohio 44135

## SUMMARY

An experimental and analytical study of the thermal behavior of spiral bevel gears is presented. Experimental data were taken using thermocoupled test hardware and an infrared microscope. Many operational parameters were varied to investigate their effects on the thermal behavior. The data taken were also used to validate the boundary conditions applied to the analytical model. A finite element-based solution sequence was developed. The three-dimensional model was developed based on the manufacturing process for these gears. Contact between the meshing gears was found using tooth contact analysis to describe the location, curvatures, orientations, and surface velocities. This information was then used in a three-dimensional Hertzian contact analysis to predict contact ellipse size and maximum pressure. From these results, an estimate of the heat flux magnitude and the location on the finite element model was made. The finite element model used time-averaged boundary conditions to permit the solution to attain steady state in a computationally efficient manner. Then time- and position-varying boundary conditions were applied to the model to analyze the cyclic heating and cooling due to the gears meshing and transferring heat to the surroundings, respectively. The model was run in this mode until the temperature behavior stabilized. The transient flash temperature on the surface was therefore described. The analysis can be used to predict the overall expected thermal behavior of spiral bevel gears.

The experimental and analytical results were compared for this study and also with a limited number of other studies. The experimental and analytical results attained in the current study were basically within 10 percent of each other for the cases compared. The experimental comparison was for bulk thermocouple locations and data taken with an infrared microscope. The results of a limited number of other studies were compared with those obtained herein and predicted the same basic behavior.

## CHAPTER 1: BACKGROUND

### 1.1 Introduction

Geared systems have many modes of failure. Fatigue failure is typically thought of as being one of two types, either bending or contact. These failure modes are the most fundamental ones considered during the design process. Other types of gear failures usually occur at the surface level and are not dependent on the number of cycles a member has accumulated. These failures fall in the following categories: abrasion, corrosion and scoring. Careful use of fine filtration and the elimination of contaminants in the lubrication system can usually control abrasion and corrosion, respectively. However, scoring is attributed to the breakdown of the elastohydrodynamic film that separates the contacting bodies and is linked to the thermal behavior of the gear system. Thus, scoring is related to the operating conditions (speed and load), surface geometry, given design parameters, lubricant properties, and the lubrication scheme of the components in question. When scoring occurs, the failure of the component follows soon afterwards because the surface is damaged beyond useful limits. Altering even one of the operating parameters can cause scoring, making surface failure imminent. For example, a geared system design may be below a load capacity limit, but the alteration of one of the operational parameters can cause scoring and imminent surface failure.

This is why load carrying capacity as a function of the operating environmental conditions for geared systems has been one of the most important aspects of a given design. The operating conditions as described above must be addressed during the design process.

When designing aerospace systems, further constraints are the requirements for light weight and high reliability. Aerospace applications usually go beyond the state-of-the-art design limits for geared systems.

Accurately assessing the load capacity of geared systems has been addressed experimentally by using a standard test fixture (Ref. [1.1]) where loading and speed could be precisely controlled for a given lubricant. While this provided a bounded region of presumed safe operation for a particular design, the fundamental aspects of the problem at hand were not being addressed. Also, these tests were conducted for parallel axis components and not for spiral bevel gears where there are obvious geometric differences. Spiral bevel gears add an additional complexity to the gear meshing process: although the teeth appear to have an involute profile, the surface geometry is quite different and is a complex kinematic problem because there is no closed-form solution to describe the profile coordinates. A numerical analysis must be conducted to determine the parameters that affect successful operation.

Spiral bevel gears as used in aviation applications are shown in Figures 1.1.1 and 1.1.2 (Refs. [1.2] and [1.3]). These gears are required to turn the corner from the horizontal engine(s) to the vertical rotor shaft and are run at very high speeds and under heavy loads. In this environment, they are jet lubricated and operate in a dry sump mode (i.e., the gears do not rotate through a lubricating bath as in an automotive rear axle application), which permits the most efficient system operation because oil churning losses can be substantial. Systems as described above are of the most concern for the study to be conducted.

### 1.2 Heat Generation in Gear Systems

Flash temperature theory has its roots in the work of Blok (Ref. [1.4]) and most other studies are based on this work. In Reference [1.4], the heat flux for different situations was derived. The resultant heat flux between moving bodies was described as the product of the coefficient of friction, applied pressure (load), and the relative velocity between the bodies.

The flash temperature methodology was extended to spiral bevel gears by Coleman (Ref. [1.5]), whose paper provides the basis for the flash temperature calculations used today during the spiral bevel gear design process. Although the accuracy of the temperatures resulting from these calculations is unknown, it is still a quick and simple method for a designer to vary design parameters and have a number to compare with past success and failure.

Another detailed study of the flash temperature methodology and its comparison with experimental results was done for spur gears by Tobe (Ref. [1.6]), whose experimental results, when compared with the flash temperature calculation, indicated that the actual tooth loads instead of the static load produced better results.

Ku (Ref. [1.7]) used the work of Coleman (Ref. [1.5]) and developed a computer code to permit a quicker calculation of the flash temperature. A limited amount of experimental data was also generated to check the predictions. Many fundamental aspects, however, were still missing from the model used.

The most recent work addressing heat transfer in spiral bevel gears is Chao's (Ref. [1.8]). In this pioneering work, a finite element program was used to calculate the dynamics, film thickness, and expected temperatures in spiral bevel gears. An influence coefficient, or more correctly a shape function analogy, was used to thermally load the model on the basis of the distance from the contact point in question. This is a shortcoming that is eliminated from the analysis conducted in the presently reported study.

### 1.3 Lubrication of Gears and Gear Scoring

**Lubrication of Gears:** In the present study, the lubricant effects are neglected. Other than the influence on the friction coefficient (based on constitutive models) the effect of the oil film interaction with the contacting bodies is neglected. However, a brief review of some research results with respect to gear lubrication will be given. Many of the ideas from these studies can be extended to include the geometry of meshing spiral bevel gears even though they are not addressed in this study. The majority of the experimental and analytical work on lubrication behavior in concentrated contacts has been done on configurations such as a sphere on a plane, a cylindrical roller on a plane, or spur gears. An overview of some of these studies is now presented.

As a starting point, Coy (Ref. [1.9]) gave an excellent review of many important studies found in the open literature and gave an assessment of the current state of the art with respect to gear lubrication. Some of the early pioneering studies on gear lubrication are found in References [1.10] to [1.17].

Many gear systems, aerospace in particular, successfully operate in a region called boundary lubrication. Boundary lubrication occurs when the asperity heights of the contacting bodies are of the same order as the lubricant film. As Coy (Ref. [1.9]) pointed out, a chemical reaction between lubricant additives and the meshing surfaces provides the mechanism for films this thin to perform successfully. Additive packages with the correct compounds must be contained in the lubricant otherwise there will be premature wear and failure of the meshing gear system.

Dowson (Ref. [1.18]) discussed the maturing of elastohydrodynamic (EHD) theory and its extension to contacts of other engineering surfaces of interest. Important surface parameters and lubricant interactions were described.

In Bartz (Ref. [1.19]), EHD theory was applied to spur gears. This study looked at lubricants without extreme pressure additives and explored the relationship between lubricant properties and the load capacity so that scoring could be avoided.

Townsend (Ref. [1.20]) applied EHD theory to the design of helicopter drive system components. Many important drive system design parameters and their effect on component life were discussed. The film thickness of all components should be determined, according to Townsend, to reduce the risk of component failure due to surface interaction.

Gu (Ref. [1.21]) performed a detailed analysis of the EHD problem on spur gears. The results of this study indicated that using the pitch point for evaluating the film thickness and maximum contact pressure gave the thinnest film and the highest contact pressure while the highest surface temperature was found at the tooth extremes. For design purposes, calculations at these points will keep a given design conservative.

Another application of EHD theory to gear drives was discussed in Wellauer (Ref. [1.22]), who conducted a comprehensive study. A graphical approach was presented to determine expected behavior based on gear geometry, speed, load, and lubricant parameters. Curves linking the probability of failure based on the  $\lambda$ -ratio (defined as the film thickness divided by a composite surface roughness) were presented. A large data base of surface distress, scoring failures, was presented for pitch line velocities to 35 000 feet per minute.

The fundamental ideas just discussed were extended to helical gears in the analytical study of Simon (Ref. [1.23]). A complete thermal EHD analysis of the helical gear mesh was accomplished. Many design parameters were shown to increase the load capacity. Relative tooth curvature, face width, pitch line velocity, and surface finish all affected the load capacity.

The last reference to be discussed in this section is Chao (Ref. [1.8]). The film thickness for spiral bevel gears was assessed using the point contact solution of Hamrock (Ref. [1.24]). The film thickness variation with respect to many variables was presented.

To summarize this section, the EHD behavior of gears is very complex. Many geometric hurdles need to be overcome to access gear behavior. Once the geometry and other dependent variables are known, a constitutive relationship (such as that given in Hamrock (Ref. [1.24])) permits an assessment of the lubrication regime in which the given gear design will be required to operate. The film-thickness-to-surface-roughness ratio will determine the lubricant type required. The key difference between actual gear applications and those of a sphere on a plane is that geometry, relative velocities, and load are all dependent on the meshing location for a given design.

**Gear Scoring:** Scoring of components occurs when the load, speed, or lubrication conditions reach a level at which the lubricant can no longer maintain a film between the interacting bodies. In the research reported herein, no attempt was made to experimentally or analytically predict the scoring of the spiral bevel gears in question. However, to provide a reference frame for the discussion of gear scoring, a short review of work done in this area is presented.

Many researchers (Refs. [1.25] to [1.30]) used the pioneering work of Blok (Ref. [1.4]) to explain the data generated on gear scoring based on gear kinematics, lubricant type, operating temperature, gear steel properties, surface finish and heat treatment, or some combination of all these. These tests were conducted using gears and cylindrical rollers. Gear tests were conducted on spur gears. The goal was to develop a factor or temperature that could be used in a simple calculation to establish the limit of safe operation.

The work of Dudley (Ref. [1.31]) presents an excellent review of flash temperature/scoring index methods to quickly analyze a gear system. This summary is the typical calculation procedure still being used by gear designers.

A complete summarization of the scoring behavior/flash temperature methods was presented in the late 1960's in Blok (Ref. [1.32]), a historical perspective of studies that had transpired over the 30 years since his

earlier work (Ref. [1.4]). Many important aspects of the scoring behavior are described along with recommendations for improving the analysis and interpretation of experimental results. One problem noted was the scatter in scoring data. Some of the discrepancies in different sets of researchers' data are related to different conditions during testing. Blok commented that the scatter attained would be no different from that found in a pitting fatigue test. Many suggestions also were given for future analytical modeling possibilities.

Research since the work of Blok has still been concerned with many of the parametric aspects of scoring. The effects of the following parameters were studied: operating conditions (Ref. [1.33]), surface roughness (Ref. [1.34]), film thickness (Ref. [1.35]), profile modification (Ref. [1.36]), lubricant jet position (Ref. [1.37]), antiwear additives (Ref. [1.38]), molybdenum disulfide and other films (Ref. [1.39] and [1.40]), and asperity interaction (Ref. [1.41]). Also, an assessment of scoring mechanisms (Ref. [1.42]) was made. Those papers presenting experimental results had basically used cylindrical disks, four-ball testers, or spur gear test specimens to conduct their studies.

The summary given herein on lubrication and scoring is to provide a sense of what has been analyzed and the kind of experiments that have been conducted. Although scoring is not the subject of the current study, one must not lose sight of the fact that parameters used in the analysis to follow or in the experiments conducted could be set so that surface scoring could be approached numerically or experimentally.

When operating in the near boundary lubrication regime, as many aerospace drive system components do, the friction coefficient can increase dramatically when, for example, the oil film breaks down. From an analytical standpoint, this in turn produces additional heat and rapidly alters the "normal" cyclic behavior of the temperature on the active profile. When this increasing rate of heat generation causes surface temperatures to reach a critical value, the surface fails because the nominal heat rejection to ambient and the surrounding gear body is insufficient.

A scoring investigation from the experimental point of view can be approached using many of the parameters mentioned. Changes in one condition, such as speed (load held constant), can effect the experimental behavior in a manner similar to the effect of friction mentioned above. Note that friction can also be a function of load as will be seen in Chapter 5.5. For a given load, no detrimental surface behavior will be found until a certain level of speed is reached. Obviously, speed is directly related to sliding velocity and is an important parameter of the heat generation mechanism.

An awareness of the interactions between parameters should be kept in mind while reviewing the rest of this study.

## **1.4 Spiral Bevel Gear Geometry**

Spiral bevel gear geometry, for the face-milled gears that are used and analyzed in this study, had its modern origin in the open literature of the 1960's. Work since this time has concentrated on analytical modeling of the generation process because no closed-form solution of this geometry exists. Face-milled spiral bevel gears, while appearing to be similar to involute geometry, are really quite different. Some of the basic geometry parameters of this gear type are shown in Figure 1.4.1. What cannot be seen clearly from this drawing is that the teeth change in height and thickness from the toe to the heel. Other types of spiral bevel gear geometry, such as the face hobbed, have equal height, or constant depth, teeth. These gears, however, cannot be final ground with the same ease as face milled (as required in most aerospace applications) and are typically hard finished. In the production of face-milled teeth, relatively simple cutter or grinding wheel shapes are permitted, and therefore attaining high quality surface geometry is possible in the hardened state after heat treatment. This geometry is currently utilized in all aerospace applications in the United States.

The ability to perform the advanced analytical studies reported herein requires an understanding of gear geometry. Therefore, a brief summary of gear geometry work reported in the open literature is given.

Early spiral bevel gear geometry investigations began with the studies of several employees of the Gleason Works, the major builder of this type of machine tool. Their reports dealt with basic geometry, tooth contact, misalignment, contact pressure, sliding velocity, and adjustment characteristics (Refs. [1.43] to [1.46]). Coleman's work (Ref. [1.5]) has already been discussed. These studies, although significant, still did not fully describe the spiral bevel gear geometry under consideration.

Baxter's study (Ref. [1.47]) provided useful equation development for nongenerated geometry, such as hypoid gears that are cut by the Formate<sup>®</sup> method, which is used in the automotive industry to produce high volumes of components. In this machining process, the gear to be cut is plunged into a cutter that removes material between adjacent teeth simultaneously. Other papers of interest on gear geometry as it relates to contact behavior are by Krenzer (Refs. [1.48] and [1.49]). The effect of load on tooth contact analysis is also presented by Krenzer (Ref. [1.50]). The Gleason Works primer on tooth contact analysis (called TCA) is presented in Reference [1.51].

In the last 10 years, several researchers have concentrated on developing the gear geometry theory for generated spiral bevel gears. Presenting his findings in the open literature, Litvin (Refs. [1.52] and [1.53]) began the formal analysis of the generation of spiral bevel gears. Since the 1980's, the evolution of gear geometry theory to date for spiral bevel gears is presented by Litvin (Refs. [1.54] to [1.57]). The basis for the analysis presented in these studies is the gear geometry work extensively described in Reference [1.57].

Recent work on the application of spiral bevel gear geometry has involved the development of finite element analysis to structurally model the components using the full gear geometry (Ref. [1.58]) and the kinematic optimization of the gear geometry (Ref. [1.59]).

For the study reported herein, the method developed in Handschuh (Ref. [1.58]) is used to generate the thermal model of interest. A thorough development of the gear geometry and the development beyond the structural model to permit building the thermal model are presented in Chapters 4 to 6.

## 1.5 Experimental Measurement of Gear Tooth Temperatures

The experimental measurement of gear tooth temperature is a very challenging task. This measurement can be made by (1) having the rotating gear members act as the thermocouple junction by the fabrication of each member from different materials; (2) attaching thermocouples to the rotating hardware; or (3) using a remote measurement of the infrared energy radiated from the gear surface. A discussion of these methods is now presented.

The measurement method using gears of two different materials was tested in the 1930's by Blok (Ref. [1.60]). This method was also used by Niemann (Ref. [1.61]), who varied such parameters as load, speed, and tooth profile. This same procedure was used in the study of Tobe (Ref. [1.6]), except that only one tooth of the gear completed the thermocouple junction. The problem with making the measurement in this manner is that compromises are required. First, contact through the oil film must be made and maintained, otherwise the thermocouple becomes an open circuit. Second, materials typically used do not have the load carrying capacity of the gear set being simulated. The results, however, can be useful to evaluate analytical models that can then be scaled to more practical design conditions.

The second measurement method uses measurement devices attached to the rotating hardware as illustrated in the following studies. Ku (Ref. [1.62]) used thermocouples attached to a spiral bevel pinion in noncontacting

locations during a scoring test in a helicopter transmission. The limited measurements made provided a temperature distribution within the pinion during scoring tests. Another study by Doi (Ref. [1.63]) used contacting bead thermistors where different lubrication locations and flow rates were varied to study the effect on the operating temperature. Winter (Ref. [1.64]) presented experimental data using thin film sensors that were produced by an ion beam sputtering technique. Some outstanding results were attained for the pressure, temperature, and film thickness of cylindrical rollers and spur gears.

The third method for temperature measurement uses an infrared microscope. Turchina (Ref. [1.65]) used this technique to measure the temperature in a sliding contact. In this study, the contact region was between a sliding steel sphere and a sapphire lens through which the infrared measurement was made. This situation is ideal for making the measurement. However, this method is not quite as ideal when measuring gear teeth, as exemplified by the study of Townsend (Ref. [1.66]) in which the spur gear contacting profile was passed in view of the infrared microscope at a location approximately  $150^\circ$  of rotation after meshing. The measurement could be made but at a location that was less desirable.

This summary of possible temperature measurement methods indicates that each has problems and shortcomings. For the study reported herein, the approach used and the measurements made are presented in Chapter 3. The results are compared with the analysis conducted and serve as a means to validate the analytical model.

## **1.6 Objective of Current Research**

The objective of the present work was to utilize the available numerical tools for surface geometry description, three-dimensional solid modeling, three-dimensional contact modeling, and lubricant behavior to conduct a thermal analysis of spiral bevel gears. A three-dimensional, time-transient, finite element model is described. Also, an experimental program using aerospace-quality spiral bevel gears was compared with the analysis. Instrumented gear mesh components were tested. Steady state thermal data and transient surface temperatures were compared with the analysis. The analysis that was developed will provide an improved method for assessing designs for thermal behavior in that the full three-dimensional behavior will be analyzed.

The accomplishment of the objective just described required tying together several complex aspects necessary to conduct the analysis at hand. All the necessary steps to conduct the analysis and the experimental study are described in Chapters 3 to 6.

## REFERENCES

- [1.1] Ryder, E.: A Gear and Lubricant Tester. ASTM Bull., No. 148, Oct. 1947, pp. 69-73.
- [1.2] Lewicki, D.; and Coy, J.: Vibration Characteristics of OH-58A Helicopter Main Rotor Transmission. NASA TP-2705, 1987.
- [1.3] Oswald, F.: Gear Tooth Stress Measurements on the UH-60A Helicopter Transmission. NASA TP-2698, 1987.
- [1.4] Blok, H.: Theoretical Study of Temperature Rise at Surfaces of Actual Contact Under Oiliness Lubricating Conditions. Proc. Inst. Mech. Eng., vol. 2, 1937, pp. 222-235.
- [1.5] Coleman, W.: A Scoring Formula for Bevel and Hypoid Gear Teeth. J. Lub. Tech., vol. 89, Apr. 1967, pp. 114-126.
- [1.6] Tobe, T.; and Kato, M.: A Study on Flash Temperatures on the Spur Gear Teeth. J. Eng. Ind., vol. 96, Feb. 1974, pp. 78-84.
- [1.7] Ku, P.; Staph, H.; and Carper, H.: Gear Tooth Scoring Investigation. Report USAAMRDL-TR-75-33, Southwest Research Institute, San Antonio, Tx., July 1975.
- [1.8] Chao, H.; and Cheng, H.: A Computer Solution for the Dynamic Load, Lubricant Film Thickness and Surface Temperatures in Spiral Bevel Gears. NASA CR-4077, 1987.
- [1.9] Coy, J.; Townsend, D.; and Zaretsky, E.: Gearing. NASA RP-1152, 1985.
- [1.10] Meldahl, A.: Contribution to the Theory of the Lubrication of Gears and of the Stressing of the Lubricated Flanks of Gear Teeth. The Brown Boveri Review, vol. 28, Nov. 1941, pp. 374-382.
- [1.11] Gatcombe, E.: Lubrication Characteristics of Involute Spur Gears. Trans. ASME, vol. 67, Apr. 1945, pp. 177-188.
- [1.12] Hutt, E.: Lubrication and the Load-Carrying Capacity of Gears. Lub. Eng., vol. 8, no. 4, 1952, pp. 180-182, 201-203.
- [1.13] Borsoff, V.; and Wagner, C.: Studies of Formation & Behavior of an Extreme-Pressure Film. J. of the Lub. Eng., vol. 79, Feb. 1957, pp. 91-99.
- [1.14] Borsoff, V.: On the Mechanism of Gear Lubrication. J. Basic Eng., vol. 81, Mar. 1959, pp. 79-93.
- [1.15] Borsoff, V.: Gear Lubrication - A Descriptive Analysis. J. Lub. Eng., vol. 83, June 1962, pp. 266-270.
- [1.16] Adkins, W.; and Radzimovsky, E.: Lubrication Phenomena in Spur Gears: Capacity, Film Thickness Variation, and Efficiency. J. Basic Eng., vol. 87, Sept. 1965, pp. 655-665.
- [1.17] Kelley, B.; and Lemanski, A.: Lubrication of Involute Gearing. Proc. Inst. Mech. Eng., vol. 182, Pt. 3A, 1967-68, pp 173-184.

- [1.18] Dowson, D.: Elastohydrodynamic Lubrication. Interdisciplinary Approach to the Lubrication of Concentrated Contacts, NASA SP-237, 1970, pp. 27-76.
- [1.19] Bartz, W.: Some Investigations of the Application of E.H.D. Theory To Practical Gear Lubrication. Proceedings of the Institution of Mechanical Engineers, P.M. Ku, ed., Paper C6/72, 1972.
- [1.20] Townsend, D.: Elastohydrodynamic Principles Applied to the Design of Helicopter Components. American Helicopter Society, Preprint 770, May 1973.
- [1.21] Gu., A.: Elastohydrodynamic Lubrication of Involute Gears. J. Eng. Ind., vol. 95, Nov. 1973, pp. 1164-1170.
- [1.22] Wellauer, E.; and Holloway, G.: Application of EHD Oil Film Theory to Industrial Gear Drives. J. Eng. Ind., vol. 98, May 1976, pp. 626-634.
- [1.23] Simon, V.: Thermo-EHD Analysis of Lubrication of Helical Gears. J. Mech. Trans. Aut. Design, vol. 110, Sept. 1988, pp. 330-336.
- [1.24] Hamrock, B. and Dowson, D.: Isothermal Elastohydrodynamic Lubrication of Point Contact, Part II: J. of Lub. Technol., vol. 98, July 1976, pp. 486-795.
- [1.25] Mansion, H.: Some Factors Affecting Gear Scuffing. Inst. Petroleum, J., vol. 38, 1952, pp. 633-645.
- [1.26] Kelley, B.: A New Look At The Scoring Phenomena of Gears. SAE Trans., vol. 61, 1953, pp. 175-188.
- [1.27] Cameron, A.: Surface Failure in Gears. Inst. Petroleum, J., vol. 40, 1954, pp. 191-196.
- [1.28] Ku, P.; and Baber, B.: The Effect of Lubricants on Gear Tooth Scuffing. ASLE Trans., vol. 2, Jan. 1959, pp. 184-199.
- [1.29] Borsoff, V.; and Godet, M.: A Scoring Factor for Gears. ASLE Trans. vol. 6, 1963, pp. 147-153.
- [1.30] Borsoff, V.: Scoring of Gears. Machine Design, vol. 37, Jan. 1965, pp. 132-136.
- [1.31] Dudley, D.: Handbook of Practical Gear Design, McGraw-Hill, Inc., New York, 1984.
- [1.32] Blok, H.: The Postulate About the Constancy of Scoring Temperature. Interdisciplinary Approach to the Lubrication of Concentrated Contacts, NASA SP-237, P.M. Ku, ed., July 1969, pp. 153-248.
- [1.33] Bell, J.; and Dyson, A.: The Effect of Some Operating Factors on the Scuffing of Hardened Steel Discs. Proceedings of the Institution of Mechanical Engineers, Paper C11/72, Oct. 1971.
- [1.34] Akin, L.: An Interdisciplinary Lubrication Theory for Gears (With Particular Emphasis on the Scuffing Mode of Failure). J. Eng. Ind., vol. 95, Nov. 1973, pp. 1178-1195.
- [1.35] Finkin, E.; Gu, A.; and Yung, L.: A Critical Examination of the Elastohydrodynamic Criterion for the Scoring of Gears. ASME Paper 73-Lub-4, Mar. 1973.
- [1.36] Matsunaga, T.: Influence of Profile Modification and Lubricant Viscosity on Scoring of Helical Gears. J. Eng. Ind., vol. 96, Feb. 1974, pp. 71-77.

- [1.37] Fujita, F.; Obata, F.; and Matsuo, K.: Instantaneous Behavior of Lubricating Oil Supplied onto the Tooth Flanks and Its Influence on the Scoring Resistance of Spur Gears. *J. Eng. for Ind.*, vol. 98, May 1976, pp. 635-644.
- [1.38] Naruse, C.; Haizuka, S.; and Nemoto, R.: Studies on Limiting Load for Scoring of Gears (Effects of Anti-Wear Agent Upon Limiting Load for Scoring of Various Kinds of Gears). *International Symposium of Gearing and Power Transmission, Proceedings, Tokyo, Japan, 1981*, pp. 371-376.
- [1.39] Terauchi, Y.; Nadano, H.; and Kohno, M.: Effect of MoS<sub>2</sub> Films on Scoring Resistance of Gears. *ASME Paper 84-DET-59*, 1984.
- [1.40] Terauchi, Y., et al.: Scoring Resistance of Spur Gears with Various Coatings. *Bull. JSME*, vol. 29, no. 247, Jan. 1986, pp. 235-240.
- [1.41] Ichimaru, K., et al.: The Effect of Asperity Interaction on Scoring in the Rolling-Sliding Contact of Two Rollers. *Bull. JSME*, vol. 29, no. 255, Sept. 1986, pp. 3165-3173.
- [1.42] Dyson, A.; and Wedeven, L.: Assessment of Lubricated Contacts: Mechanisms of Scuffing and Scoring. *NASA TM-83074*, 1983.
- [1.43] Baxter, M.: Basic Geometry and Tooth Contact of Hypoid Gears. *Ind. Math.*, vol. 11, Pt. 2, 1961, pp. 19-42.
- [1.44] Baxter, M.: Effect of Misalignment on Tooth Action of Bevel and Hypoid Gears. *ASME Paper 61-MD-20*, 1961.
- [1.45] Coleman, W.: Contact Pressure and Sliding Velocities on Hypoid Gear Teeth. *J. Lub. Eng.*, vol. 85, May 1964, pp. 189-194.
- [1.46] Spear, G.; and Baxter, M.: Adjustment Characteristics of Spiral Bevel and Hypoid Gears. *ASME Paper 66-MECH-17*, 1966.
- [1.47] Baxter, M.: Exact Determination of Tooth Surfaces for Spiral Bevel and Hypoid Gears. *American Gear Manufacturer's Association Standards, AGMA 139.02*, Oct. 1966.
- [1.48] Krenzer, T.: The Effect of the Cutter Radius on Spiral Bevel and Hypoid Tooth Contact Behavior. *American Gear Manufacturer's Association Standard, AGMA 129.21*, Oct. 1976.
- [1.49] Krenzer, T.: Computer Aided Corrective Machine Settings for Manufacturing Bevel and Hypoid Gear Sets. *AGMA Paper No. 84FTM4*, Oct. 1984.
- [1.50] Krenzer, T.: Tooth Contact Analysis of Spiral Bevel and Hypoid Gears Under Load. *SAE Paper 810688*, 1981.
- [1.51] Understanding Tooth Contact Analysis. The Gleason Works, Rochester, NY, 1981.
- [1.52] Litvin, F.; and Gutman, Y.: Methods of Synthesis and Analysis for Hypoid Gear Drives of Formate and Hexiform. *J. Mech. Design*, vol. 103, Jan. 1981, pp. 83-113.

- [1.53] Litvin, F.; Rahman, P.; and Goldrich, R.: Mathematical Models for the Synthesis and Optimization of Spiral Bevel Gears. NASA CR-3553, 1982.
- [1.54] Litvin, F.; Tsung, W.; and Lee, H.: Generation of Spiral Bevel Gears With Conjugate Tooth Surfaces and Tooth Contact Analysis. NASA CR-4088, 1987.
- [1.55] Litvin, F.; and Lee, H.: Generation and Tooth Contact Analysis of Spiral Bevel Gears With Predesigned Parabolic Functions of Transmission Errors. NASA CR-4259, 1989.
- [1.56] Litvin, F.; and Zhang, Y.: Local Synthesis and Tooth Contact Analysis of Face-Milled Spiral Bevel Gears. NASA CR-4342, 1991.
- [1.57] Litvin, F.: Theory of Gearing. NASA RP-1212, Dec. 1989.
- [1.58] Handschuh, R.; and Litvin, F.: A Method for Determining Spiral Bevel Gear Tooth Geometry for Finite Element Analysis. NASA TP-3096, Aug. 1991.
- [1.59] Fong, Z.; and Tsay, C.: Kinematical Optimization of Spiral Bevel Gears. J. Mech. Design, vol. 114, Sept. 1992, pp. 498-506.
- [1.60] Blok, H.: Measurement of Temperature Flashes on Gear Teeth Under Extreme Pressure Conditions: Proceedings of the Institution of Mechanical Engineers, Proc. vol. 1-2, 1937, pp. 14-20.
- [1.61] Niemann, G.; and Lechner, G.: The Measurement of Surface Temperatures on Gear Teeth. J. Basic Eng., vol. 87, Sept. 1965, pp. 641-654.
- [1.62] Ku, P.; Staph, H.; and Carper, H.: Gear Tooth Scoring Investigation. Report USAAMARDL-TR-75-33, Southwest Research Institute, San Antonio, TX, July 1975.
- [1.63] Doi, Y., et al.: On Bulk Temperature in High-Speed and Heavy-Duty Gears. International Symposium of Gearing and Power Transmissions, Proceedings, Tokyo, Japan, 1981, pp. 247-252.
- [1.64] Winter, H., et al.: Measurement of Pressure, Temperature, and Film Thickness in Disk and Gear Contacts. MPT'91: JSME International Conference on Motion and Power Transmission, Proceedings, Hiroshima, Japan, 1991, pp. 1035-1042.
- [1.65] Turchina, V.; Sanborn, D.; and Winer, W.: Temperature Measurements in Sliding Elastohydrodynamic Point Contacts. J. Lub. Technol., vol. 96, July 1974, pp. 464-471.
- [1.66] Townsend, D.; and Akin, L.: Gear Lubrication and Cooling Experiment and Analysis. NASA CP-2210, 1983, pp. 477-490.

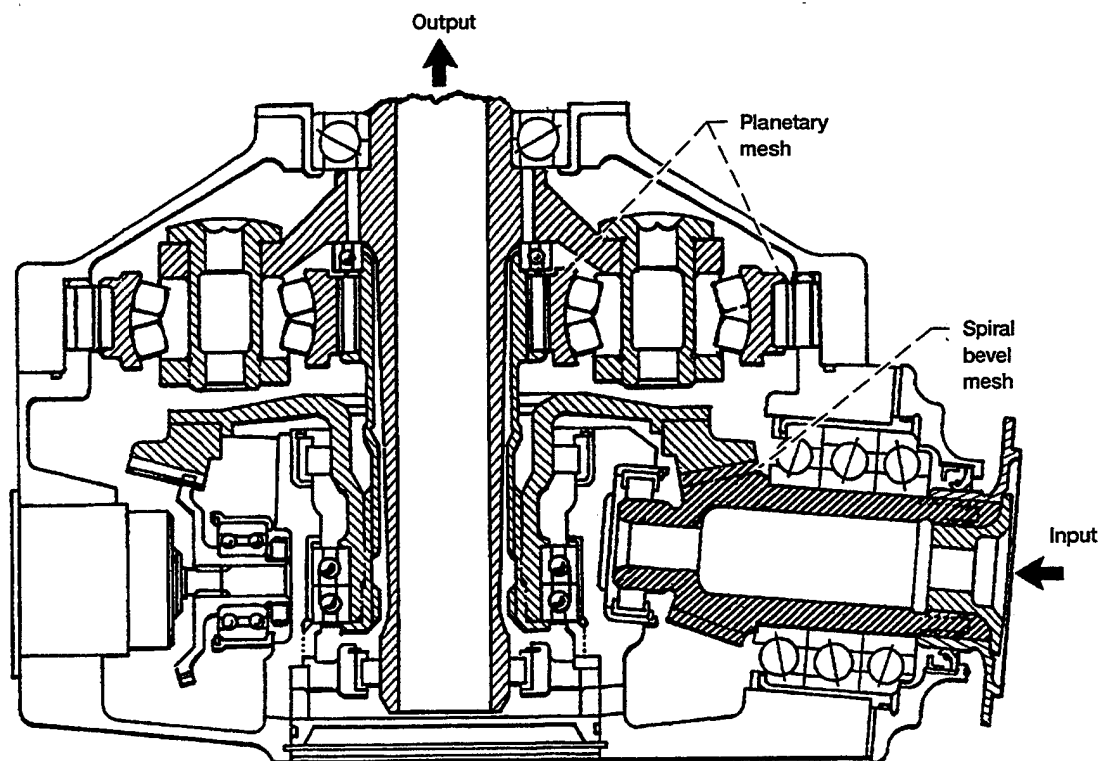


Figure 1.1.1.—OH-5A helicopter main rotor transmission. (Ref. [1.2]).

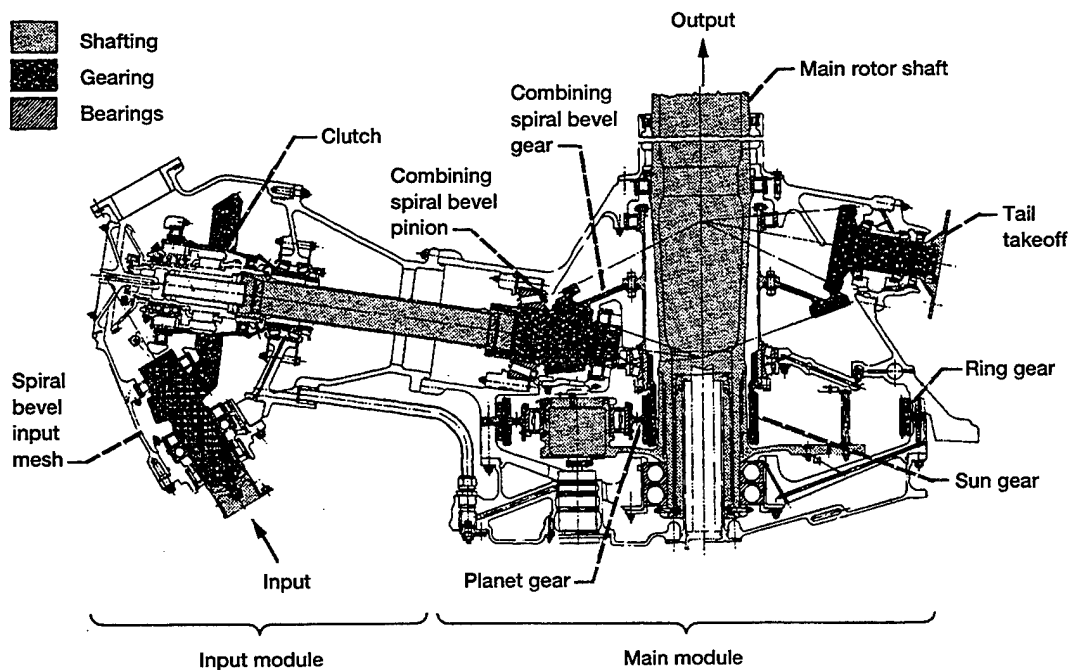


Figure 1.1.2.—Section view along input module and tail of UH60A helicopter transmission (Ref. [1.3]).

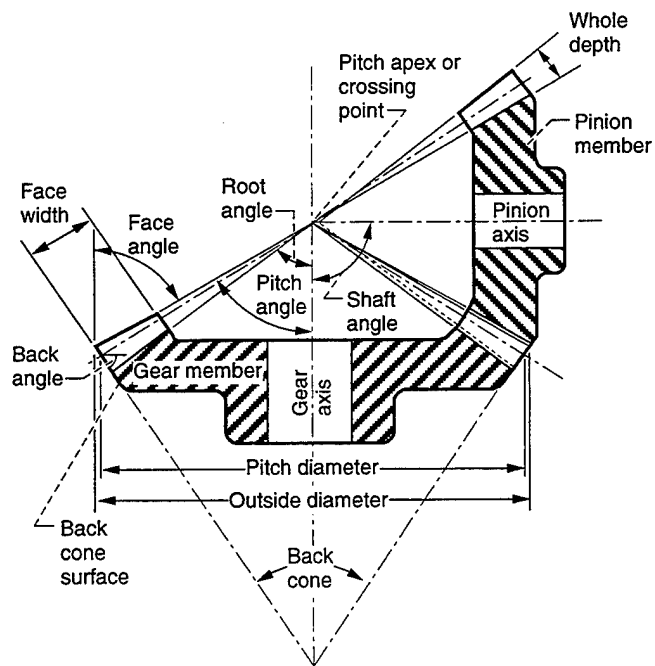


Figure 1.4.1.—Bevel gear nomenclature.

## CHAPTER 2: FLASH TEMPERATURE EVALUATION

### 2.1 Introduction

When any gear system is being designed, an iterative process is required to meet size and weight requirements as well as those for tooth performance with respect to bending and contact stress. The flash temperature expected, or the propensity to have scoring wear, may only be calculated if the combination of high load or high pitch line velocities is among the design requirements. The necessity for investigating flash temperature is shown in Figure 2.1.1 (Refs. [2.1] and [2.2]). The speed and load at which a given gear set must operate determine the wear or failure modes with which one must be concerned.

Spiral bevel gears, as used in typical helicopter applications, usually operate in the range of conditions where scoring is a concern. Most companies that manufacture these gears have their own data base that correlates successes and failures with the conditions imposed on a wide variety of designs. This trial and error approach from the past helps these companies deal with new designs.

In this chapter, the methods currently in use for flash temperature calculation are presented along with the history behind the current practice. Experimental tests to determine flash temperature are investigated and reviewed. The implications and usefulness of the current methods with respect to spiral bevel gears are described.

### 2.2 Historical Perspective of the Flash Temperature Calculation

Flash temperature theory states that under load surfaces that have relative sliding motion will exhibit a large temperature rise in close proximity to the contact region; this temperature rise quickly dissipates via conduction. In gear systems, this flash of temperature quickly decays and the cycle repeats as the contact point again goes through mesh. This phenomenon is shown in Figure 2.2.1. In high speed gearing, this phenomenon also includes forced convection imposed on the surfaces in addition to the conduction that helps to remove heat after the surface in question has had the heat flux applied.

The flash temperature methodology currently utilized began with the work of Blok (Refs. [2.3] and [2.4]). In Reference [2.3], the heat flux mechanism as a function of imposed conditions was analyzed. Several sets of conditions were investigated. One case basically modeled the sliding action behavior in gear systems. In Reference [2.4] these methods were applied to a planetary system in which the gear friction and flash temperature were measured. The gears were chosen so that their contact represented the measurement junction of a thermocouple. Even though the experimental apparatus and measurement system were dated, the basic phenomena measured validated the analytical model that was developed.

The flash temperature equation developed in Reference [2.3] for a moving band heat source is given as

$$T_f = \frac{C_3 \mu P_l |V_{S1} - V_{S2}|}{\left( C_1 \sqrt{V_{S1}} + C_2 \sqrt{V_{S2}} \right) \sqrt{b}} \quad (2.2.1)$$

where  $T_f$  is expressed in degrees centigrade and

$C_3$       0.83, a constant

$\mu$         coefficient of friction

P	specific line load, kg/cm
$V_{S1}, V_{S2}$	sliding velocity of surfaces 1 and 2, cm/s
$C_1, C_2$	thermal parameter equal to the square root of the product of the thermal conductivity, density, and specific heat, $\text{kg}/(\text{°C} \cdot \text{s}^{3/2})$ of gear teeth 1 and 2, respectively
b	half width of the contact band, cm

Equation (2.2.1) is the basis for all calculation procedures that are currently used by designers. The differences, depending on gear type, are geometrical and account for parameters such as load sharing, speed, gear support arrangements, etc. Many of these differences are described in Section 2.3.

This calculation procedure was extended for spiral bevel gears by Coleman (Ref. [2.5]) in whose study the procedure for applying flash temperature theory is developed. The current calculation procedure used by designers of spiral bevel gears has its basis in this work. This work is also presented in great detail with examples in Reference [2.6].

Reference [2.6] also presents the method for determining the geometry factor for a given spiral bevel gear design with known speed and load conditions. This factor is based on tooth geometry (relative radius of curvature), load location and the amount of load sharing, rolling and sliding velocities of the meshing teeth, the size and location of the contact, and the contact orientation. In this reference, some common design configurations are presented graphically. The value of the geometry factor is such that it is based on that contact location where the value will be a maximum. For standard designs, this location is on the pinion addendum and gear dedendum. Along with this value, material properties, loading, diametral pitch, and pinion speed are then used to predict the flash temperature. This is discussed in the next section.

In Ku's study (Ref. [2.7]), among items of interest described and tested were the frictional behavior of typical aerospace materials and lubricants and the associated scoring behavior of spur, helical, and spiral bevel gears. A computerized version of the flash temperature calculation of Reference [2.6] was developed, and a limited number of tests were conducted to check the theory. Ku concluded that some areas needing further attention were understanding the scoring mechanism and the effects of overall gear mechanics.

Analyses of gear thermal behavior using the finite element method are presented in References [2.8] to [2.11]. References [2.8] and [2.9] conducted a thermal analysis of spur gears. Patir (Ref. [2.8]) investigated the effects of heat flux distribution on the bulk temperature distribution. El-Bayoumy (Ref. [2.9]) went further to include a moving heat source (transient boundary conditions) along the meshing tooth surface. Temperature contours through the tooth section were plotted as a function of time for their finite element model. The effects of varying the load and heat transfer coefficient along the model boundaries were studied.

Chao (Refs. [2.10] and [2.11]) conducted a comprehensive study on spiral bevel gears. Dynamic load, lubricant film thickness, and surface temperatures were calculated. An influence coefficient formulation was developed for tooth stiffness and bulk temperature. This formulation was used to predict the dynamic load and the resulting temperature. The prediction of bulk and flash temperatures was made via a three-dimensional model. Only the central contact prediction for temperatures was shown in their results, which were not shown over a complete revolution or a complete transient cycle to document how well their model described the expected outcome based on the original flash temperature theory. Many of their results, however, are consistent with those expected in References [2.5] and [2.6] and in the present study.

This section has described the history of flash temperature calculation procedures and the advances made over the last 50 years with respect to gear systems. As discussed, the recent modeling efforts have used finite

elements, an analysis technique that is very advantageous with respect to the three-dimensional models required for spiral bevel gear studies.

### 2.3 Flash Temperature Calculation for Spiral Bevel Gears

In this section, the flash temperature calculation procedure currently in use for spiral bevel gears is described. This procedure is found in References [2.12] and [2.6]. From Drago (Ref. [2.12]), the equation for flash temperature above the bulk operating temperature for spiral bevel gears is given as

$$T_f = 1.291GW_e^{0.75}S_fP_d^{0.6875}n_p^{0.3125} \quad (2.3.1)$$

where  $T_f$  is in degrees Fahrenheit and

$G$  geometry factor that is a function of spiral angle, pressure angle, and number of teeth in both meshing gears

$W_e$  function of torque and factors that are affected by the design configuration, accuracy of the gears, and operating speed, lb

$S_f$  factor for surface roughness of meshing gears,  $S_f = 50/(50 - S)$  where  $S$  is average roughness,  $\mu\text{in}$ .

$P_d$  diametral pitch, 1/in.

$n_p$  pinion speed, rpm

For the designer, the geometry factor for the meshing point that is critical for flash temperature is represented graphically (Ref. [2.6]) in Figure 2.3.1. Therefore, the speed, load, surface roughness, diametral pitch, and pinion rotational speed determine the magnitude of the flash temperature. This value is then compared with allowable values based on past successes or, if this information is not available, on the information contained in Table 2.3.1 (Ref. [2.12]). This table represents values typically used in aerospace applications. An example of this calculation procedure is given in Appendix A.

If a gear set design is known, the effects of speed and load are found by the repeated use of Equation (2.3.1). For the gear set used in the present study (see Appendix A), the effect of torque with the pinion speed held constant is shown in Figure 2.3.2 and the effect of speed with torque held constant is shown in Figure 2.3.3.

This calculation procedure provides a basis for comparing designs with respect to the flash temperature. To determine an acceptable design, this information is then utilized with the bending and contact stress indices typically found using the methodology of Reference [2.13].

### 2.4 Experimental Measurement of Flash Temperature

The measurement of flash temperature is an extremely difficult task. Meshing gears operating at extremely high loads and high shaft speeds are the important parameters that effect flash temperature and scoring. Instrumentation access to the locations of interest is either extremely difficult or impossible. This section discusses the types of schemes used to measure temperatures in the concentrated contact of gears and other machine elements.

An early work using a geared system was already mentioned in Blok (Ref. [2.4]). The technique used was having two different metallic gear members completing the thermocouple circuit. Experiments conducted in this manner are constrained to operate at low loads with a minimum amount of or no lubricant to maintain the

electrical contact required in the thermocouple circuit. Although these experiments can be helpful to validate the general characteristics of a given analysis model, measurements in this form are not applicable to the high speed and load conditions of a normally operating gearbox.

In a later work (Ref. [2.14]) for spur gears, experimental results also obtained using the meshing gears as a thermocouple were compared with values from the calculation procedure of Blok (Ref. [2.4]). Using a dynamic load measured via strain gages produced good agreement with the analytical prediction.

Infrared and other optical techniques have also been used to characterize the behavior within concentrated contacts (Refs. [2.15] and [2.16]). In these references, a sapphire disk is used to allow optical access to the location in question. Measurements are made with the sapphire member in contact with a steel member of a geometrical configuration of interest. Only simple geometry can be used in this type of study and maximum contact pressures are limited to about 50 percent of what is considered a maximum for a gear tooth surface. These studies, however, are beneficial in verifying the analytically predicted behavior in concentrated contacts, and they also demonstrate that very high temperatures can be attained within these contacts. This technique has also been used to study other temperatures of interest in grinding (Ref. [2.17]) and in face seal systems (Ref. [2.18]).

The problem with using the infrared technique for gear systems is that the measurements cannot be made in the desirable contact region because of the lack of a line of sight: the meshing teeth mask the area of interest.

The infrared technique has been used to study spur gears (Refs. [2.19] and [2.20]) and spiral bevel gears (Refs. [2.21] and [2.22]). Although measurements cannot be made at the source of the heat generation between the meshing gears, the information obtained can still be used to check transient thermal models. The measurement location is fixed, but the rotating teeth present a position-varying temperature signal when the gear profile is in view and in motion. Even though the heat flux applied is being conducted and convected away, a position-varying temperature corresponding to different conditions along the gear profile is measurable. This means that the position-varying flashes of temperature on the active profile cause a nonuniform temperature over the gear body.

The most recent and promising technique for experimentally investigating the phenomena associated with concentrated contacts is to make measurements using thin-film sensors (Refs. [2.23] and [2.24]). These sensors, sputtered onto the surface in question, are very thin with the entire sensor being just a few micrometers thick. In References [2.23] and [2.24], resistance gages were used to measure the temperature. Kannel (Ref. [2.23]) used this technique on a spur gear mesh. The sensor thin film was titanium. The gear tooth that mated with the instrumented one was machined so that contact occurred only over a portion of the face width; thus, contact with the instrument connection wires was avoided. The high frequency response of the sensor was attained and the temperature change due to the meshing process was measured.

In Winter (Ref. [2.24]), disks and gears were tested. Temperature and pressure measurements were also made using the thin-film technique. Manganine was used for the pressure sensors and platinum for the temperature sensors.

In both References [2.23] and [2.24], measured temperatures were compared with theory. In both studies the experimental measurements were close to the theoretical predictions.

## **2.5 Improvements Needed in the Flash Temperature Methodology for Spiral Bevel Gears**

The method presented herein and currently being used to rank designs with respect to flash temperature still does not fully account for all the possible variables. For aerospace applications in a dry sump mode with

jet-lubricated and scavenged lubrication systems, jet positioning can have a great effect on bulk temperature for the same operational speed and load (Ref. [2.22]). Also, depending on the jet location, the lubrication system can act as a "flash cooling" heat sink to the active profiles of the meshing gear teeth. Lubrication system effects on the flash temperature are currently totally neglected.

Another shortcoming of the current flash temperature calculation method is that seemingly similar designs of spiral bevel gears can have differences in contact patterns and meshing kinematics. Slight variations in manufacturing machine tool settings can produce gear systems with drastically different contact patterns and heat generation. These differences cannot be examined on the basis of the analysis of Reference [2.6] because only the basic gear design data are used to conduct the analysis. A tooth contact analysis of the meshing gear systems and the surface geometry must be used simultaneously to calculate meshing point velocities and curvatures and orientations of the surfaces at these locations.

Another simplifying assumption made in the current flash temperature calculation is that only conduction causes the flash temperature to quickly subside and return to some overall bulk temperature of the gear/lubrication system combination. This phenomenon occurs such that the bulk temperature is reached and the process is then repeated in a cyclic manner. In high speed gear systems, forced convection to the surroundings also must be considered a participant in the removal of the meshing heat flux. From the bulk temperature measurements of Handschuh (Ref. [2.22]) for spiral bevel gears, it is obvious that different locations of the gear tooth can operate at drastically different temperatures. Therefore, to have a better characterization of this phenomenon, a more complete analysis methodology as well as experimental evidence are needed. Experimental tests using aerospace quality gears are described in Chapter 3. In Chapters 4 to 6, an analytical procedure using a three-dimensional model is developed to conduct a three-dimensional finite element heat transfer analysis of meshing spiral bevel gears.

## REFERENCES

- [2.1] Borsoff, V.: Predicting the Scoring of Gears. *Mach. Design*, vol. 37, Jan. 1965, pp. 63-71.
- [2.2] Townsend, D.: Lubrication Considerations in Gear Design. NASA TMX-52942, 1970.
- [2.3] Blok, H.: Theoretical Study of Temperature Rise at Surface of Actual Contact Under Oiliness Lubricating Conditions. *Proceedings of the Institution of Mechanical Engineers. Gen Disc. Lubrication*, vol. 2, 1937, pp. 222-235.
- [2.4] Blok, H.: Measurement of Temperature Flashes on Gear Teeth Under Extreme Pressure Conditions. *Proceedings of the Institution of Mechanical Engineers*, vol. 1-2, 1937, pp. 14-20.
- [2.5] Coleman, W.: A Scoring Formula for Bevel and Hypoid Gear Teeth. *J. Lub. Technol.*, vol. 89, Apr. 1967, pp. 114-126.
- [2.6] Scoring Resistance of Bevel Gear Teeth. The Gleason Works, Rochester, NY, 1966.
- [2.7] Ku, P.; Staph, H; and Carper, H.: Gear Tooth Scoring Investigation. Report USAAMRDL-TR-75-33, Southwest Research Institute, San Antonio, TX, July 1975.
- [2.8] Patir, N.; and Cheng, H.: Prediction of the Bulk Temperature in Spur Gears Based on Finite Element Temperature Analysis. ASLE Preprint 77-lc-3b-2, Oct. 1977.
- [2.9] El-Bayoumy, L.; Akin, L.; and Townsend, D.: An Investigation of the Transient Thermal Analysis of Spur Gears. *J. Mech., Trans., and Aut. Design*, vol. 107, Dec. 1985, pp. 541-548.
- [2.10] Chao, H.; and Cheng, H.: A Computer Solution for the Dynamic Load, Lubricant Film Thickness and Surface Temperatures in Spiral Bevel Gears. NASA CR-4077, 1987.
- [2.11] Chao, H.; Baxter, M.; and Cheng, H.: A Computer Solution for the Dynamic Load, Lubricant Film Thickness, and Surface Temperatures in Spiral Bevel Gears. *Gear Technol.*, Mar./Apr., 1986, pp. 9-15, 26-30.
- [2.12] Drago, R.: *Fundamentals of Gear Design*, Butterworth Publishers, Stoneham, MA, 1988.
- [2.13] Rating the Pitting Resistance and Bending Strength of Generated Straight Bevel, ZEROL Bevel, and Spiral Bevel Gear Teeth. American National Standard Institute/American Gear Manufacturer's Association Standard, ANSI/AGMA 2003-A86, June, 1988.
- [2.14] Tobe, T., and Kato, M.: A Study on Flash Temperature on the Spur Gear Teeth. *J. Eng. Ind.*, vol. 96, Feb. 1974, pp. 78-84.
- [2.15] Wedeven, L.: Preliminary Study of the Use of Infrared Radiation to Reveal Lubrication Behavior. NASA TM X-67883, 1971.
- [2.16] Turchina, V.; Sanborn, D.; and Winer, W.: Temperature Measurements in Sliding Elastohydrodynamic Point Contacts. *J. Lub. Technol.*, vol. 96, July, 1974, pp. 464-472. (Also, ASME Paper 73-LUB-23, 1973.)

- [2.17] Chandrasekar, S.; Farris, T.; and Bhushan, B.: Grinding Temperatures for Magnetic Ceramics and Steel. *J. Tribol.*, vol. 112, July 1990, pp. 535-541.
- [2.18] Tournier, B.; Reungoat, G.; and Frene, J.: Temperature Measurements by Infrared Thermography in the Interface of a Radial Face Seal. *J. Tribol.*, vol. 112, Oct. 1990, pp. 1-6.
- [2.19] Townsend, D.; and Akin, L.: Analytical and Experimental Spur Gear Tooth Temperature as Affected by Operating Variables. *J. Mech. Design*, vol. 103, Jan. 1981, pp. 219-226.
- [2.20] Townsend, D.; and Akin, L.: Gear Lubrication and Cooling Experiment and Analysis. Presented at the International Symposium on Gearing and Power Transmission, Proceedings, Tokyo, Japan, Sept. 1981.
- [2.21] Wymer, D.; and Macpherson, P.: An Infra-Red Technique for Monitoring Gear Tooth Surface Temperatures. Research Paper RP 458, Imperial College, London, England, Jan. 1974.
- [2.22] Handschuh, R.: Effect of Lubricant Location on Spiral Bevel Gear Operating Temperatures. NASA TM-105656, 1992.
- [2.23] Kannel, J.; and Bell, J.: A Method for Estimation of Temperatures in Lubricated Rolling-Sliding Gear of Bearing Elastohydrodynamic Contacts. *Proceedings of the Institution of Mechanical Engineers*, Jan. 1972, pp. 118-130.
- [2.24] Winter, H., et al.: Measurement of Pressure, Temperature, and Film Thickness in Disk and Gear Contacts. MPT'91: JSME International Conference on Motion and Power Transmission, Proceedings, Hiroshima, Japan, 1991, pp. 1035-1042.

TABLE 2.3.1—ALLOWABLE FLASH TEMPERATURE  
FOR 9310 GEAR STEEL AND SPIRAL BEVEL

GEAR DESIGN (From Ref. [2.12])

Oil type	Allowable flash temperature	
	°C	°F
MIL-L-7808 or 23699	257	495
Mineral oil (SAE 30)	182	360
MIL-L-2105	343	650
EP90	649	1200

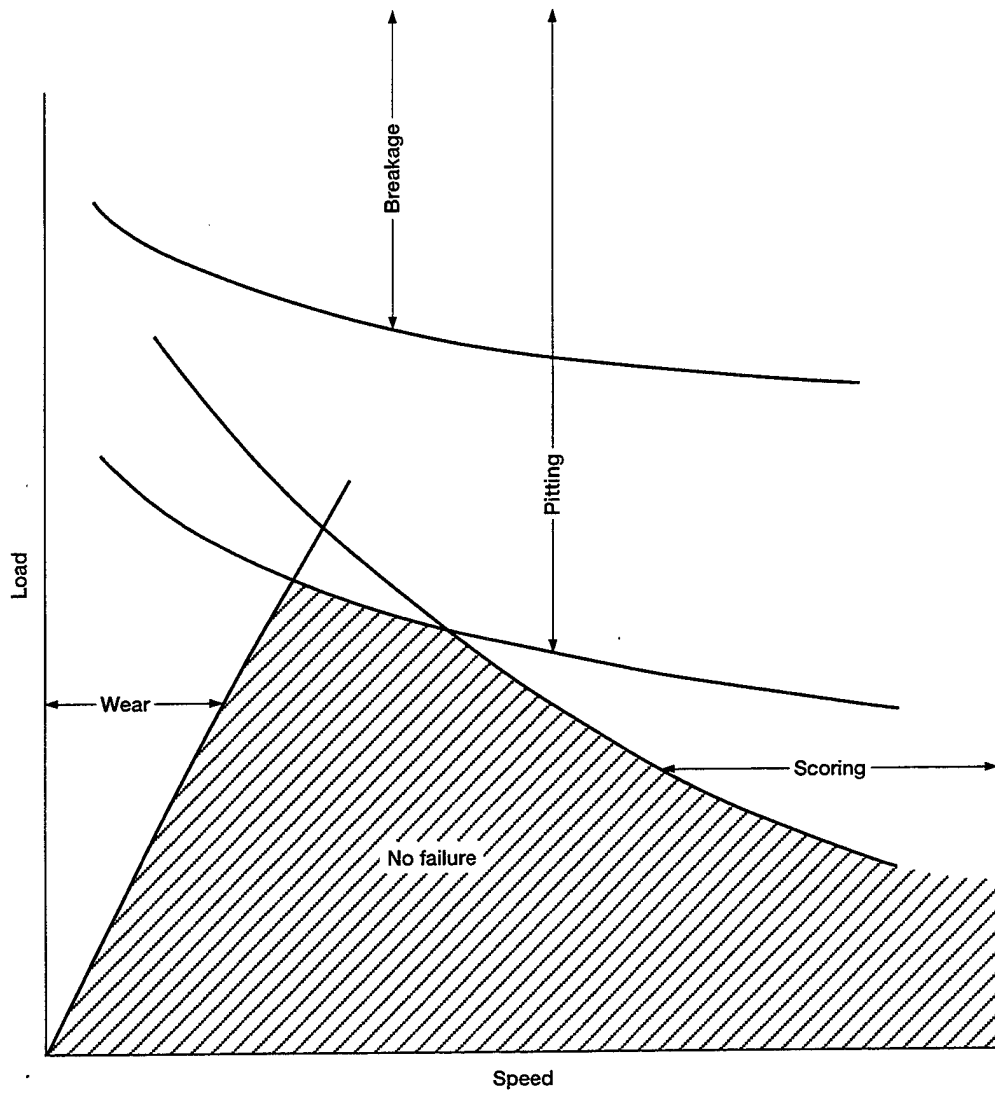


Figure 2.1.1.—Gear design parameters of concern based on operating conditions (Ref. [2.1, 2.2]).

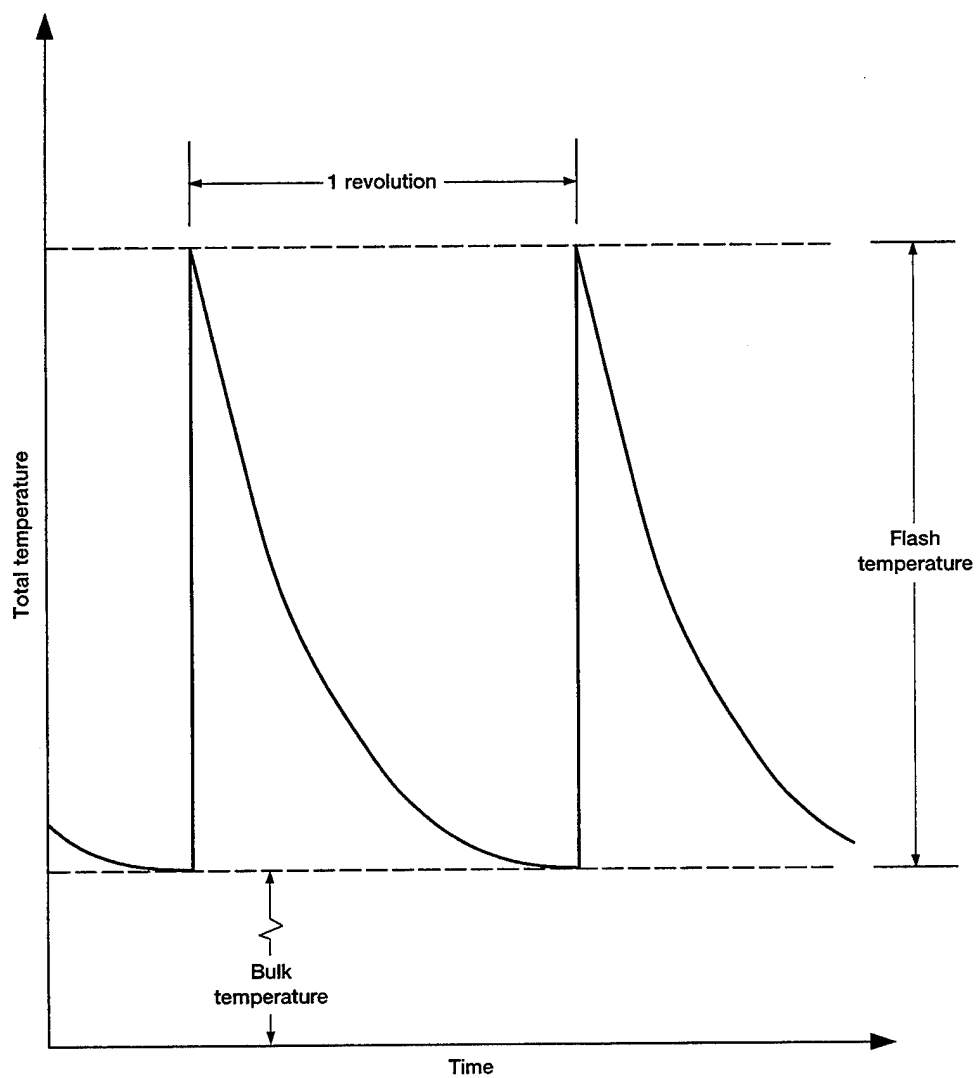


Figure 2.2.1.—Temperature history of a point on the surface of a body exposed to a heat flux due to relative sliding as in a gear system.

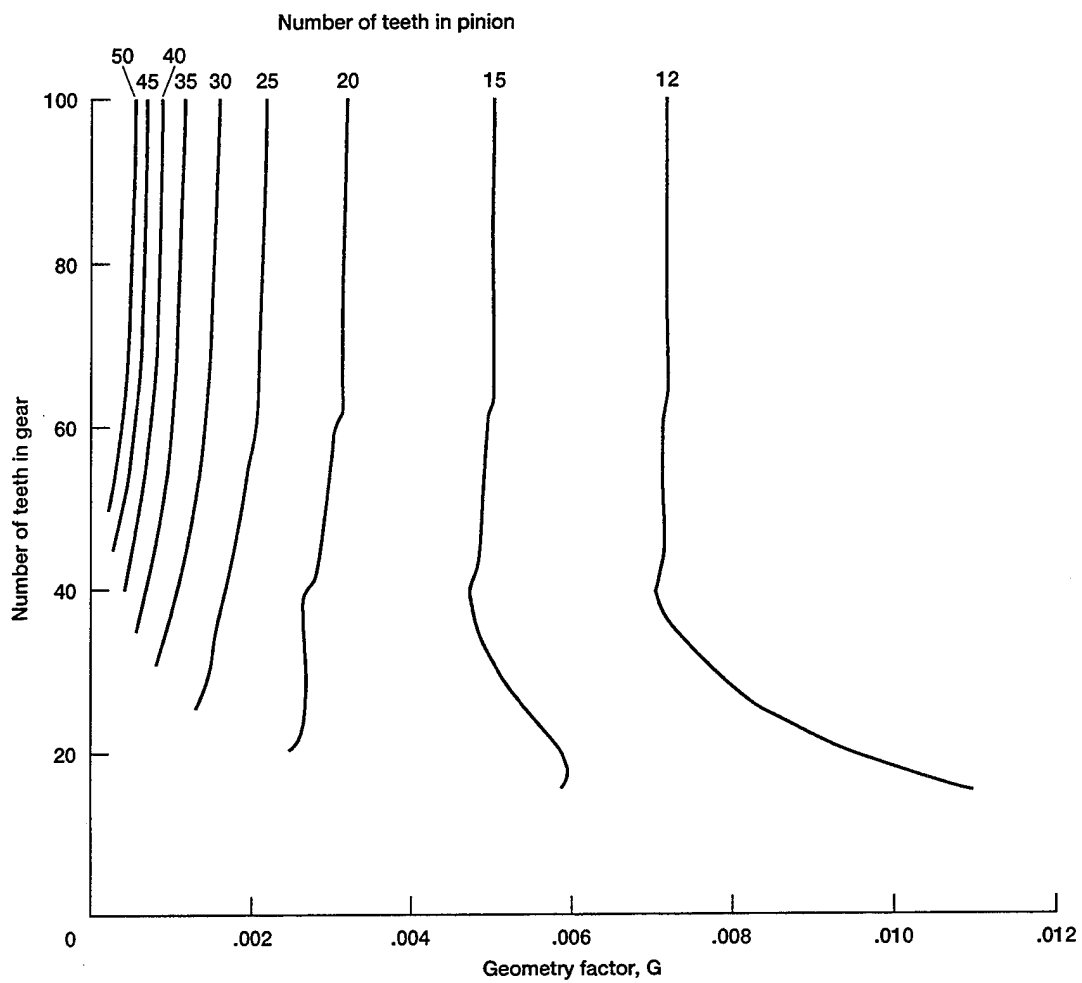


Figure 2.3.1.—Geometry factor for spiral bevel gears with 25° pressure angle, 35° spiral angle, and 90° shaft angle (Ref. [2.6]).

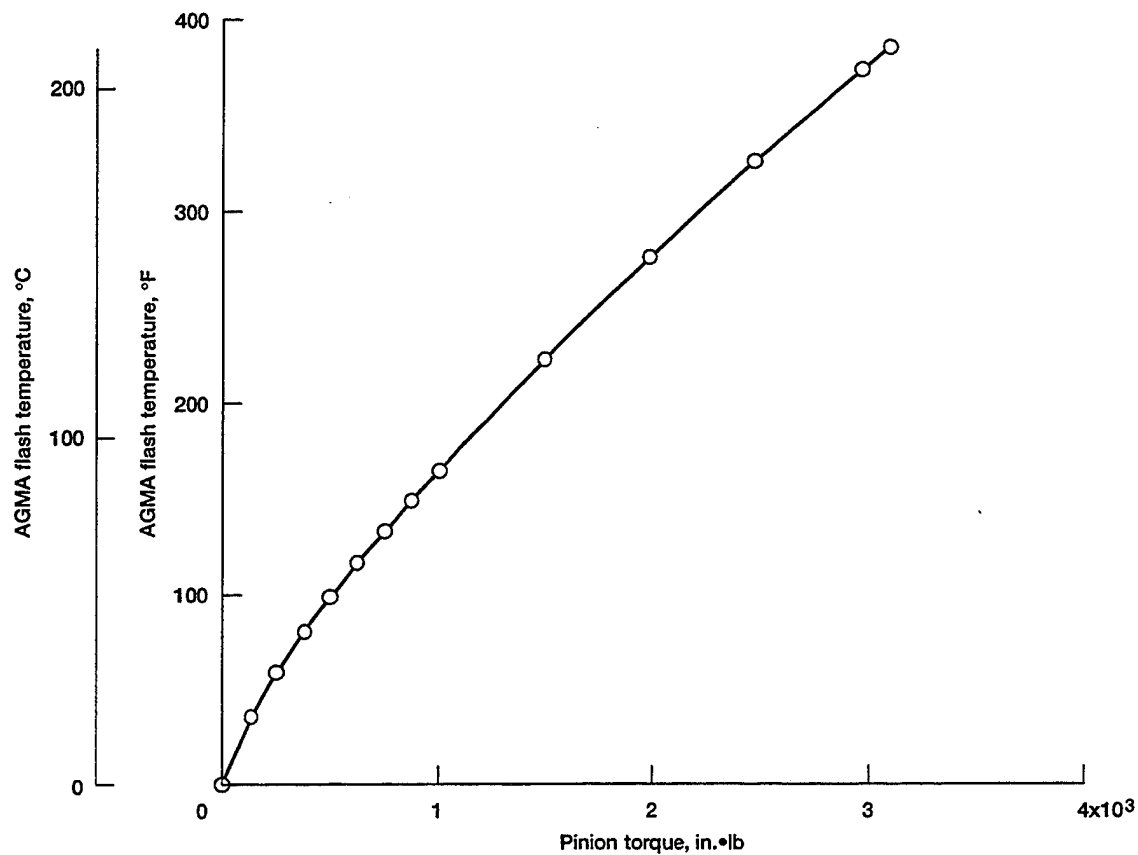


Figure 2.3.2.—Flash temperature based on Equation 2.3.1 for constant speed with torque varying. Pinion speed held constant at 14 400 rpm.

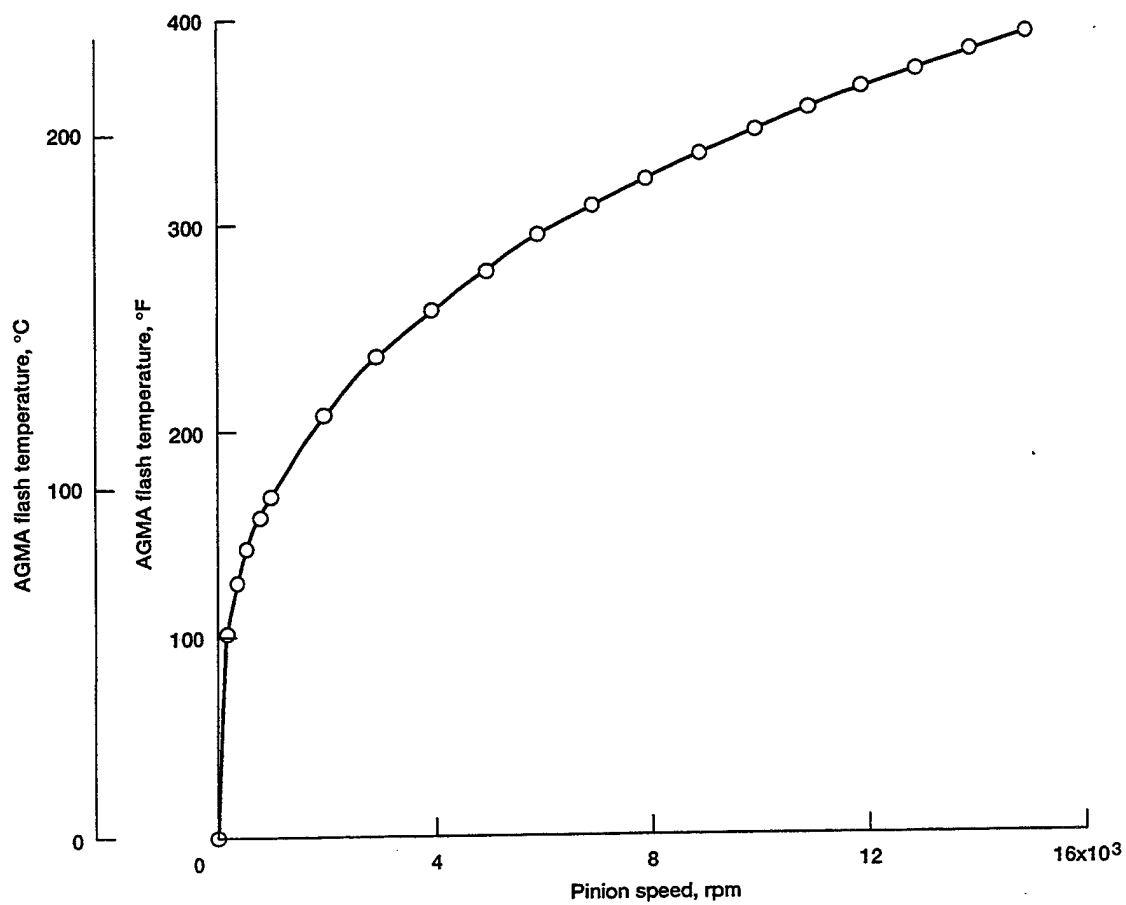


Figure 2.3.3.—Flash temperature based on Equation 2.3.1 for constant torque with varying speed. Pinion torque held constant at 3130 in•lb.

## CHAPTER 3: TEST FACILITY AND EXPERIMENTAL RESULTS

### 3.1 Introduction

The test facility used in the experimental evaluation described in this study is the Spiral Bevel Gear Test Rig at the NASA Lewis Research Center. The facility uses a closed-loop system in which two sets of spiral bevel gears are tested simultaneously. A facility such as this allows high power and high speed operation with a minimum amount of supply power. The drive motor only needs to overcome the system losses from the gears and bearings. This keeps the cost of operation low in comparison with an open-loop system.

The experimental hardware and the test results are also discussed. Three measurement schemes for the thermocouple placement and type were attempted. The use of an infrared microscope to determine the operating temperature of the test hardware was also investigated. The data collected are compared with the analysis developed in this study in Chapter 7.

### 3.2 Description of Test Facility

A thorough description of the test facility operation is now presented. A sketch of the facility is shown in Figure 3.2.1. Rotational motion of the facility is provided by V-belts from the drive motor to the axial stationary helical gear shaft. A second helical gear is used to apply or change the loop load by moving axially with respect to the stationary helical gear. A nitrogen-gas-activated thrust piston moves the helical gear axially. The axial motion provides the thrust load component of the helical gear forces. The loop load is measured with an in-the-loop torquemeter. Shaft speed is measured by a 60-tooth gear and magnetic pickup inside the torquemeter. A cross section of the facility is shown in Figure 3.2.2. The spiral bevel gear set on the left side operates in the normal speed reducer mode where the pinion drives the gear. The right side operates in reverse where the gear drives the pinion. Both gear meshes, however, are loaded in the typical mode of the concave side of the pinion meshing with the convex side of the gear. The overall facility operational parameters are shown in Table 3.2.1 and the basic gear design parameters of the test hardware are shown in Table 3.2.2. A photograph of the test hardware is shown in Figure 3.2.3. The installation of the components in the facility is shown in Figure 3.2.4. The left side is the test side and the right the slave side. All instrumented pinion and infrared measurements were taken from the test, or left, side of the facility.

The facility and test hardware lubrication schematic is shown in Figure 3.2.5. An overall system pump supplies oil at approximately 0.62 MPa (80 psi) to the facility components after running through a 3- $\mu$ m filter and heat exchanger. The oil inlet temperature to the facility, not including the test hardware, is maintained at 38 °C (100 °F). Also, from the high pressure supply of the lubrication system, a boost pump can increase or decrease the system pressure. This pump takes the oil from the facility lubrication system and increases pressure as well as oil inlet temperature independent of the facility components. This allows test hardware to be exposed to a wide variation of lubrication conditions.

### 3.3 Description of Test Instrumentation

The test facility instrumentation is used not only to take some of the test data but also to monitor the facility's operational state. A sketch of the facility instrumentation locations is shown in Figure 3.3.1.

Four facility parameters are monitored: temperature, acceleration, lubricant flow, and lubricant pressure. Thermocouple data are monitored continuously during the test, and other data such as speed and load are

manually taken at approximately 10-minute intervals during experimental tests. A sample of typical thermocouple data is shown in Figure 3.3.2. Not only facility bearing temperatures are monitored but test data such as oil inlet temperature and oil fling-off temperature at the test hardware are recorded. Note that modification to parameters such as flow to the test hardware had no effect on the test facility. Only the temperature of the oil being flung from the meshing gears changed.

Three lubrication parameters for the test gears are continuously monitored: lubricant jet pressure, lubricant flow rate, and oil inlet temperature just prior to the test hardware lubricant jet. These data are necessary for conducting the present study of the experimental results.

Accelerometers are used to monitor the facility's vibrational output. For the tests conducted herein, their use was only for assessing test facility health. Increased levels beyond set limits will cause automatic facility shutdown.

### 3.4 Description of Test Hardware

The spiral bevel gear test specimens that were instrumented for the experimental phase of this project are now described. Three different instrumentation schemes were used in this study.

The first specimen was instrumented as shown in Figure 3.4.1 (Ref. [3.1]). Here, thermocouples on the top, toe, and heel were buried approximately 0.76 mm (0.03 in.) below the gear surface. In the root area, the thermocouple was attached to the surface using an epoxy adhesive. The purpose of this thermocouple scheme was to provide bulk gear temperatures at various locations on the gear body where contact with the mating gear member was avoided. This scheme will provide heat distribution data for the faces of the gear body.

The second instrumented specimen had thermocouples buried in the active profile. The thermocouple wires were run from the tooth top to approximately one half the tooth height at three axially spaced locations along the face width of the pinion. Grooves were electrodischarged machined (EDM) into the active surface to form a channel 0.25 by 0.25 mm (0.01 by 0.01 in.). These grooves were made on two different teeth with two different diameters of thermocouple wire, 0.25 and 0.75 mm (0.001 and 0.003 in.). A sketch of the test specimen is shown in Figure 3.4.2. Two thermocouples were also installed at the tooth top and root as with the first instrumented specimen. The purpose of this gaging scheme was to determine whether conventional thermocouples could capture the thermal transient during gear meshing. For these small-diameter thermocouples, if the response is calculated assuming a one-dimensional model the same thickness as the wire nominal diameter (0.025 mm (0.001 in.)), the response rate should be to 50 kHz.

The third instrumented specimen used thin-film sensors. The gages were sputtered onto the surface with an accumulated layer thickness of 6.0  $\mu\text{m}$  (236  $\mu\text{in.}$ ). This thickness included a  $\approx 4\text{-}\mu\text{m}$ - ( $\approx 157\text{-}\mu\text{in.}$ ) thick insulating layer and a 2- $\mu\text{m}$  (79- $\mu\text{in.}$ ) thermocouple layer (see Table 3.4.1). A sketch of the test hardware is shown in Figure 3.4.3. The purpose of this gaging system was to determine whether this technology was applicable to transient surface measurements in gear tooth contacts. This gaging system requires full film lubrication to separate the meshing gears. Photographs of the three instrumented test pinions are shown in Figures 3.4.4 to 3.4.6.

Data from the rotating test hardware were transferred to the data acquisition system via a slip ring. A diagram of the wire connection used for the tests is discussed in Section 3.7. A photograph of the slip ring used during the tests is shown in Figure 3.4.7. Depending on the speed at which the data were to be taken, the thermocouple output was either read directly by a lab computer (steady state data) with an internal reference junction or from a tape recorder (transient data). The taped data can then be played back into a personal computer, which contains an analog-to-digital board with conversion speeds in excess of 250 000 samples per

second. Therefore, tape-recorded data can be replayed and analyzed later rather than trying to accomplish the high speed analog-to-digital conversion during the actual test.

### 3.5 Calibration of Test Instrumentation

The focus of the test instrumentation was calibrating the infrared microscope used to monitor the surface temperature of the test hardware. Many of the techniques used to calibrate the infrared system for a gearing application came from the work of Wymer and Townsend (Refs. [3.2] and [3.3]). The measurement presents many problems when trying to view the gear system in this study. All the environmental effects simulated during the calibration were accounted for in the results extracted from the actual test data. The following discussion documents how the infrared system was calibrated for making steady state and transient gear surface temperature measurements. The following effects are discussed: surface emissivity, lubricant, and sapphire lens attenuation.

First, a brief description of the system, as used in the tests conducted herein, is presented. An overall facility schematic of the infrared microscope is shown in Figure 3.5.1. The infrared microscope (Ref. [3.4]) consists of a liquid-nitrogen-cooled sensor that responds to infrared radiation in the wavelength band from 1 to 10  $\mu\text{m}$  (39.4 to 394  $\mu\text{in.}$ ). An eyepiece that uses the same optical path is used to align the location where the measurement will be made. The instrument lens had a focal length of 23 cm (9 in.) with a measurement spot size of 0.51 mm (0.02 in.). The system has a transient response capability to 15 kHz.

The instrument can be operated in a time-averaged or transient mode. When operated in the time-averaged mode, the incoming signal is chopped by an internal chopper. A comparison of the ambient chopper temperature and the incoming infrared signal is then displayed on an analog meter. The emissivity of the measured surface must be known to directly read out the time-averaged temperature. Five scales can be assessed to determine the measured value. Two of the scales permit measuring temperatures from 15 to 165  $^{\circ}\text{C}$  and the other three scales permit reading out infrared power ( $\text{W}/(\text{cm}^2\text{-ster})$ ), which the manufacturer refers to as radiance. Thus, one instrument can be used in the time-averaged mode to measure temperatures from 0 to 3000  $^{\circ}\text{C}$ . The data presented herein were all read via the 15 to 165  $^{\circ}\text{C}$  range on the instrument.

Operation of the instrument in the transient mode is quite different. The instrument's internal chopper stops and the output is a time-varying voltage that is related to the temperature fluctuations of the surface passing beneath the measurement spot. For the tests performed herein, the signal was band-pass filtered before being displayed or stored in a dual-channel oscilloscope (see Fig. 3.5.1). At the same time, a proximity probe was used to locate the tooth tip in the dual time signal being recorded by the oscilloscope.

Before the test was conducted, the orientation between the infrared signal and the proximity probe was established. A protractor was fixed to the housing that contains the pinion shaft. An orientation line scribed on the end of the pinion shaft was used as the measurement source. The proximity probe was first aligned by looking at the oscilloscope and determining when the gap was minimized or the tooth top center was above the probe; then the angular location was noted. Next, while looking through the eyepiece of the infrared microscope, the pinion was rotated until the center of the tooth top appeared in the cross hairs of the lens. Again, the angular orientation was noted. The difference between the two positions provides the lead-lag of the two instrumentation signals.

A detailed view of the infrared path between the gear tooth surface and the microscope sensor is shown in Figure 3.5.2. As seen from this figure, many obstacles must be considered in the measurement process. To fully understand the measurement being made, the effects of all of these obstacles must be considered when making calibrations.

To be able to look optically inside a gear box at the gear surfaces requires a lens with at least high transmissibility, or minimum signal attenuation, in the infrared wavelength range as well as the ability to keep the lubricant inside. Even though the lubricant used for the results presented herein was jet fed and gravity scavenged away from the rotating components, a great deal of windage still resulted. As described, this infrared measurement could only be made when the lubricating jet was placed in certain locations: otherwise, the air-oil-mist windage obstructed the optical path between the infrared microscope and the gear surface.

Again, referring to Figure 3.5.2, the scheme used in the test facility to measure the infrared signal is discussed. The system consists of the sapphire lens, an air purge port, a large outer tube, and a small inner tube. The large outer tube prevents the overall windage from passing in the optical path. The inner tube is supplied with a purge air (shop air at approx 0.03 MPa (5 psi)) to keep the sapphire lens free of oil mist and to keep any other windage from climbing up the smaller measurement tube. Many schemes were tried but this arrangement was the best. During the facility operation, visual tests were conducted to verify the scheme described.

**Steady State Calibration:** The first parameter, surface emissivity, is a function of the thickness of the oil film layer (Ref. [3.2]). When a layer of oil is between the infrared microscope and the surface of interest, the measurement made includes the infrared radiation emitted from the oil as well as that of the surface. To investigate this effect, a calibration dish was constructed (Fig. 3.5.3). The dish was made from the same material and was machined to the same surface finish as the test gears. A thermocouple was located at the surface to provide an independent temperature reference.

The dish was heated, and data were taken for the indicated infrared temperature versus the actual temperature. These data are shown for three different conditions in Figure 3.5.4. What can be seen is that the effect of the oil film thickness on the indicated temperature can be adjusted by the emissivity setting on the infrared microscope. This setting effectively acts as an amplifier adding gain to the signal as the emissivity decreases to values less than 1.0 (blackbody). The actual surface emissivity is determined using the calibration methodology presented here along with the thermocouple data.

The effect of the sapphire lens on the infrared signal is to attenuate the signal strength. The effect of the attenuation was found by inserting the sapphire lens used during testing into and out of the optical path of the infrared microscope. This effect is shown in Figure 3.5.5. The net result is that the sapphire lens has an approximately constant 10 °C (18 °F) attenuation over the range of the calibration from 75 to 125 °C (167 to 257 °F).

**Transient Calibration:** The instrument used in the test reported herein has a transient response capability of 15 kHz. This value is five times that of the gear meshing frequency so the instrument is capable of responding to the surface-varying temperature. The transient calibration procedure basically follows that of the steady state already presented, with one addition. A mechanical shutter was required to present the infrared system with a time-varying temperature field because in the transient mode, if a constant temperature, regardless of magnitude, is presented to the detector, no output will be indicated. A sketch of the mechanical shutter system is shown in Figure 3.5.6. Tests were conducted using either a blackbody source or the calibration dish made from the same material and having the same surface finish as the spiral bevel gear test hardware. An example of the calibration data obtained is shown in Figure 3.5.7. The effects of system output with respect to surface emissivity differences are shown in Figure 3.5.8. The temperature of the rotating shutter was near ambient and the blackbody source, or calibration dish, was heated. What can be seen from this figure is that the lower the emissivity, the lower the system detector output. The effect of the lens in the optical path was again checked during the transient calibration. The results of these tests are shown in Figure 3.5.9.

It has been shown that the proper calibration of the test system is essential to fully understand the output from the test components. Neglecting any of these effects will underestimate the actual operating conditions of the test hardware because the measured signal can, in the tests conducted herein, be an attenuated level of the

actual surface temperature. What also should be mentioned at this point is that the measurements are made at a rotational distance away from the location of meshing, or heat flux input into the gear surfaces. In this study, the location was approximately 120° out of mesh on the pinion. The data given are therefore an indication of the surface temperature field at the position of the measurement.

### 3.6 Calibration of Test Hardware

The test hardware calibration was checked using three known reference temperatures: ice water bath and ambient and boiling water. This calibration was done on the bulk temperature thermocoupled pinion. Circuitry was connected through slip rings, connecting wiring, and laboratory computer just as it would be used in the actual test. Thermocouples were typically within 0.6 °C (1 °F) of the expected temperature.

One of the major concerns when making a temperature measurement from rotating test hardware is the effect of the slip ring, discussed in the following section.

### 3.7 Rotating Thermocouples and Slip Rings

The data taken from the rotating test hardware, in all cases, had to pass through a slip ring. While at first glance this may appear to be of little significance, a measurement error problem can occur as a result of this arrangement. The problem can be thought of as one of lead wire effects with multiple material changes and temperature junctions as treated by Moffat (Ref. [3.5]). In this reference, Moffat discusses the effects of lead wire changes and thermal gradients in the measurement circuit and demonstrates a method, based on thermal gradients along the lead wires, to analyze the thermocouple circuit.

In the measurement system used in the experiments reported herein for the instrumented pinion, the same problem can exist. The circuit used is shown in Figure 3.7.1. For the bulk thermocouples, measurements were made by a lab computer that had an internal reference temperature compensation. Note from Figure 3.7.1 that there is more than one junction contained in the measurement circuit; at the slip ring, there are connections for the static and rotating thermocouple leads as well as contacts between the stationary slip ring brushes and rotating rings. Each of these can affect the measurement, but if all junctions remain at essentially the same temperature, their effects disappear. It seems plausible that the internal rings and brushes would operate at nearly the same temperature. Of concern was whether or not the stationary thermocouple wire connection and the rotating thermocouple connection would remain at similar temperatures during a test. This slip ring was used at shaft speeds to 14 400 rpm. The circuit arrangement to test this effect is shown in Figure 3.7.2. One thermocouple was on the test hardware as used during the tests; a second was attached to the static connection terminal; and the third was run through the slip ring and attached on a rotating terminal of the slip ring. A number of tests were run to check out this effect. A typical set of test conditions is shown in Figure 3.7.3. In this figure, the facility was started and ramped to full conditions quickly (14 400 rpm; 354 N · m (3130 in. · lb)). From these measurements it is apparent that the rotating and stationary thermocouple measurements were similar, and also over the test time shown here, the slip ring had not reached steady state operational temperature. The test hardware had reached steady state prior to the slip ring. Since the two thermocouples gave very similar measurements, the effect of temperature differences across the slip rings on the measured data was assumed to be negligible. No corrections were applied to the data that will be presented later. If there had been a large differential, the gradient approach discussed by Moffat (Ref. [3.5]) would have been required to correct the measurements made.

### 3.8 Experimental Results From Thermocoupled Pinions

The results obtained from the thermocoupled spiral bevel pinions are now discussed. As mentioned in Section 3.4, three measurement schemes were used on the pinions. Thermocouple locations on the pinions were chosen to permit certain types of measurements to be made. As will be seen for specific schemes, a great deal of data was taken and in other cases the useful data obtained before pinion/instrumentation failure were limited. In all tests, the lubricant used was that comparable to, or the same as, the synthetic lubricant used in aerospace drive systems. Parameters with respect to flow and pressure were only changed on the test hardware. Oil inlet conditions for the test facility were maintained at 38 °C (100 °F) for most of the test program.

**Bulk Temperature Measurement Pinion:** The first test specimen results discussed are those made from the bulk temperature measurement pinion. Instrumentation locations were shown schematically in Figure 3.4.1 and in the photograph of Figure 3.4.4. Four locations were monitored. All instrumentation locations were in regions that were not in direct contact with the gear meshing action. This arrangement provided a very robust measurement system with the drawback that active profile data were not attainable. The data to be presented on this hardware, however, were used with the infrared data (to be discussed in Section 3.9) to help tune the convection boundary conditions needed for the analysis and comparisons to be made in later chapters.

With the system just described, many parameters of interest could be varied and the effect on the pinion temperature measured. Data were taken by a laboratory computer that had reference temperature compensation provided electronically. Connection to the computer was accomplished using slip rings as shown in Figure 3.7.1.

The bulk temperature was measured once the facility had reached steady state from either the initial startup or a new operational condition. Reaching steady state usually took about 10 minutes and then the data were recorded. Load, flow rate, shaft speed, lubricating jet location, lubricant jet type, lubricant jet size (diam), and oil inlet temperature were the parameters varied during the course of testing.

The results were obtained using a single lubricating jet of two different types as shown in Figure 3.8.1. (Ref. [3.1]). When a fan jet was used, it was positioned such that the fan width matched the tooth width at the tooth top. A given lubricant flow condition would be set by maintaining a given jet pressure.

The first parameter investigated was the lubricant flow rate. The data are presented in Figure 3.8.2. The facility was maintained at a constant speed and load (14 400 rpm and 354 N · m (3130 in. · lb)) and the jet pressure (flow) was varied. The oil inlet temperature was maintained at a constant 38 °C (100 °F). The oil inlet was located on the gear approximately 80° out of mesh. The data shown here, ranking the thermocouple locations, are typical of all the results to be presented on this hardware. The tooth top was always the highest temperature; next, the root and toe gages usually produced about the same measured temperature, followed by the tooth heel gages having the lowest temperature. The pinion was not in danger of scoring due to a lack of lubricant, and the trend of temperature increase with lubricant pressure (flow) decrease was found.

The effect of load on the pinion operating temperature is shown in Figure 3.8.3. All four measurement locations increased in temperature in a fairly linear fashion. Speed, lubricant temperature, and lubricant flow rate were all held constant as the gears were lubricated on the gear member 90° before going through mesh.

The last all fan lubricating jet data are shown in Figure 3.8.4. The data are plotted for five lubricating jet positions at two jet pressures. The upper symbols are for the lower flow rate condition and the lower symbols are for the higher flow rate condition. In either flow condition, it is obvious that jet placement can drastically affect the pinion bulk operating temperature. The lowest operating temperature using the fan jets was measured when the jet was positioned into or out of the region just before or after the gears go into mesh. From an efficiency standpoint, out-of-mesh lubrication is the best choice because power would not be required to pump the

oil out of the meshing region. This extra pumping action, however, did not cause the thermocouple measurements to increase; therefore, this effect must be minimal in the dry sump operational mode used in the tests conducted herein.

Next, the results using the fan jet are compared with those obtained with a pencil jet. The pencil jet is basically a tube with an orifice of a given diameter at its end. Instead of the lubricant being spread out to form a sheet as in the fan jet, the pencil jet delivers a column of fluid to the gear surface where it is spread upon impact. The pencil jet was positioned at a distance similar to that of the fan jet from the tooth top and was centered at half the face width of the pinion or gear. Tests were conducted to compare the operational temperature of the spiral bevel pinion with these two different jets. The results are shown in Figure 3.8.5. Four operational settings were run. The oil inlet temperature and lubricant jet operating pressures were not identical for the two jets, but some conclusions can still be drawn from these data. The fan jet was run at a higher pressure and a slightly lower oil inlet temperature, which resulted in the flow being approximately double that of the pencil jet for the results shown. Even with the difference in oil flow, the measured gear temperatures were nearly the same. The conclusion that can be drawn is that in this application the pencil jet produced similar results with a reduced lubricant flow requirement.

Next, the effect of oil inlet temperature on the operational characteristics of the pinion are presented in Figure 3.8.6. Three oil inlet temperatures were tested while other test conditions were held constant. A pencil jet with a 0.76-mm- (0.030-in.-) diameter orifice located 90° before mesh on the gear was used. Note from this figure that the measured values increased at a lower rate than the oil inlet temperature. A total increase in the oil inlet temperature of 67 °C (120 °F) resulted in a thermocouple-measured temperature maximum increase of 17 °C (30 °F). Clearly, the surrounding facility and shaft connection hardware limited the effect of raising the oil inlet temperature. In low load and speed conditions, thermocouple readings would be lower than the oil inlet temperature (see Fig. 3.8.5). In actual helicopter or other applications, maintaining the surrounding hardware at a lower temperature is usually not possible. The result is that in practice the surroundings are operating at a temperature somewhere between the oil inlet temperature and the average temperature of the heat-producing rotating components.

The last data to be presented on the bulk thermocouple pinion are for pencil jet position effects when the oil inlet lubricating jet is positioned on the pinion. Two locations on the pinion were tested, and one test from the lubricant jet on the gear is included for comparison. Because the oil inlet temperature and pressure varied slightly for the three sets of data shown, the temperature differences between the thermocouple-measured and oil inlet temperature are used in Figure 3.8.7. The same jet was used for all three sets of data. From this figure, the pinion ran the coolest by being lubricated 90° before going through mesh.

In summary, for this test hardware, jet location is an important parameter for the steady state operating temperature measured with this pinion. From the data acquired, the best place to lubricate the pinion was at the into- or out-of-mesh locations. Jet placement also affects the way analytical model boundary conditions would be applied and in Chapter 6, it will be compared with the boundary conditions imposed on the analytical model.

**Surface Temperature Thermocouple Pinion:** The surface temperature pinion is shown schematically in Figure 3.4.2 and by photograph in Figure 3.4.5. Because of the unknown operational life of an instrumentation system such as this, some data were taken at low speed and load conditions. At these conditions the level of heat generated is also low and a rapid increase in temperature was not found. The thermocouples were in regions on the active profile where temperature increases should have been measurable.

The instrumentation connection used for the tests is shown in Figure 3.8.8. The thermocouple output was connected either to the laboratory computer or to a tape recorder, depending on the time or type of test. Initial data taken at low speed and load conditions were tape recorded.

After the initial light load and low speed tests, the test hardware was run to full conditions. Lubricant jet location and flow rate were similar to those used with tests on the bulk thermocouple pinion. A 0.76-mm- (0.030-in.-) diameter pencil jet was used. It was located 90° before mesh on the gear and had a jet pressure of 1.38 MPa (200 psi). Speed and load were ramped to full conditions in approximately 60 seconds. Data taken in 4-second intervals by the laboratory computer are shown in Figure 3.8.9. After approximately 150 seconds had elapsed, the instrumentation is believed to have begun to fail. The adhesive holding the alloy wires within the thin slots was broken and the toe and mid profile surface temperature thermocouples continued a rapid increase in temperature as they interacted with the meshing gear surface. Then their output began to decay and at approximately 350 seconds the tooth top and root thermocouple temperatures increased rapidly. At 360 seconds the tooth top thermocouple had reached a temperature in excess of 343 °C (650 °F) and smoke was visually spotted along with the normal windage generated from the rotating gears within the air-oil environment.

The test was stopped and inspection of the gears revealed evidence of scoring damage. The damage basically appeared only on the instrumented teeth that had been electrodischarge machined. Since data were not taken with the tape recorder connected, the facility was started again. Full conditions were again attained as in the last test and the thermocouple signals were recorded. During this test, further scoring damage was not evident. Most of the surface thermocouples continued to operate but their actual measurement point was unknown. A photograph of one of the instrumented tooth locations is shown in Figure 3.8.10. Note that the scoring occurred on the tooth with the instrumentation slots. Therefore, the amount of surface that was disturbed, because of the addition of the instrumented slots, was enough to cause scoring at the elevated loads applied at full condition. Apparently, the surface deviation was sufficient to cause a localized collapse of the oil film separating the meshing surfaces. This localized heat and damage spread over most of the active profile that is loaded from the top of the tooth down to where the instrumentation slot ends.

The thermocouple measurement scheme could possibly be accomplished by a different machining procedure. Instead of marring the active profile to the extent that was done in this study, it may be better to electrodischarge machine a hole from the coast side of the tooth to the active profile side. This would reduce the amount of meshing and load-carrying profile disruption by having only a small hole instead of a thin slot that extends to approximately one-half of the tooth height.

**Thin-Film Thermocoupled Pinion:** The results using the thin-film instrumented pinion are now discussed. The run-time life of this hardware was an unknown for this instrumentation scheme. The effect of highly concentrated loads was unknown, and whether the oil film would be thick enough to keep the thermocouples from being rubbed off was a concern. The thin-film coatings were sputtered onto the surface in the thicknesses shown in Table 3.4.1 to make a localized layer approximately 2  $\mu\text{m}$  (79  $\mu\text{in.}$ ) higher than the surrounding insulated gear surface (4  $\mu\text{m}$  (158  $\mu\text{in.}$ ) of  $\text{Al}_2\text{O}_3$ ). One wire and five thin-film thermocouples were installed on the pinion. Three thin-film thermocouples were on the active drive side profile and the other three thermocouples were on the coast side of the same tooth. A sketch of the instrumentation scheme and the actual hardware are shown in Figures 3.4.3 and 3.4.6, respectively. In Figure 3.4.6 two additional circular sputtered areas are seen located between the actual thermocouples. These were used to check the adhesive strength of the coating during a pull test.

The thin-film test hardware was then installed in the test facility pinion housing and the setup of the hardware to attain the correct backlash and a reasonable contact pattern was initiated. Since the hardware robustness was unknown, a minimum amount of setup was accomplished. The contact pattern was slightly higher than normal with the correct backlash after a few setup trials. The slip ring was then connected and the thermocouple circuitry checked. At this point it was determined that the contact pattern checks, even though done with virtually no load and by hand rotation, had caused the destruction of three of the five thin-film thermocouples. Instead of repeating the entire thin-film processing procedure, it was decided to test the robustness of the coatings.

After the instrumentation was connected to the tape recorder system (see Section 3.4), a low speed and load test was conducted. By the time the facility reached the set point conditions of 3000 rpm (pinion) and 37 N · m (330 in. · lb), another thermocouple failed on the coast side of the pinion. The facility was started from a torque of 0 N · m (0 in. · lb); actually, the inertia of the system, when the speed is changed during startup, causes the torque in the loop to go negative which would load the coast side of the pinion. The thermocouple that failed at this point was the wire thermocouple which had a nominal diameter of 0.025 mm (0.001 in.) and was on the coast side of the tooth.

The one thin-film thermocouple that continued to work only output a temperature near ambient because the load was never directly applied to this region based on the contact pattern from the setup and the metal blueing coating applied to the pinion. This thermocouple was located on the heel end of the drive side of the tooth.

The thin-film thermocouple technique applied in this study failed to provide any research data to help fine tune and verify the analysis to be developed later. These data would have been extremely valuable in validating some of the assumptions necessary to perform the analysis.

In summary, with regard to the instrumented pinion tests, keeping the instrumentation off the active profile allowed a great deal of data to be taken, but it was only useful in attaining the bulk temperature information and the infrared microscope data to be discussed in the next section. Thermocouples imbedded in the active profile could also be an alternative to obtain the required surface data; however, the machining required to position them must use something other than the technique tried in this study. Finally, the thin-film thermocouples must be applied so that their appearance on the active profile does not cause localized profile abnormalities that would lead to their early destruction. If the coating could be applied such that the surface net change is the same, the coatings should have a longer run-time life. The other alternative is to use a lubricant with very high viscosity: film thickness would be increased and the chance of thin-film-coating gear surface interactions would be reduced. This type of lubricant does not have application, however, to the aerospace applications that this study has under consideration.

### 3.9 Experimental Results Using an Infrared Microscope

In this section the infrared-microscope-generated data are presented. Steady state as well as transient or time-varying data are shown. These infrared data were taken from many different tests using the bulk thermocouple pinion described in Section 3.8. The data generated with thermocouples are used to determine certain parameters necessary to make calculations for the transient data to be presented.

As mentioned in the earlier study of Handschuh (Ref. [3.1]), infrared measurements could only be made when the jet was positioned in certain locations with respect to the rotating gears. The locations for possible use were on the gear at either 90° out-of- or into-mesh positions. At other locations, such as on the pinion, oil windage did not permit a reasonably clear optical path to the test location of interest so the measurement using these locations was abandoned.

**Steady State Results:** When the infrared microscope is used in the steady state mode, the emissivity of the surface being measured must be known. As described in Section 3.5, oil film thickness on the gear surface can affect the emissivity of the measurement being made. Therefore, when a given test was being conducted, measurements for each condition were taken at a number of emissivities. The microscope output varies as the emissivity setting is changed because a lower emissivity adds amplifier gain to the signal being measured. To exemplify this phenomenon, a series of tests were conducted. The speed and load were varied and the infrared measurements were taken with three emissivity settings. These data are shown in Figure 3.9.1. Also plotted in this figure is the bulk surface temperature, the average of the root and top thermocouples from the instrumented pinion. The tests

then were conducted with the same lubrication system parameters. Note that no correction for sapphire lens attenuation was made to this figure. The effect of the lens correction would be to add approximately 10 °C (18 °F) to the measured quantities shown.

The data from Figure 3.9.1 show that the speed and load conditions affect the emissivity of the measurement being made. At the low speed and load condition, adding in the sapphire lens attenuation, the emissivity was approximately 0.3; at the elevated speed and load condition that value was reduced to 0.25. The data just described are essential for calculating the transient data that are based on the emissivity and temperature level of the surface under consideration and the calibration constant of the infrared microscope.

Similar figures could be generated to show the effect of other system parameters on the infrared output at different emissivities. The basic trends shown in Figure 3.9.1 would be repeated for varying the lubricant jet pressure or oil inlet temperature, for example.

**Radiance Output and Calculations for Transient Data:** The calculation method to quantify the transient data to be presented later in this section is now described. The data measured will be a voltage differential that will determine the temperature differential of the surface under consideration.

From the manufacturer (Ref. [3.4]), a curve of adjusted blackbody radiance versus temperature is given. This curve is shown in Figure 3.9.2 and will be used to determine temperature differentials from the transient data. Values from the curve over a range from 50 to 350 °C (122 to 662 °F) were used to fit the following equation to the curve:

$$N = a 10^{T^b} + c \quad (3.9.1)$$

where N is the radiance in watts per square centimeter-ster; the following values of a, b, and c were found:  $a = 6.7745 \times 10^{-6}$ ,  $b = 0.28101$ , and  $c = 5.805 \times 10^{-4}$ , and T is the temperature in centigrade to produce the radiance value. Since the graph is plotted on a semilog scale, radiance changes and temperature variation are dependent on the reference temperature used. In other words, different reference temperatures with the same radiance change would produce different temperature differentials.

The surface emissivity is estimated from the steady state data using the infrared microscope. For example, see Figure 3.9.1 where the value ranged from about 0.3 to 0.25 depending on the test conditions. Once the measurement is made, the voltage differential between the minimum and maximum voltage is found. At this point, the attenuation effect of the sapphire lens must be added to the voltage differential found. For this task, Figure 3.5.9 is used. Similar curves for an emissivity less than 1.0 were available from calibration studies with emissivity as low as approximately 0.2 for the 9310-gear steel dish without oil.

Next, the radiance change is calculated as given by the following equation (Ref. [3.4]):

$$\Delta N = \frac{\Delta V_{adj}}{\epsilon k} \quad (3.9.2)$$

where

$\Delta N$  radiance change, W/(cm<sup>2</sup>·ster)

$\Delta V_{adj}$  adjusted voltage differential, V

$\epsilon$  oil-gear surface emissivity

$k$  manufacturer's calibration constant ( $k = 9.77$ ) for the instrument in use,  $(V \cdot \text{cm}^2 \cdot \text{ster})/W$

At this time, a known reference point on the gear body in close proximity to the location of the infrared measurements is useful. In this study, the root thermocouple is used as the reference point. This thermocouple was attached to the root surface with an adhesive (Chapter 3). Radiance changes from this temperature are given by the following equation:

$$N_{\max} = N_{\text{ref}} + \Delta N \quad (3.9.3)$$

where  $N_{\text{ref}}$  is the radiance at the root temperature and  $\Delta N$  is the radiance change due to the measured voltage differential. Therefore, the maximum temperature  $T_{\max}$  is found by solving Equation (3.9.1) for  $T$  and substituting  $N_{\max}$  for  $N$ :

$$T_{\max} = \left[ \log_{10} \left( \frac{N_{\max} - c}{a} \right) \right]^{1/b} \quad (3.9.4)$$

This procedure was used to evaluate the measured data. A reference temperature, adjusted voltage differential, and surface emissivity are necessary to change the data into engineering units.

**Transient Experimental Data:** The actual measured data taken with the infrared microscope are now presented. These data were typically band-pass filtered to remove noise from the signal. This band was from about 60 Hz to 20 kHz. Therefore, the effects of filtering the data are presented first and are shown in Figure 3.9.3. When the signal is filtered, the output is smoother but there is also a phase shift between the once-per-tooth signal and a given location in the measurement output. The once-per-tooth signal was generated by a proximity probe located close to the pinion tooth top at approximately one-half the face width of the tooth. The phase between the proximity probe and the infrared microscope was established statically by rotating the pinion shaft until the cross hairs in the infrared microscope aligned with the tooth top midsection and then by rotating the pinion until the proximity probe indicated that the tooth top was at a position directly above the probe. The orientation angle between the two measurements was then known. The effect of filtering is seen in Figure 3.9.3 where the filtered data have moved in relation to the unfiltered signal.

The filtered infrared output signal is shown in Figure 3.9.4 for over one revolution of pinion rotation. From this figure, a large spike in the infrared output is indicated once per revolution. This spike is believed to be caused by the tooth top thermocouple adhesive coming into view each revolution. Apparently, the epoxy adhesive has a much higher emissivity that produces a stronger signal output for that particular tooth. This part of the measurement was not used for any of the data to be discussed later in this section.

At this point it is useful to relate the rotation of the pinion to the infrared output produced. A test was conducted to visually determine the location on the surface that the infrared system would view as a function of pinion rotation angle. This was accomplished by mounting a transparent plastic sheet with cross hairs (similar to the infrared microscope) centered on the end of the inner tube of the system shown in Figure 3.5.2. Using a protractor on the pinion shaft and rotating the pinion in  $5^\circ$  increments produced the result shown in Figure 3.9.5. Also shown in this figure is a typical infrared measurement and the once-per-tooth proximity probe output. Positions 1 to 7 are shown along the infrared signal. In the figure can be seen a large negative-going spike when the tooth top edge is approached at position 1. This spike can be attributed to the corner top edge coming into view for the infrared microscope. There is no physical reason for the temperature to decrease this rapidly over that

part of the tooth surface on the active profile side. Also to be noted is that the highest temperature measured occurs at the top land midpoint. From the bulk temperature data shown in the last section, this region always had the highest temperature. However, this position's indicating a higher temperature than the active profile is discussed further in Chapter 7.

The lowest part of the signal-per-one-tooth measurement is located just after position 2 (see Fig. 3.9.5). This location will be used as the reference temperature location and the highest part of the signal will be that of the tooth top. From the change in voltage between these two locations the infrared transient will be calculated.

To exemplify the effects of operating conditions on the infrared signal, four conditions were run for the same setup of the infrared microscope. The band-pass filtered data are shown in Figure 3.9.6. A pencil jet 0.51 mm (0.020 in.) in diameter at an oil inlet pressure of 1.38 MPa (200 psi) and an oil inlet temperature of 57 °C (135 °F) was used for the test results shown in Figure 3.9.6. Note the voltage scale change for each of the sets of data. The calculated infrared signal data are shown in Table 3.9.1 The calculations were made as mentioned earlier in this section.

Note in all signals (see Fig. 3.9.6) that an active profile position was never measured far in excess of the tooth top temperature (Table 3.9.1). Another interesting point to observe from the infrared measured output shown in this section is that the signal had variability from tooth to tooth as well as from revolution to revolution. Probably the most reasonable explanation is that this lack of repeatability is attributed to the measurement environment. First, the windage from the gears can remove the possibility of making the measurement. This is due to the momentum change imparted to the lubricating oil as it impinges on the gear surface. Also, as the oil is flung from the teeth and then impinges on the rig housing, oil droplets fall into the optical path. Even with the amount of work done to make the most of a difficult test, the measurements made are at best only an indicator of temperature differentials across a particular location of the active profile as well as the tooth top. Other measurements that were made with the infrared microscope used a fan jet; these are presented in Table 3.9.2. Note from Tables 3.9.1 and 3.9.2 that the calculated results for maximum temperature agreed within 7 percent of the thermocouples over the eight cases given in these two tables.

This section has shown that making measurements in a highly reliable fashion from rotating gears is very difficult. The bulk temperature measurement scheme has proven to be a very reliable way to generate a great deal of information about the nonactive profile areas of the gear. Higher risk instrumentation such as thermocouples imbedded in the active profile or deposited by thin films would be beneficial in providing a more thorough validation of the numerical models to follow in this work. The data generated by the infrared microscope are useful in showing that temperature differentials exist across the active profile surface; however, this measurement scheme still does not permit measurement to be made in the most desirable location where the gear teeth are in mesh.

## REFERENCES

- [3.1] Handschuh, R.: Effect of Lubricant Jet Location on Spiral Bevel Gear Operating Temperatures. NASA TM-105656, 1992.
- [3.2] Wymer, D.; and Macpherson, P.: An Infra-Red Technique for Monitoring Gear Tooth Surface Temperatures. Research Paper RP 458, Contract No. K 25B/534/CB25B, Imperial College, London, England, Jan. 1974.
- [3.3] Townsend, D.; and Akin, L.: Analytical and Experimental Spur Gear Tooth Temperature as Affected by Operating Variables. J. Mech. Design, vol. 103, no. 1, Jan. 1981, pp. 219-226.
- [3.4] Instruction Manual, Infrared Radiometric Microscope Model RM-2A. Barnes Engineering Co., Stamford, CT, 1982.
- [3.5] Moffat, R.: The Gradient Approach to Thermocouple Circuitry. Temperature, Its Measurement and Control in Science and Industry, Van Nostrand Reinhold, Princeton, NJ, 1961.

TABLE 3.2.1—SPIRAL BEVEL GEAR TEST FACILITY PARAMETERS AT  
FULL SPEED AND LOAD CONDITIONS

Pinion shaft speed, rpm	14 400
Pitch line velocity, m/s (ft/min)	44.7 (8803)
Pinion shaft power, kW (hp)	537 (720)
Test section flow rate maximum, cm <sup>3</sup> /s (gal/min)	51 (0.8)
Oil inlet temperature (variable), °C (°F)	38 to 189 (100 to 300)
Oil pressure maximum, MPa (psi)	1.38 (200)

TABLE 3.2.2—TEST SPECIMEN DESIGN PARAMETERS

Number of teeth pinion/gear	12/36
Diametral pitch	5.141
Mean spiral angle, deg	35
Mean cone distance, mm (in.)	81.1 (3.191)
Face width, mm (in.)	25.4 (1.0)
Nominal pressure angle, deg	22.5
Shaft angle, deg	90
AGMA class	12
AGMA bending stress index, MPa (ksi)	398 (57.7)
AGMA contact stress index, MPa (ksi)	2406 (349)

TABLE 3.4.1—THIN-FILM LAYER INFORMATION

Layer	Thickness		Material
	μm	μin.	
Insulating	≈4	≈157	Al <sub>2</sub> O <sub>3</sub>
Thermocouple	≈2	≈79	Chromel-constantan

TABLE 3.9.1—CALCULATED INFRARED TEMPERATURE FROM DATA SHOWN

IN FIGURE 3.9.6 FOR FOUR OPERATING CONDITIONS

Pinion operating conditions			Voltage differential, V	Adjusted voltage, V	Thermocouple location				Oil/gear emissivity	Maximum infrared temperature <sup>a</sup>	
Speed, rpm	Torque				Root reference		Top			°C	°F
	N · m	in. · lb			°C	°F	°C	°F			
7 200	177	1567	0.040	0.050	75	167	103	217	0.5	104	219
10 800	267	2363	.097	.120	118	244	146	295	.35	148	298
14 400	267	2363	.121	.150	136	277	166	331	.35	166	331
14 400	354	3133	.214	.264	154	309	188	370	.35	194	381

<sup>a</sup>From Equation (3.9.4).

TABLE 3.9.2—CALCULATED INFRARED MAXIMUM TEMPERATURE FOR TWO

JET POSITIONS AND TWO JET PRESSURES

[From Ref. [3.1] ( $\epsilon \approx 0.37$ ).]

Jet location on gear <sup>a</sup>	Pinion operating conditions			Lubricant fan jet			Adjusted voltage differential, V <sub>adj</sub>	Thermocouple location				Infrared maximum temperature	
	Speed, rpm	Torque		Pressure, MPa	Flow			Root reference		Top		°C	°F
		N · m	in. · lb		cm <sup>3</sup> /sec	gal/min		°C	°F	°C	°F		
A	14 400 ↓	357	3160	1.38	49	0.78	0.132	124	255	164	327	153	307
A		354	3133	.35	25	.40	.170	134	273	175	347	166	331
B		354	3133	1.40	49	.78	.115	123	253	154	309	149	300
B		354	3133	.35	25	.40	.130	127	261	161	322	155	311

<sup>a</sup>A = 90° out-of-mesh on the gear.

B = 90° into-mesh on the gear.

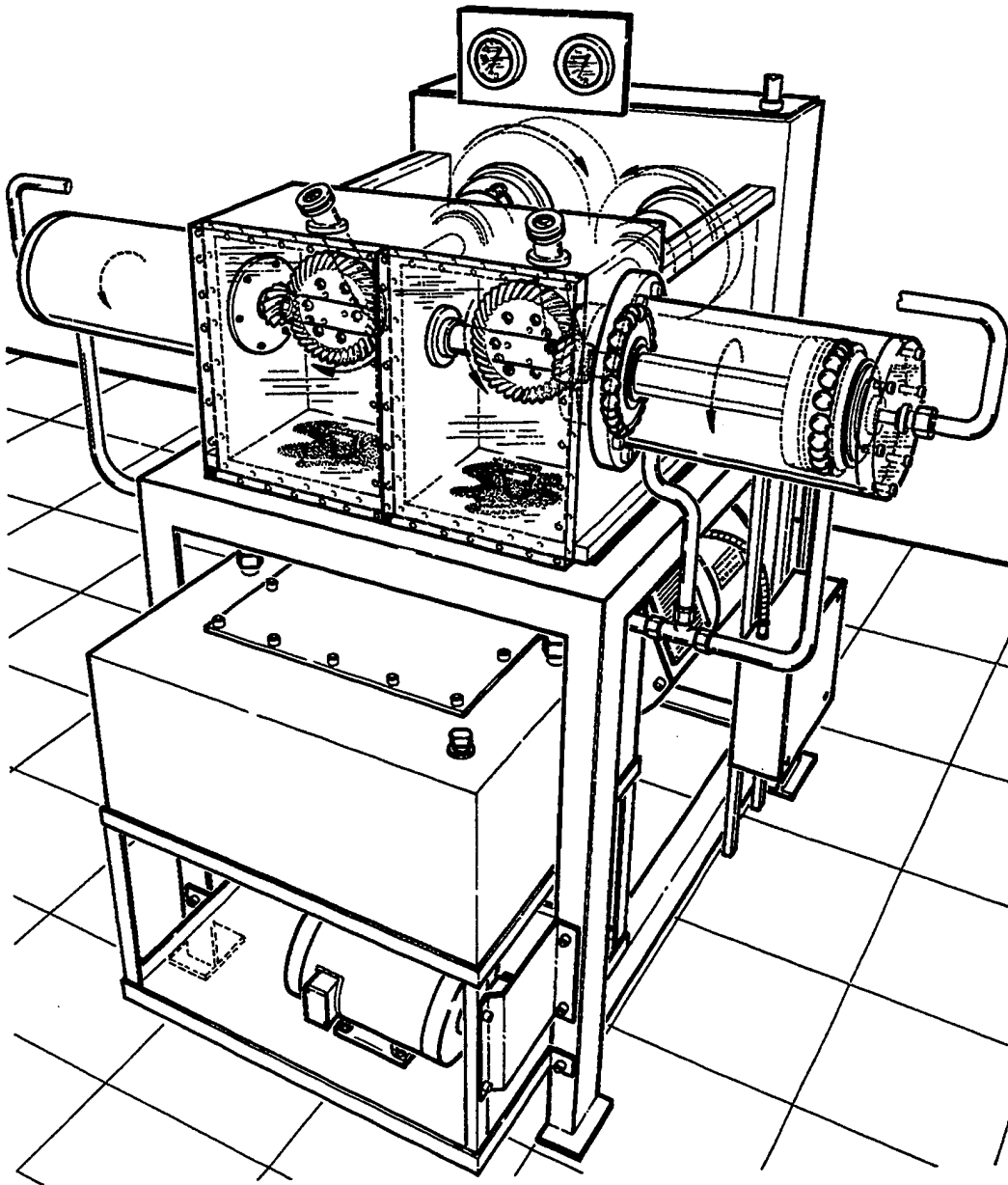


Figure 3.2.1.—Spiral bevel test facility sketch.

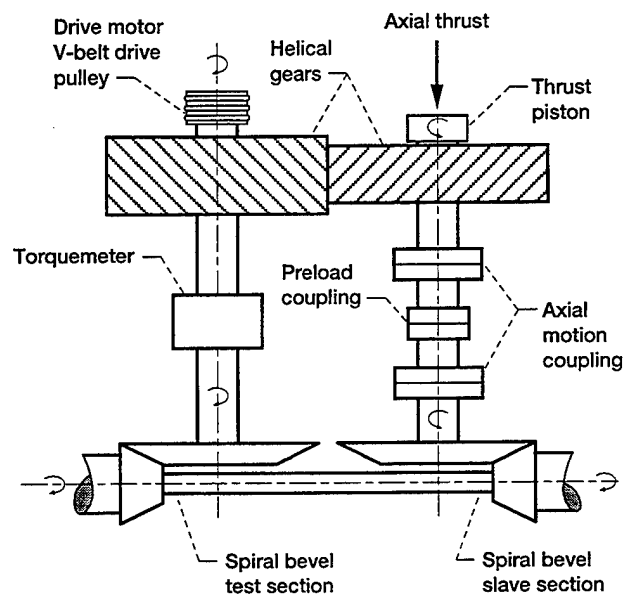


Figure 3.2.2.—Cross-sectional view of spiral bevel test facility.

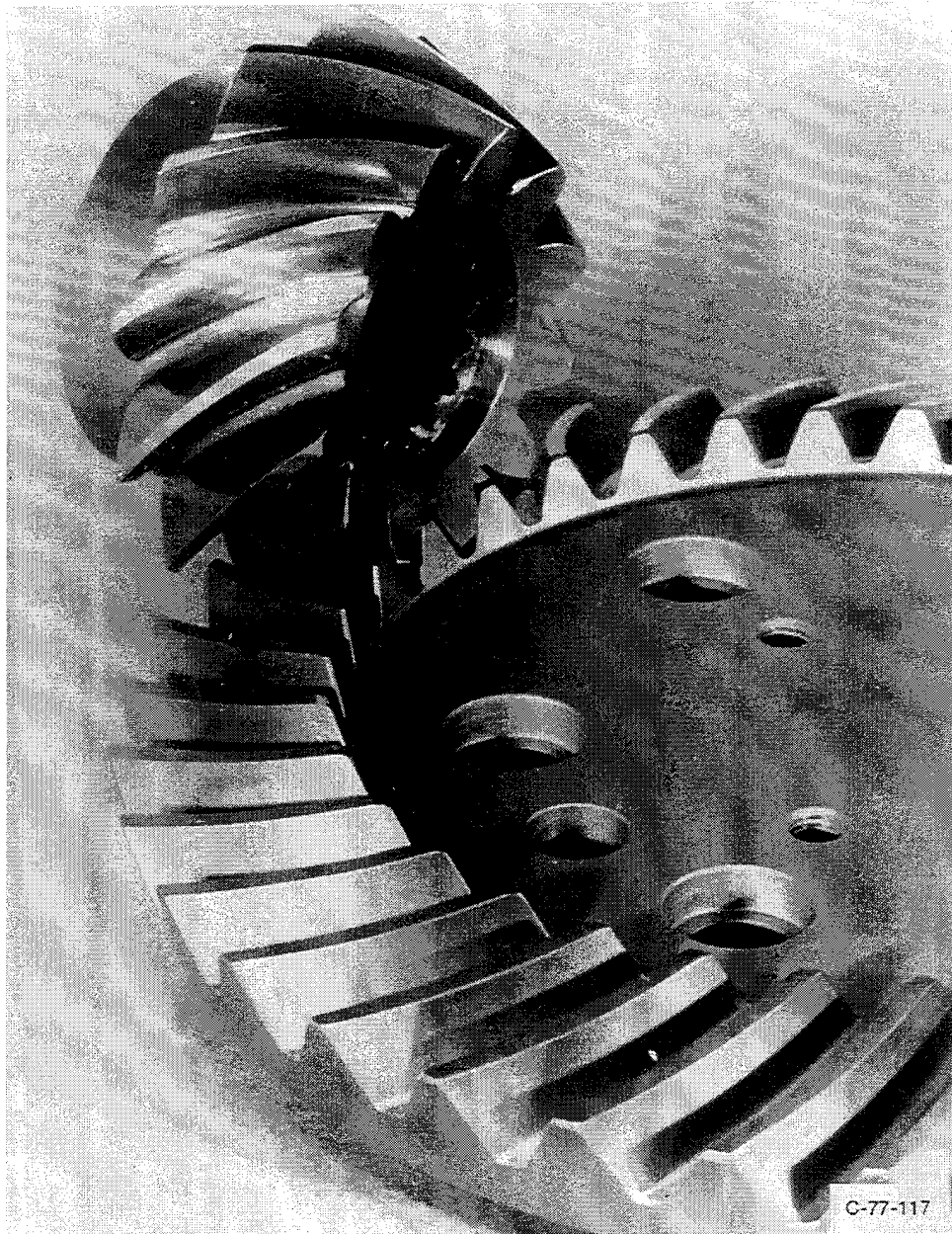


Figure 3.2.3.—Typical spiral bevel test hardware.

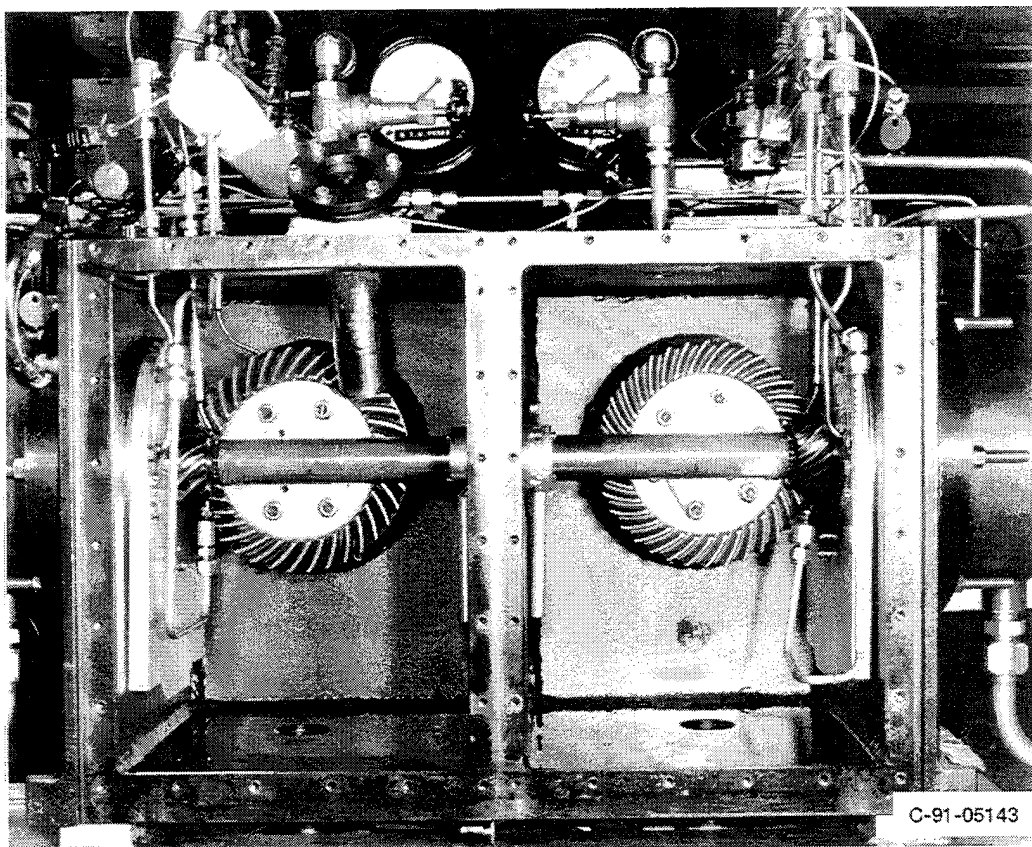


Figure 3.2.4.—Spiral bevel gear components installed in the test stand.

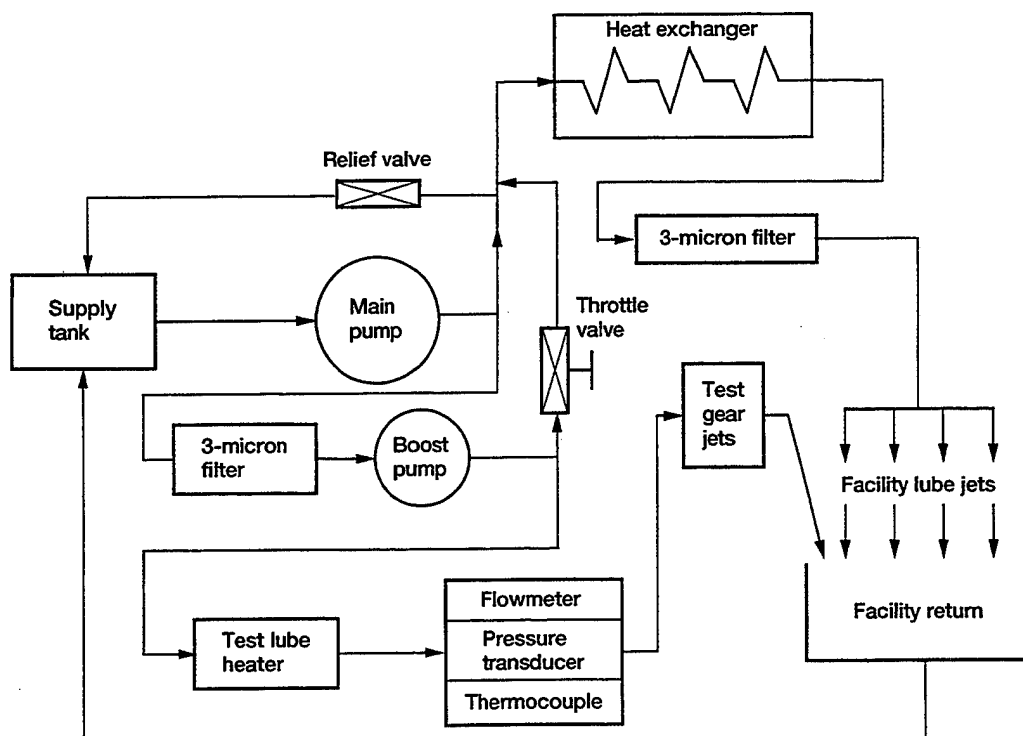
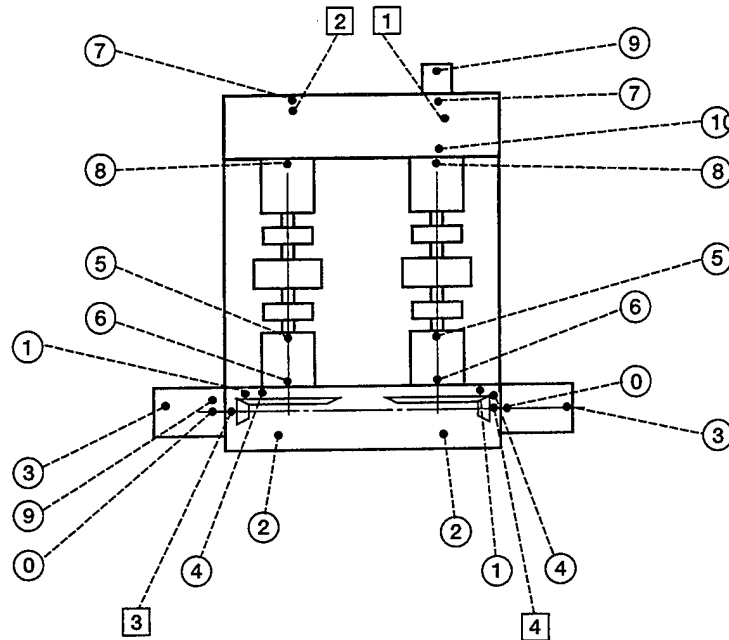


Figure 3.2.5.—Lubrication system schematic.

Top view of test rig



○ Thermocouple  
□ Accelerometer

Left side	
Thermocouple name	T.C. number
High speed pinion bearing	0
Pinion and gear oil inlet	1
Test oil outlet	2
High speed outboard bearings	3
Pinion/gear fling off	4
Low speed bevel shaft (outboard)	5
Low speed bevel shaft (inboard)	6
Low speed helical (outboard)	7
Low speed helical (inboard)	8
High speed bearing oil inlet	9

Right side	
Thermocouple name	T.C. number
High speed pinion bearing	0
Pinion and gear oil inlet	1
Test oil outlet	2
High speed outboard bearings	3
Pinion/gear fling off	4
Low speed bevel shaft (outboard)	5
Low speed bevel shaft (inboard)	6
Low speed helical (outboard)	7
Low speed helical (inboard)	8
Load piston bearing	9
Low speed thrust bearing	10

Figure 3.3.1.—Facility instrumentation locations for temperature and vibration.

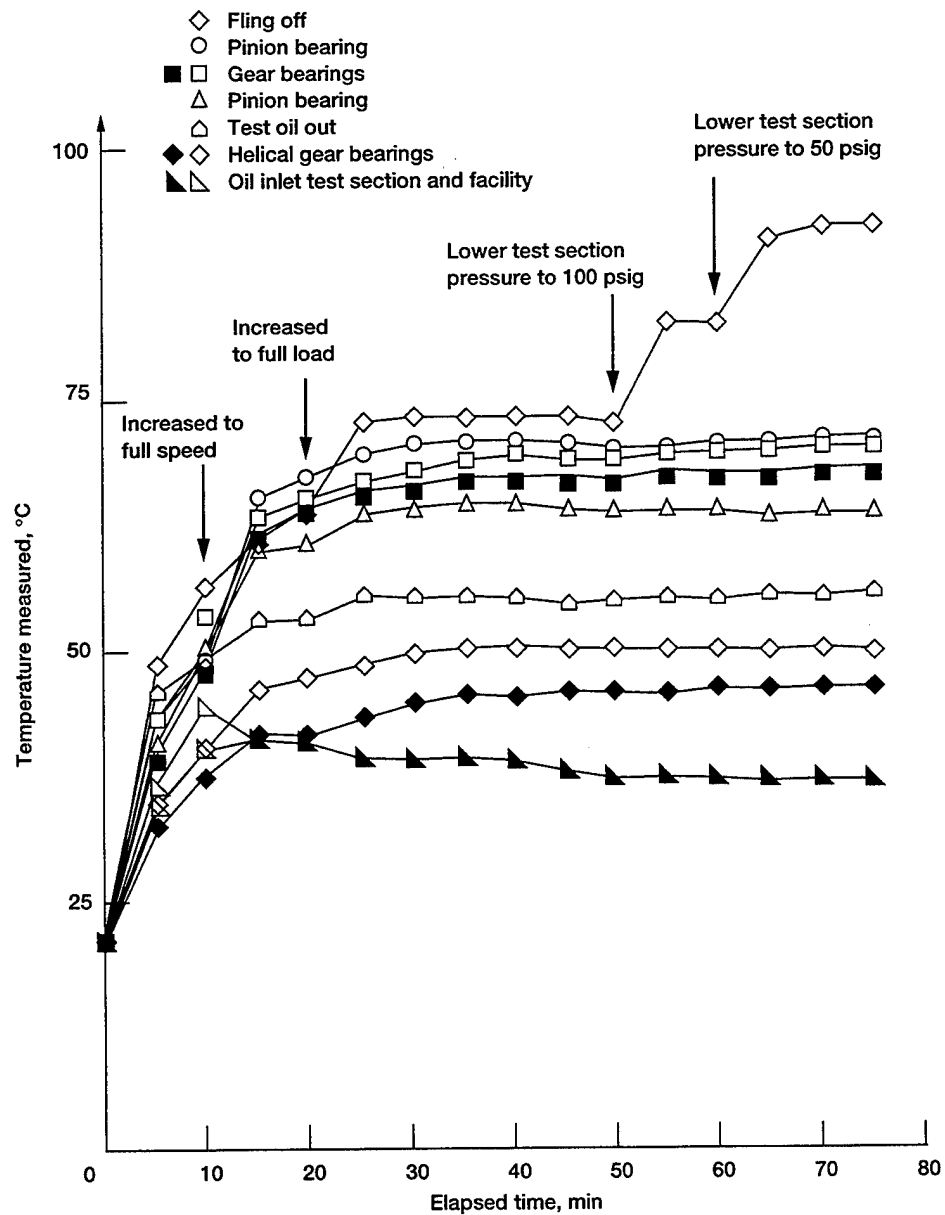


Figure 3.3.2.—Facility thermocouple measurements for a typical test. Test section lubricant pressure was varied from 200→50 psig.

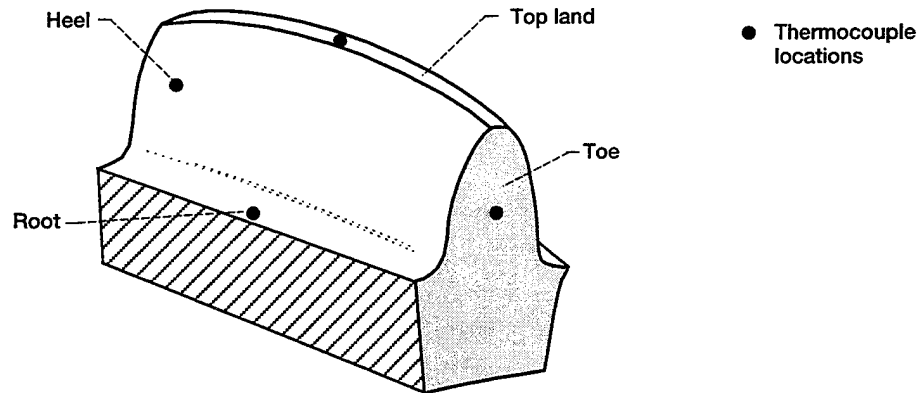


Figure 3.4.1.—Thermocouple locations for bulk gear temperature measurements. Thermocouples at toe, top land, and heel are located approximately 0.030 in. below surface.

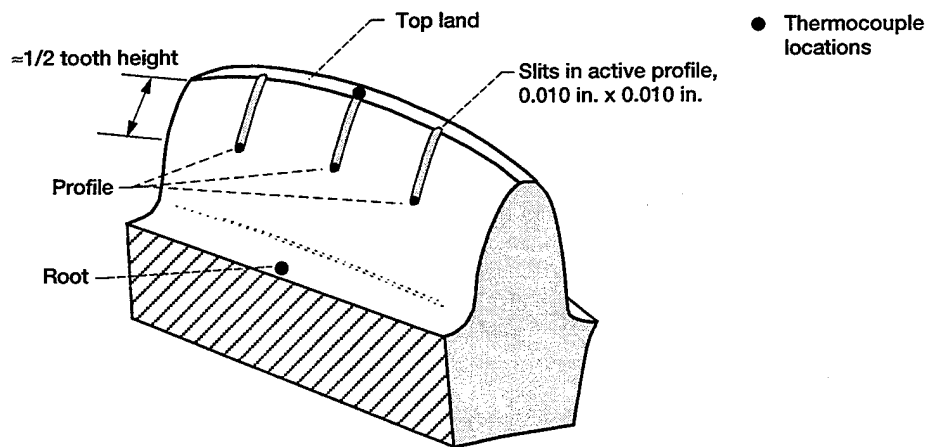


Figure 3.4.2.—Sketch of active profile thermocouples. Slits were electro-discharge machined in hardened gear surface.

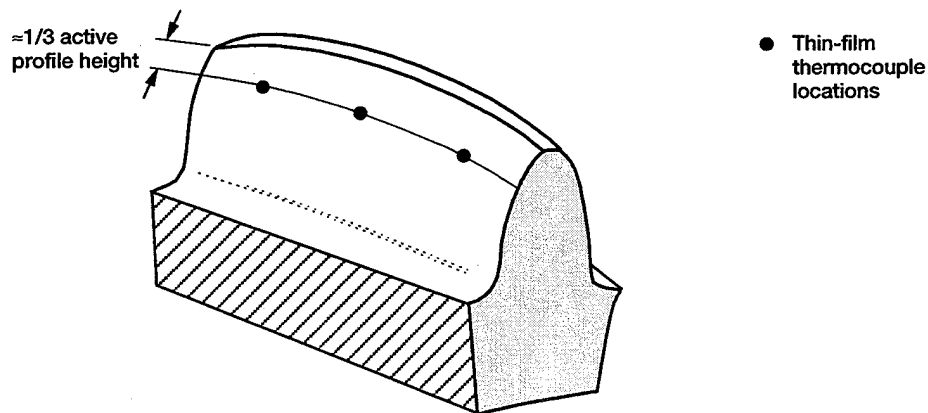


Figure 3.4.3.—Thin-film gage locations on active profile.

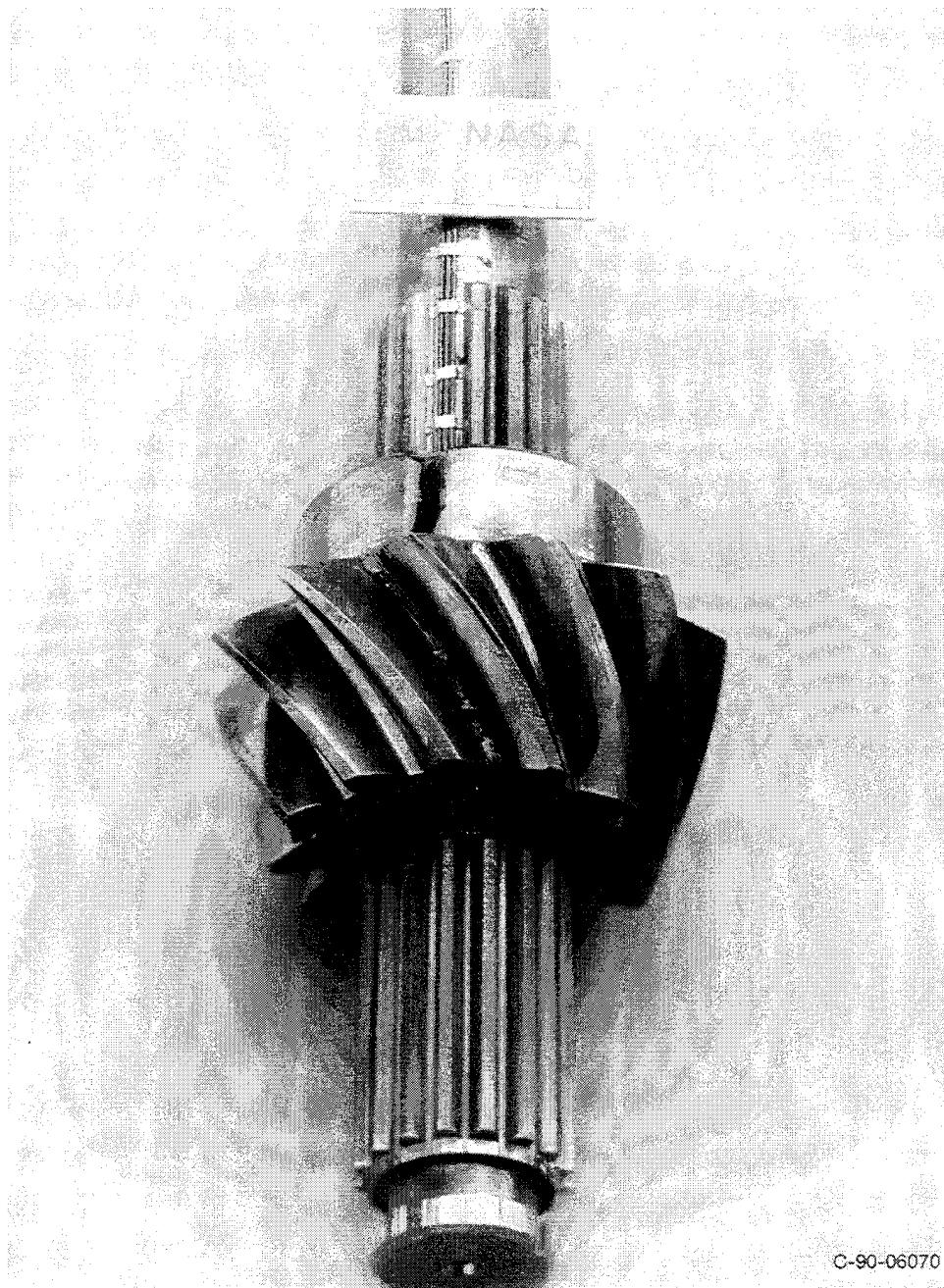


Figure 3.4.4.—Bulk thermocouple pinion.

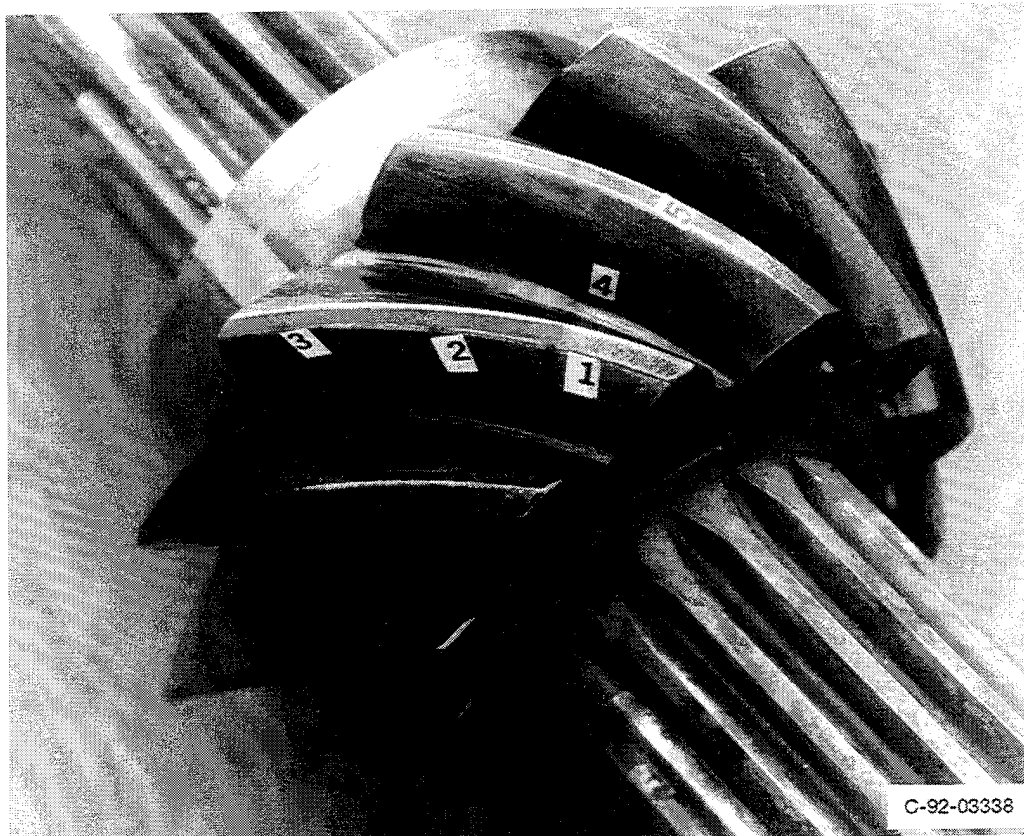


Figure 3.4.5.—Surface-embedded thermocouple.

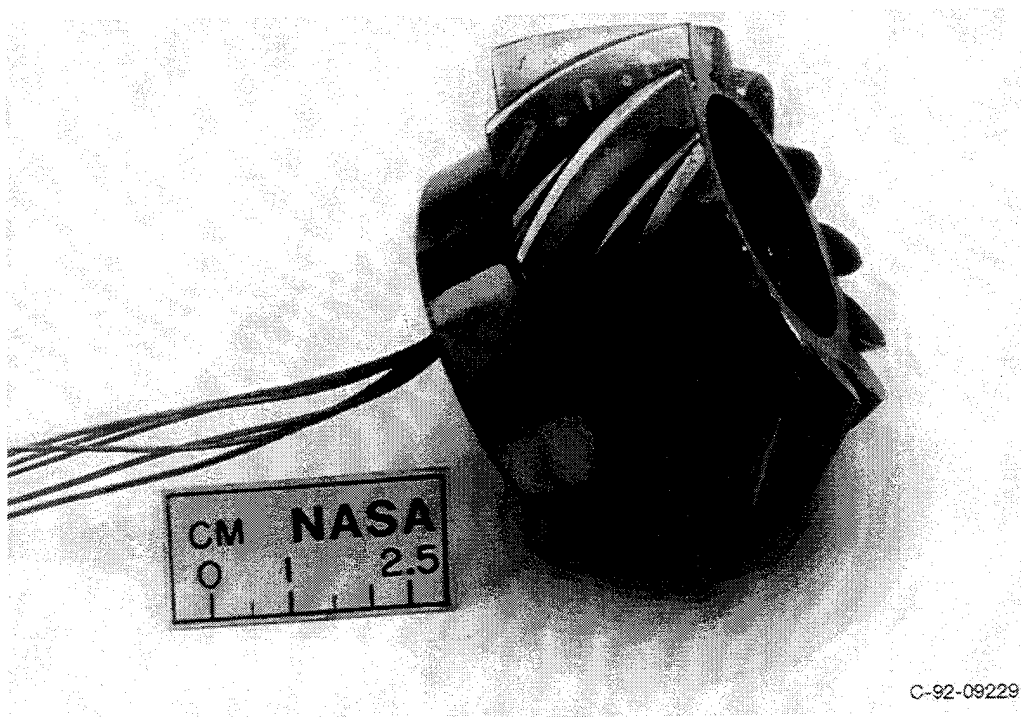


Figure 3.4.6.—Photo of thin-film thermocouple pinion.

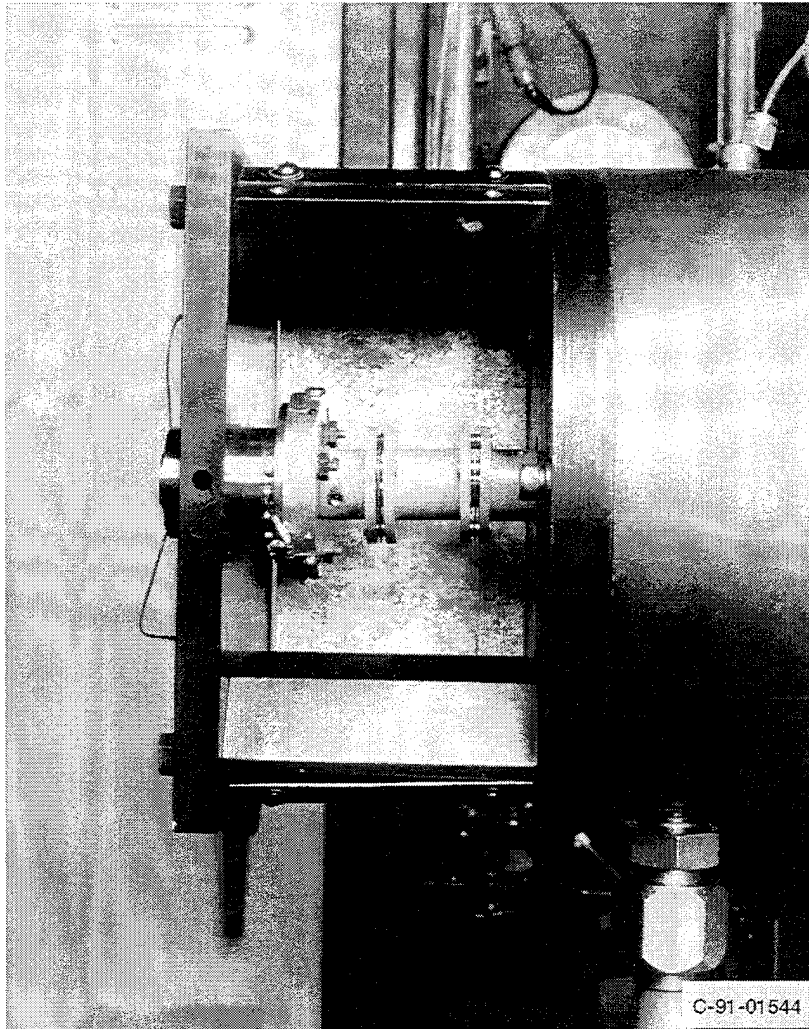


Figure 3.4.7.—Photo of slip ring assembled in the facility.

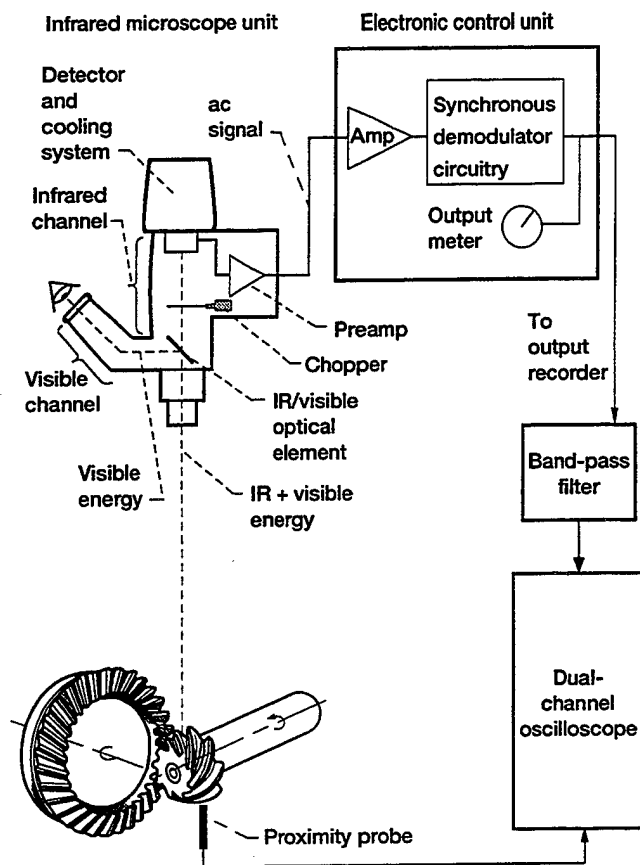


Figure 3.5.1.—Transient temperature measurement system.

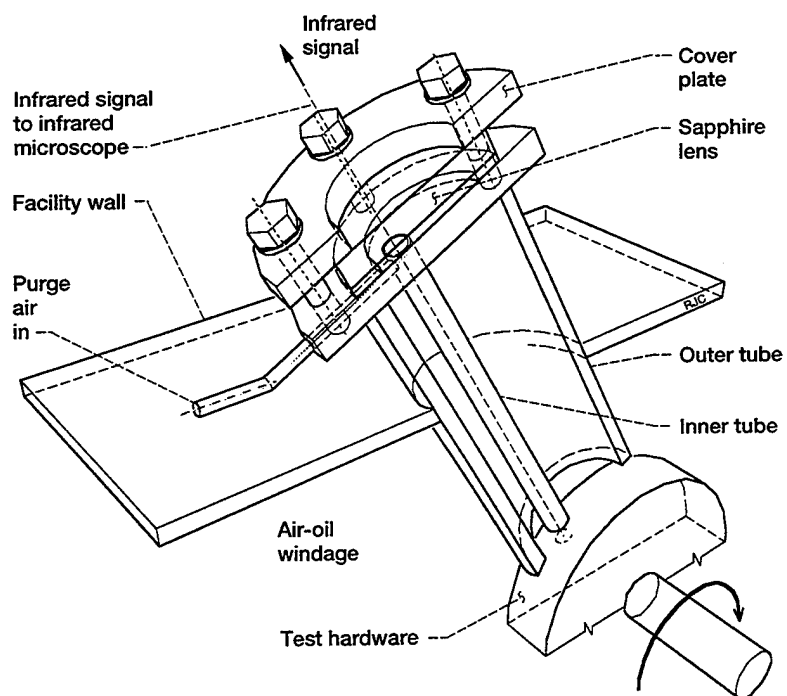


Figure 3.5.2.—Infrared optical path between test hardware and instrument.

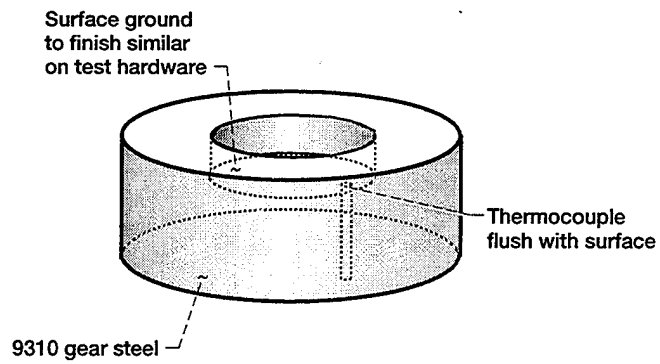


Figure 3.5.3.—Sketch of gear steel calibration dish.

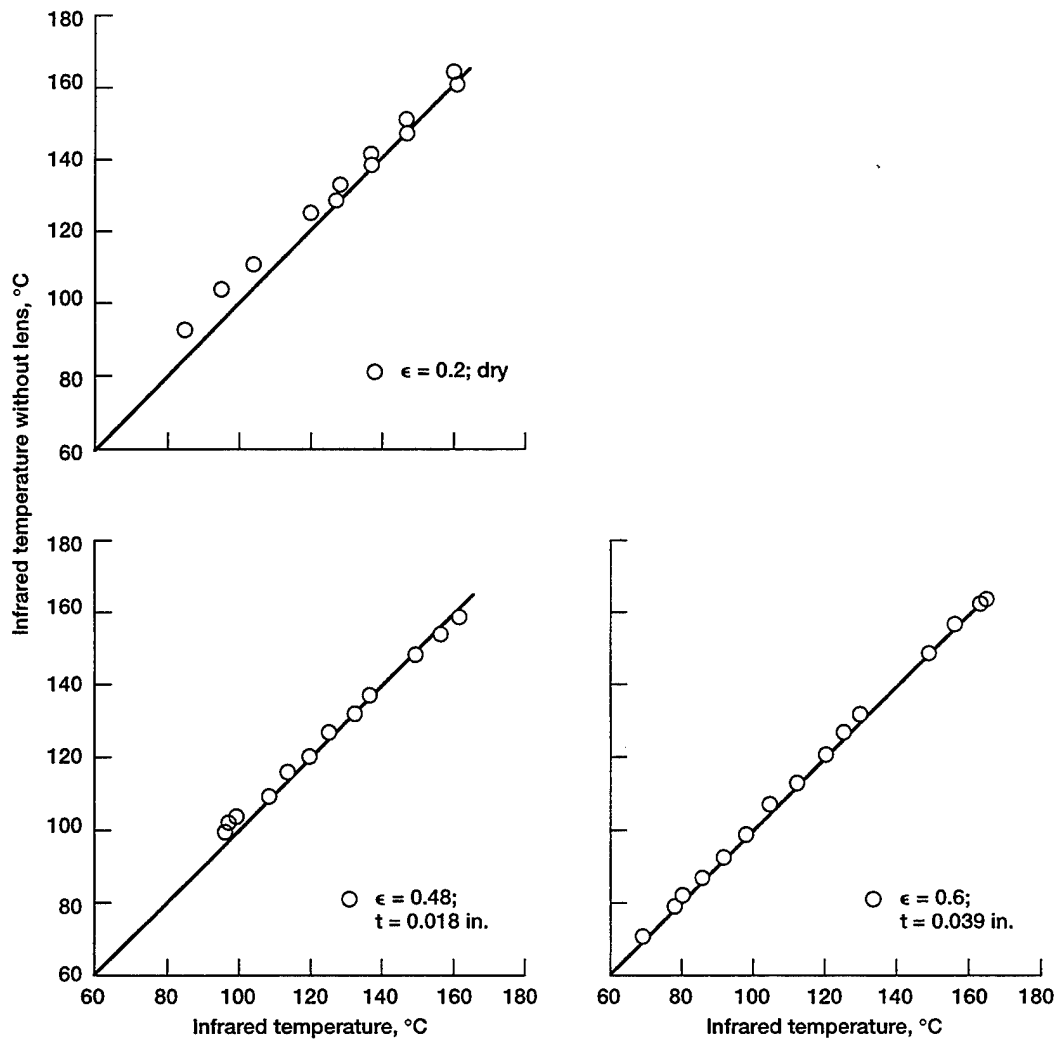


Figure 3.5.4.—Effect of lubricant film thickness "t" on steady state temperature.

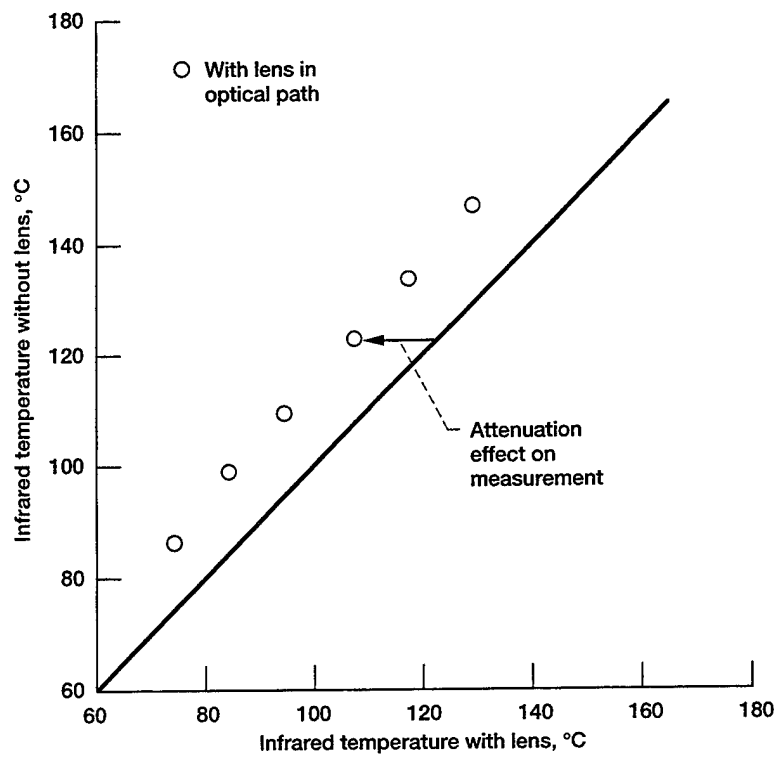


Figure 3.5.5.—Effect of sapphire lens attenuation on indicated infrared temperature using a blackbody source.

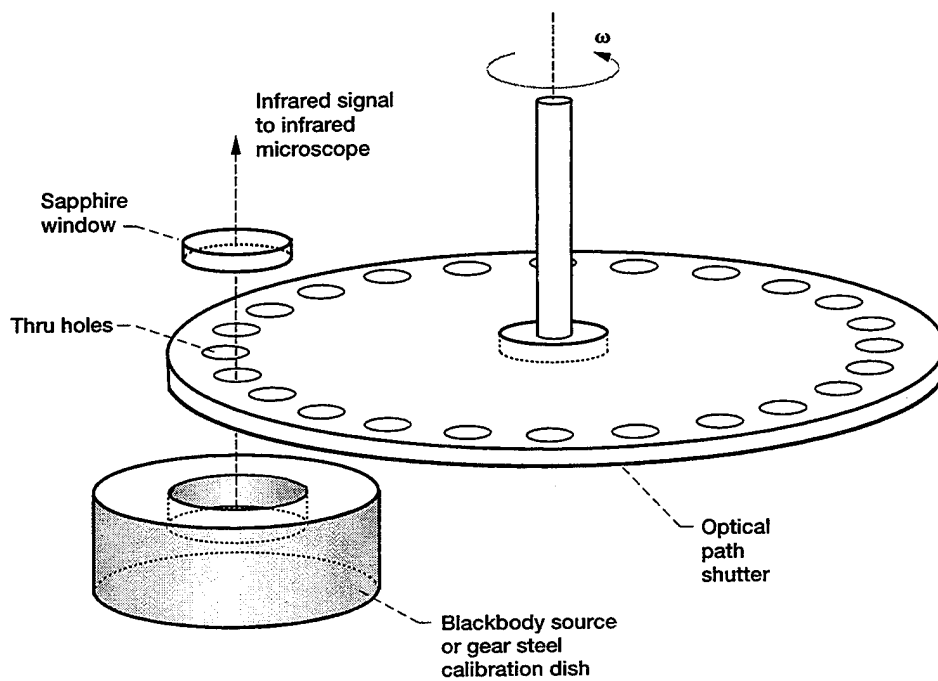


Figure 3.5.6.—Transient temperature calibration assembly.

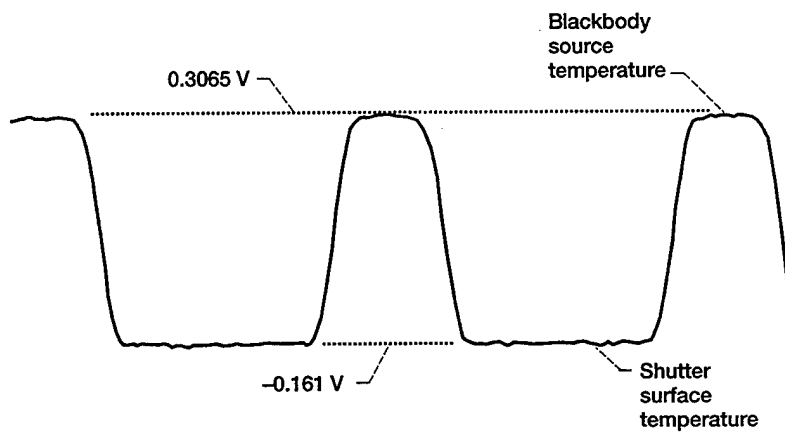


Figure 3.5.7.—Typical transient temperature data (blackbody calibration source without sapphire window).

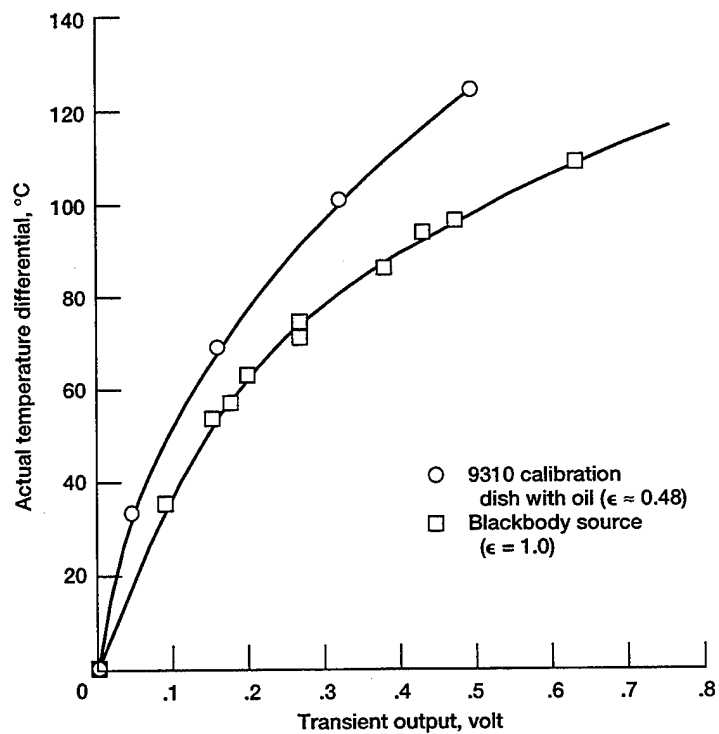


Figure 3.5.8.—Effect of emissivity on transient temperature measurement. (Without sapphire lens in optical path).

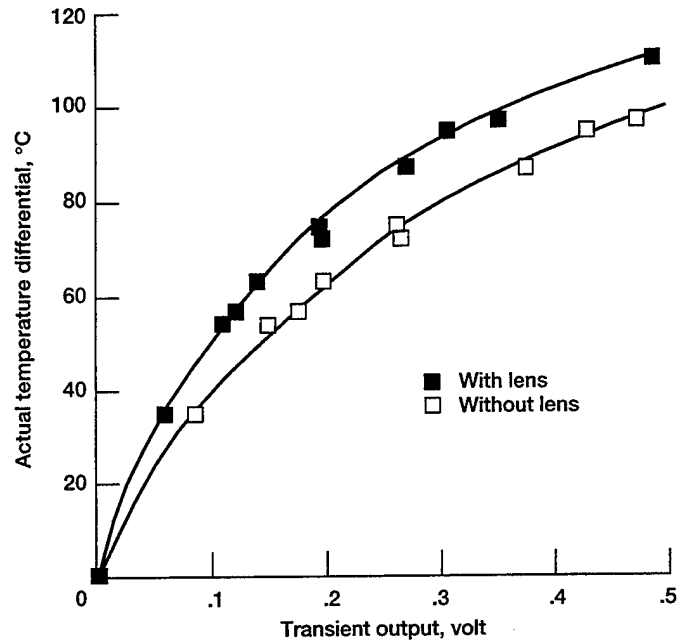


Figure 3.5.9.—Effect of sapphire lens on transient output voltage using a blackbody source.

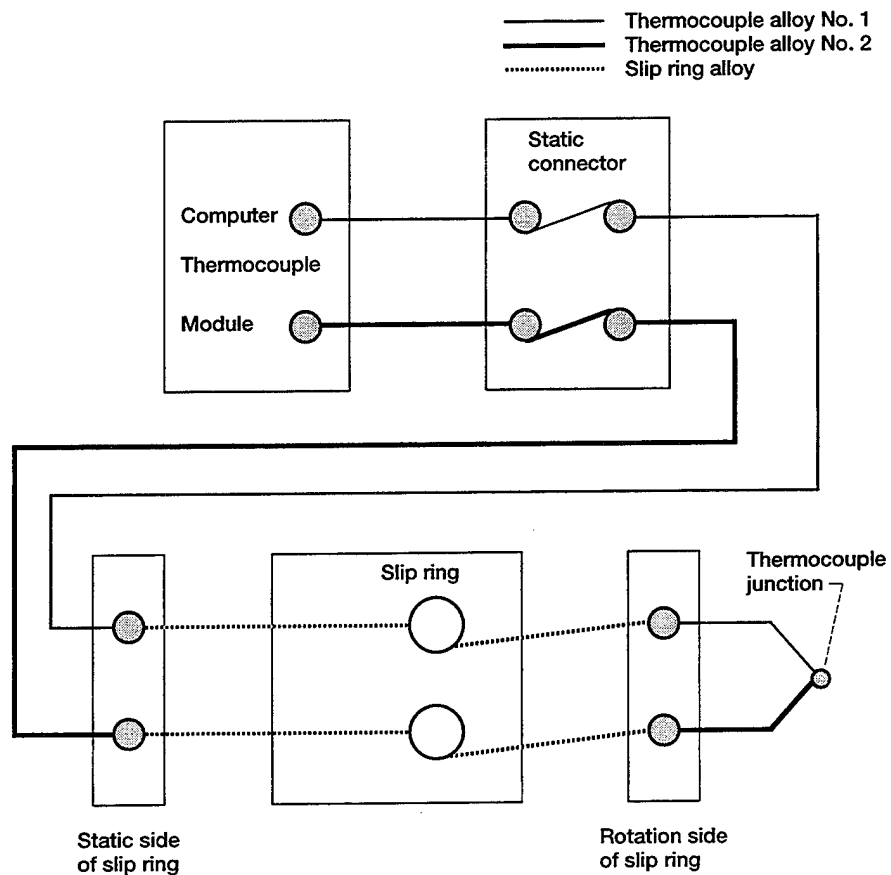


Figure 3.7.1.—Connection circuit used for bulk thermocouple measurements.

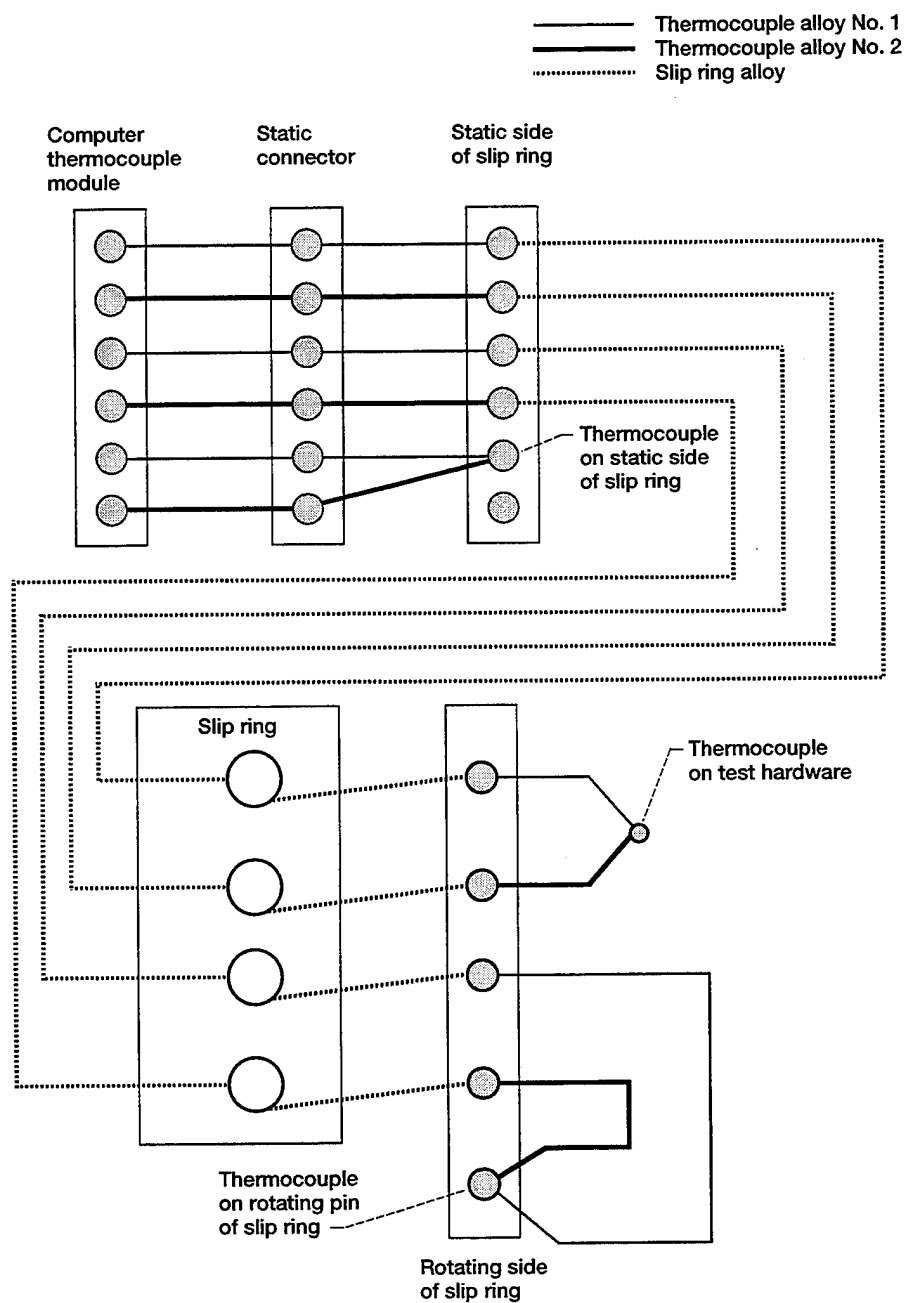


Figure 3.7.2.—Thermocouple circuit connection to determine slip ring effect on measurements.

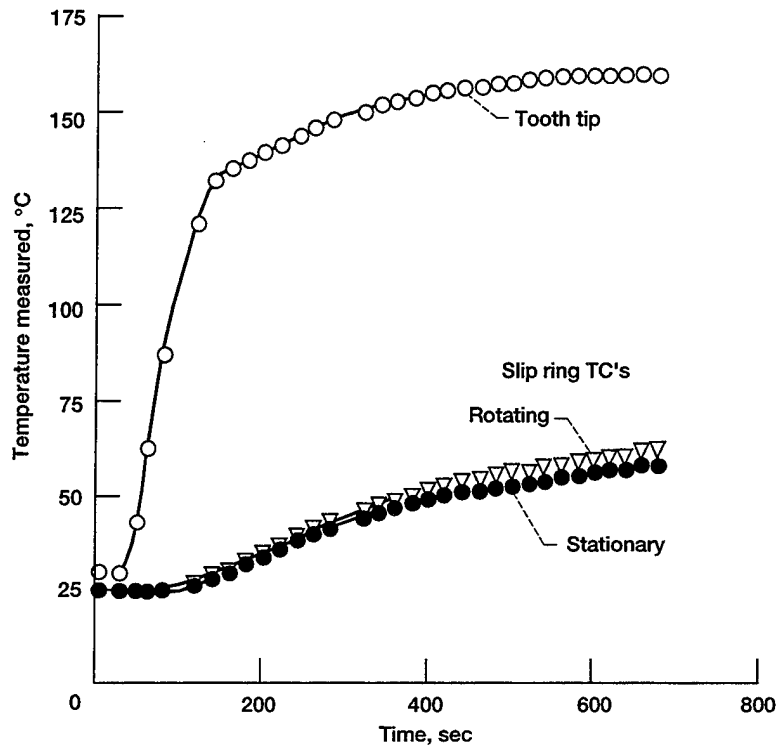
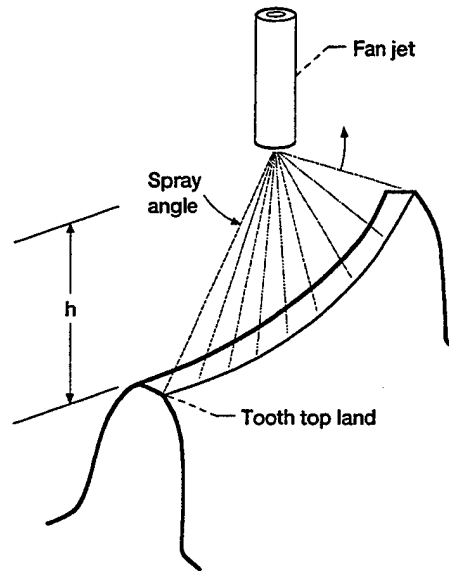


Figure 3.7.3.—Stationary and rotating thermocouple temperatures of slip ring compared to test hardware thermocouple measurement.



Distance $h$ ,**	10.2 mm (0.4 in.)
Equivalent orifice diameter	1.09 mm (0.043 in.)
Flow capacity (water)*	42 cm <sup>3</sup> /s (0.67 gal/min)
Spray angle*	90°

\* Based on 1.38 MPa (200 psi) at jet

\*\* Distance perpendicular to tooth top land

Figure 3.8.1.—Fan jet design used during part of the test program. Pencil jet tests had jet positioned in a similar height relative to tooth top.

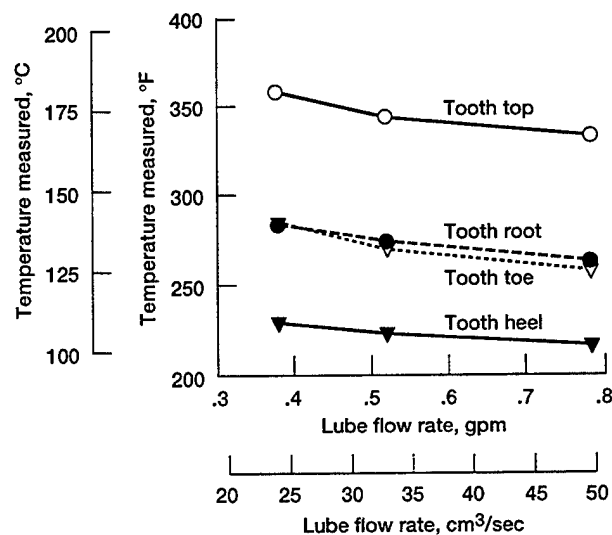


Figure 3.8.2.—Effect of flow rate on tooth temperature. Lubricant pressure varied from 0.35-1.42 MPa (51-206 psi).

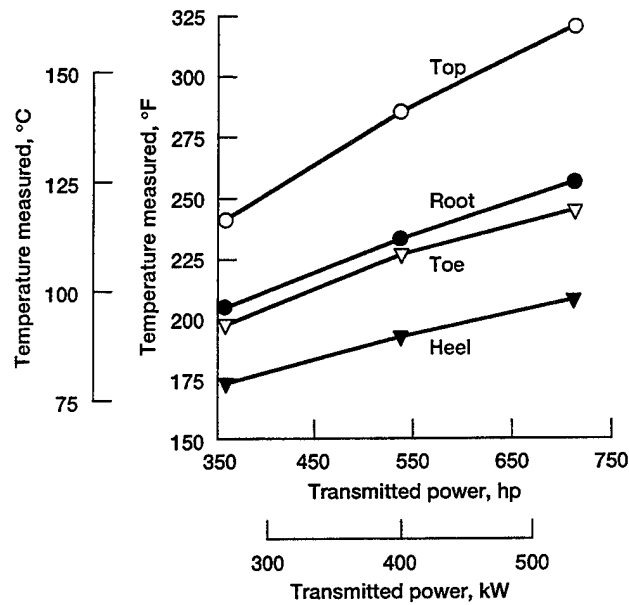


Figure 3.8.3.—Effect of load on pinion tooth temperatures at three power levels. All data taken at 38 °C (100 °F) oil inlet temperature and 14 400 rpm pinion shaft speed.

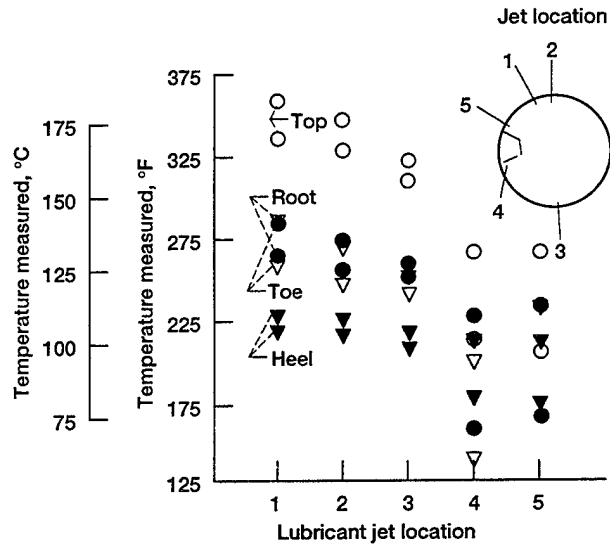


Figure 3.8.4.—Effect of lubricant jet location on pinion thermocouple measurements for two flow rates at 526-538 kW (705-721 hp). Upper symbol is for 24 cm³/sec (0.38 gpm) and lower symbol is for 49 cm³/sec (0.77 gpm).

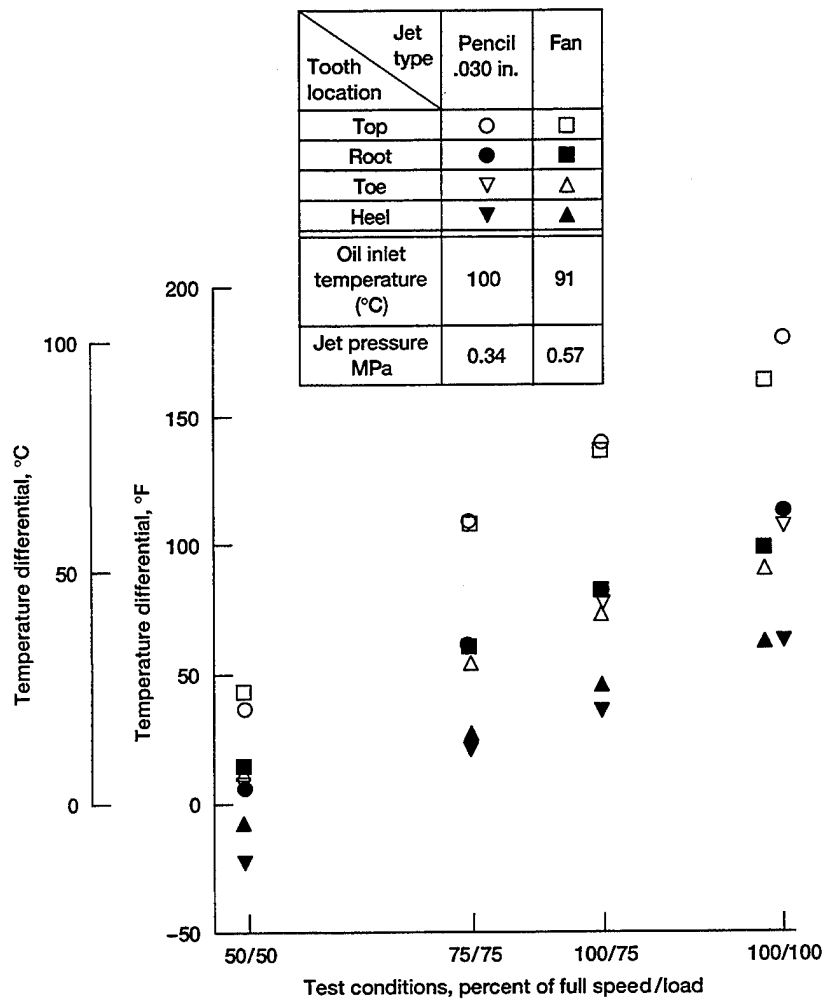


Figure 3.8.5.—Comparison of fan and pencil jets. Jet located 90° before mesh on the gear. Temperature differential is the oil inlet temperature subtracted from the measured temperature.

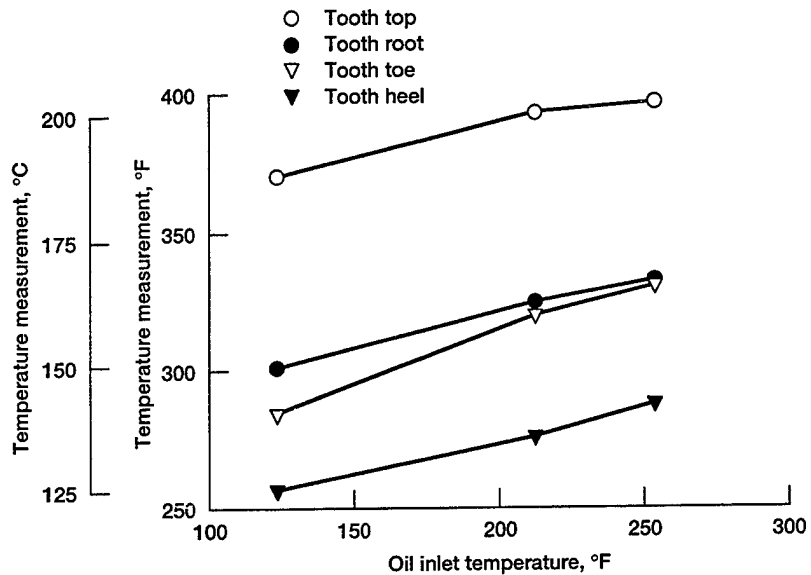


Figure 3.8.6.—Effect of oil inlet temperature on pinion temperature. Pencil jet oriented on the gear 90° before mesh. Oil jet pressure, speed, load held constant at 0.34 MPa, 14 400 rpm, 359 N•m (3130 in.•lb) respectively.

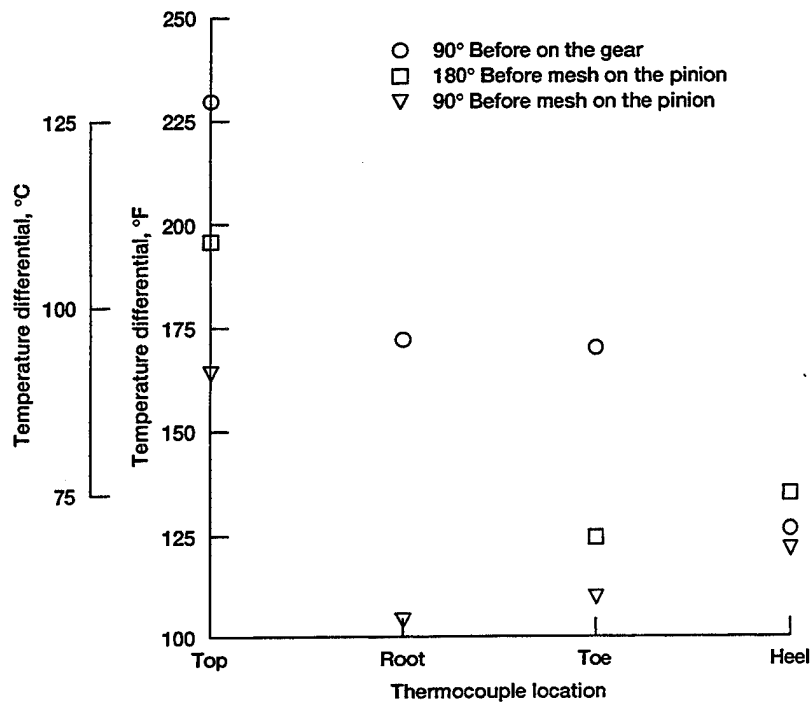


Figure 3.8.7.—Comparison of pencil jet test locations on the pinion to one location on the gear. Temperature differential is the oil inlet temperature subtracted from the measured temperature. Oil inlet temperature range was 48 – 58 °C (118 – 139 °F), oil jet pressure range was 1.36 – 1.43 MPa (198 – 207 psi), with 0.51 mm (0.02 in.) diameter jet. Speed and load were 14 400 rpm and 354 N•m (3130 in.•lb) respectively.

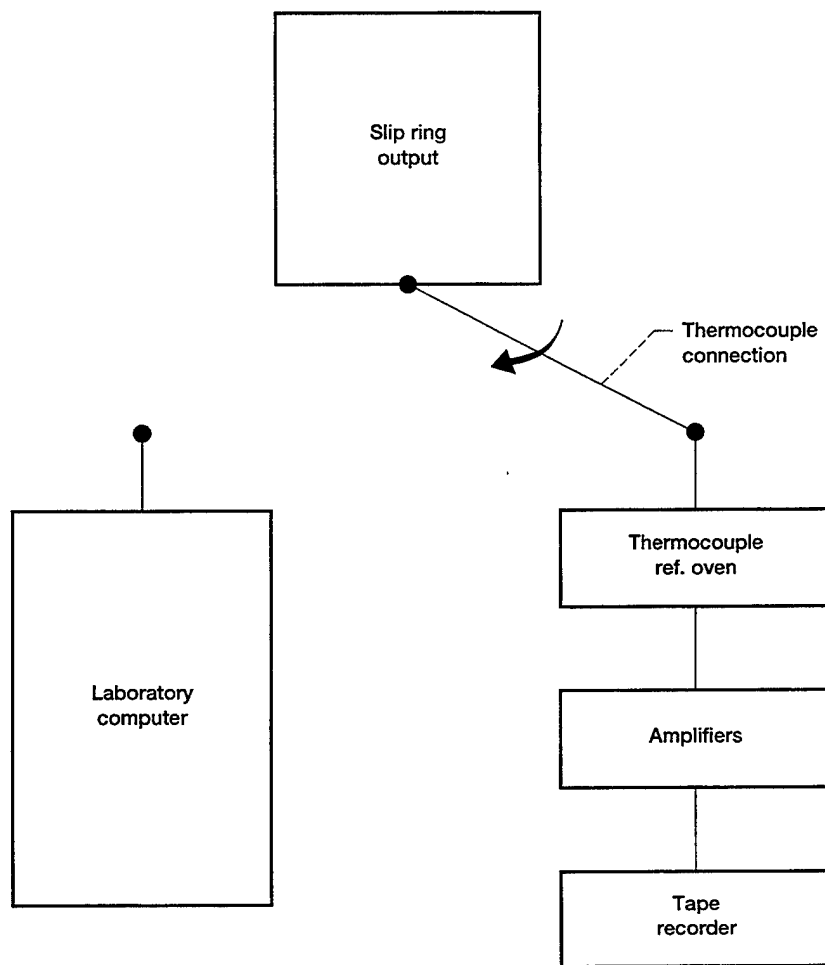


Figure 3.8.8.—Data acquisition connection possibilities for either laboratory computer measurement or tape recorder storage.

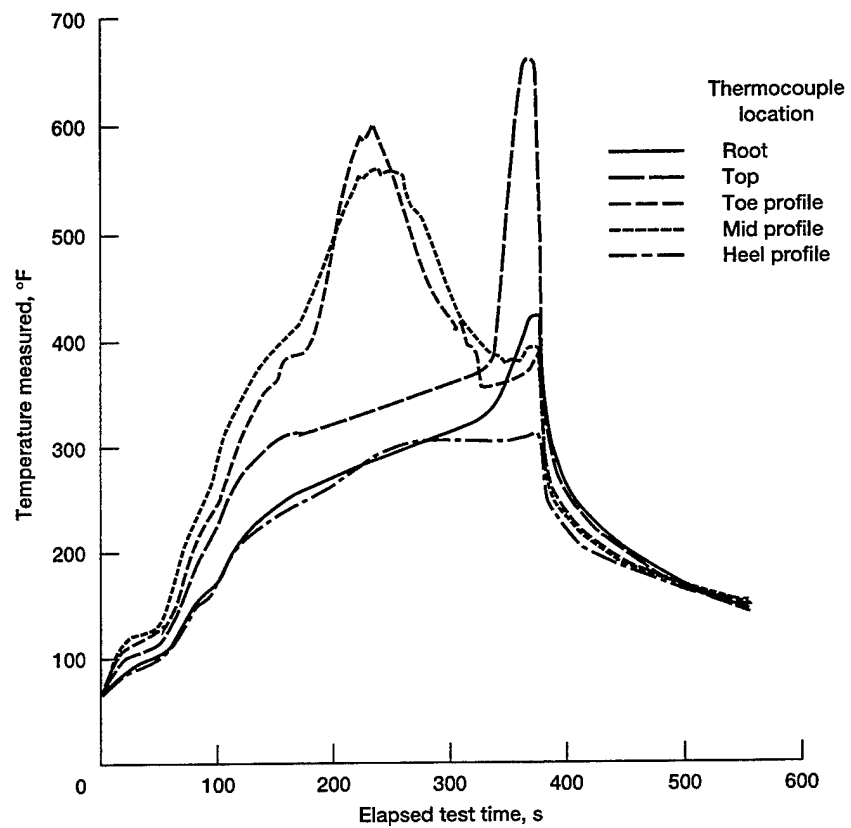


Figure 3.8.9.—Data taken via a laboratory computer when instrumentation failure and gear scoring occurred.

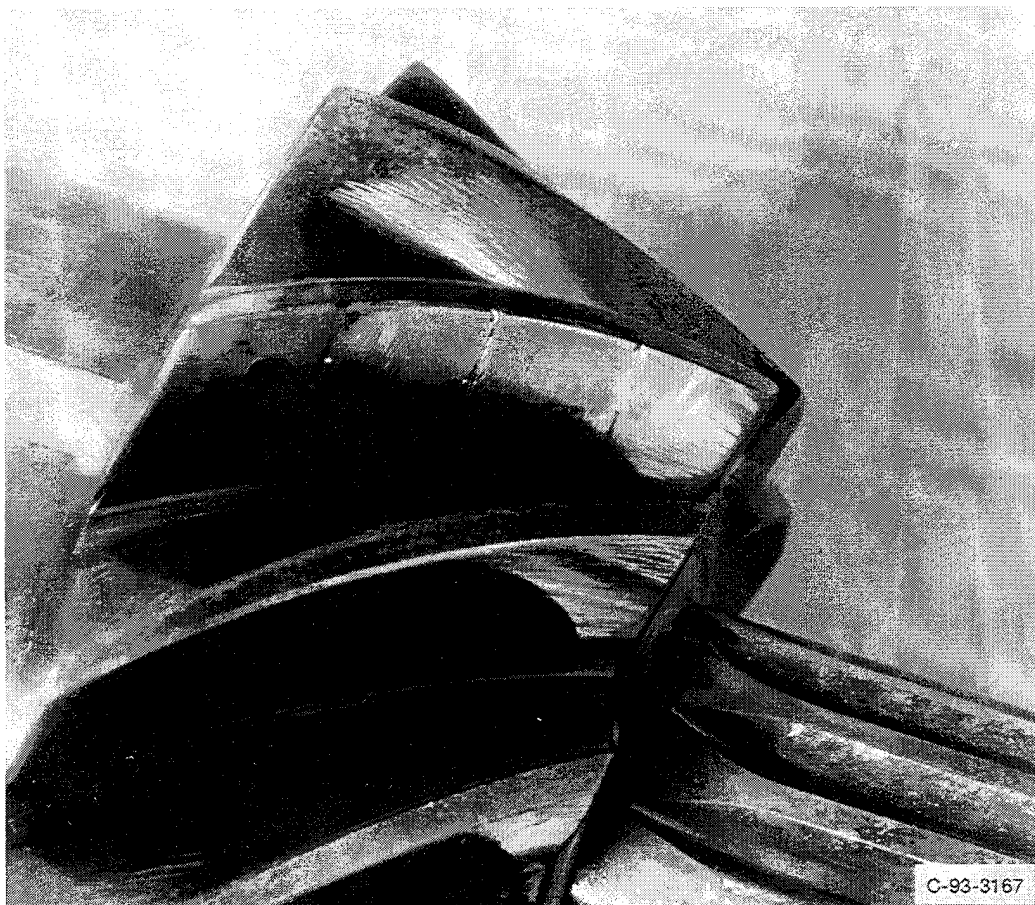


Figure 3.8.10.—Active profile thermocoupled pinion after gear surface scored.

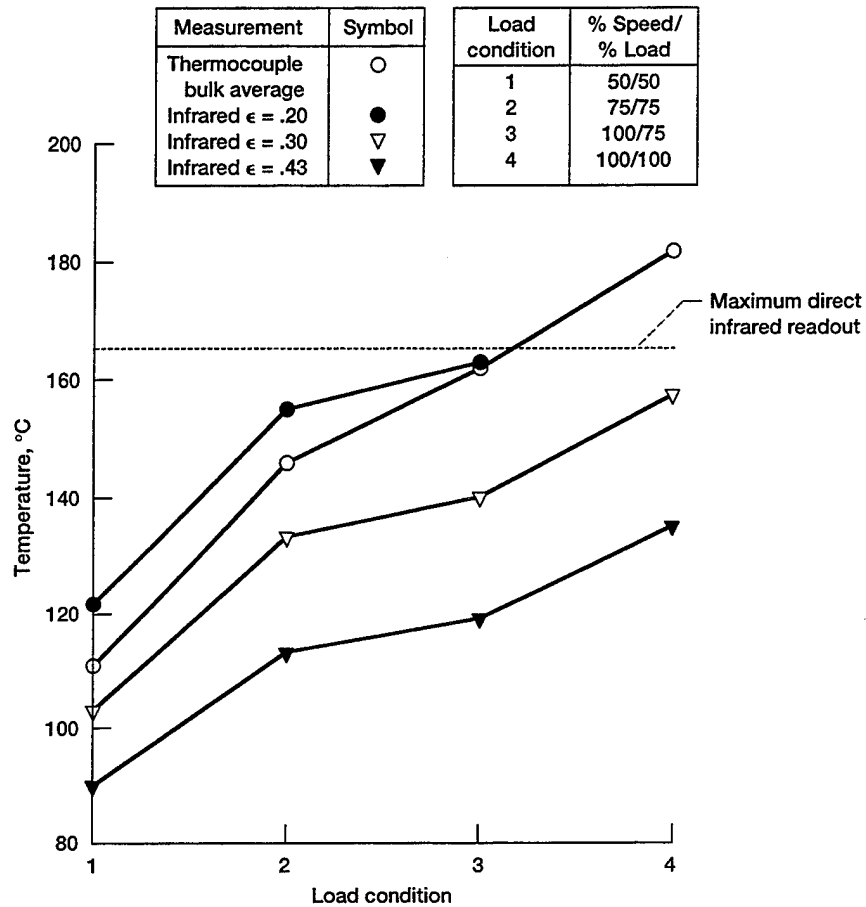


Figure 3.9.1.—Steady state infrared microscope measurements as a function of speed (100% = 14 400 rpm) and load (100% = 354 N•m(3130 in.•lb)). Lubrication jet was 0.76 mm (0.03 in.) pencil jet located on the gear 90° before mesh.

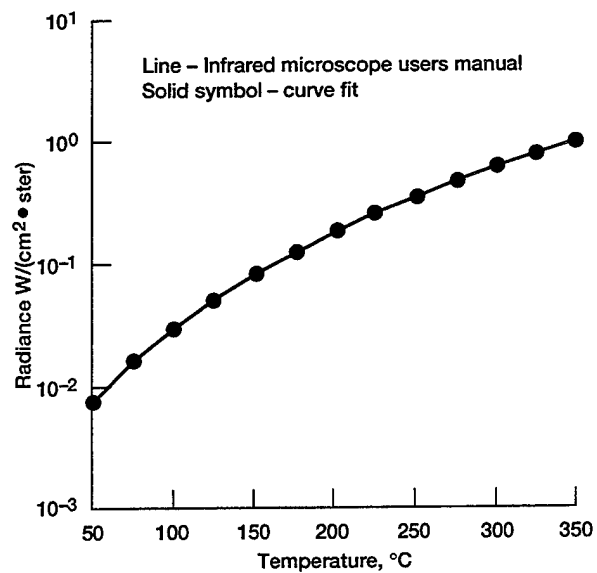


Figure 3.9.2.—Adjusted blackbody radiance as a function of temperature (Ref. [3.4]).

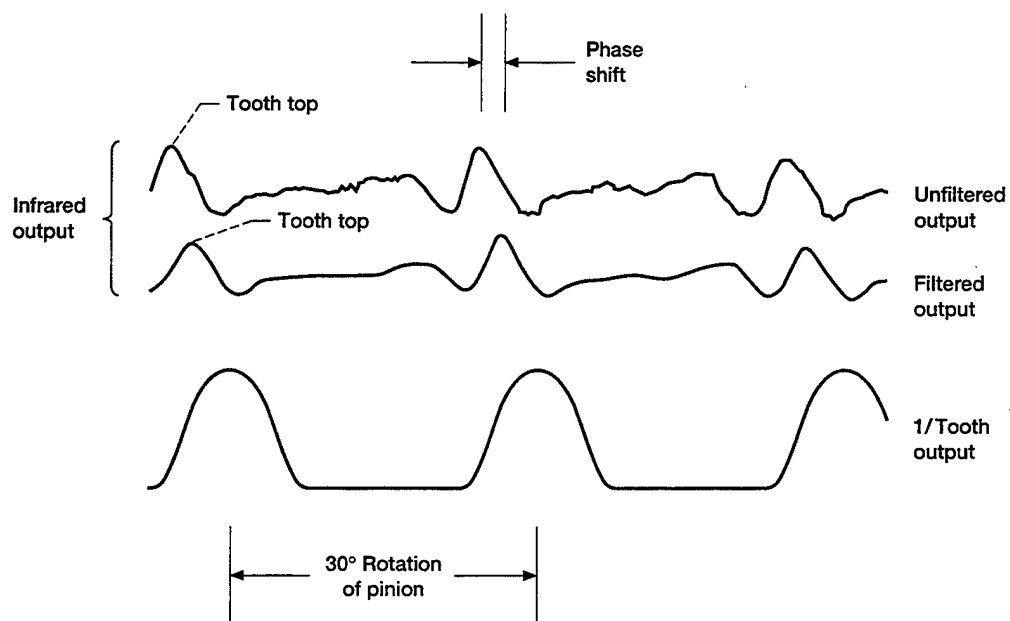


Figure 3.9.3.—Smoothing and phase shift effect of band-pass filtering of infrared microscope output. Band-pass was set at 30 Hz – 20 kHz, voltage differential maximum to minimum was approximately 0.25V.

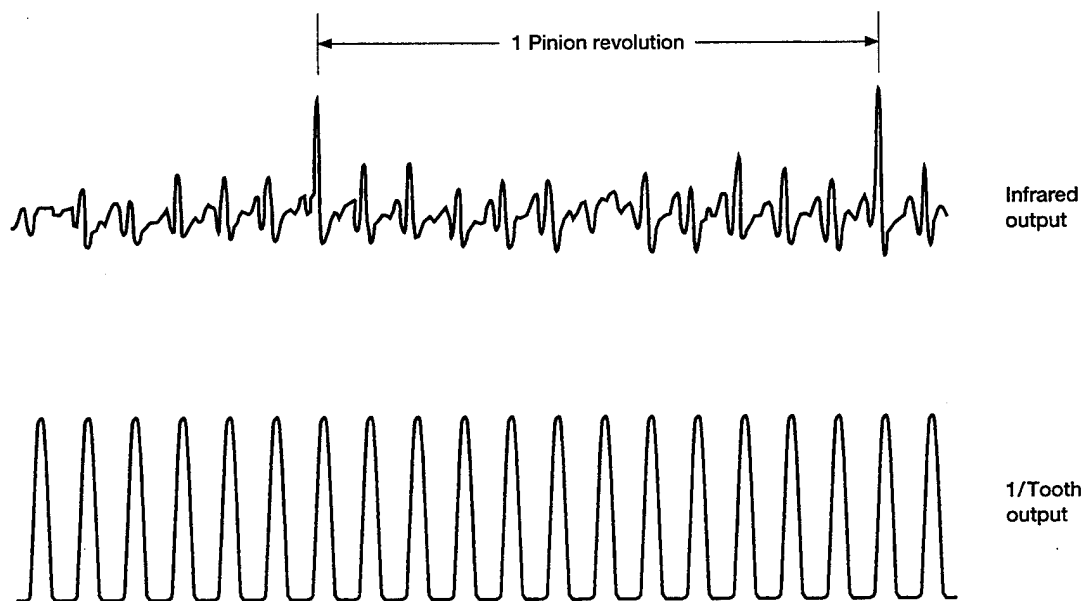
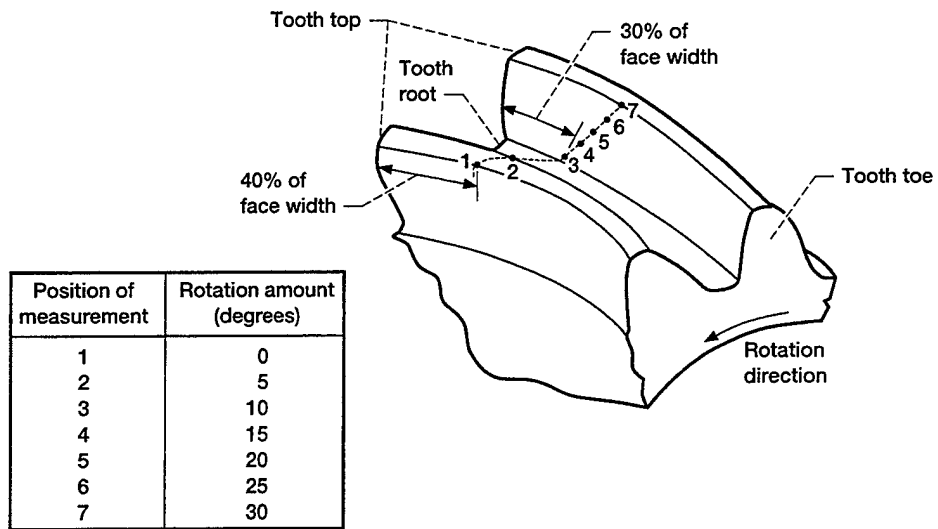
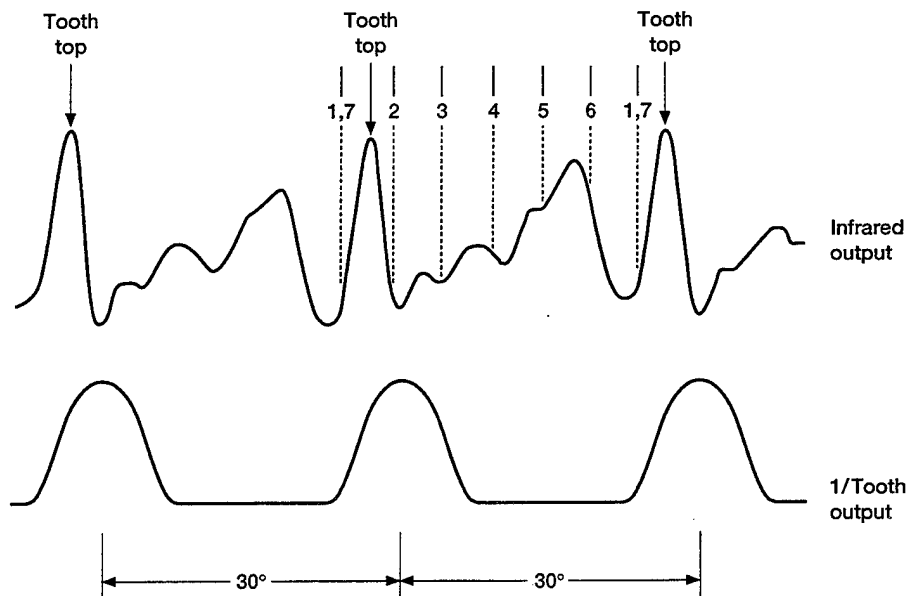


Figure 3.9.4.—Infrared microscope output for one pinion revolution.



(a) Infrared measurement path.



(b) Infrared path located on infrared output.

Figure 3.9.5.—Infrared path with respect to an infrared output measurement.

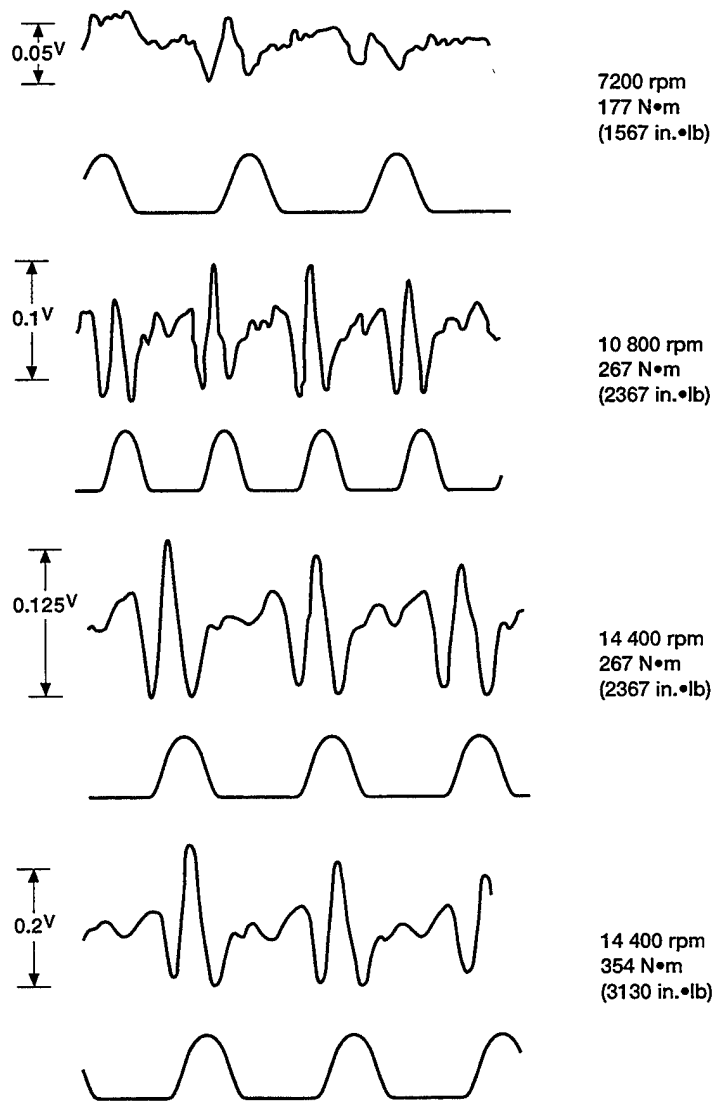


Figure 3.9.6.—Infrared data from four different operating conditions.

## CHAPTER 4: SPIRAL BEVEL GEAR GEOMETRY AND CONTACT MODELING

### 4.1 Introduction

Past research, with respect to spiral bevel gears, has concentrated on the development of gear geometry and the understanding of the meshing action (Refs. [4.1] to [4.16]). This meshing action often results in much vibration and noise due to an inherent lack of conjugate motion. This lack of conjugate motion, however, permits operation of the gear set in a satisfactory manner over a wide range of operating conditions found in typical aerospace applications. In these applications very flexible, lightweight housings lead to large nominal position changes of the meshing gear members. The mismatch of the meshing surfaces is the only way to have these gears operate satisfactorily for the life of the drive system. Understanding the complex geometry of spiral bevel gears is therefore essential to starting any advanced analytical procedure.

Parallel-axis components (involute tooth forms) have closed-form solutions that determine surface coordinates which can be used as input to finite element methods and other analysis tools. Spiral bevel gears, in contrast, have no closed-form solution to describe their surface coordinates; coordinate locations must be solved numerically. This process is accomplished by modeling the kinematics of the cutting or grinding machinery and the geometry of the basic gear design.

### 4.2 Spiral Bevel Gear Geometrical Approach

Recently, researchers have utilized this type of methodology to develop finite element models of spiral bevel gears (Refs. [4.17] to [4.21]). These models, except Chao (Ref. [4.18]), have basically investigated the structural characteristics of the spiral bevel gears. Only Chao (Ref. [4.18]) has ever addressed the thermal behavior of this type of gear from a finite element point of view. Wilcox (Ref. [4.17]) utilized the finite element method to investigate spiral bevel gear structural characteristics. The study used a combined finite element analysis and transfer matrix approach (influence coefficient analysis) to investigate bending stress as well as load sharing in the meshing gear members. The models had rather coarse mesh density but demonstrated the use of finite elements.

In Chao (Ref. [4.18]), the gear manufacturing mechanism was developed in great detail and led to the development of their finite element model. This model was utilized to study dynamic load, lubricant film thickness, and surface temperature. The same type of analysis as used in Wilcox (Ref. [4.17]) was used to model the load sharing and thermal distributions on the meshing teeth. The study of Chao (Ref. [4.18]) assumed many important quantities necessary to accurately characterize the thermal behavior of these gear members. That study, however, is the only known thermal study done on spiral bevel gears other than the one being described herein.

Other studies (Refs. [4.19] to [4.21]) have capitalized on recent developments in gear geometry theory (Ref. [4.22]) and advances in three-dimensional solid modeling packages (such as Ref. [4.23]) to develop highly detailed finite element models. Mesh density is relatively easy to reformulate, thereby reducing the time-consuming efforts required in some of these prior studies. Also, Reference [4.23] can display results in color, with the capability of sectioning models to see parameter changes that in the past required searching through large outputs of elemental stresses returned from the finite element method analysis.

In the present study, the method developed in Handschuh (Ref. [4.20]) is used. This methodology was originally developed to study gear structural behavior; however the same geometry modeling can be used to perform the thermal analysis.

### 4.3 Description of Spiral Bevel Gear Manufacture

The spiral bevel gear machining process described herein is the face-milled type, commonly known as the Gleason System. Spiral bevel gears manufactured in this way are used extensively in aerospace power transmissions where power from the horizontal gas turbine engines must be transmitted to the nearly vertical rotor shaft. Because spiral bevel gears can accommodate various shaft orientations, they allow greater freedom for the design of the given aircraft. The analytical basis for describing the tooth surface geometry comes from dissecting the manufacturing process kinematically. Equations are developed to relate the machine and workpiece motions during manufacture. The results are simultaneous nonlinear algebraic equations that require their solution numerically. The following is a description of this process.

Spiral bevel gears are manufactured on machinery like that shown in Figure 4.3.1. This machine removes material between the concave and convex tooth surfaces of adjacent teeth simultaneously (for the typical gear member). The machining process is further illustrated in Figure 4.3.2. The head cutter holds the cutting blades or grinding wheel, rotates about its own axis at the proper speed to efficiently remove metal, and is independent of the cradle or workpiece rotation. The head cutter is connected to the cradle by an eccentric to allow adjustment of the axial distance between the cutter center and the cradle center. These adjustments with the cutter radius provide the proper mean cone distance as well as the required spiral angle for the gear in question. The cradle and the workpiece are connected through a series of gears and shafts in the case of older machines. Optical encoders are used in the latest state-of-the-art computer numerically controlled (CNC) machines. In either case, the motion between the cradle and workpiece are the same, since the CNC version mimics the original gear-shaft system by point-to-point control of the machining surface and location of the workpiece.

### 4.4 Analytical Development of Gear Surface Geometry

The surface of a generated gear is an envelope to the family of surfaces of the head cutter. In simple terms, the points on the generated tooth surface are points of tangency to the cutter surface during manufacture. The conditions necessary for envelope existence are given kinematically by the equation of meshing (Ref. [4.22]), which can be stated as follows: the normal of the generating surface must be perpendicular to the relative velocity between the cutter and the gear tooth surface at the point in question.

The coordinate transformation procedure that is now described is required to locate any point from the head cutter into a coordinate system rigidly attached to the gear being manufactured. Homogeneous coordinates are used to allow rotation and translation of vectors simply by multiplying the matrix transformations. The method used for the coordinate transformations is found in References [4.10] and [4.20].

The process begins by starting with the head-cutter coordinate system  $S_c$  shown in Figure 4.4.1. For the analysis that is presented herein, the cutters are assumed to be straight sided. When the gears are ground, there may be curvature added to the cutting surface to preferentially remove gear surface material from the tip and root regions on the active profile to control the tooth contact behavior. Cutter surface parameters  $u$  and  $\theta$  determine the location of a current point of the cutter surface as well as the orientation of the current point with respect to coordinate system  $S_c$ . Angles  $\psi_{ib}$  and  $\psi_{ob}$  are the inside and outside blade angles. The inside and outside blades cut the convex and concave sides of the gear teeth, respectively. A point on the cutter blade surface is determined by the following:

$$r_c = \begin{bmatrix} r \cot \psi - u \cos \psi \\ u \sin \psi \sin \theta \\ u \sin \psi \cos \theta \\ 1 \end{bmatrix} \quad (4.4.1)$$

where fixed value  $r$  is the point radius of the blade at  $x_c = 0$ , and  $\psi$  is the blade angle. Parameters  $u$  and  $\theta$  locate a point in system  $S_c$  and are two of the three unknowns that are determined numerically.

The head-cutter coordinate system  $S_c$  is rigidly connected to coordinate system  $S_s$  (see Fig. 4.4.2). System  $S_s$  is rigidly connected to the cradle that rotates about the  $x_m$  axis of the machine coordinate system  $S_m$ . Coordinate system  $S_m$  is a fixed coordinate system and is connected to the machine frame.

To reference the head cutter in coordinate system  $S_s$ , the following coordinate transformation is required:

$$M_{sc} = \begin{bmatrix} 1 & 0 & 0 & 0 \\ 0 & \cos q & \mp \sin q & \mp s_1 \sin q \\ 0 & \pm \sin q & \cos q & s_1 \cos q \\ 0 & 0 & 0 & 1 \end{bmatrix} \quad (4.4.2)$$

where  $q$  is the cradle angle and  $s_1$  is the distance between the cradle center and cutter center. The upper and lower signs preceding the various terms in this matrix transformation (and in the rest of the spiral bevel gear geometry presented herein) pertain to left- and right-hand gears, respectively.

To transform from coordinate system  $S_s$  to  $S_m$ , the roll angle of the cradle  $\phi_c$  is used;  $\phi_c$  is the third and final unknown parameter in this analysis. This transformation is given by

$$M_{ms} = \begin{bmatrix} 1 & 0 & 0 & 0 \\ 0 & \cos \phi_c & \pm \sin \phi_c & 0 \\ 0 & \mp \sin \phi_c & \cos \phi_c & 0 \\ 0 & 0 & 0 & 1 \end{bmatrix} \quad (4.4.3)$$

Coordinate system  $S_m$  locates the machine center, and coordinate system  $S_p$  orients the pitch apex of the gear being manufactured. The transformation from coordinate system  $S_m$  to coordinate system  $S_p$  requires the machine tool settings  $L_m$  and  $E_m$  along with dedendum angle  $\delta$  from the component design (shown in Figs. 4.4.3 and 4.4.4). Machine tool settings  $L_m$  and  $E_m$  can be found from either the summary sheet that typically accompanies a gear or from the methods in Litvin (Ref. [4.10]). Using the method shown in Reference [4.10], the conversion of the standard machine tool settings for the sliding base, the machining offset, and the machine center-to-back into settings  $L_m$  and  $E_m$  are made as shown in Table 4.4.1. The transformation matrix that includes the dedendum angle  $\delta$  and machine settings  $L_m$  and  $E_m$  is given by

$$M_{pm} = \begin{bmatrix} \cos \delta & 0 & -\sin \delta & -L_m \sin \delta \\ 0 & 1 & 0 & \pm E_m \\ \sin \delta & 0 & \cos \delta & L_m \cos \delta \\ 0 & 0 & 0 & 1 \end{bmatrix} \quad (4.4.4)$$

This transformation is shown in Figure 4.4.3 for a right-hand gear member and in Figure 4.4.4 for a left-hand gear member. Figure 4.4.5 is given to further clarify the orientation of the coordinate systems and the machine tool settings just discussed.

The next coordinate transformation involves the rotation of coordinate system  $S_p$  to  $S_a$ . The common origin for coordinate systems  $S_p$  and  $S_a$  locates the apex of the gear under consideration with respect to coordinate system  $S_m$ . This requires a rotation about  $y_a$  by the pitch angle  $\mu$  as shown in Figure 4.4.5. This transformation is given by

$$M_{ap} = \begin{bmatrix} \cos \mu & 0 & \sin \mu & 0 \\ 0 & 1 & 0 & 0 \\ -\sin \mu & 0 & \cos \mu & 0 \\ 0 & 0 & 0 & 1 \end{bmatrix} \quad (4.4.5)$$

The final required transformation is from the coordinate system  $S_a$  to the workpiece fixed coordinate system  $S_w$ . A rotation about the  $z_a$ -axis through the roll angle of the work  $\phi_w$  is needed (see Fig. 4.4.6). Angle  $\phi_w$  is related to the angle of rotation of the cradle  $\phi_c$ . This relationship is discussed later in this section. The transformation of coordinate system  $S_a$  to  $S_w$  is given by

$$M_{wa} = \begin{bmatrix} \cos \phi_w & \pm \sin \phi_w & 0 & 0 \\ \mp \sin \phi_w & \cos \phi_w & 0 & 0 \\ 0 & 0 & 1 & 0 \\ 0 & 0 & 0 & 1 \end{bmatrix} \quad (4.4.6)$$

Using the five coordinate transformations given above, it is possible to determine the coordinates of a point in the gear fixed coordinate system. This is accomplished by multiplication of these transformations in the prescribed manner (shown below) along with machine settings  $L_m$ ,  $E_m$ ,  $q$ ,  $s_1$ ,  $r$ , and  $\psi$ ; with parameters  $u$ ,  $\theta$ , and  $\phi_c$ ; and with gear design data  $\mu$  and  $\delta$ .

The complete transformation process is described by

$$r_w = M_{wa} M_{ap} M_{pm} M_{ms} M_{sc} r_c(u, \theta) \quad (4.4.7)$$

The tooth surface coordinate solution procedure is now presented. To solve for the coordinates of a spiral bevel gear tooth surface, the manufacturing process and the gear's design must be considered simultaneously. The transformation process described in the previous section locates a point from the head-cutter coordinate system to that in the coordinate system fixed to the gear being manufactured. Therefore, there are three parameters  $u$ ,  $\theta$ , and  $\phi_c$ , which require that three equations be developed to solve for these quantities.

Values for the parameters just described are used to satisfy the equation of meshing given in Litvin (Ref. [4.22]):

$$\mathbf{n} \cdot \mathbf{V} = 0 \quad (4.4.8)$$

where  $\mathbf{n}$  is the normal vector to the cutter and workpiece surfaces at the specified location of interest, and  $\mathbf{V}$  is the relative velocity between the cutter and workpiece surfaces at the specified location. From Litvin (Ref. [4.10]), the equation of meshing for straight-sided cutters with a constant ratio of roll between the cutter and workpiece, Equation (4.4.8), is found to be

$$\begin{aligned} & (u - r \cot \psi \cos \psi) \cos \gamma \sin \tau \\ & + s_1 [(m_{cw} - \sin \gamma) \cos \psi \sin \theta \mp \cos \gamma \sin \psi \sin(q - \phi_c)] \\ & \pm E_m (\cos \gamma \sin \psi + \sin \gamma \cos \psi \cos \tau) \\ & - L_m \sin \gamma \cos \psi \sin \tau = 0 \end{aligned} \quad (4.4.9)$$

where  $\gamma$  is the root angle of the manufactured component and

$$\tau = (\theta \mp q \pm \phi_c) \quad (4.4.10)$$

where  $\tau$  is an auxiliary variable that combines angles  $q$ ,  $\theta$ , and  $\phi_c$ , and

$$m_{cw} = \frac{\omega^{(c)}}{\omega^{(w)}} \quad (4.4.11)$$

Here  $m_{cw}$  is the ratio of the angular velocity of the cradle  $\omega^{(c)}$  to that of the workpiece  $\omega^{(w)}$ . Since the ratio of roll is considered a constant in this study, it can be shown that the cradle and work rotation angles are related by the following (Ref. [4.20]):

$$\phi_w = \frac{\phi_c}{m_{cw}} \quad (4.4.12)$$

This relationship is used directly in Equation (4.4.6) for the coordinate transformation given. Now, gear design information is used to establish an allowable range of values of the radial and axial positions that are known to exist on the gear being generated. This is shown schematically in Figure 4.4.7.

As mentioned earlier in this section, there are three parameters that must be used to satisfy the equation of meshing. Also the relationship between the cutter and known workpiece geometrical constraints must be utilized. These two basic ideas are combined to permit the numerical solution of the parameters  $u$ ,  $\theta$ , and  $\phi_c$ .

The equation of meshing is already in the following form:

$$f_1(u, \theta, \phi_c) = 0 \quad (4.4.13)$$

At this point, the gear design information is already known and is utilized to form the other two equations. First, a known axial position must match the value found from the transformation from the cutter  $S_c$  to the workpiece coordinates  $S_w$ . This position is given as

$$z_w - \bar{z} = 0 \quad (4.4.14)$$

or

$$f_2 u, \theta, \phi_c = 0 \quad (4.4.15)$$

Finally, the radial location from the work axis of rotation must be satisfied. This location is found from the magnitude sum of the  $x_w$  and  $y_w$  components and is expressed as

$$\bar{r} - x_w^2 + y_w^2 = 0 \quad (4.4.16)$$

or

$$f_3 u, \theta, \phi_c = 0 \quad (4.4.17)$$

Therefore, a system of three equations ((4.4.13), (4.4.15), and (4.4.17)) is used to solve for the three parameters  $u$ ,  $\theta$ , and  $\phi_c$ . These are nonlinear algebraic equations and require a numerical solution. A commercially available routine (Ref. [4.24]) is used to accomplish this task.

The equations developed above are solved for various radial and axial positions along the gear active profile, as shown in Figure 4.4.8. In a computer program developed by Handschuh (Ref. [4.20]), a 10-point-by-10-point grid is used to describe each side of the gear tooth surface profiles.

#### 4.5 Three-Dimensional Contact Methodology for Application to Spiral Bevel Gears

In the following discussion, the method of applying the thermal load on the teeth is described. The thermal load is applied to the gear body by the contacting ellipse between the pinion and gear. The contact ellipse changes in size and orientation during the process of meshing.

The gear geometry characteristics (Litvin, Ref. [4.25]) were combined with classical Hertzian theory as described by Boresi et al. (Ref. [4.26]). This combination enabled the calculation of the contact ellipse size, orientation, and location on the active profile of the spiral bevel gear.

The following assumptions were made to conduct the analysis presented herein: (1) The material of each of the two bodies is homogeneous, isotropic, and elastic (in our case, both bodies have the same properties but this is not required for the analysis); (2) at the point of contact under no load, there is a common tangent plane and corresponding points that are an equal distance from the plane. Under a given amount of loading, these equidistant points will then be in contact.

**Gear Geometry Considerations:** As already mentioned earlier in this chapter, Litvin's method (Ref. [4.25]) for the description of the gear contacting geometry will be used. The gear contacting geometry is based on gear manufacturing data and operation boundary conditions. The output from this analysis is the following: (1) the contact position; (2) the orientation and magnitude of the principal surface curvatures at the contact position; (3) the gear rotation error; (4) the sliding and rolling velocities; and (5) the load based on a single pair of teeth.

Litvin (Ref. [4.25]) also conducts a tooth contact analysis that is purely geometrical. An "elastic approach" of the surfaces is input and the resulting contact ellipse size is found. The criteria are that within the neighborhood of the contact point, all surfaces within the elastic approach are then considered to be in contact. For a light load, as might be applied in a contact pattern checking machine used in the inspection process of spiral bevel gears, the value for the elastic approach is typically assumed to be 0.0064 mm (0.00025 in.). From Litvin (Refs. [4.12] and [4.22]), the following equations are utilized to calculate the magnitude and orientation of the principal curvatures of the contacting gears and the ellipse size (see Fig. 4.5.1):

$$A = \frac{1}{4} \left[ \kappa_e^{(1)} - \kappa_e^{(2)} - (g_1^2 - 2g_1g_2 \cos 2\sigma^{(21)} + g_2^2)^{1/2} \right] \quad (4.5.1)$$

$$B = \frac{1}{4} \left[ \kappa_e^{(1)} - \kappa_e^{(2)} + (g_1^2 - 2g_1g_2 \cos 2\sigma^{(21)} + g_2^2)^{1/2} \right] \quad (4.5.2)$$

$$a = \left( \left| \frac{\Lambda}{A} \right| \right)^{1/2}; \quad b = \left( \left| \frac{\Lambda}{B} \right| \right)^{1/2} \quad (4.5.3)$$

$$\tan 2\Gamma = \frac{g_1 \sin 2\sigma^{(21)}}{g_2 - g_1 \cos 2\sigma^{(21)}} \quad (4.5.4)$$

$$\kappa_e^{(i)} = \kappa_I^{(i)} + \kappa_{II}^{(i)}; \quad g_i = \kappa_I^{(i)} - \kappa_{II}^{(i)} \quad (i = 1, 2) \quad (4.5.5)$$

$$\cos \sigma^{(21)} = \mathbf{i}_I^{(2)} \cdot \mathbf{i}_I^{(1)} \quad (4.5.6)$$

$$\sin \sigma^{(21)} = \pm \mathbf{n} \cdot [\mathbf{i}_I^{(2)} \times \mathbf{i}_I^{(1)}] \quad (4.5.7)$$

where

- $\kappa_j^{(i)}$ ;      (i=1,2;j=I,II) principal curvature of gear i with principal direction j
- $\kappa_e^{(i)}$       sum of principal curvatures of gear i
- $g_i$       difference of principal curvatures of gear i
- $\Lambda$       assumed elastic approach
- $\mathbf{i}_j^{(i)}$       principal direction j of gear i
- $\mathbf{n}$       normal vector of contacting bodies
- $\sigma^{(21)}$       angle between principal directions (see Fig. 4.5.1)
- $\Gamma$       angle from major principal direction of contact ellipse to principal direction I of gear member 1
- a,b      semimajor and semiminor lengths of contact ellipse, respectively
- $\eta, \xi$       directions of semimajor, semiminor ellipse lengths a,b, respectively.

**Hertzian Contact:** The method used to model the contact is taken from Boresi (Ref. [4.26]). Another more historical source of information on the three-dimensional contact between bodies is found in Timoshenko and Goodier (Ref. [4.27]). Within both of these analyses, the same basic principals are applied. The boundary conditions that were assumed above are used. The basic premise is that contact under no load starts at a point. Upon

application of a load, the surfaces elastically deform such that points on both bodies that were the same distance from a tangent plane are in contact when a certain level of load is reached. The distance  $Z$  between corresponding points is given by

$$Z = Ax^2 + By^2 \quad (4.5.8)$$

where  $x$  and  $y$  lie in the above-mentioned tangent plane and  $A$  and  $B$  are positive constants that are a function of the principal curvatures and orientation at the point of contact.  $A$  and  $B$  are given by

$$A = C_1 - C_2; \quad B = C_1 + C_2 \quad (4.5.9)$$

where

$$C_1 = \frac{1}{4} \left( \frac{1}{R_1} + \frac{1}{R_2} + \frac{1}{R_1'} + \frac{1}{R_2'} \right) \quad (4.5.10)$$

$$C_2 = \frac{1}{4} \left\{ \left[ \left( \frac{1}{R_1} - \frac{1}{R_1'} \right) + \left( \frac{1}{R_2} - \frac{1}{R_2'} \right) \right]^2 - 4 \left( \frac{1}{R_1} - \frac{1}{R_1'} \right) \left( \frac{1}{R_2} - \frac{1}{R_2'} \right) \sin^2 \sigma^{(21)} \right\}^{1/2} \quad (4.5.11)$$

Here the  $R$ 's are the principal curvatures of the surfaces 1 and 2,  $\sigma^{(21)}$  is the angle between the principal curvatures. Curvatures are positive if the radius is contained with the body and negative if it is exterior to the body in question.

Boresi (Ref. [4.26]) condensed the analysis in a series of graphs to present an easy format to calculate the parameters of interest. The results presented are not only for contact ellipse size and surface deflection, but also to determine the level of stress in the vicinity of the contact. Because, in the present work the stress level is not of the utmost concern, the focus is on extracting what is necessary for the development of the thermal model.

In the graphical solution, the geometric ratio  $B/A$  is the starting point of the analysis (Eqs. (4.5.9) to (4.5.11)). Once this ratio is found, the graphs (Figs. 4.5.2 and 4.5.3) are used to determine the parameters of interest. From these figures, the values of  $C_b$ ,  $C_\delta$ ,  $k$ , etc. are found directly. In the present study, there is only concern for three of the plotted quantities:  $k$ ,  $C_b$ , and  $C_\delta$ . Where these quantities are given by

$$k = \frac{b}{a} \quad (4.5.12)$$

$k$  is the ratio of the minor to major ellipse dimensions,

$$C_b = \left( \frac{3kE(k')}{2\pi} \right)^{1/3} \quad (4.5.13)$$

$C_b$  is related to the minor ellipse dimension,

$$C_\delta = \frac{3kK(k')}{2} \quad (4.5.14)$$

$C_\delta$  is related to the deflection at the point of contact.

The functions  $E(k')$  and  $K(k')$  are found by evaluation of the elliptical integrals  $H(\phi, k')$  and  $F(\phi, k')$  given by

$$E(k') = H\left(\frac{\pi}{2}, k'\right) = \int_0^{\pi/2} (1 - k'^2 \sin^2 \theta)^{1/2} d\theta \quad (4.5.15)$$

$$K(k') = F\left(\frac{\pi}{2}, k'\right) = \int_0^{\pi/2} \frac{d\theta}{(1 - k'^2 \sin^2 \theta)^{1/2}} \quad (4.5.16)$$

$$k' = (1 - k^2)^{1/2} \quad (4.5.17)$$

An additional equation is required to find the appropriate value of  $k$ , based on the three-dimensional contacting geometry, and is given in Reference [4.26] as

$$\frac{B}{A} = \frac{\left(\frac{1}{k^2}\right)E(k') - K(k')}{K(k') - E(k')} \quad (4.5.18)$$

which could also be rearranged to be

$$\frac{B}{A}[K(k') - E(k')] + K(k') - \left(\frac{1}{k^2}\right)E(k') = 0 \quad (4.5.19)$$

The results from this analysis procedure are plotted in Figures 4.5.2 and 4.5.3. A fairly straightforward procedure is followed to determine the size of the ellipse, the deflection at the point of contact, and the maximum pressure. For the analysis described herein, the process was automated because a great deal of hand calculations would be required using the plots shown, and the accuracy would be compromised. The following automated procedure was utilized.

An iterative solution was required since the value  $k$  is contained in the transcendental equation (Eq. (4.5.18) or (4.5.19)). An interval halving technique (Ref. [4.28]) was used to find the solution to Equation (4.5.19). The following procedure was numerically established:

- (1) Calculate  $A$  and  $B$  using the given gear geometry with Equations (4.5.9) to (4.5.11).
- (2) Assume a value for  $k$ , calculate  $k'$ .
- (3) Integrate equations (4.5.15) and (4.5.16) numerically by Simpson's Rule from 0 to  $\pi/2$  with 100 increments.
- (4) Substitute elliptical integral values into Equation (4.5.19).
- (5) Increment  $k$  until the absolute value of Equation (4.5.19) is less than  $1 \times 10^{-6}$ .

The procedure for numerical integration of the elliptical equations was tested against the tabulated results found in a mathematics handbook (Ref. [4.29]). The values were within 0.5 percent of the tabulated results.

Once convergence was established, Equations (4.5.13) and (4.5.14) were used to find  $C_b$  and  $C_s$ . The minor ellipse half-length  $b$  is found from

$$b = C_b(P\Delta)^{1/3} \quad (4.5.20)$$

where P is the applied load and,

$$\Delta = \frac{1}{A + B} \left( \frac{1 - \nu_1^2}{E_1} + \frac{1 - \nu_2^2}{E_2} \right) \quad (4.5.21)$$

where  $E_i$  and  $\nu_i$  are the elastic modulus and Poisson's ratio for body i. Next, the major ellipse half-length is found from

$$a = \frac{b}{k} \quad (4.5.22)$$

The deflection at the point of contact is found from

$$\delta = c_\delta \frac{P}{\pi} \left[ \frac{\Delta(A + B)}{b} \right] \quad (4.5.23)$$

and, finally, the maximum pressure is found from

$$Q_{\max} = \frac{3}{2} \left( \frac{P}{\pi ab} \right) \quad (4.5.24)$$

The values obtained from Equations (4.5.20), (4.5.22), and (4.5.24) are necessary to establish the size of the contact ellipse and the maximum pressure applied.

In summary, a procedure was developed to merge the actual gear geometrical data, curvatures, and orientations with Hertzian theory to provide the size of the contacting ellipse. This information is required to determine the location on the gear tooth surface where the heat flux will be applied. Both the maximum pressure found from this analysis and the gear mesh sliding and rolling velocities will be needed to determine the friction between the bodies in contact and, thus, the heat flux generated.

## REFERENCES

- [4.1] Understanding Tooth Contact Analysis. The Gleason Works, Rochester, NY, 1981.
- [4.2] Litvin, F.; and Coy, J.: Spiral Bevel Gear Train Precision. Advanced Power Transmission Technology, NASA CP-2210, 1981.
- [4.3] Huston, R.; and Coy, J.: A Basis for the Analysis of Surface Geometry of Spiral Bevel Gears. Advanced Power Transmission Technology, NASA CP-2210, 1981.
- [4.4] Cloutier, L.; and Gosselin, C.: Kinematic Analysis of Spiral Bevel Gears. ASME Paper 84-DET-177, Oct. 1984.
- [4.5] Litvin, F., et al.: New Generation Methods for Spur, Helical and Spiral Bevel Gears. NASA TM-88862, 1986.
- [4.6] Litvin, F., et al.: Method for Generation of Spiral Bevel Gears With Conjugate Tooth Surfaces. J. Mech. Trans. Aut. Design, vol. 109, no. 2, June 1987, pp. 134-142.
- [4.7] Tsai, Y.; and Chin, P.: Surface Geometry of Straight and Spiral Bevel Gears. J. Mech. Trans. Aut. Design, vol. 109, no. 4, Dec. 1987, pp. 348-356.
- [4.8] Litvin, F.; Tsung, W.; and Lee, H.: Generation of Spiral Bevel Gears With Conjugate Tooth Surfaces and Tooth Contact Analysis. NASA CR-4088, 1987.
- [4.9] Litvin, F., et al.: Transmission Errors and Bearing Contact of Spur, Helical and Spiral Bevel Gears. SAE Paper 881294, Sept. 1988.
- [4.10] Litvin, F.; and Lee, H.: Generation and Tooth Contact Analysis of Spiral Bevel Gears With Predesigned Parabolic Functions of Transmission Errors. NASA CR-4259, 1989.
- [4.11] Chang, S.; Huston, R.; and Coy, J.: Computer Aided Design of Bevel Gear Tooth Surfaces. Proceedings of 1989 International Power Transmission and Gearing Conference, 5th, Vol. 2 ASME, 1989, pp. 585-592.
- [4.12] Litvin, F.; and Zhang, Y.: Local Synthesis and Tooth Contact Analysis of Face-Milled Spiral Bevel Gears. NASA CR-4342, 1991.
- [4.13] Litvin, F.; Zhang, Y.; and Handschuh, R.: Local Synthesis and Tooth Contact Analysis of Face-Milled Spiral Bevel Gears. NASA TM-105182, 1991.
- [4.14] Gosselin, C.; Cloutier, L.; and Brousscue, J.: Tooth Contact Analysis of High Conformity Spiral Bevel Gears. JSME International Conference on Motion and Power Transmission, Proceedings, Hiroshima, Japan, Nov. 1991, pp. 725-730.
- [4.15] Fong, Z.; and Tsay, C.: Kinematic Optimization of Spiral Bevel Gears. J. Mech. Design, vol. 114, Sept. 1992, pp. 498-506.
- [4.16] Gosselin, C.; Cloutier, L.; and Nguyen, Q.: The Influence of the Kinematical Motion Error of Spiral Bevel Gears. Presented at the American Gear Manufacturer's Association Fall Technical Meeting 1992.

- [4.17] Wilcox, L.: An Exact Analytical Method for Calculating Stresses in Bevel and Hypoid Gear Teeth. International Symposium on Gearing and Power Transmission, Proceedings, Tokyo, Japan, 1981, pp. 115-121.
- [4.18] Chao, H.; and Cheng, H.: A Computer Solution for the Dynamic Load, Lubricant Film Thickness and Surface Temperatures in Spiral Bevel Gears. NASA CR-4077, 1987.
- [4.19] Fong, Z.; and Tsay, C.: A Mathematical Model for the Tooth Geometry of Circular-Cut Spiral Bevel Gears. J. Mech. Design, vol. 113, June 1991, pp. 174-181.
- [4.20] Handschuh, R.; and Litvin, F.: A Method for Determining Spiral Bevel Gear Tooth Geometry for Finite Element Analysis. NASA TP-3096, 1991.
- [4.21] Fong, Z.; and Tsay, C.: A Study on the Tooth Geometry and Cutting Machine Mechanisms of Spiral Bevel Gears. J. Mech. Design, vol. 113, Sept. 1991, pp. 346-351.
- [4.22] Litvin, F.: Theory of Gearing, NASA RP-1212, 1989.
- [4.23] PDA Engineering. PATRAN Plus, Release 2.5, Costa Mesa, CA, 1991.
- [4.24] The IMSL Libraries. Houston, TX, 1984.
- [4.25] Litvin, F.; Zhang, Y.; and Chen, J.: User's Manual for Tooth Contact Analysis of Face-Milled Spiral Bevel Gears with Given Machine Tool Settings. NASA CR-189093, 1991.
- [4.26] Boresi, A., et al.: Advanced Mechanics of Materials. John Wiley & Sons, New York, 1978.
- [4.27] Timoshenko, S.; and Goodier, J.: Theory of Elasticity. McGraw-Hill, New York, 1951.
- [4.28] Carnahan, B.; Luther, H.; and Wilkes, J.: Applied Numerical Methods. John Wiley & Sons, New York, 1969.
- [4.29] CRC Standard Mathematical Tables. 26th ed, CRC Press, Boca Raton, FL, 1981.

TABLE 4.4.1—SIGN CONVENTIONS OF MACHINE TOOL SETTINGS

[From Ref. [4.10].]

Setting	Sign	Right-hand member	Left-hand member
Cradle angle, $q$	+ –	Counterclockwise (CCW) Clockwise (CW)	Clockwise (CW) Counterclockwise (CCW)
Machining offset, $E_m$	+ –	Above machine center Below machine center	Below machine center Above machine center
Machine center-to-back, $X_{MCB}$	+ –	Work withdrawal Work advance	Work withdrawal Work advance
Sliding base, $X_{SB}$	+ –	Work withdrawal Work advance	Work withdrawal Work advance
Vector sum, $L_m$ , of $X_{SB}$ and $X_{MCB}$	+ –	$X_{SB}, +; X_{MCB}, -$ $X_{SB}, -; X_{MCB}, +$	$X_{SB}, +; X_{MCB}, -$ $X_{SB}, -; X_{MCB}, +$

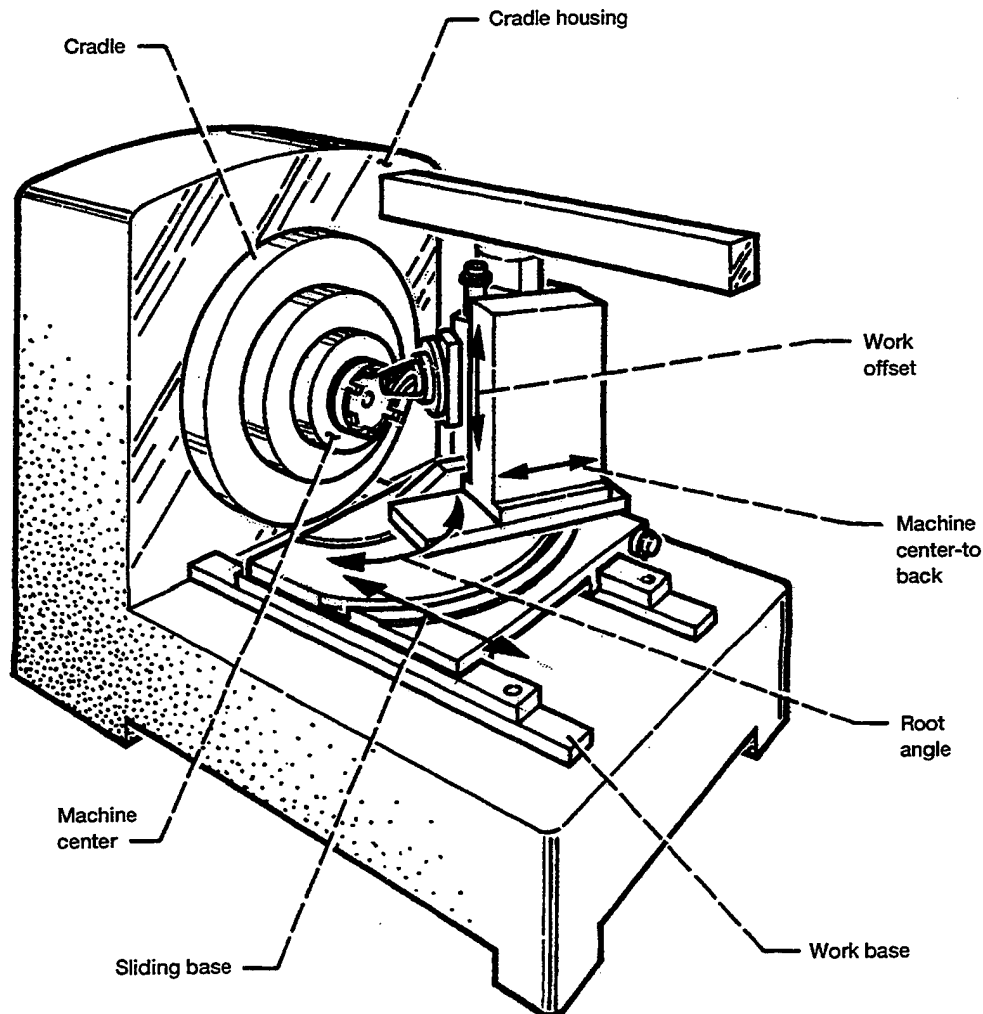


Figure 4.3.1.—Machine used to generate spiral bevel gear tooth surface.

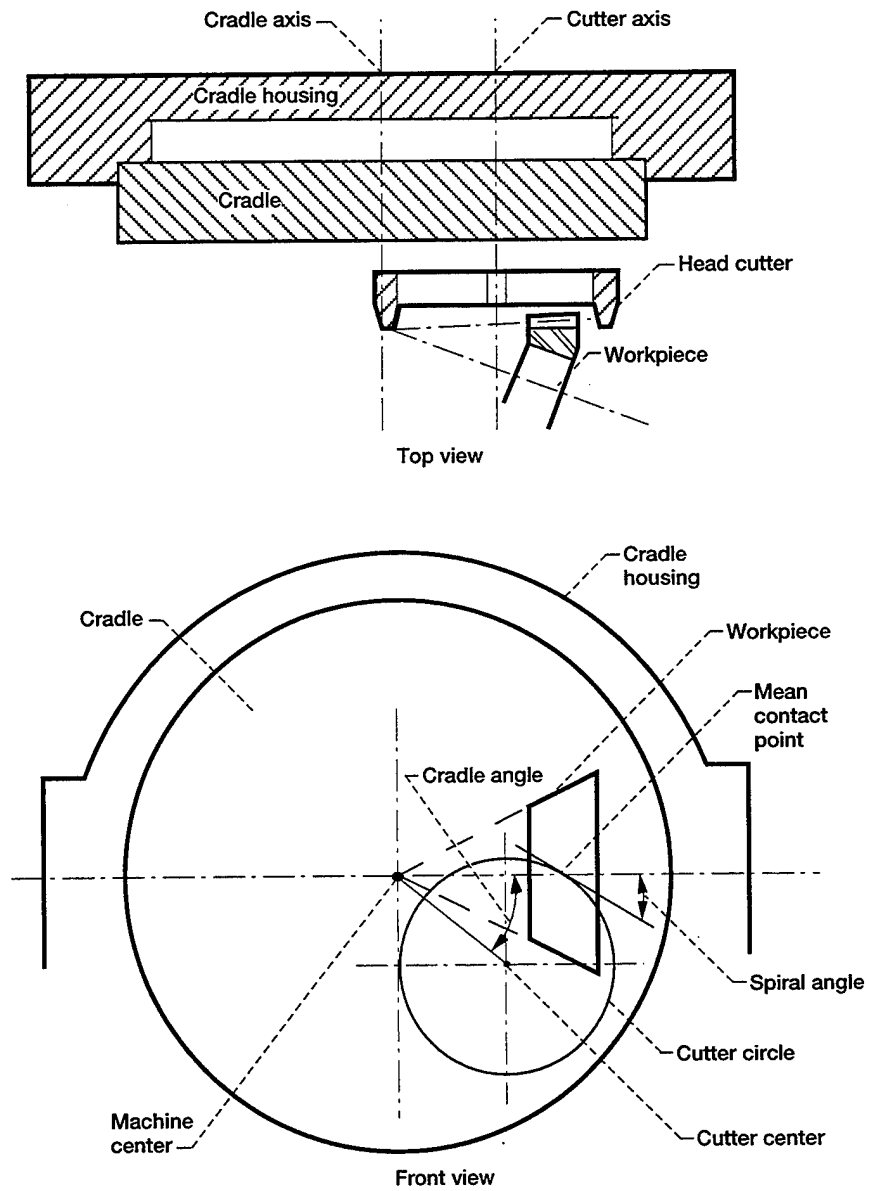


Figure 4.3.2.—Orientation of workpiece to generation machinery.

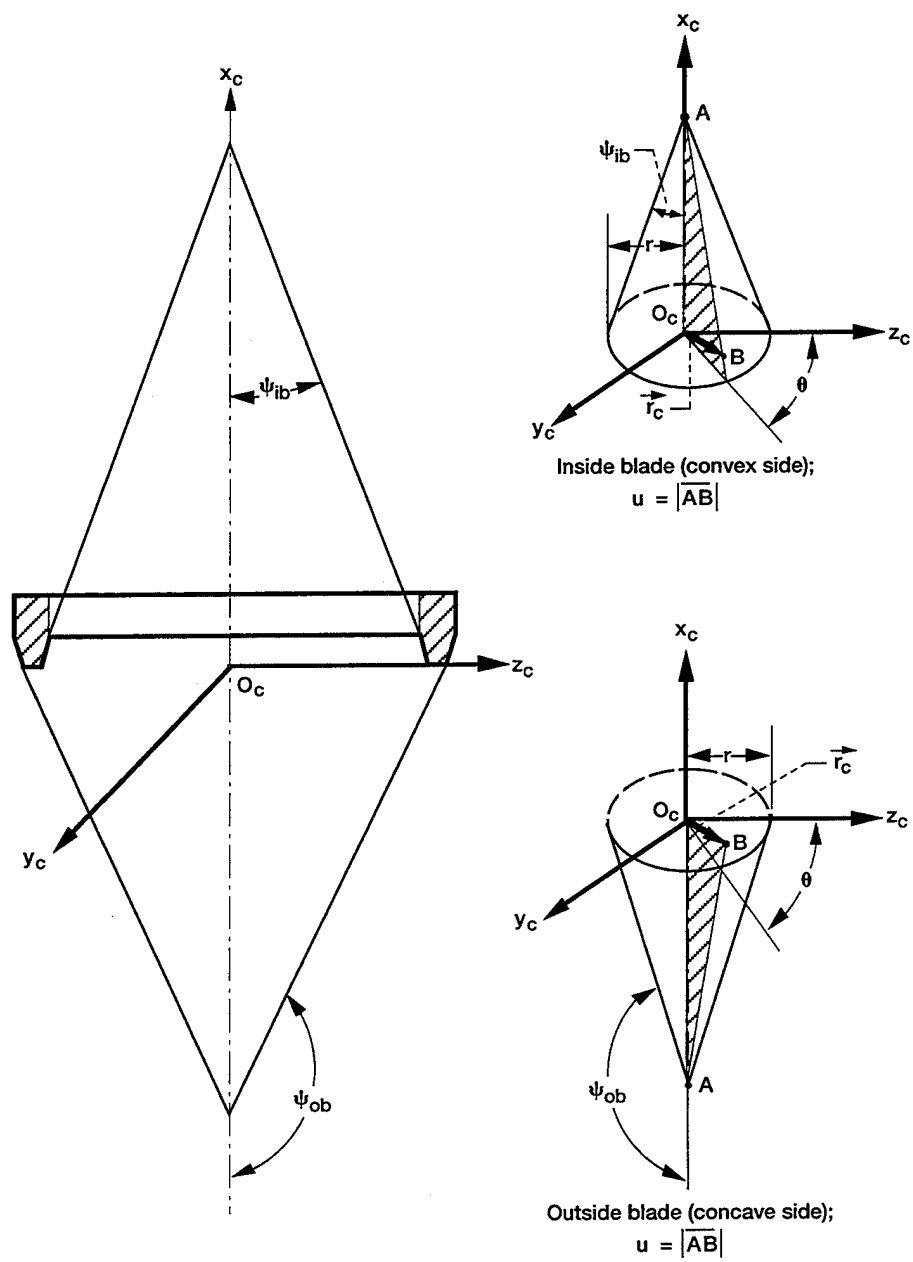


Figure 4.4.1.—Head-cutter cone surfaces (coordinate system  $S_D$ ).

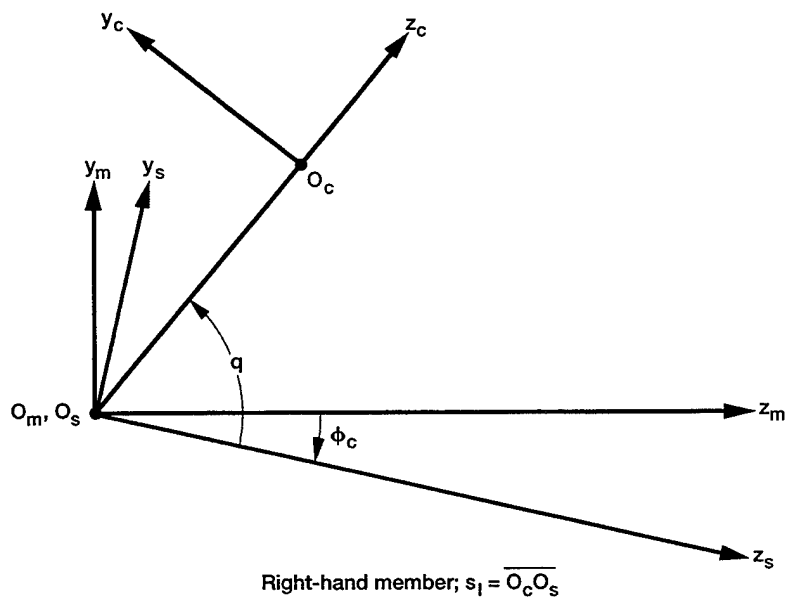
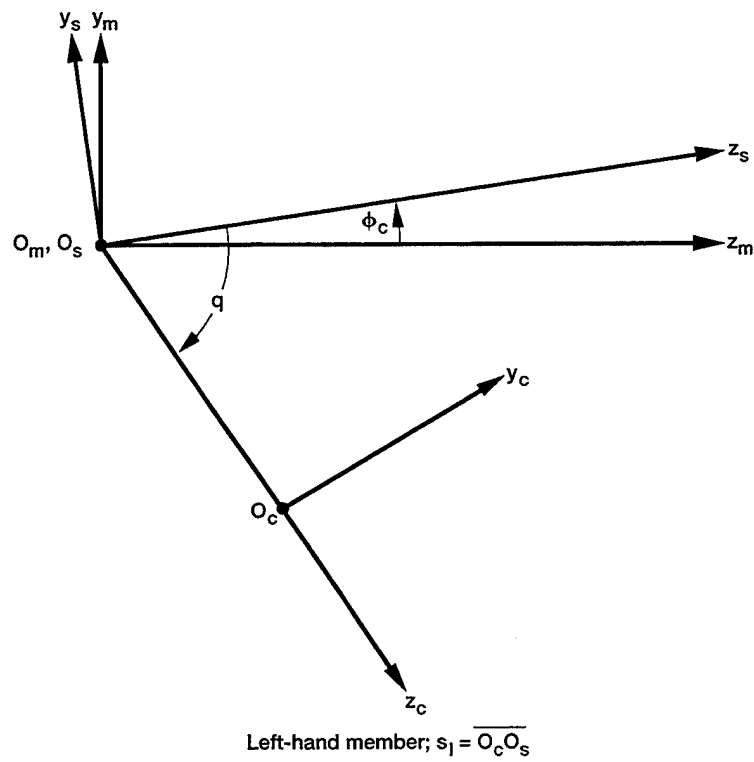


Figure 4.4.2.—Orientation of cutter, cradle, and fixed (or machine) coordinate systems  $S_c$ ,  $S_s$ , and  $S_m$ , respectively.

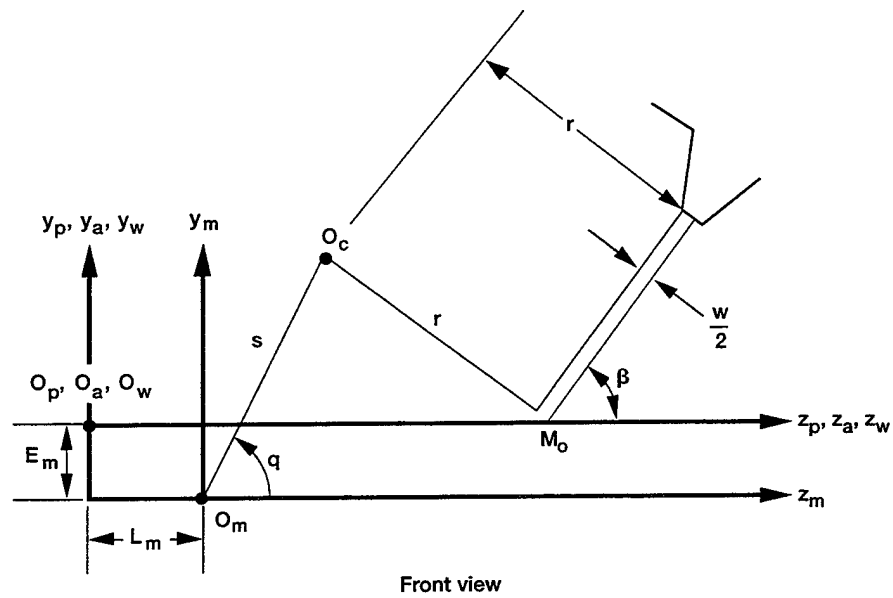
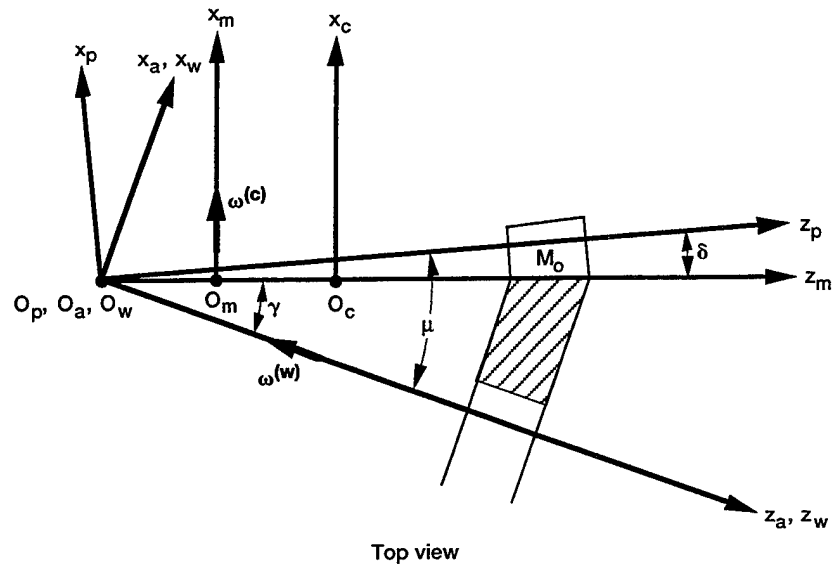


Figure 4.4.3.—Coordinate system orientation to generate a right-hand gear surface ( $\phi_c = 0$  shown here).

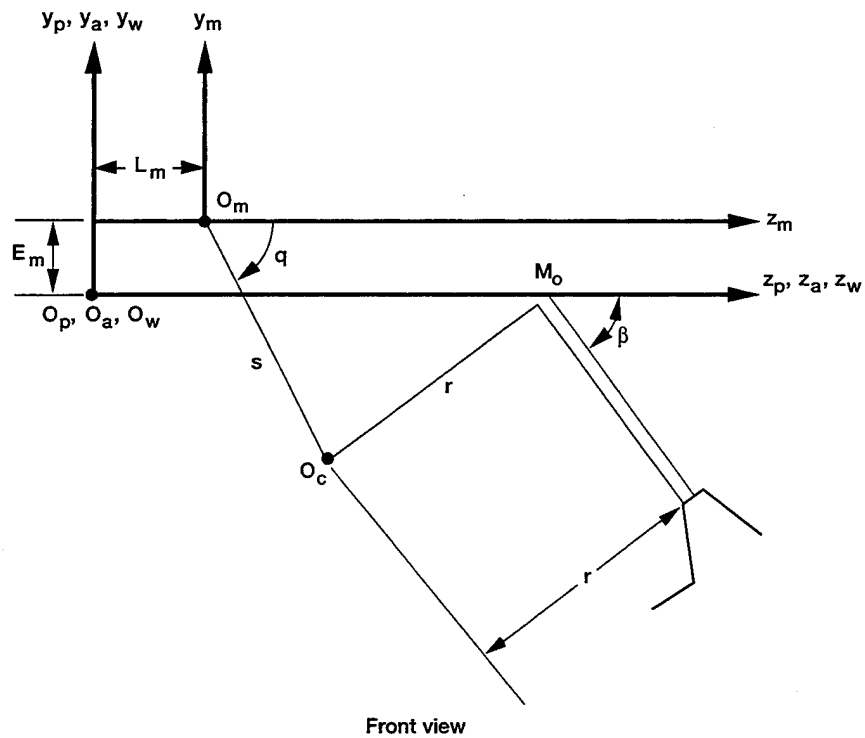
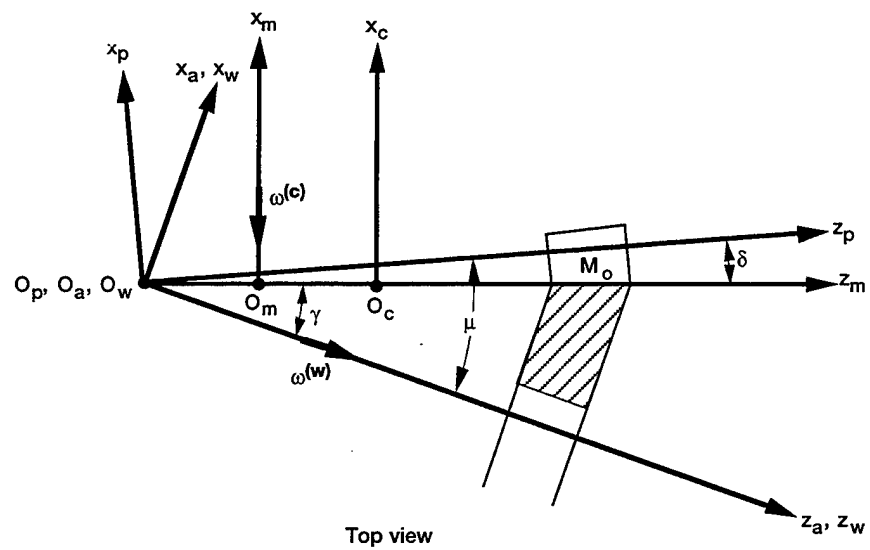
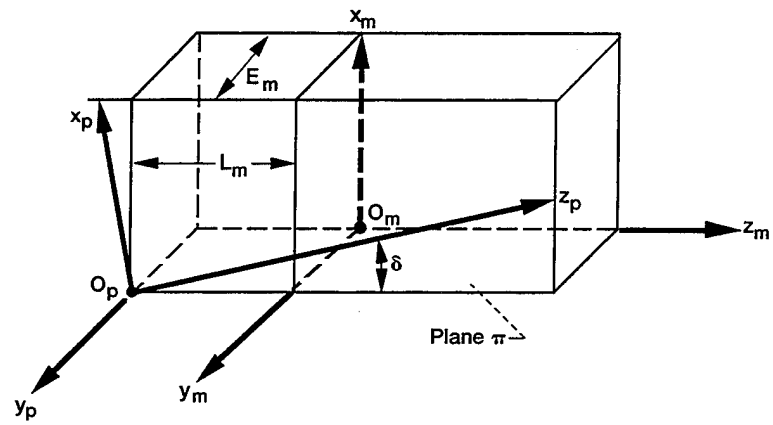
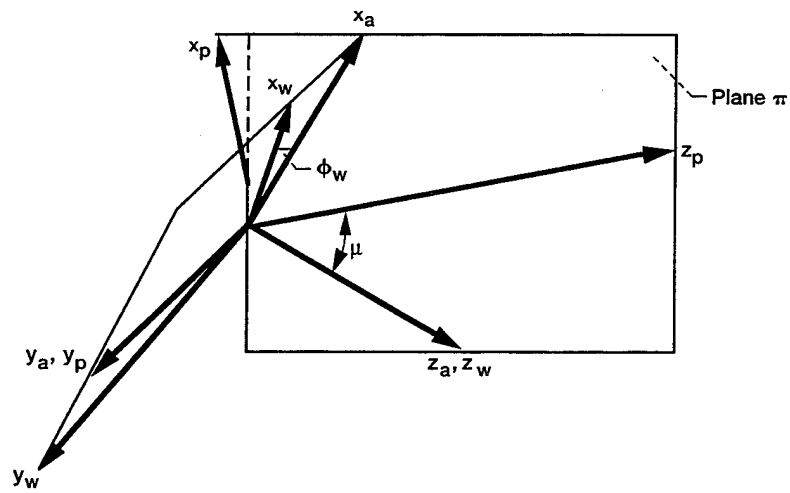


Figure 4.4.4.—Coordinate system orientation to generate a left-hand gear surface ( $\phi_c = 0$  shown here).



(a) Machine settings and orientation.



(b) Plane  $\pi$  and orientation of generated gear coordinates.

Figure 4.4.5.—Orientation of machine settings and generated gear coordinate systems.

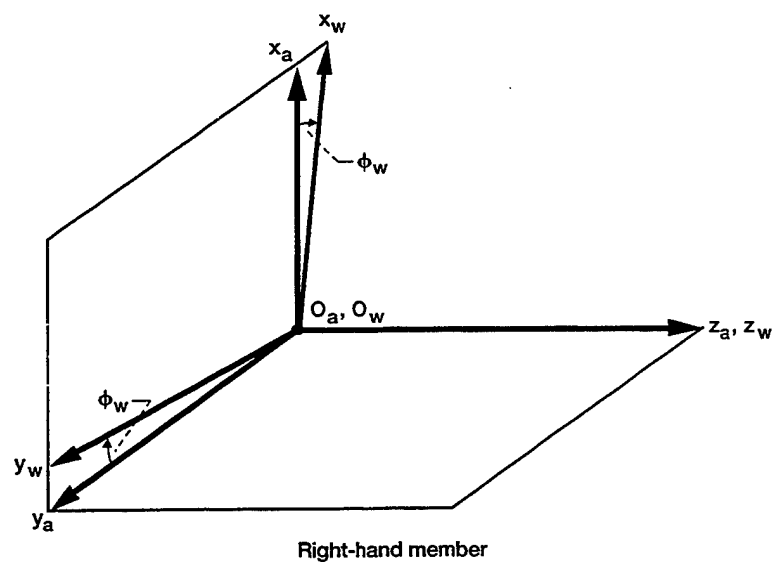
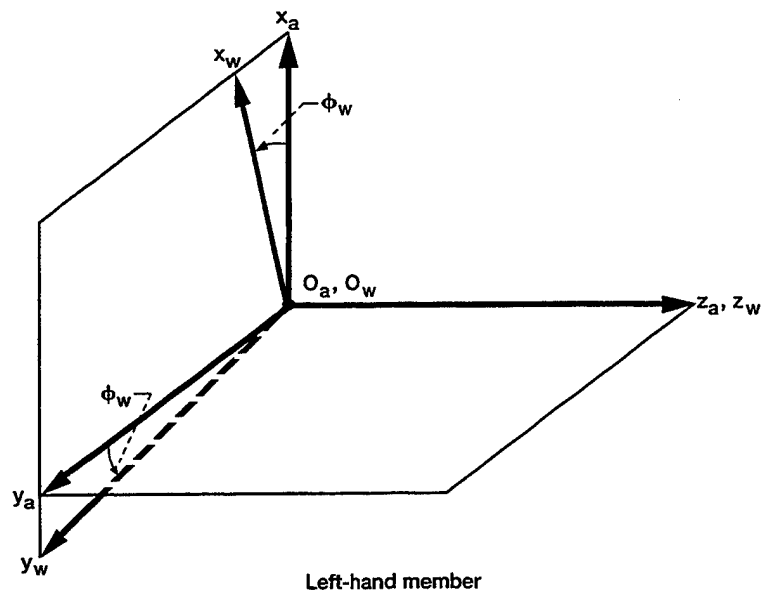


Figure 4.4.6.—Rotation of workpiece for left- and right-hand gears during tooth surface generation.

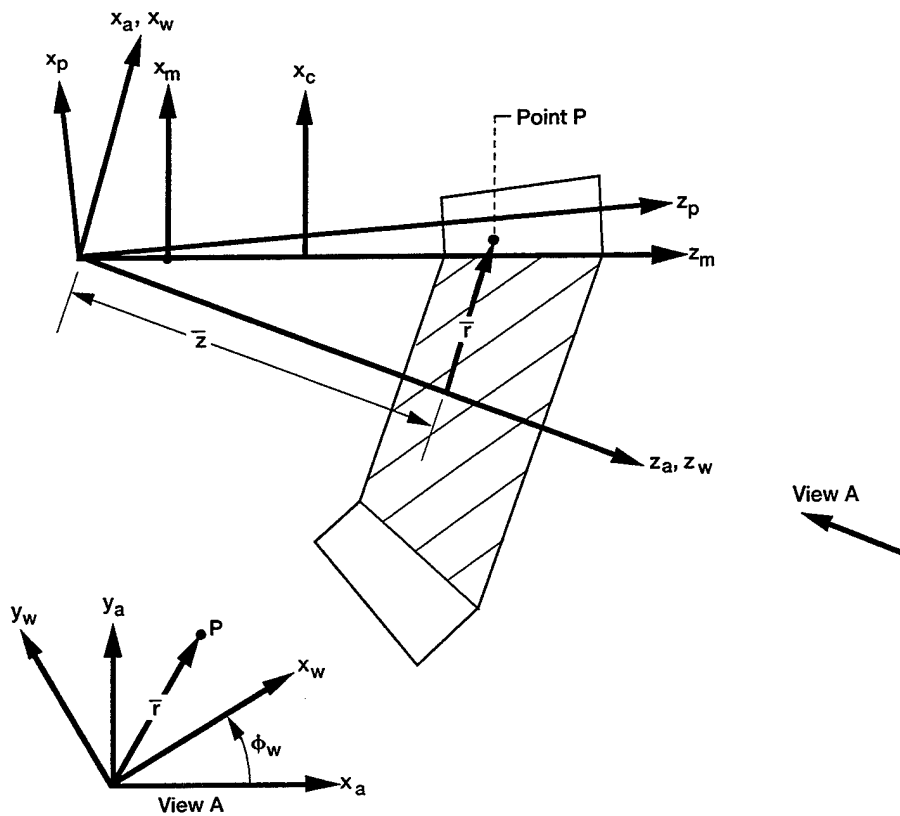


Figure 4.4.7.—Orientation of gear to be generated, with assumed positions  $r$  and  $z$ .

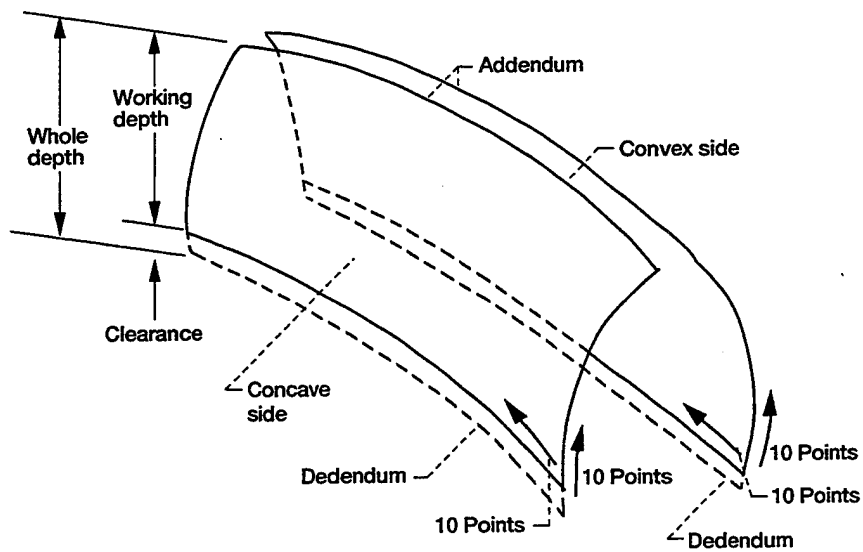


Figure 4.4.8.—Calculation points (10-by-10 grids, i.e., 100 points each side) for concave and convex sides of tooth surface.

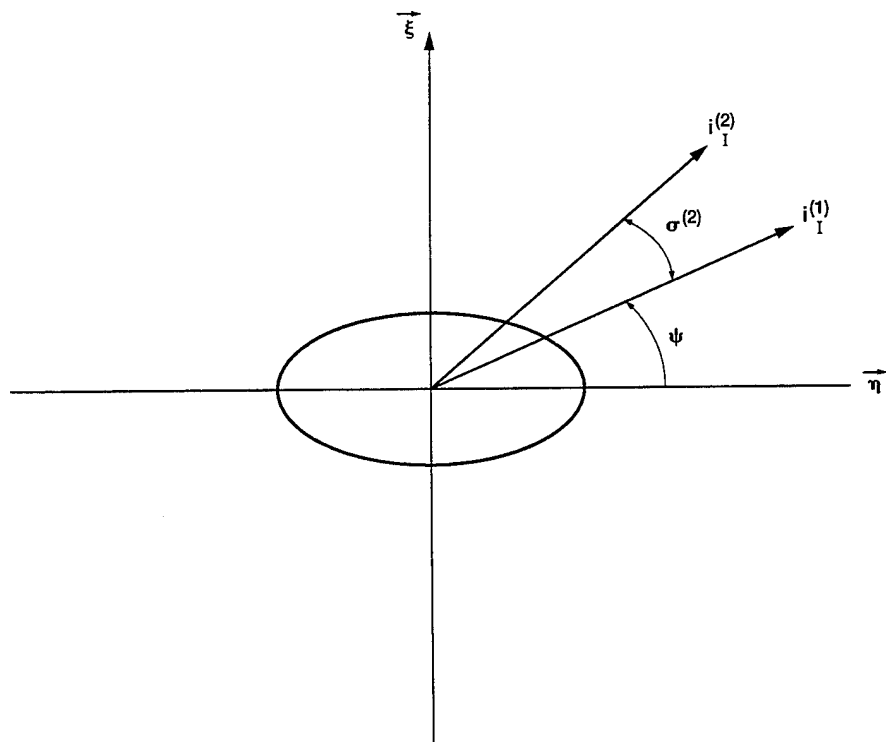


Figure 4.5.1.—Contact ellipse orientation with respect to principal directions "I" of surfaces 1 and 2.

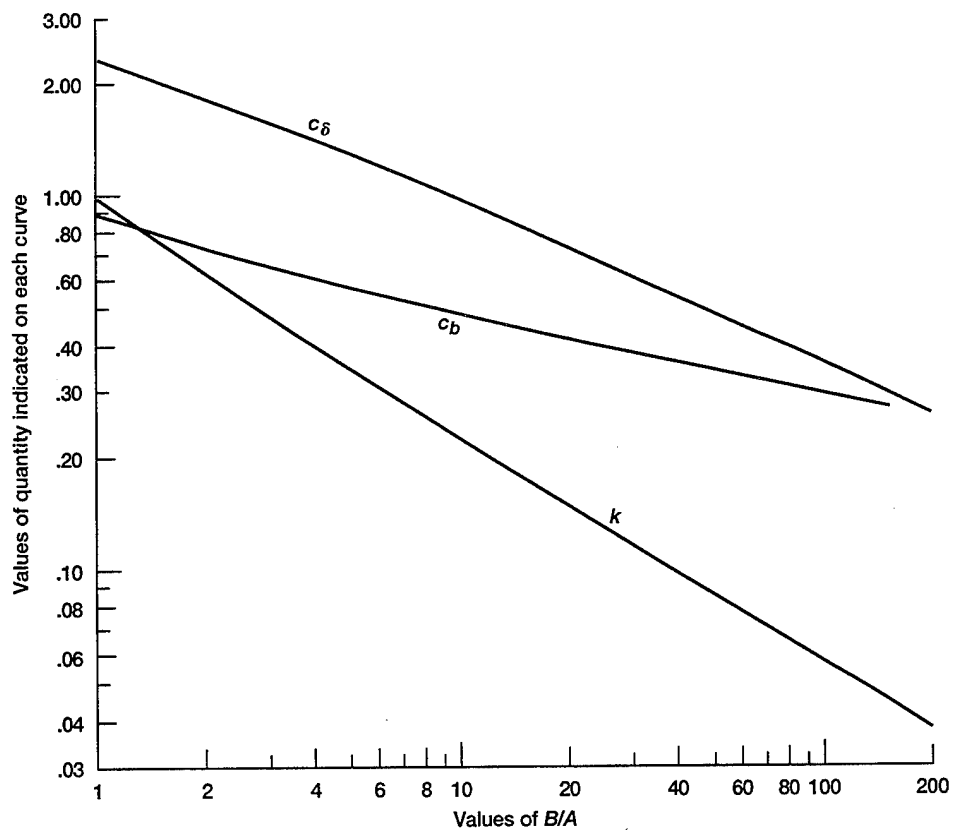


Figure 4.5.2.—Graphical solution for three-dimensional contact by Reference [4.26] for  $1 \leq B/A \leq 200$ .

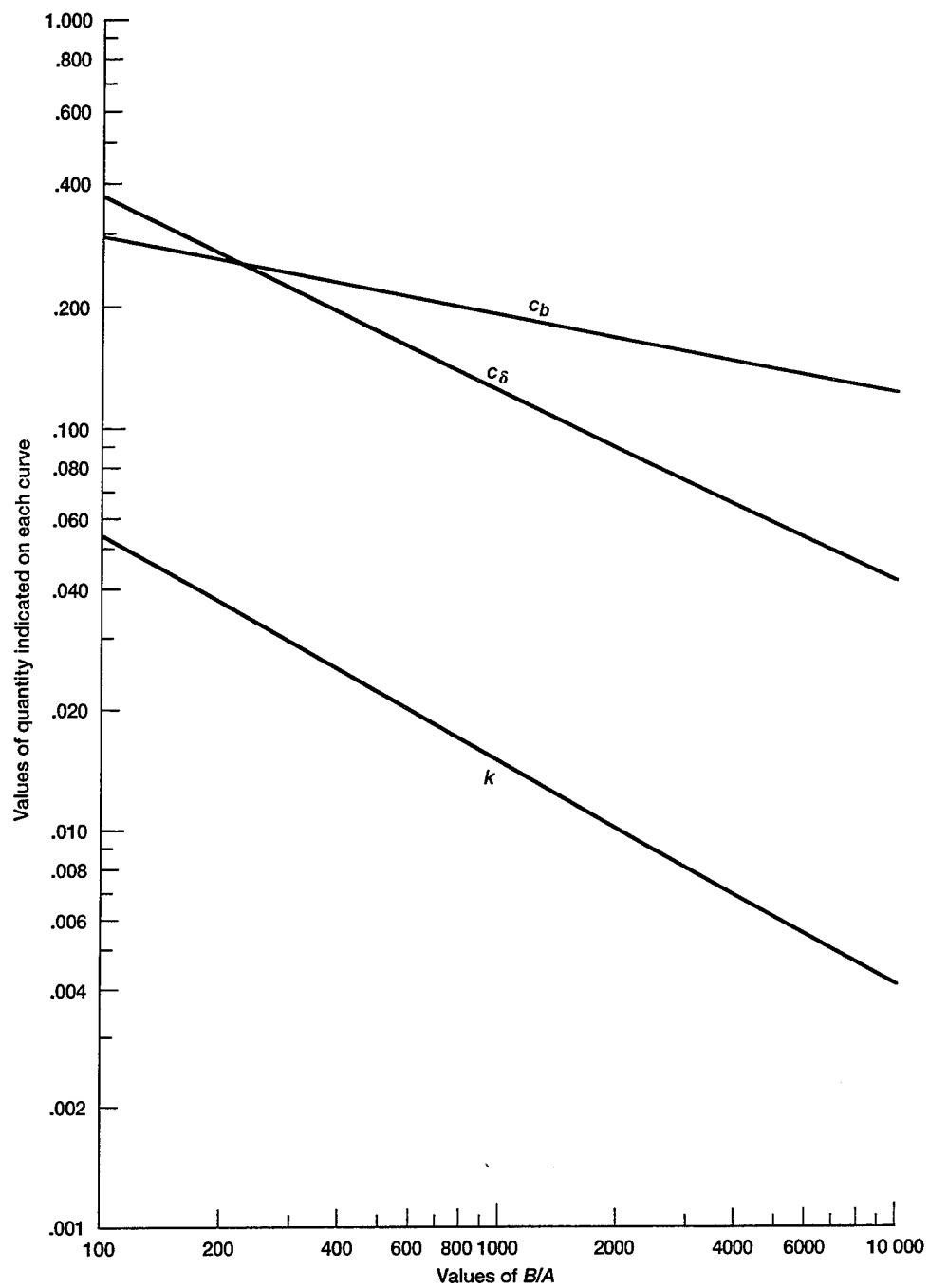


Figure 4.5.3.—Graphical solution for three-dimensional contact by Reference [4.26] for  $200 \leq B/A \leq 1 \times 10^4$ .

## CHAPTER 5: HEAT GENERATION AND HEAT TRANSFER

### 5.1 Introduction

In this chapter the methodology used to conduct a heat transfer analysis is developed and a simulation using a simple two-dimensional model is presented. The two-dimensional model has all the boundary and time-varying conditions of the full three-dimensional model and is used to develop the strategy to successfully model a spiral bevel gear. Transient and steady state results of the model developed using finite elements is compared with corresponding solutions found using an explicit finite difference technique. The finite element method used to solve the heat transfer problem at hand (Ref. [5.1]) can also be used to solve a wide variety of engineering problems and has nonlinear capabilities.

In this finite element program, user subroutines are used with the typical model bulk data. These subroutines permit a transient model with time- and position-varying boundary conditions. When solving a heat transfer problem, items such as heat flux or heat transfer coefficients can be specified on a nodal or element basis and be time varying. This permits very complex boundary conditions to be used.

Models for the finite element analysis were developed using a geometric solids modeling program (Ref. [5.2]). Bulk data and boundary conditions are generated within the solids modeling program, which removes the arduous task of generating the bulk data (grids, elements, and element connectivity) required. Also, since the grid and element data are generated within the solid modeling program, a model with a large quantity of elements can be generated just as easily as a coarser model. In most instances, model coarseness can affect the calculated results; therefore, a way to ease the modeling process is very useful. The solid modeling program also can be used to display the results of the analysis in a graphical form, a useful feature when models become very complex.

In this chapter the two-dimensional model simulation is utilized as a stepping stone to the much more complex three-dimensional spiral bevel gear. Also, the methodology to determine the traction (friction) characteristics is presented. The data attained by Tevaarwerk (Ref. [5.3]) for typical aerospace and automotive lubricants is used to determine the friction coefficient necessary for heat flux calculations. One last topic for this chapter is the heat transfer boundary conditions for high speed gears. The combination of these elements then permits a thermal analysis to be conducted.

### 5.2 Two-Dimensional Simulation of Time and Position Variable Heat Transfer Analysis

The two-dimensional model used for the simulation is rectangular to facilitate the comparison of the calculated results obtained with the finite element method and those obtained with the finite difference method. The model shown in Figure (5.2.1) has 121 grid points and 100 elements. The values for the size and material parameters used are given in Table 5.2.1. This simulation includes time- and position-varying boundary conditions. The rectangular model, simulating a cross section of a gear tooth, can be thought of as being attached to a rotating shaft (Fig. 5.2.2). As the shaft rotates, the heat flux is applied sequentially along one face to simulate the load moving along the tooth flank. After the heat flux has passed over this surface, the surface then becomes a convection boundary. The heat flux per unit area can be calculated by the following equation for surfaces with relative motion and a normally applied load (Ref. [5.4]):

$$Q_{in} = f V_s W \quad (5.2.1)$$

where  $f$  is the friction coefficient,  $V_s$  is the sliding velocity at the point of contact and  $W$  is the normally applied load. To simulate the heat flux varying as a function of position for this test model, the following equation was assumed:

$$Q_j = Q_{\max}(0.2 + 0.8) \left\{ 1 - \sin \left[ \frac{\pi(Y_i - \Delta Y)}{d - 2\Delta Y} \right] \right\} \quad (5.2.2)$$

In this equation,  $Q_{\max}$  refers to the assumed values of  $f$ ,  $V_s$ , and  $W$  for the design to be studied later. The heat flux variation from Equation (5.2.2) is shown in Figure 5.2.3. Also,  $Y_i$  is the  $Y$ -value of the current flux location;  $\Delta Y$  is the increment distance between  $Y$ -direction grid points, and  $d$  is the total  $Y$ -height of the model as shown in Figure 5.2.4 and in Table 5.2.1. This variation is consistent with the type of heat flux from meshing gears where at each point there is a combination of rolling and sliding between the surfaces that produce heat. For the assumed heat flux variation, the highest heat fluxes occur where the sliding velocity between the teeth is the highest (near the tip and root). The heat flux is lowest where the sliding is low and that occurs at or near the pitch cone (for spiral bevel gears).

The last part of the simulation contains the applied convection conditions. The convection condition values used in the simulation are shown in Figure 5.2.4.

One last item that must be mentioned is that there were slight differences between the application of certain boundary conditions for the two types of analysis. These conditions were the applied heat flux and the boundary surface ( $x = 0$ ,  $y = y$ ). For the heat flux boundary for the finite difference method, the first and last grid points were skipped. Therefore, in this model, heat flux entered through a total of nine grid points. In the finite element model, the heat flux on the surface between grid points was specified. The heat flux at the grid points for the finite difference method was halved and summed for the surface between grid points. The finite element model had the heat flux applied at the surface of 10 elements. The sum of the heat fluxes remained unchanged but the distribution was slightly different. The heat fluxes are shown in Figure 5.2.5.

For the boundary  $y = 0$ ,  $x = x$ , two different boundary conditions were used but numerically they have the same effect. In the finite difference solution, the boundary was treated as being insulated. In the finite element solution, the convection coefficient chosen was very small ( $h = 0.001 \text{ W/(m}^2\cdot\text{°C)}$ ) and essentially eliminated the surface as a heat transfer path. As the heat transfer coefficient approaches zero, the normal boundary condition for equating the heat fluxes at a boundary (conduction and convection) becomes just the insulated boundary condition.

**Finite Difference Method:** The finite difference method used is now presented. This model was used to verify the findings by the finite element method. Because of the simplistic nature of this simulation model with regard to model shape, the calculation procedure was simple to set up. For two-dimensional heat transfer, the following discretized equation can be written for the temperature  $T$  of the interior grid points (Ref. [5.5]):

$$T_{i,j}^{n+1} = T_{i,j}^n \left[ 1 - 2\Delta t \alpha \left( \frac{\Delta X^2 + \Delta Y^2}{\Delta X^2 \Delta Y^2} \right) \right] + \Delta t \alpha \left[ \left( \frac{T_{i-1,j}^n + T_{i+1,j}^n}{\Delta X^2} \right) + \left( \frac{T_{i,j-1}^n + T_{i,j+1}^n}{\Delta Y^2} \right) \right] \quad (5.2.3)$$

where  $\Delta t$  is the time step length,  $\Delta X$ ,  $\Delta Y$  the distance between grid points in the X- and Y-directions, and  $\alpha$  the thermal diffusivity which is equal to  $\alpha = k/\rho C_p$ , where  $k$  is the thermal conductivity,  $\rho$  is the material density, and  $C_p$  is the specific heat.

For the heat flux boundary the temperature is specified by setting  $i = 1$ , where  $T_{0,j}^n$  is given by

$$T_{0,j}^n = T_{2,j}^n + \frac{2\Delta X}{k} \left( \frac{Q_j}{A} \right) \quad (5.2.4)$$

Note that  $T_{0,j}^n$  is a fictitious node used to satisfy the gradient condition at the boundary;  $Q_j$  is the heat flux at the  $j^{\text{th}}$  grid point. For the convection boundary conditions, the following can be obtained for a constant X boundary position ( $X = 0$  for example):

$$T_{0,j}^n = T_{2,j}^n + (T_{\infty} - T_{1,j}^n) \left( \frac{2\Delta X h}{k} \right) \quad (5.2.5)$$

where  $h$  is the heat transfer coefficient and  $T_{\infty}$  is the surrounding ambient temperature. This fictitious node is once again used in Equation (5.2.3). For an insulated boundary (i.e.,  $\Delta T/\Delta Y = 0$ ), another fictitious node is used outside the model equal in value to the first node inside the model in the direction of the nonvarying gradient. This value is then used as before in Equation (5.2.3).

Although the finite difference numerical procedure has been described, a few comments on this method should be made. Because the method described herein is an explicit finite difference method, the next time step is based on information generated in the last time step. This procedure can be carried out for a great number of time steps with a reasonably small amount of computer run time. The present finite difference model also used time step variation. Small time steps were only taken when the heat flux was being applied. The rest of the time where only convection boundaries existed, larger steps were taken to further the model's computational efficiency. Stability requirements were easily satisfied and would only be violated if the time step was many revolutions of the simulation model. The unfortunate disadvantage of the finite difference method is that irregular geometry causes a major modeling crisis. For this reason, the finite element method will be used for the spiral bevel gear model.

**Finite Element Method:** The finite element model used for this two-dimensional simulation has 121 nodes and 100 elements. The bulk data were created using a solid modeling package (Ref. [5.2]). Heat convection boundary conditions were established within the solid model program and are also referenced by the finite element computer program through user subroutines. For this model, the heat flux boundary is time and position variant. Since elapsed time is a parameter that can be assessed within the subroutine, control of the boundary conditions is such that the heat flux moves and heat convection boundary conditions change.

The time-transient finite element analysis is an implicit technique. The equations are based on thermal gradients on an elemental basis and are solved simultaneously by integration (Ref. [5.6]). Implicit techniques permit the efficient solution of a time-transient problem by taking arbitrarily long time steps. There is no stability requirement that must be satisfied as is found in the explicit finite difference techniques. The implicit technique is very powerful as long as boundary conditions are not functions of time.

The problem is that arbitrarily long time steps are of no use when considering the model at hand where the time step size is on the order of  $t = 3 \times 10^{-6}$  seconds because of the time- and position-varying heat flux. Still, the use of a finite element analysis was essential to avoid using a finite difference technique. This method, when

compared with the finite difference technique for computational time for the same number of time steps, took 280 times longer. This presents quite a dilemma when thinking ahead to the full three-dimensional spiral bevel gear model. Based on the time step size used in the simulation, which is believed to be on the order of what will be required, millions of time step increments will be required to reach steady state operation. Thus, some procedure to overcome this problem was required and is discussed in the next section.

### 5.3 Time-Averaged Boundary Conditions

The dilemma presented in the last section was overcome by using time-averaged boundary conditions for the prescribed heat flux. The procedure is now described.

The first consideration is the heat flux at a given location as a function of time (see Fig. 5.3.1). The heat flux is only present on a particular surface element for one time step in the two-dimensional model presented herein. The rest of the time after the tooth comes out of mesh the surface is a convection boundary. Therefore, if it is desirable to go out to some elapsed time and then conduct the transient thermal analysis, the most expeditious manner is to take advantage of the implicit technique used to solve the equations. Here, time step size can be chosen arbitrarily large without problems of numerical stability.

With respect to Figure 5.3.1, the time-averaging technique is now described. If the instantaneous heat flux is instead represented as a constant value throughout the entire revolution, this would be the time-averaged heat flux. Therefore, the area under the instantaneous heat flux curve ( $Q_j$ , curve 1) is then averaged over the  $n$  time steps that normally would take place. The value  $Q_{j,ave}$  is then constant throughout the revolution. Therefore, the full advantage of the implicit technique can be taken;  $Q_{j,ave}$  for each element with a heat flux is input into the user subroutine.

The power of this scheme and the finite element program being used is that the model has restart capabilities. Therefore, the time-averaged conditions can be used until a given elapsed time has been reached and then the model stopped and the user subroutine switched with the transient heat flux and convection boundary conditions. Then the model is restarted with the time- and position-varying boundary conditions and is run for a number of revolutions until the solution stabilizes. Using this technique allows the transient model calculation with the least computer usage time.

### 5.4 Comparison of Finite Element and Finite Difference Results on Two-Dimensional Model

In this section a comparison between finite element and finite difference methods for the two-dimensional model already described is presented. Both transient and steady state results are compared. The effects of time averaging the boundary conditions as well as finite element time step size were investigated.

**Transient Heat Transfer:** For the transient and steady state comparison, the finite difference model used was the same. Output from this analysis was requested at predetermined elapsed times in the simulation. For the finite element model, output was chosen for every five revolutions of the model. The time step size was slightly different for the two models because of the number of heat flux locations considered. In the finite difference model, 11 grid points were exposed to the position-varying heat flux. At the first and last grid points the flux was set equal to zero. For the finite element method, 10 elements were exposed to the heat flux each revolution. Therefore, the time step size during meshing was found by

$$\Delta t = \frac{1}{\omega_s i Z_t} \quad (5.4.1)$$

where  $\omega_s$  is the shaft speed in hertz;  $i$  is the number of heat flux increments;  $Z_t$  is the number of teeth on the simulated gear member in question.

Temperatures were calculated using the heat flux distribution shown in Figure 5.2.5 and the convection boundary conditions of Figure 5.2.4. The results from the two analyses at five-revolution increments are given in Table 5.4.1. Three positions along the heat flux boundary are compared. The first, mid, and last heat flux locations are shown and correspond to the Y-direction grid points 2, 6, and 10, respectively from Figure 5.2.5. The model was initially at ambient conditions (38 °C). The two analyses agree within 2 °C over the entire model. The reason for these differences is attributed to the slight boundary condition variation that was required. A complete temperature field plot of the finite element results is shown in Figure 5.4.1 after 50 revolutions of the model. The finite element model had completed approximately 6000 time steps ( $\Delta t = 3.472 \times 10^{-5}$  sec) in the figure shown. At this point the temperature field over half the model was still at ambient conditions.

**Steady State:** The steady state comparison of the finite difference and finite element analyses was conducted after 50 000 revolutions of the model had occurred, which was well beyond the point at which the steady state temperature field was reached. The results are shown in Figure 5.4.2, which plots the temperature over three of the exterior faces. The temperatures at the grid points from the bottom of the drive side to the top of the tooth, across the tooth top, and then down the coast side are plotted in that order from left to right. The two analyses show good agreement. The largest deviation in the results occurred where boundary conditions were not duplicated exactly. A full temperature field output of the finite element method is shown in Figure 5.4.3. The highest temperatures were in the regions where the maximum heat flux was exposed on the model.

Because the finite element method is an implicit technique, time step size effects on the time-averaged solution were investigated. The same model was analyzed for fewer increments and a longer time step size. A comparison of these results with those for the finite difference model is shown in Table 5.4.2. The time step size was increased 2 orders of magnitude with virtually no effect on the results. This capability will be very useful when the full complex spiral bevel gear model is analyzed later.

## 5.5 Friction Coefficient in Meshing Gear Systems

The frictional characteristics of most mechanical systems, such as the ones under study herein, are determined using empirical results. Typically these experiments are conducted using rollers with the provision of having differing rotational speeds so that known sliding and rolling velocities are present (see Fig. 5.5.1). A given load between the rollers is applied and the resultant torque required is a measure of the frictional force that is present. Tests are run with a range of parameters of interest and then a curve fit or constitutive model is developed depending on the level of sophistication.

Over the last 30 years, many contributions that base their prediction of friction coefficient on experimental results have been made. The lubricants used in the studies ranged from mineral oils (Ref. [5.7]) to synthetic turbine oils (Ref. [5.3]). Even traction fluids for use in friction drives such as roller (traction) drives have been studied (Ref. [5.8]). The obvious conclusion reached from the results obtained by these researchers is that the friction coefficient is sensitive not only to the conditions, load, and geometry, but also to the fluid being used.

Once the frictional behavior of a given fluid is known along with the geometry and loads imposed, the heat generated or power loss as a function of meshing position can be found. Therefore, the efficiency of the gear system with respect to the sliding and other losses can be calculated. This has been accomplished analytically by several researchers for spur gears (Refs. [5.9] to [5.11]), for planetary systems (Refs. [5.12] and [5.13]), and for complete gearboxes (Ref. [5.14]).

**Friction Coefficient:** Three fairly recent studies are described. In Ku (Ref. [5.15]), a number of disks with different surface finishes and final grinding orientations were presented. An example of the results is shown in Figure 5.5.2. The model for the friction coefficient that was developed includes only the load, mean surface roughness, and sliding velocity. Also, beyond a value of  $WV_s^{-1/3} > 200$  ( $W$  = load (lb.);  $V_s$  = sliding velocity (in./sec)), the friction coefficient is basically constant. The effects of surface roughness or final grinding orientation generated different curves. These curves, however, all had the same general behavior. In this study, the slide-to-roll ratio was basically held constant and only the rolling velocity and load were increased. The friction coefficient ranged from about 0.015 to 0.08 depending on the disk conditions.

The curve fit developed for the data of Reference [5.15] had the general form

$$\begin{aligned} f(\zeta_i, W, V_s) &= \left( c_1 + c_2 \zeta_i \right) \left( WV_s^{-1/3} \right) \quad \text{for } WV_s^{-1/3} < 200 \\ f(\zeta_i, W, V_s) &= (c_3 + c_4 \zeta_i) \quad \text{for } WV_s^{-1/3} > 200 \end{aligned} \quad (5.5.1)$$

where  $\zeta_i$  is the mean surface roughness of the meshing gears,  $c_1$  to  $c_4$  are curve fit constants,  $W$  is the applied load, and  $V_s$  is the sliding velocity.

Therefore, a fairly simple model was developed and contained some major variable considerations when dealing with gear surfaces.

In the second work investigated herein, several operational parameters as well as oil types were tested (Ref. [5.16]). Their results showed a decrease in friction coefficient with a sliding velocity increase. The range of friction coefficient, using turbine engine oil, was  $0.013 < \mu < 0.06$  for sliding velocities of 1.5 to 15 m/sec, respectively.

In the third study by Tevaarwerk (Ref. [5.3]), seven different lubricants were evaluated. The parameters varied in these tests were temperature, contact pressure, rolling speed, slip (sliding velocity divided by rolling velocity), and lubricant type. Typical test results are shown in Figure 5.5.3 for an aerospace lubricant used in gas turbine engines as well as in helicopter main rotor transmissions. In this study, a constitutive model using contact geometry, operating conditions, material, fluid, and traction data was developed. By changing curve-fitting parameters, the effects of lubricant type could be investigated. The contacting conditions and modeling geometry used for this study were developed for spur gears (two-dimensional modeling used for maximum pressure, etc). Therefore, a direct application is not possible to the spiral bevel gears under study here.

In the present study, four parameters are used to determine the friction coefficient by curve fitting the data for the typical current aerospace lubricant: maximum contact pressure, inlet/bulk temperature, and sliding and rolling velocities. Therefore, the data contained in Reference [5.3] for a typical turbine engine oil were curve fit over the following range of parameters:

Contact pressure, $p$ , GPa	1 to 1.92
Inlet/bulk temperature, $T$ , °C	31 to 79
Slip or slide-to-roll ratio, $\Delta U^a$	0.01 to 1.0
Rolling velocity, $U$ , m/sec	10 to 30

<sup>a</sup> $\Delta U/U > 0.14$  friction coefficient assumed constant and equal to that value found at 0.14.

Values calculated from the equation obtained by curve fitting are plotted against the experimental results in Figure 5.5.4. The equation is

$$f\left(U, \frac{\Delta U}{U}, T, P\right) = a_1 U + a_2 \exp\left[a_3 \left(\frac{\Delta U}{U}\right)\right] + a_4 T + a_5 P \quad (5.5.2)$$

Although there is scatter in the results, the same level of scatter also was demonstrated in the correlations contained in Reference [5.3].

Therefore, given the sliding and rolling velocities of the contacting point in question, along with the maximum pressure found using Hertzian theory and the temperature assumed for the lubricant, the friction coefficient can be found from Equation (5.5.2).

**Spiral Bevel Gear Geometry Effects:** Because of the contacting geometry of spiral bevel gears, an additional problem arises. At the central contact point, the sliding and rolling velocities are not oriented in the minor ellipse direction as in the case for spur gears. For a given contact location of interest, the velocities of a spiral bevel gear could look more like those shown in Figure 5.5.5. What can be seen is that the rolling and sliding velocities are not necessarily aligned with the normally-thought-of-direction for fluid entrainment. Therefore, to utilize the friction model described in the previous section, some assumptions as to how the velocities will be described with respect to the contact ellipse are now made.

To match the orientation to that attained experimentally, the calculated sliding and rolling velocities found from the analysis of Litvin (Ref. [5.17]) are projected in the minor ellipse direction, as shown schematically in Figure 5.5.6.

## 5.6 Load Sharing in Meshing Gear Systems

Because gears are always designed with a contact ratio greater than 1, load sharing exists during at least part of the meshing cycle. Therefore, the level of load carried by a given tooth can change dramatically depending on the contact location. For gears with a contact ratio between 1 and 2 (typically called low contact ratio), the level of load carried by a single tooth as well as the total mesh stiffness can be assumed to appear as shown in Figure 5.6.1. During part of the meshing cycle, two pairs of teeth carry the load and therefore the level of load that one pair has to carry changes.

An extensive historical summary of published works on tooth stiffness and deformation for spur gears is given by Valco (Ref. [5.18]). The majority of the models, however, basically had the same stiffness profile as that shown in Figure 5.6.1. What differed between these models was the actual stiffness values that were found. Therefore, the load sharing to be used in the analysis conducted herein for spiral bevel gears will be a 50/50 split when two pairs of teeth are in contact and full load when only one tooth pair is in mesh. In the future when a complete contacting three-dimensional finite element study is conducted on this type of gear system, the load sharing and distribution will be determined from the gear mesh structural model.

The results of a tooth contact analysis (TCA) of the spiral bevel gears will be used to determine the locations of multiple teeth in contact. From the TCA a plot of the gear output transmission error, defined as the difference between the nominal position based on the gear ratio and the actual position due to the contact of the meshing gears, for  $\pm$  one-half pitch of rotation of the pinion can be made as shown in Figure 5.6.2. For the preceding and following teeth, similar plots can be constructed by adding or subtracting  $2\pi/N_p$  to the original tooth rotation angle as the teeth are separated in space by this amount. After this is performed the curves intersect at what is usually called the transfer points (Ref. [5.19]) and then cross as shown in Figure 5.6.3. Therefore, the

extent of the crossing curves in terms of the pinion rotation angle will be where two teeth are in contact, the load is split 50/50, and the locations between the crossing regions will be when a single pair carries the total load.

In the analysis of Litvin (Ref. [5.17]), load sharing is not considered; however, the input torque and speed are data used by the program and all the meshing properties and geometry are output as well as the total normal load at the center of the contact. This calculated value for the load is the one that will be affected by the load sharing, which in turn affects the Hertzian analysis computed afterward and, subsequently, heat flux applied within the contacting ellipses.

## 5.7 Convection Heat Transfer Coefficients for Rotating Gears

To conduct a heat transfer analysis of any kind, the boundary conditions to the surroundings must be applied. In gear systems, coefficients for forced-convection heat transfer, unfortunately, are not something that can be looked up in a heat transfer text. Therefore, to approximate these coefficients, simple shapes that experimental work has been conducted on are used. In the model to be developed in the next chapter, the following surfaces will have heat transfer coefficients specified. On the pinion to be modeled, the active profile (concave side), tooth top, coast side profile (convex side), tooth root, front (toe) face, and back (heel) face all have coefficients applied. Other sections of the model are assumed to be insulated or to have a heat transfer coefficient that is very small.

A few analytical studies investigated the effects of lubricating jet cooling (Ref. [5.20]) and continuous fling-off cooling (Ref. [5.21]) of gear teeth. On the basis of lubricating jet pressure and other conditions, predictions were made as to the amount of heat carried away by the lubricant. The conclusion was drawn, from Reference [5.20], that in heavy-duty gears intermittent cooling may not be sufficient. In Reference [5.21] a method was proposed to continuously feed lubricant to the meshing surfaces via holes in the gear root. Although this would provide better cooling, holes in this region would obviously invite problems in the local structural behavior because they would be located in the region of very high bending stress.

In the discussion to follow, the model to be used does not have the lubrication jet directly applied to the gear member. Lubrication between surfaces is maintained by the other member carrying along lubricant that has not been flung off because of centrifugal and other forces. If a jet were directly applied to the model at some point during a cycle of rotation, a large heat flux removal from the model would have to be considered as part of the time- and position-varying boundary conditions. Therefore, these coefficients are determined with the assumption that the gear speed used is the 100 percent speed condition (14 400 rpm) from the experimental work. This translates into a pitch line velocity of this gear mesh of 38.65 m/sec. This velocity is used in the many calculations to follow.

The active profile (concave side) of the pinion member that is used in the analysis to follow in later chapters is discussed first. Because of the basic design configuration of the pinion, this surface, when viewed with respect to this discussion, will be thought of as a flat plate moving perpendicular to the nominal ambient plate conditions. Therefore, this coefficient can be calculated as found in Holman (Ref. [5.22]). First, the oil-air mixture of the ambient conditions needs to be made. Based on the dimensions of the experimental test facility described in Chapter 3 and a lubricant flow rate of  $1.9 \times 10^{-5}$  m<sup>3</sup>/sec (0.3 gal/min), the oil-air volume ratio is approximately 0.0004. This ratio is then used to calculate the fluid properties of the mixture at an assumed temperature of 100 °C (assumed mean between the inlet condition and the actual gear surface temperature). From Reference [5.22], based on the conditions just stated, the Prandtl number of the mixture was 0.8 and the Reynolds number was found from

$$Re_{mix} = \frac{Vd}{\nu} \quad (5.7.1)$$

where  $V$  is the pitch line velocity,  $d$  is the average tooth height, and  $\nu$  is the kinematic viscosity.

Again, using Reference [5.22], the Nusselt number is given from empirical formulation as

$$Nu = C(Re)^n(Pr)^m \quad (5.7.2)$$

where  $C$ ,  $n$ , and  $m$  are constants equal to 0.228, 0.731, and 0.333, respectively. Using the assumptions above, the active profile heat transfer coefficient was 4450 W/(m<sup>2</sup>·°C).

For the toe and heel ends of the pinion in question, the work of Harnett (Ref. [5.23]) was utilized. In this study, an analysis was conducted on rotating disks and cones of varying geometry and temperature fields. The outcome of this work was an expression for the Nusselt number based on the given geometry, rotational speed, fluid properties, and temperature distribution:

$$Nu = \frac{h}{k} \left( \frac{\nu}{\omega \sin \alpha} \right)^{0.5} \quad (5.7.3)$$

Where  $k$  and  $\nu$  are the thermal conductivity and kinematic viscosity, respectively,  $\alpha$  is the half-angle of the cone apex, and  $\omega$  is the rotational speed. The Nusselt number, in this case, is the slope of the dimensionless temperature distribution evaluated at the solid surface.

Using the values for the air-oil mixture, the rotational speed, and the orientation angles of the toe and heel ends of the gear teeth, approximately the same as the pitch angle in this case, resulted in a heel and toe heat transfer coefficient of 160 W/(m<sup>2</sup>·°C).

The tooth top, tooth root, and tooth coast sides are assumed to have the same heat transfer coefficient. Because these boundaries do not present a situation where some simplifications could lead to a heat transfer coefficient, by a handbook calculation, a value of 50 W/(m<sup>2</sup>·°C) was assumed. This value was chosen to be somewhere between the value of an insulated boundary (heat transfer coefficient approaching zero) and that of the toe or heel tooth faces. A sketch of the surfaces with the heat transfer coefficient values found or assumed are shown in Figure 5.7.1.

Using the foregoing approximations and assumptions permits construction of the convective boundary conditions. It would be much better if some empirical data base were available; however, this would require a separate, very involved experimental effort to accomplish. The analytical results to be perused in this study are based on the boundary condition limitations given above and can be adjusted to compare more closely with the results of the experiments of Chapter 3.

## REFERENCES

- [5.1] MARC Finite Element Program. Rev., K.4-1. MARC Analysis Research Corporation, Palo Alto, CA, 1990.
- [5.2] PDA Engineering. PATRAN Plus, Release 2.5, Costa Mesa, CA, 1991.
- [5.3] Tevaarwerk, J.: Constitutive Modeling of Lubricants in Concentrated Contacts at High Slide to Roll Ratio. NASA CR-175029, 1985.
- [5.4] Coleman, W.: A Scoring Formula for Bevel and Hypoid Gear Teeth. J. Lub. Technol., vol. 89, Apr. 1967, pp. 114-126.
- [5.5] Carnahan, B.; Luther, H.; and Wilkes, J.: Applied Numerical Methods. John Wiley & Sons, Inc., New York, 1969.
- [5.6] Handbook For Thermal Analysis. MSC/NASTRAN Ver. 65, The MacNeal-Schwendler Corp, Nov. 1986.
- [5.7] Benedict, G.; and Kelley, B.: Instantaneous Coefficient of Gear Tooth Friction. ASLE Tran., vol. 4, no. 1, Apr. 1961, pp. 59-70.
- [5.8] Tevaarwerk, J.: Traction Drive Performance Prediction for the Johnson and Tevaarwerk Traction Model. NASA TP-1530, 1979.
- [5.9] Anderson, N.; and Loewenthal, S.: Spur-Gear Efficiency at Part and Full Load. NASA TP-1622, 1980.
- [5.10] Anderson, N.; and Loewenthal, S.: Design of Spur Gears for Improved Efficiency. J. Mech. Design, vol. 104, Oct. 1982, pp. 767-774.
- [5.11] Anderson, N.; and Loewenthal, S.: Efficiency of Nonstandard and High Contact Ratio Involute Spur Gears. J. Mech. Trans. Aut. Design, vol. 108, no. 1, Mar. 1986, pp. 119-126.
- [5.12] Handschuh, R.; and Rohn, D.: Efficiency Testing of a Helicopter Transmission Planetary Reduction Stage. NASA TP-2795, 1988.
- [5.13] Krantz, T.; and Handschuh, R.: Efficiency Study Comparing Two Helicopter Planetary Reduction Stages. NASA TM-103106, 1990.
- [5.14] Anderson, N.; Loewenthal, S.; and Black, J.: An Analytical Method to Predict Efficiency of Aircraft Gearboxes. NASA TM-83716. (Also, AIAA Paper 84-1500, 1984) 1984.
- [5.15] Ku, P.; Staph, H.; and Carper, H.: Gear Tooth Scoring Investigation. Report USAAMRDL-TR-75-33, Southwest Research Institute, San Antonio, TX, July 1975.
- [5.16] Naruse, C.; and Haizuka, S.: Limiting Loads for Scoring and Coefficient of Friction on a Disk-Machine. Bull. JSME, vol. 21, no. 158, Aug. 1978, pp. 1311-1317.
- [5.17] Litvin, F., et al.: User's Manual for Tooth Contact Analysis of Face-Milled Spiral Bevel Gears With Given Machine-Tool Settings. NASA CR-189093, 1991.

- [5.18] Valco, M.: Planetary Gear Train Ring Gear and Support Structure Investigation. Ph.D. Dissertation, Cleveland State University, Cleveland, OH, June 1992.
- [5.19] Understanding Tooth Contact Analysis. The Gleason Works, Rochester, NY, 1981.
- [5.20] DeWinter, A.; and Blok, H.: Fling-Off Cooling of Gear Teeth. J. Eng. Ind., vol. 96, Feb. 1974, pp. 60-70.
- [5.21] van Heijningen, G.; and Blok, H.: Continuous as Against Intermittent Fling-Off Cooling of Gear Teeth. J. Lub. Technol., vol. 96, Oct. 1974, pp. 529-538.
- [5.22] Holman, J.: Heat Transfer. Fourth Ed., McGraw-Hill Book Co., New York, 1976.
- [5.23] Harnett, J.; and Deland, E.: The Influence of Prandtl Number on the Heat Transfer From Rotating Nonisothermal Disks and Cones. J. Heat Transfer, Feb. 1961, pp. 95-96.

TABLE 5.2.1—MODEL PARAMETERS USED IN  
TWO-DIMENSIONAL SIMULATION

Thermal conductivity, W/(m·°C)	43.25
Density, kg/m <sup>3</sup>	7801
Specific heat, J/(kg·°C)	473
Maximum heat flux, W	1788
Model width, mm	7.5
Model height, mm	9.0
Model depth, mm	10.0

TABLE 5.4.1—COMPARISON OF TRANSIENT  
RESULTS FROM FINITE DIFFERENCE AND  
FINITE ELEMENT ANALYSIS TECHNIQUES

Analysis type <sup>a</sup>	Revs.	Flux point		
		First	Mid	Last
		Temperature, °C		
FD	5	50	42	50
FE	5	52	43	49
FD	15	58	46	59
FE	15	60	47	57
FD	25	63	49	63
FE	25	65	50	62
FD	35	67	51	67
FE	35	67	53	65
FD	45	69	53	69
FE	45	70	55	68

<sup>a</sup>FD, finite difference; FE, finite element.

TABLE 5.4.2—EFFECT OF TIME STEP SIZE ON TIME-AVERAGED  
BOUNDARY CONDITIONS AND COMPARISON  
TO FINITE DIFFERENCE SOLUTION

Analysis	Increments	Time step, msec	Flux point		
			First	Mid	Last
			Calculated temperature, °C		
FE <sup>a</sup>	6 000	3.47	135.68	116.71	125.89
FE	600	34.7	135.67	116.70	125.88
FE	60	347.0	135.57	116.60	125.80
FD <sup>b</sup>	110 000	.032	135.51	115.02	128.38

<sup>a</sup>Finite element.

<sup>b</sup>Finite difference values are average of minimum and maximum after 5000 revolutions. Variable time step size used. Eleven time steps were short (0.032 msec) plus eleven long (12-tooth model) time steps (0.347 msec).

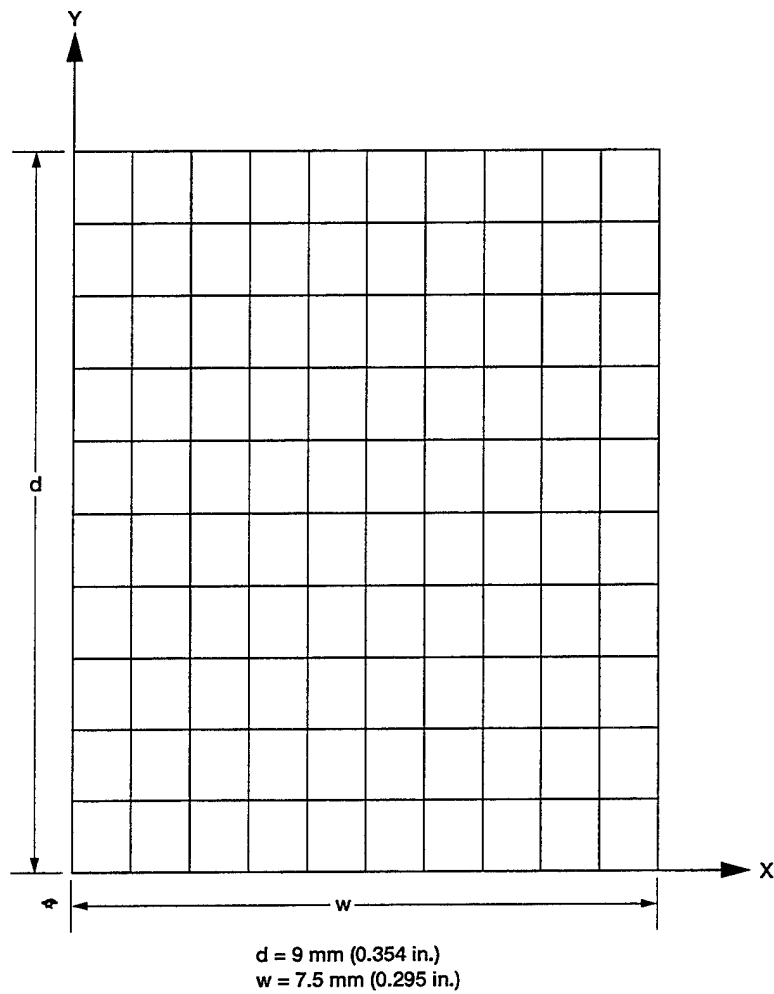


Figure 5.2.1.—Two-dimensional grid for modeling method simulation (121 grid points and 100 elements).

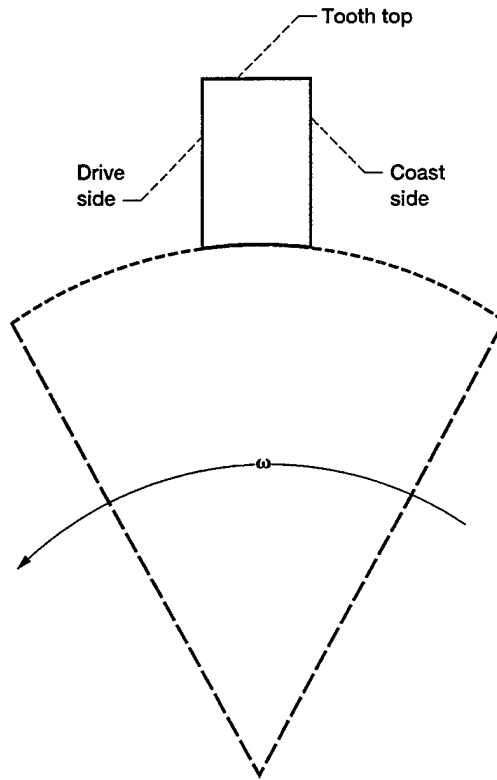


Figure 5.2.2.—Model for two-dimensional heat transfer simulation.

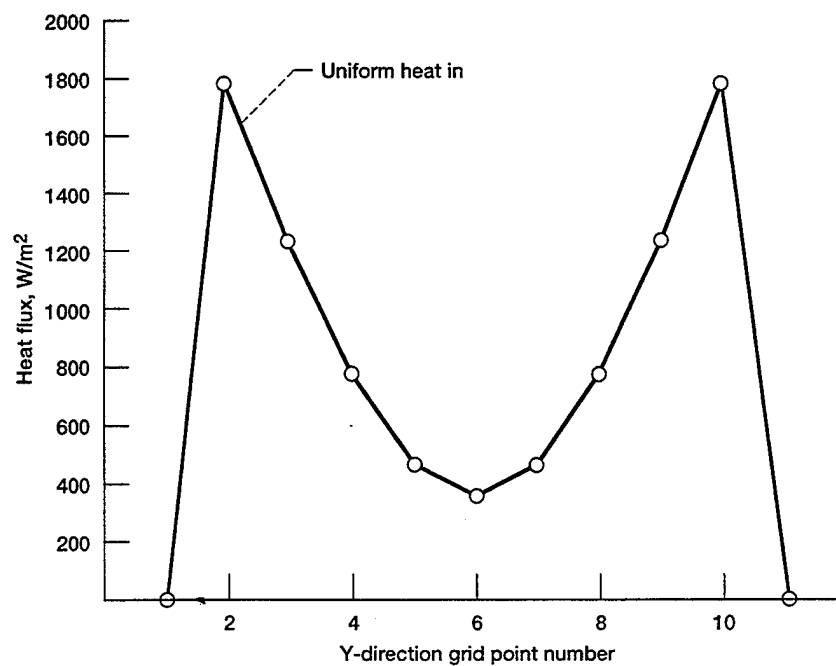
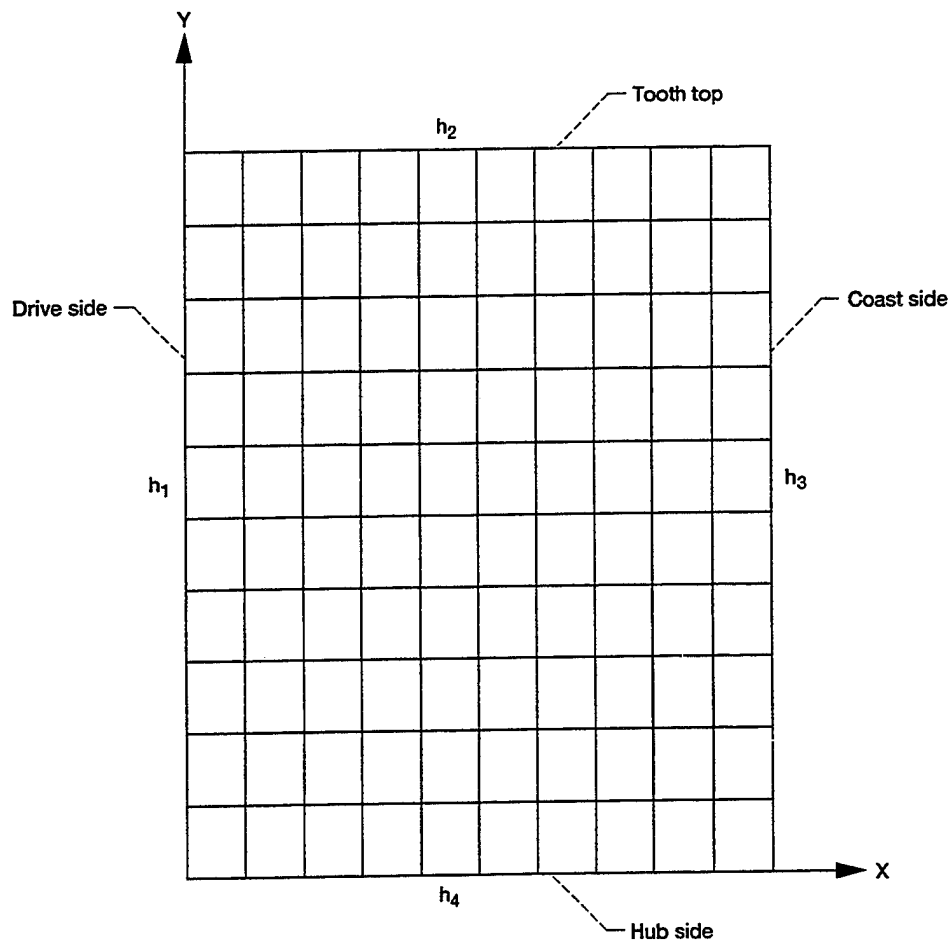


Figure 5.2.3.—Heat flux distribution used in finite difference method.



	Heat transfer coefficient, $W/m^2 \times ^\circ C$
Drive side	8000
Tooth top	2000
Coast side	200
Hub side	0.0001

Figure 5.2.4.—Convection coefficients used in the analysis (hub side for finite difference method,  $h = 0.0$ ).

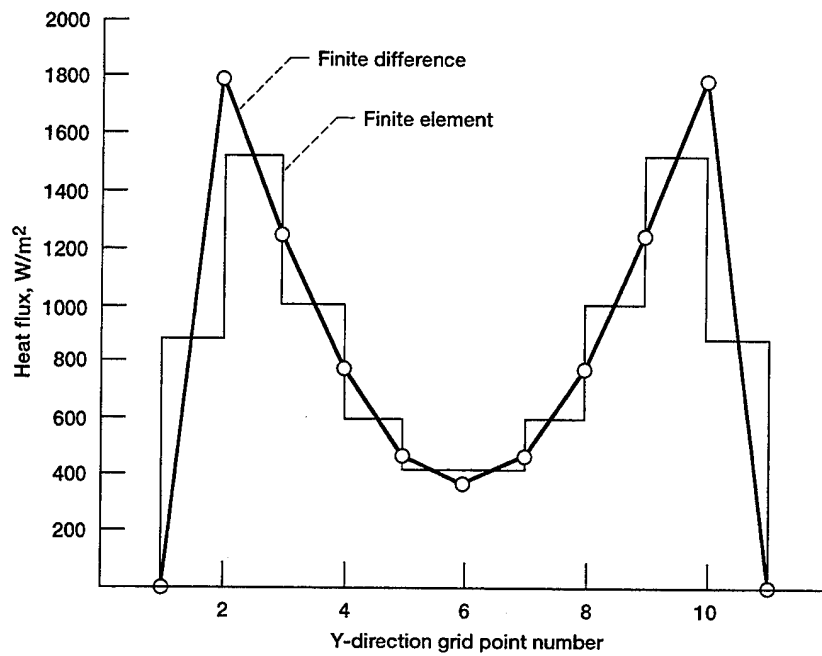


Figure 5.2.5.—Comparison of heat flux distribution for finite element and finite difference analysis.

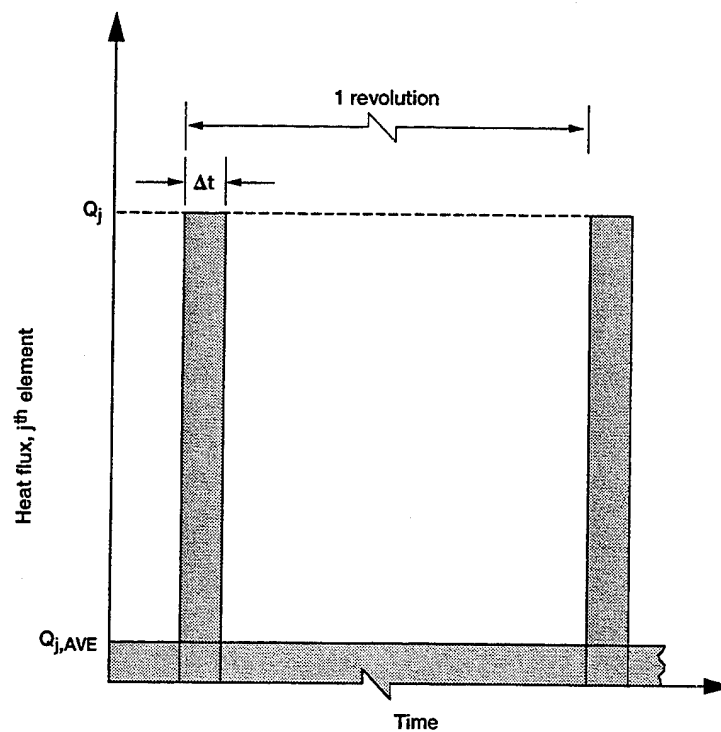


Figure 5.3.1.—Instantaneous and time-averaged heat flux.

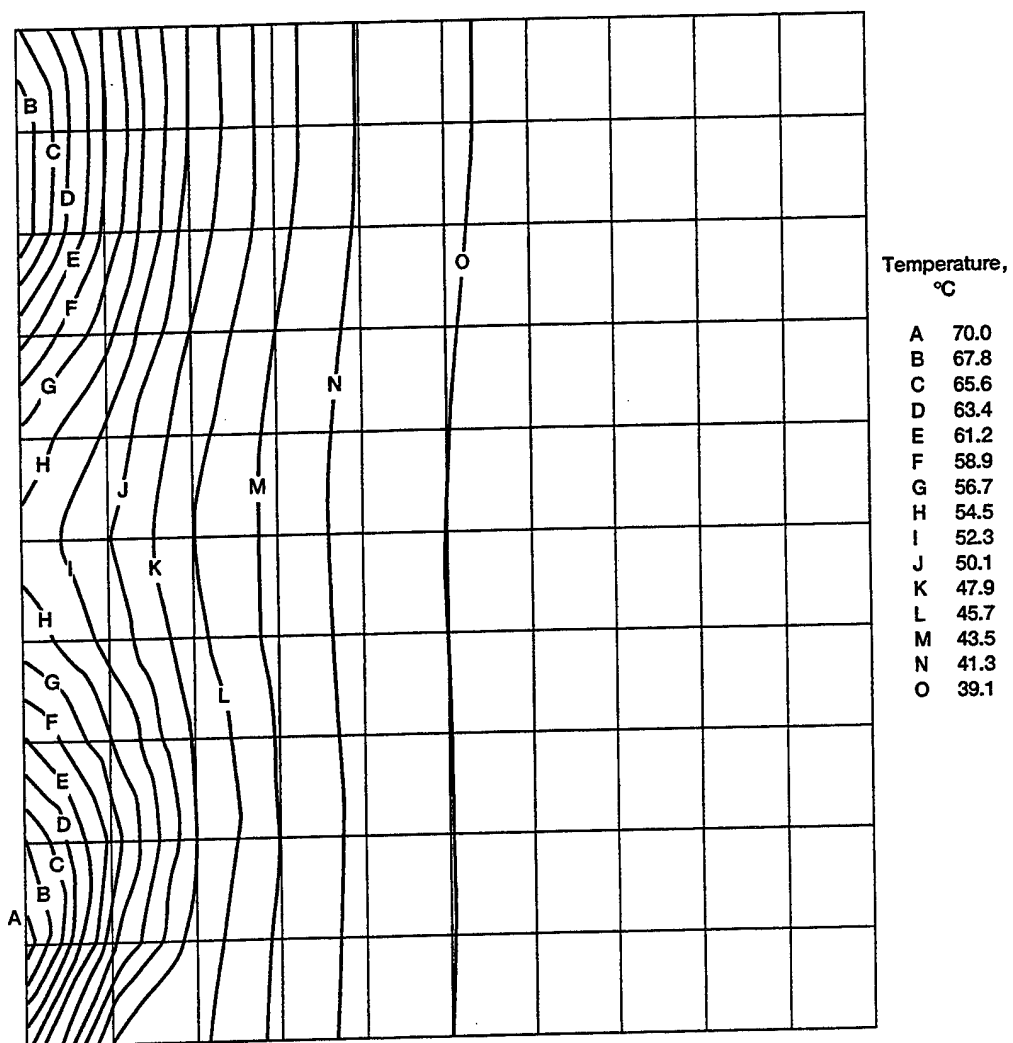


Figure 5.4.1.—Transient results from two-dimensional simulation at 50 revolutions.

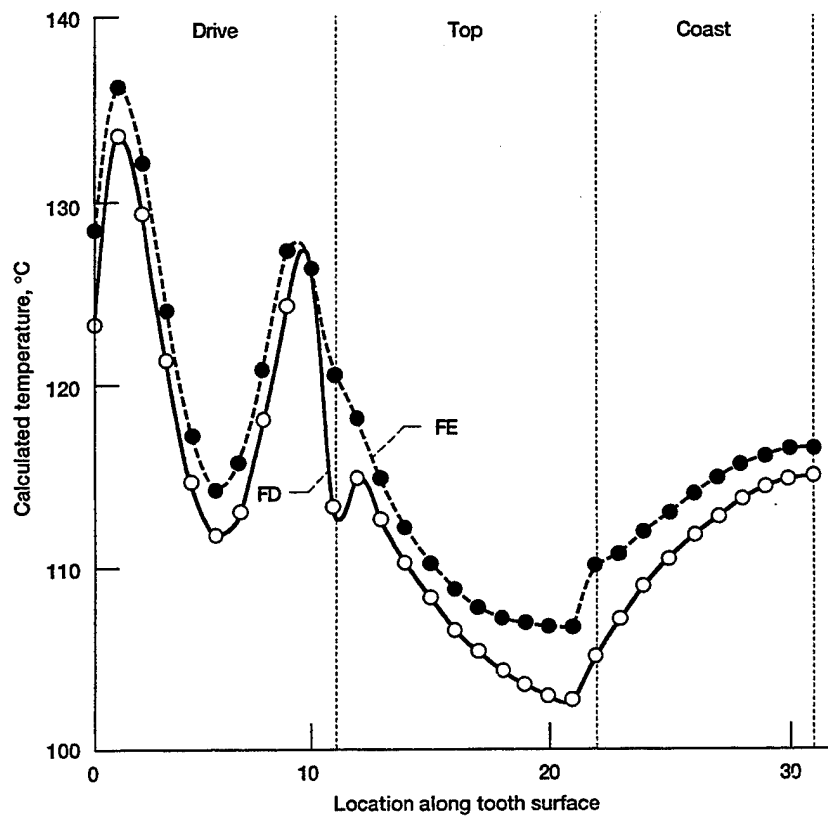


Figure 5.4.2.—Comparison of steady state results from finite element (FE) and finite difference (FD) analysis for two-dimensional simulation.

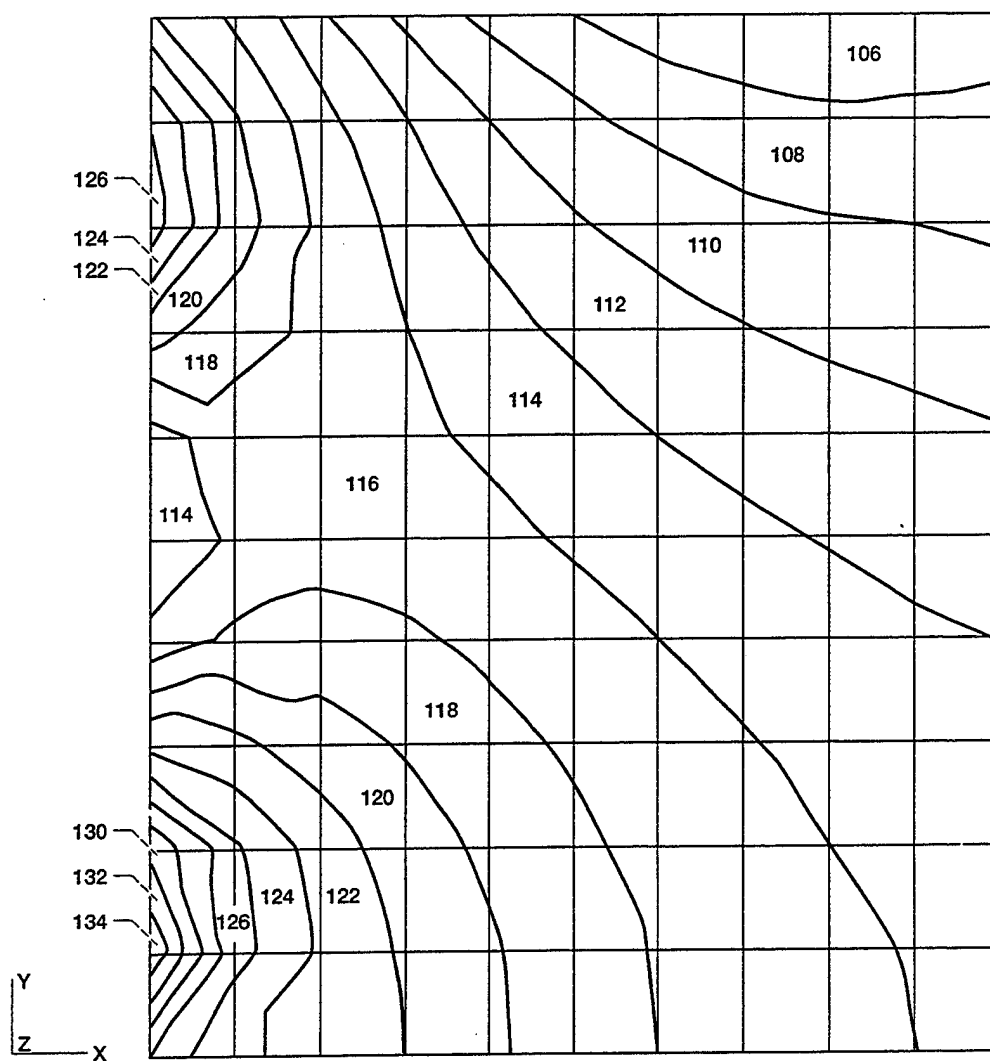


Figure 5.4.3.—Steady state temperature distribution; two-dimensional simulation (temperature, °C).

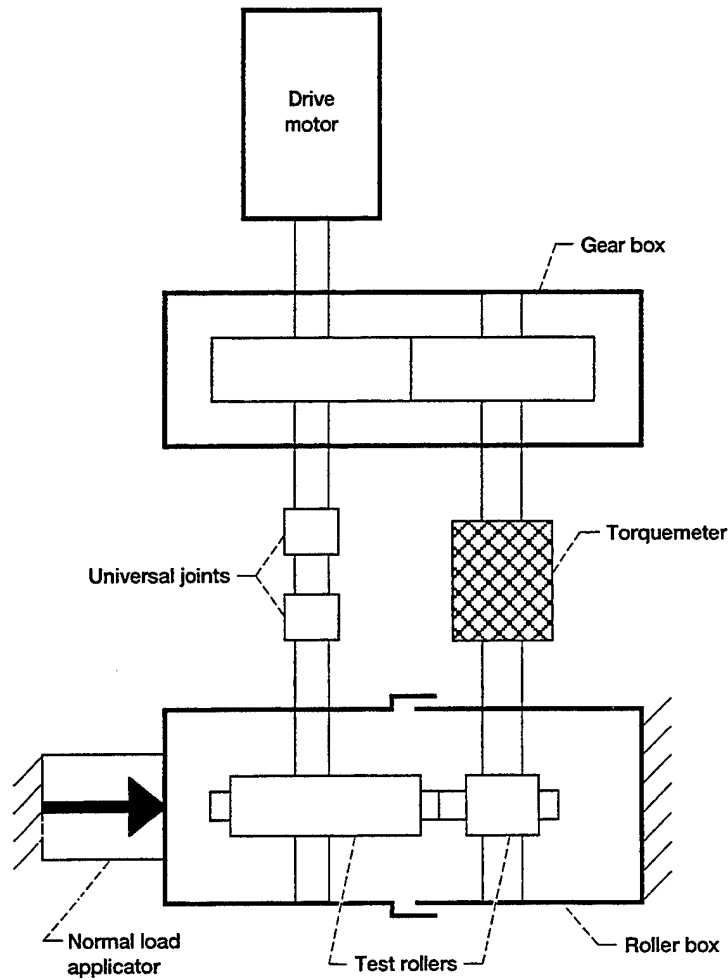


Figure 5.5.1.—Typical friction measurement apparatus that uses rollers with known and geometrically fixed operational parameters.

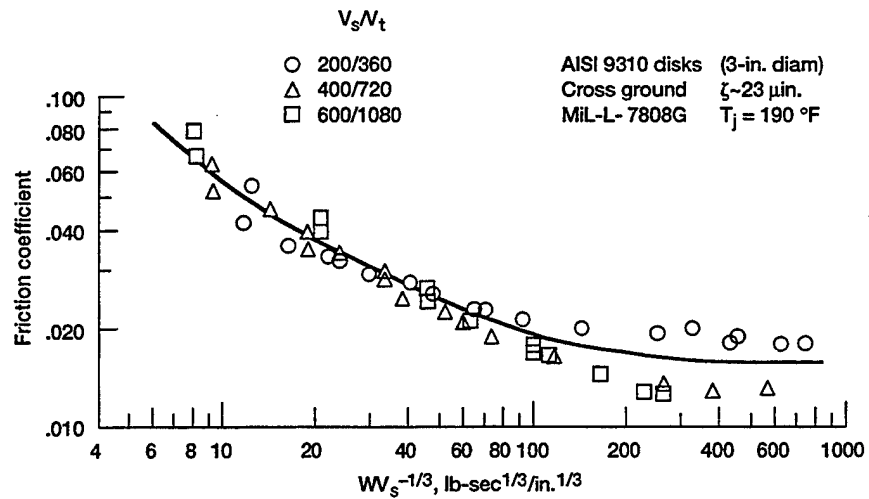


Figure 5.5.2.—Friction data as reported in Ref. [5.15] for typical gear steels ( $W$ -load, lb;  $V_s$ -sliding velocity, in./sec).

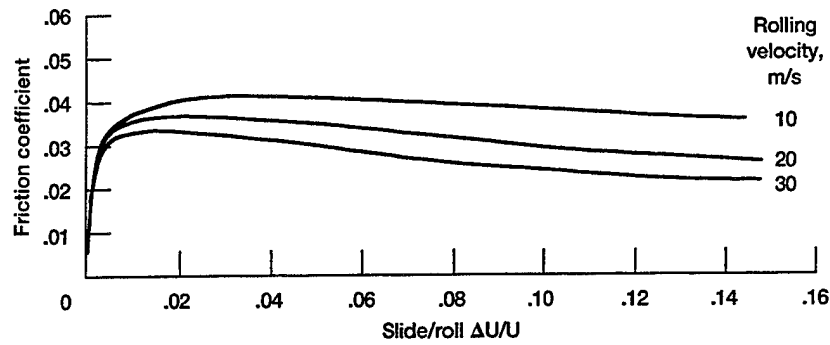


Figure 5.5.3.—Typical friction data as taken from Ref. [5.3]. For a turbine engine lubricant at 37 °C and maximum contact pressure of 1.92 GPa.

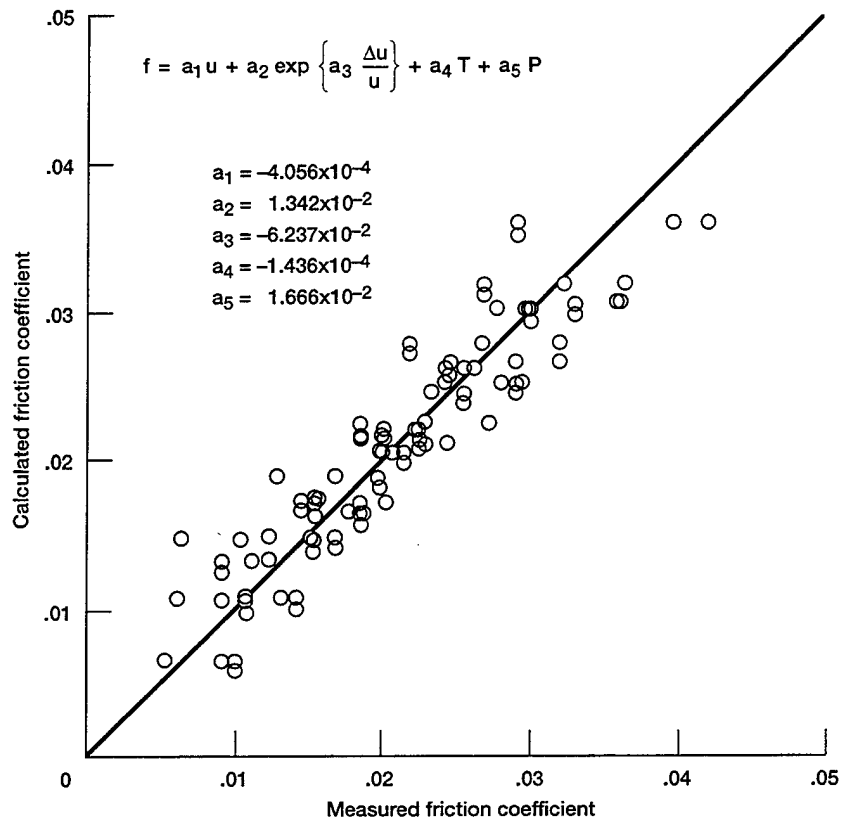
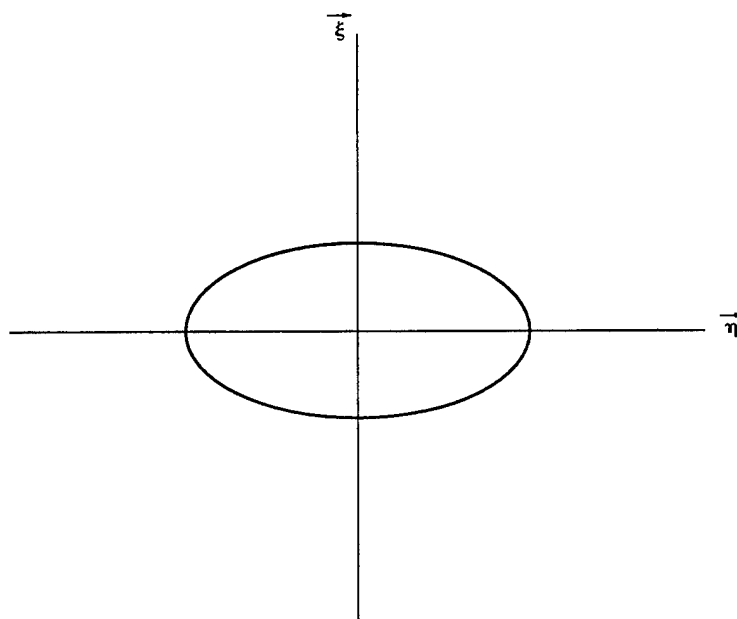
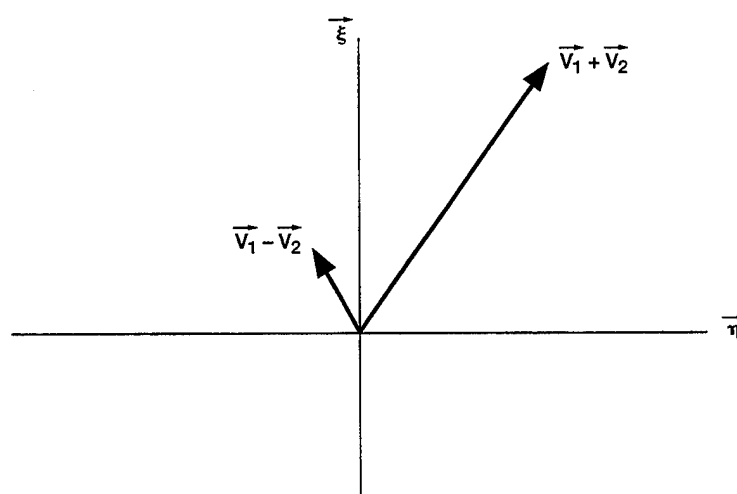


Figure 5.5.4.—Curve fit of data taken from Ref. [5.3] for typical turbine engine oil.



(a) Ellipse orientation.



(b) Rolling and sliding velocity.

Figure 5.5.5.—Contact ellipse orientation with respect to contact point velocities.

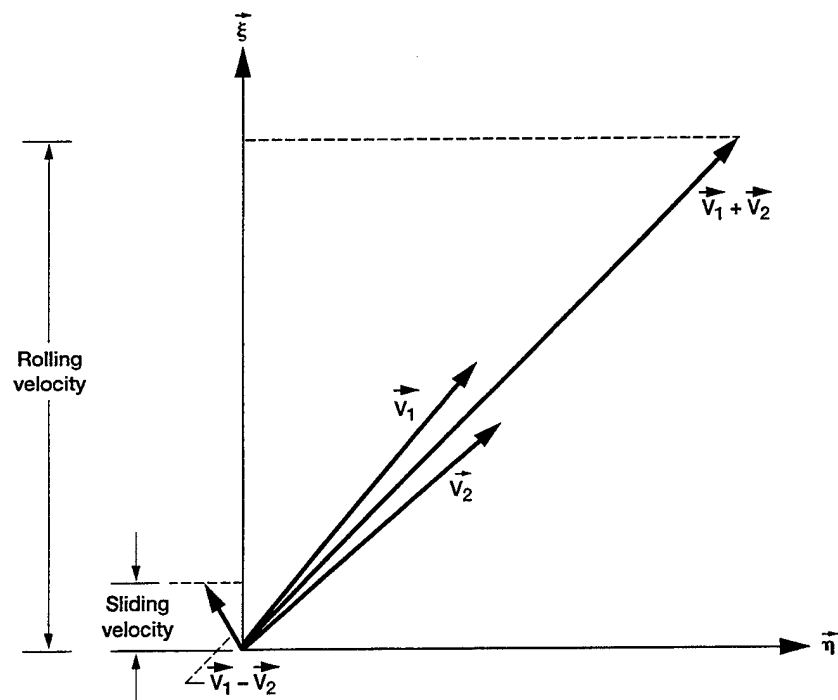


Figure 5.5.6.—Rolling and sliding velocities with respect to the major-minor directions of the contact ellipse.

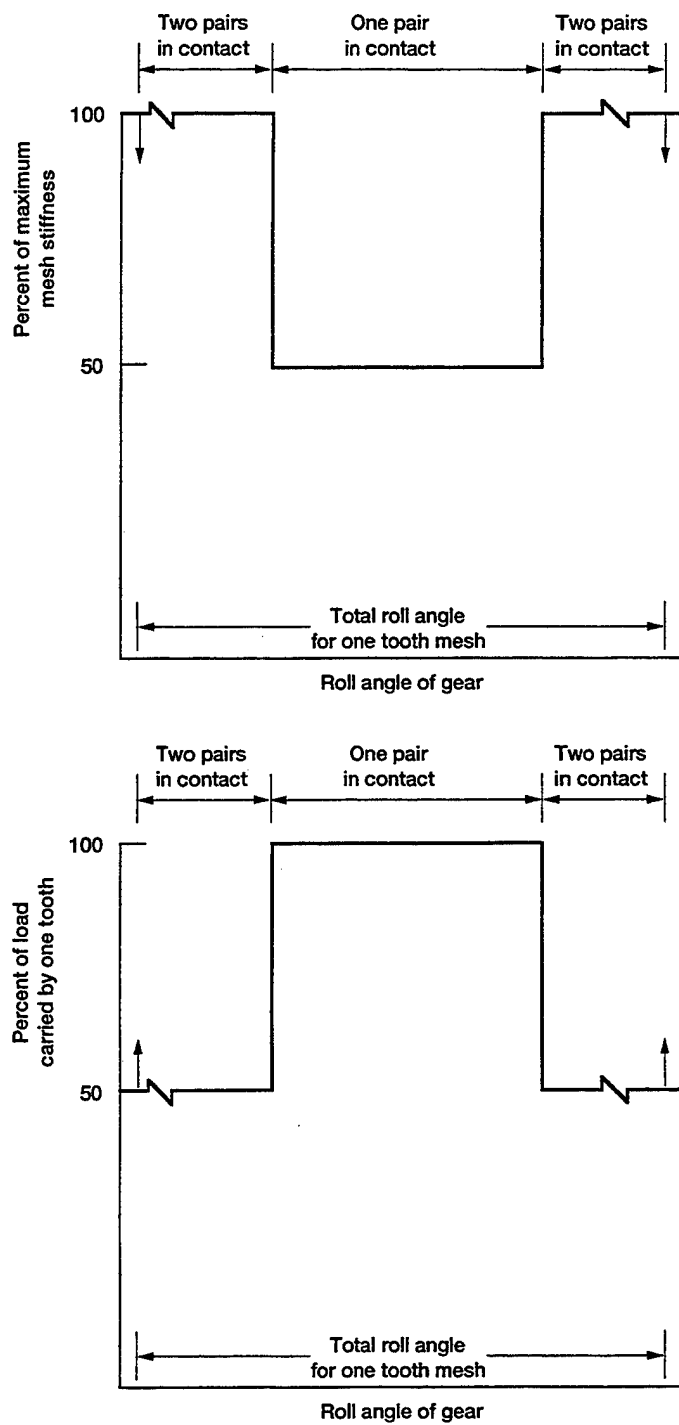


Figure 5.6.1.—Tooth mesh stiffness and load sharing typically assumed.

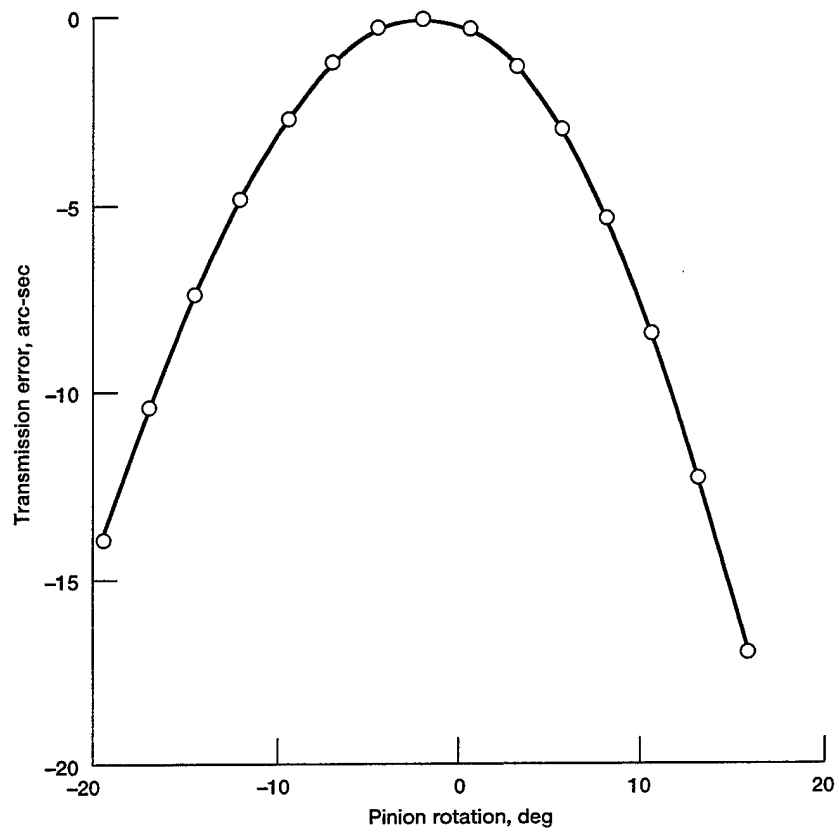


Figure 5.6.2.—Transmission error as a function of pinion rotation angle for one pitch of rotation or total meshing cycle.

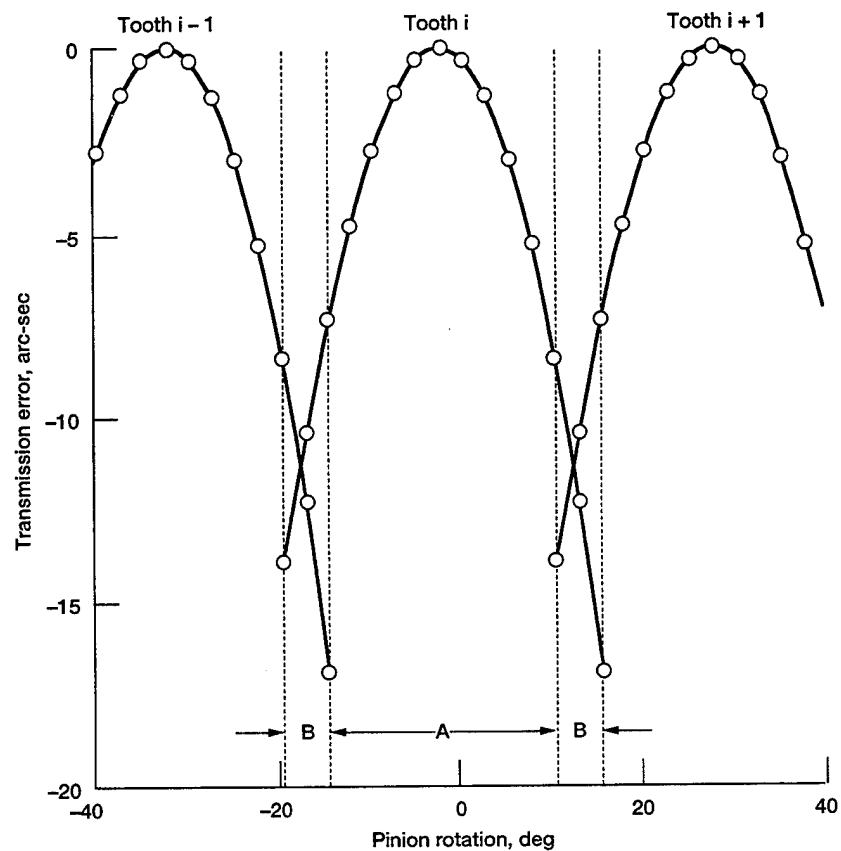


Figure 5.6.3.—Transmission error of output gear rotation as a function of pinion rotation angle (region A — 1 tooth pair in contact; B — 2 pairs in contact).

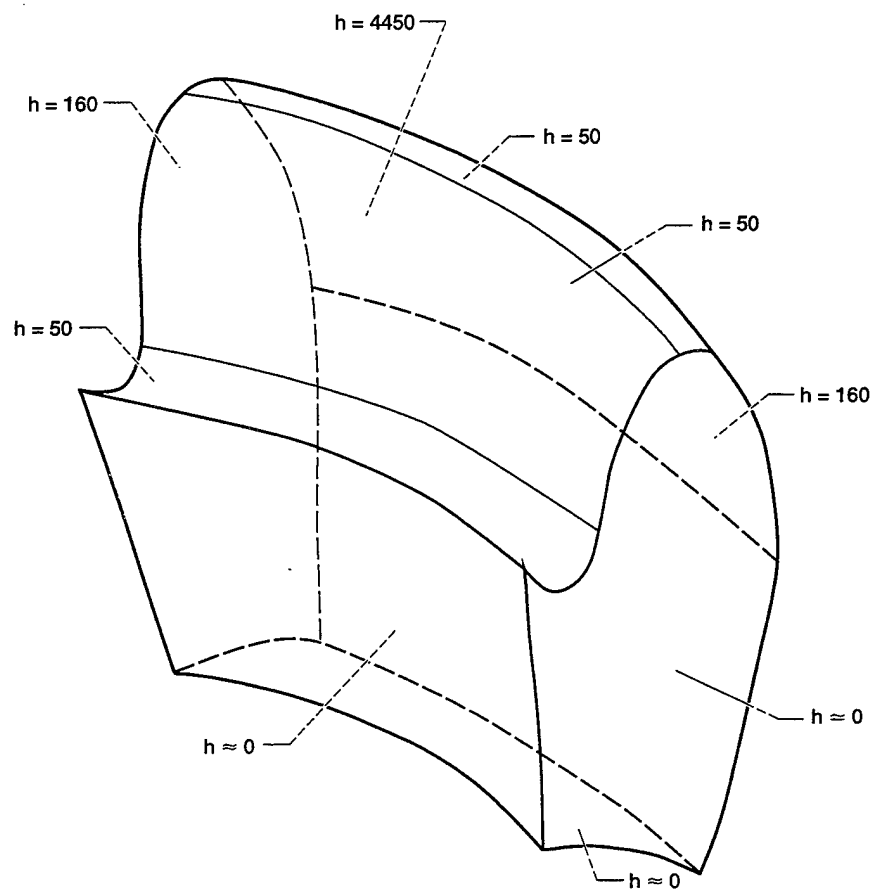


Figure 5.7.1.—Heat transfer convection coefficients to be specified for analysis ( $W/M^2 \times ^\circ C$ ).

## CHAPTER 6: THREE-DIMENSIONAL SPIRAL BEVEL GEAR

### MODEL AND RESULTS

#### 6.1 Introduction

To initiate model development, certain design parameters must be known. Gear ratio, power capacity, spatial envelope, and other variables are required. These parameters can be used initially to investigate the bending and contact stress index (Ref. [6.1]). The model is usually iterated about design parameters such as the pitch or number of teeth required to achieve the best balance of the stress indices while providing the required operation life.

**Machine Tool Settings:** Once the design is determined, based on the aforementioned variables, the geometric nature of the gears under consideration can be ascertained. The basic design data can then be used as input to determine the generation machine tool settings required and the no-load tooth contact behavior that can be expected from the meshing gears (Refs. [6.2] and [6.3]). The machine tool settings, described in Chapter 4, are the basis upon which the kinematics of manufacture are described analytically.

**Contacting Conditions:** If the tooth contact analysis (TCA) is of an acceptable behavior, if the transmission error is low and the predicted contact between surfaces is acceptable, the next step can be taken. At the contacting points (from the TCA), the geometry of the meshing surfaces can be extracted. Using the input design and operational parameters of the given gear mesh, the following information can be found: the principal curvatures, the orientation of these curvatures with respect to each of the surfaces, the sliding and rolling velocities, the normal load (assuming only one tooth in contact), and the contact ellipse orientation. This information is essential to the thermal model under consideration in this study. The principal curvatures and their orientation are used to determine the size of the contact ellipse via a three-dimensional Hertzian theory described in Chapter 4. The velocities and load are needed to determine the amount of heat generated. The contact orientation is required so that the elliptical heat source can be applied to the tooth surface and oriented in the proper direction as the contact moves over the active finite element grid of the tooth surface profile.

**Three-Dimensional Finite Element Model Development:** In a parallel effort to the development of the gear model just described, once the machine tool settings are frozen on a given design, the three-dimensional finite element model development can begin. A computer program (Refs. [6.4] and [6.5]) can be used to automatically determine the active profile geometry as well as the gear body information. The combination of active profiles and gear body result in a one-tooth model that is representative of the gear member in question. This information can be cloned to develop a complete gear model if desired. At this point, element density (number of elements), material properties, and boundary conditions can be applied. The procedure used in this study is described in Appendix B.

**Active Profile Grid Points:** After the mesh density and boundary conditions are chosen, the surface grid points on the active profile where meshing takes place must be assembled. These grid points are possible locations where the heat flux will be applied in the thermal model. This information is extracted from the finite element model to permit the determination of the number and location of surface heat flux grid points that are contained in each of the contacting ellipses. This information must be properly bookkept for application in the user subroutines and appended to the finite element bulk data file. The grid points where the heat flux is applied changes for each time step during the meshing period. Once the tooth moves out of mesh, there is only convection from the active profile until the next meshing period. This process is repeated during the entire operation time of the actual meshing gears. The overall bulk temperature of the model increases until a steady state

operation condition exists. Even though temperatures stabilize, there still are local transients due to the once-per-revolution heat flux application.

The interrelatedness of the various analysis procedures is shown in Figure 6.1.1. What can be seen from this figure is that a number of computer programs must be run. Each program basically requires information calculated in a prior analysis. Therefore, a design that is near to the final expected configuration should be available before the analysis begins, or possibly the methodology can be utilized to analyze a current design in more depth.

## 6.2 Relationship Between Hertzian Analysis and Three-Dimensional Finite Element Spiral Bevel Gear Model

As mentioned in an earlier analysis (Chapter 4), the contact of the meshing pinion and gear are found in three-dimensional space. Based on the Hertzian analysis, the size (lengths of major and minor ellipse) is known. The analysis used herein assumes that the curvatures of the contacting bodies are identical to those found at the mean point of contact. In actuality the surface principal curvatures change from point to point. However, because a full three-dimensional contact analysis (based on the finite element method) for spiral bevel gears is not available, the above approximation is used. From the calculations provided by the analysis of Litvin (Ref. [6.2]), the orientation of the ellipse major and minor directions is known with respect to a set of gear member fixed coordinates. The issue at hand is to determine which surface grid points of the three-dimensional finite element model are within each of the contacting ellipses. The material that follows is used to explain how this is accomplished.

The process begins by looking at the contact ellipse of the meshing gear surfaces in three-dimensional space (Fig. 6.2.1). At each contacting ellipse, the size, orientation, and location changes during the meshing process. Also, there can be locations where the actual ellipse becomes truncated due to the limiting active profile of the gear tooth. In the Hertzian analysis, the bodies are assumed to be infinite, with constant principal curvatures equal to that of the center of contact. The contact ellipse is contained in a plane that is perpendicular to the load (see Fig. 6.2.1). Therefore, these contact ellipses will be projected onto an axial and radial plane. The same procedure is applied to the active surface grid points from the finite element model to determine which grid points will have heat fluxes applied during a particular time step.

**Contact Ellipse in Radial-Axial Plane:** The contact ellipse based on size, location, and orientation is projected in a two-dimensional space by using the principal directions and the ellipse major and minor lengths and then forming the projections of these onto a radial and axial coordinate plane. After this step, the orientation of the major and minor ellipse directions mentioned earlier can have the effect of "bending" the ellipse in the radial-axial plane. What this means is that the principal axis projection may not be collinear along its length, as shown in Figure 6.2.2. This development further complicates the solution procedure to determine the active grid points contained within the ellipse. In the method developed (in Calculation Procedure), the ellipse is broken into four separate parts (or quadrants or regions) to take this effect into account.

**Calculation Procedure:** The following procedure documents how the determination of which finite element grid points of the active profile are contained in an ellipse under study. The method to be described is numerically accomplished by using a computer program.

Based on earlier analysis (Section 4.5), the contact ellipse size and orientation are known. The next step is to put these into a radial-axial plane. The radial direction consists of the magnitude of the x, y-positions of the four extreme corners of the contact ellipse and the center mean position shown in Figure 6.2.3. The radial-axial projections of an example ellipse are shown in Figure 6.2.4. These projections differ in length from those found

in three-dimensional space. In the case used herein, straight lines are assumed to exist from the mean point M to the ellipse extremes (both major and minor directions). In actuality, if midposition projections or other locations between the contact center and the ellipse extremes were found and plotted in the radial-axial plane, they would not lie on the straight line approximation. The path from one ellipse extreme to the other along one of the principal directions is a curved path in the radial-axial plane.

Next, a new coordinate system is assembled so that the origin is centered at the mean contact point of the contact ellipse (Fig. 6.2.5). At this point, the orientation of the major ellipse directions to the new coordinate system is found. The locations of the major and minor ellipse extremes are found by subtracting the  $\bar{R}$ ,  $\bar{Z}$ -coordinates of the mean point from each of the four extreme values.

Now the finite element model active grid points are put into a similar radial-axial coordinate system in the same manner. At this point, the mean ellipse point radial and axial values are again subtracted from the grid point  $\bar{R}$ ,  $\bar{Z}$ -values to put them into the local coordinate system where the mean point of the ellipse is at the origin. The grid points are also rotated based on the ellipse orientation with respect to the new local coordinate system. The net  $\bar{R}$ ,  $\bar{Z}$ -sign determines in which quadrant or region the point will be checked. In each quadrant, the major and minor ellipse lengths can be different because of the projections from the initially oriented contact ellipse. This is shown in Figure 6.2.6. For example, if the active profile grid point is positive in sign, after relocation into the local coordinate system ( $\bar{\bar{R}}$  and  $\bar{\bar{Z}}$ ), then that quadrant is checked to see if the point lies within the ellipse. This checking is done by satisfying the following equation:

$$\left( \frac{\bar{\bar{R}}_{\text{grid}}}{b_{\text{region}}} \right)^2 + \left( \frac{\bar{\bar{Z}}_{\text{grid}}}{a_{\text{region}}} \right)^2 \leq 1.0 \quad (6.2.1)$$

If the equation is satisfied, the grid point number is associated with the ellipse in question. This process is repeated for all active grid points of the finite element model for each ellipse. Thus, a number of sets of grid points based on the number of contact ellipses is produced. The level of the flux attached to each grid point depends on the operating conditions, ellipse location, load sharing, and flux distribution over the ellipse.

An example of grid point projections of the active profile of a spiral bevel gear finite element model in the radial-axial plane is shown in Figure 6.2.7. Heat flux grid points and contact ellipse major directions are shown in Figure 6.2.8. The ellipse major axis dimension is shown as a line, and the active surface grid points are shown as the small circles.

### 6.3 Heat Flux Distribution on the Three-Dimensional Gear Model

At this point, the grid points of the active profile that are in contact for a given ellipse are known. Thus, the question to be addressed is how to distribute the flux. If a complete three-dimensional contact model were available, the distribution would be made based on the force distribution associated with the grid points in contact; however, one is not available so an assumption of the distribution must be made. Of the many different distributions that could be assumed, average, parabolic, Gaussian, or elliptic, the type chosen will obviously have an effect on both the time-averaged- and time-transient temperature field of the model to be discussed later in this chapter.

For this study, an elliptical distribution was chosen, a choice that would parallel the pressure profile shape. The calculated contacts, although elliptical, have a high aspect ratio that is typically 10 or greater. Therefore, a one-dimensional distribution with an aspect ratio of 10 was chosen to distribute the heat flux generated in the

contact (see Fig. 6.3.1). The amount of flux contributed to an individual grid point is based on the distance from the center of the contact ellipse to the grid point under consideration as well as on the number of grid points contained in the ellipse.

Because the number of grid points and the magnitude of the flux for the ellipse in question are known, the flux weighting is now determined. Starting first with the equation of an ellipse as given by

$$\frac{x^2}{a^2} + \frac{y^2}{b^2} = 1 \quad (6.3.1)$$

where the values  $a = 10$  and  $b = 1$  are set for an aspect ratio of 10 (see Fig. 6.3.1). The  $x$ -value pertains to the distance from the ellipse center and the  $y$ -value pertains to the flux value associated with the  $x$ -value. Next, the distance from each grid point within the ellipse to the mean contact point at the center is found. Then, using Equation (6.3.1), a value for  $y$  is found. The  $y$ -values for all grid points within the ellipse are calculated along with the sum of all  $y$ -values. The flux that is given to a grid point is found from

$$(\text{Flux})_i = (\text{Total flux}) \frac{y_i}{\sum_{i=1}^n y_i} \quad (6.3.2)$$

where  $n$  is the number of grid points within the ellipse. An example of a heat flux distribution for one of the ellipses of the model to be used later in this chapter is shown in Figure 6.3.2. Also shown is the average heat flux per grid point if that distribution had been chosen.

#### 6.4 Three-Dimensional Finite Element Model and Application of Steady State and Transient Boundary Conditions

The basic design information for the three-dimensional finite element model to be used in this study was obtained from the gear set manufacturer's summary sheet. Adjustments to these settings for model development purposes was accomplished using computer programs developed in Litvin (Ref. [6.2]) in which the design data as well as the contact path orientation are the required inputs. The resultant machine tool settings reflect this input. A sketch of the typical contact pattern attained for this gear set is shown in Figure 6.4.1. Since the test hardware was manufactured long before the recent advances in gear measurement (Refs. [6.6] and [6.7]) and in computer numerically controlled machines (Refs. [6.8] to [6.10]), this procedure was used. Only the most basic machine setting and gear design data were known; therefore, not all details on the test hardware were available.

**Finite Element Model:** The gear design information and machine settings produced using the analysis of Reference [6.2] are shown in Table 6.4.1. The method described in Chapter 4 was used to develop the finite element mesh. Eight-node three-dimensional heat transfer elements were used. A reasonably fine mesh that was developed is shown in Figure 6.4.2. This model contains 20 250 elements and 22 586 grid points; 12 960 elements are contained in the tooth section of the model.

A tooth contact analysis was conducted and 15 locations were analyzed from the point at which the tooth comes into contact until it goes out of mesh. The transmission error associated with the pinion rolling through mesh is shown in Figure 6.4.3. The procedure mentioned earlier for load sharing was applied and the combined geometry conditions, loading, contact ellipse size and maximum pressure are shown in Table 6.4.2. This

information was then used to estimate the friction coefficient and, ultimately, the heat flux. These data are shown in Figures 6.4.4 and 6.4.5, respectively, along with the sliding velocity and normal load.

**Boundary Conditions:** The next step is to take this information and put it into the time- and position-varying boundary conditions required. The procedure outlined and described earlier in this chapter is used. Because of the large number of surface grid locations, methods to automate the procedure were developed. For the mesh shown in Figure 6.4.2, 874 grid points were on the active profile. The active profile grid points projected in the radial-axial plane are shown in Figure 6.4.6. Using the analysis that was developed, many ellipses of the 15 used in the present model had greater than 40 grid points contained within the ellipse boundaries. Therefore, automation was necessary to expeditiously build the user subroutines for the time-transient and time-averaged cases (see Appendix C).

The active profile grid projected onto a radial-axial plane for this model is shown in Figure 6.4.6. As an example of the foregoing discussion, data from the calculations for ellipse 10 are shown in Figure 6.4.7. The diamond-shaped symbols indicate the locations of the ellipse mean point and major-minor extreme locations in the radial-axial plane. The solid symbols indicate grid points from the surface contained within ellipse 10. At this point the pinion is approximately 2/3 complete in its meshing cycle. Similar ellipses can be plotted for the entire meshing period, the resultant composite tooth contact region being based on the analyses contained in this report. This composite pattern for the pinion under study is shown in Figure 6.4.8.

**Time-Averaged Boundary Conditions:** In the time-averaged heat flux boundary conditions described in Chapter 5, the heat flux is assumed to be constant. For a particular grid point, the number of ellipses in which this location may be contained must be determined along with the total flux applied at this location. Therefore, in the analysis mentioned earlier (Section 6.2), each active grid point is checked to determine the number of ellipses it appears in and the amount of heat flux applied over the complete meshing cycle and summed. The heat flux that is then applied to the model at a given grid point is the total heat flux sum divided by the number of time step increments that the transient model would have in one revolution. This information is then bookkept in the data contained in the user subroutine.

In the example to be used herein for the time-averaged or time- and position-varying boundary conditions, 402 of the 874 surface grid points have heat fluxes applied to them. For each of these points, the heat flux applied to the time-averaged conditions is the sum from all 15 ellipses. If the number of ellipses were increased, a given heat flux grid would appear in more than one or two ellipses. The number of ellipses to have for an analysis is related to how fine the mesh is because a very large number of ellipses on a course model would not yield any more information but would be more costly in terms of computer time. The most efficient use of the number of ellipses and mesh density would be to have a fairly complete coverage of heat flux grid points over the contact locations dictated from the Hertzian analysis. In Figure 6.4.8, there was only one grid point (near the top of the tooth) that should have had a heat flux applied but did not receive one.

**Time- and Position-Varying Boundary Conditions:** The time- and position-varying boundary condition case is more complicated because in addition to keeping track of grid points that participate in the heat flux and values of applied heat flux, the ellipse in which they occur must be organized. Also, within the user subroutine, the location of the tooth under study with respect to the meshing zone must be known. Therefore, in the case being studied herein, 144 time steps per revolution are used. Of this amount, 15 flux conditions in sequence are applied to the tooth in question. The remaining 129 time steps only have convection heat transfer from the tooth to the surroundings. This process is repeated for every revolution that the analysis is conducted in the transient mode.

For the model considered herein, 15 ellipses were found during the meshing cycle. At each ellipse location, the number of grid points and heat flux amount to each grid point changed. The number of grid points and heat

flux to be applied within a given ellipse is shown in Table 6.4.3. The number of ellipses chosen must be considered carefully. A large number of ellipses on a coarse model would not yield better results. The same could be said about a few ellipses on a fine-element mesh. Therefore, the number of ellipses chosen should have no missed nodes over the resulting contact region, and many of the active grid points should have a heat flux applied for more than one ellipse position.

**Heat Flux Distribution:** As discussed earlier in this chapter, the contact ellipse is basically a narrow band with an aspect ratio typically greater than 10 and an elliptical distribution of the heat flux applied. The distribution for ellipse 10 is shown in Figure 6.3.2. Also shown in this figure is the average in comparison with the chosen distribution.

With respect to the calculations contained in this report, one other important assumption to be made relates to the partitioning of the heat flux between the pinion and gear. The assumption used herein is that the heat flux generated is evenly split between the pairs of teeth in mesh. Partitioning in some other amount would obviously vary the results to be presented. This assumption is discussed, along with others necessary to perform the analysis, in the next chapter when the experimental and analytical results are compared.

## 6.5 Time-Averaged and Time-Transient Analytical Results

Based on the model development, as mentioned earlier in this chapter, the finite element analysis can now be conducted. Three sets of conditions are analyzed. First, the time-averaged boundary conditions; next, the time- and position-varying solution, starting from the time-averaged solution; and finally, the time- and position-varying solution, beginning from startup at ambient conditions. All three analyses are conducted on the same basic finite element model, the only difference being the type of user subroutine or the position of the model with respect to elapsed time.

**Time-Averaged Boundary Condition Model:** As mentioned earlier in Section 5.3, during the time-averaged boundary condition part of the analysis, time step size in the finite element model does not matter because of the unconditional stability of the implicit numerical scheme used. For the model under considered herein, the total elapsed time of 20 minutes with 60 time increments was used. These conditions place the model well beyond the steady state solution. The time-averaged boundary condition solution at steady state is shown in Figure 6.5.1. In this figure, the temperature field of the model ranged from 70 to 170 °C. The composite time-averaged heat flux was applied as shown in Figure 6.4.8, where each grid point flux sum was averaged over one complete revolution.

**Time- and Position-Varying Boundary Conditions From Restart:** This section discusses the predicted model behavior using the time- and position-varying boundary conditions to restart the model after obtaining the time-averaged solution. The time-averaged boundary condition model is used for the initial conditions to begin the solution for this case. As mentioned earlier in Section 6.4, 15 contact increments across the tooth were chosen, which amounts to the pinion rotating 2.5° per time increment or 144 time steps per revolution. Therefore 15 increments involve the addition of heat flux at designated nodes and the other 129 increments involve the transfer of heat to the rest of the gear and the surroundings.

The motion of the contact ellipse over the surface determined by the methods already discussed is shown in Figure 6.5.2. In this figure, the odd-numbered ellipses are shown with respect to the active tooth surface profile grid. Ellipses 1, 3, 5, and 7 are shown in Figure 6.5.2a and ellipses 9, 11, 13, and 15 are shown in Figure 6.5.2b. Figure 6.5.2 represents the movement of the contact and heat flux across the gear surface during the meshing process. The flux distribution is based on the distance the grid point in question is from the center of the ellipse.

The time-transient solution was carried out for over 600 time steps, or slightly over four revolutions. Each revolution took almost 4 hours of CPU time on a super computer.

To determine when the transient model had reached its cyclic changing temperature field repeatably, an active profile grid point that received heat flux each revolution was followed. Data from all the transient increments run are shown in Figure 6.5.3 along with the location of the grid point in question. As seen from this figure, the temperature initially decays after the time-averaged boundary condition is removed. Then with each meshing period, the heat flux is applied and the grid point temperature climbs drastically. The solution has reached its periodic, or cyclic, equilibrium when the temperature profile found is repeated. In this figure this happens rather rapidly and within a couple of revolutions.

The entire temperature field is now shown on the three-dimensional model. Different positions during one revolution are presented. The model is first displayed at the last increment before any of the heat fluxes have been applied. At this location, the overall changing temperature field is at its lowest value. The predicted temperature is shown in Figure 6.5.4. Next, the model is shown at the increment when the heat flux for ellipse 5 is being applied. This increment is shown in Figure 6.5.5. The only difference seen is the slight temperature increase where ellipses 1 to 4 have taken place prior to this increment. The reason the temperature does not drastically increase during this stage of meshing can be found by a closer examination of Figures 6.4.4 and 6.4.5. At the initial few contact positions, the load and the sliding velocity are low; therefore, the resultant heat flux generated at these positions is low.

Increment 10 is the next displayed. By the time the model reaches this point, temperatures in the contact region have reached a maximum of approximately 175 °C. This increment is shown in Figure 6.5.6. At this step, the heat flux is still increasing in magnitude as the sliding velocity is increasing and a single tooth is carrying the entire load.

The last heat flux increment shown here is number 13. The resultant temperature field is presented in Figure 6.5.7. At this position, the heat flux is a maximum because of the even higher sliding velocity combined with single tooth pair contact. Temperature maximums are approximately 195 °C. In comparison with the maximum temperature positions for the temperature field displayed in Figure 6.5.4, the temperatures in Figure 6.5.7 are approximately 40 °C higher at these locations.

After the last heat flux increment is applied, the temperature field decreases in temperature as a result of conduction into the gear body as well as convection to the surroundings. A couple of locations after the heat flux positions are now presented.

After the pinion has rotated 70° since the last heat flux increment, the temperature field appears as shown in Figure 6.5.8. The maximum temperature at this point is approximately 175 °C. Next, after the pinion has rotated a total of 195° since the last heat flux, the temperature field appears as shown in Figure 6.5.9. The temperature peak at this point in the rotation has dropped to 165 °C. The cooling process therefore continues until the next meshing increment begins the process all over again at which point the maximum temperature going back into mesh is about 155 °C.

The interesting observation from Figures 6.5.4 to 6.5.9 is that the transient heat flux has virtually no effect on the temperature field at positions a distance from the flux locations. Clearly, the ends of the teeth, tooth top, and gear body do not realize that the heat flux boundary conditions changed from time-averaged to time- and position-varying boundary conditions. This observation will be useful in the next chapter when the comparison between this analytical model and experimental results is made.

**Time- and Position-Varying Solution (From  $t = 0$ ):** The time- and position-varying solution starting from  $t = 0$  out to steady state would be computationally prohibitive. From experimental tests, steady state conditions are reached in approximately 10 minutes. The average CPU usage, in this mode, is about 4 hours per revolution. Based on these assumptions and using the current computing power, it would require 65 years of nonstop computing to reach a steady state solution.

The initial startup is of interest to verify that the expected behavior from  $t = 0$  is found. A grid point on the active profile, the same one used in Figure 6.5.3, will be followed for many revolutions. The behavior of this point from  $t = 0$  for approximately five revolutions is shown in Figure 6.5.10. The temperature change per revolution found for this solution is similar to that found in Figure 6.5.3. In Figure 6.5.10 the minimum and maximum temperature values are increasing during each revolution, as would be expected. The increases are a couple of degrees Centigrade per revolution at this point in the solution. This increase per revolution would continue until the steady state response shown in Figure 6.5.3 is reached.

## REFERENCES

- [6.1] Rating the Pitting Resistance and Bending Strength of Generated Straight Bevel, ZEROL, Bevel, and Spiral Bevel Gears. American Gear Manufacturer's Association Standard, ANSI/AGMA 2003-A86, June 1988.
- [6.2] Litvin, F.; and Zhang, Y.: Local Synthesis and Tooth Contact Analysis of Face-Milled Spiral Bevel Gears. NASA CR-4342, 1991.
- [6.3] Litvin, F.; Zhang, Y.; and Chen, J.: User's Manual For Tooth Contact Analysis of Face-Milled Spiral Bevel Gears With Given Machine Tool Settings. NASA CR-189093, 1991.
- [6.4] Handschuh, R.; and Litvin, F.: A Method for Determining Spiral Bevel Gear Tooth Geometry for Finite Element Analysis. NASA TP-3096, 1991.
- [6.5] Handschuh, R.; and Litvin, F.: How to Determine Spiral Bevel Gear Tooth Geometry for Finite Element Analysis. NASA TM-105150, 1991.
- [6.6] Frint, H.: Automated Inspection and Precision Grinding of Spiral Bevel Gears. NASA CR-4083, 1987.
- [6.7] Frint, H.; and Glasow, W: Enhanced Automated Spiral Bevel Gear Inspection. NASA CR-189125, 1992.
- [6.8] Goldrich, R.: Theory of 6-Axis CNC Generation of Spiral Bevel and Hypoid Gears. The Gleason Works, Rochester, NY, 1989.
- [6.9] Scott, H.: Computer Numerical Control Grinding of Spiral Bevel Gears. NASA CR-187175, 1991.
- [6.10] Handschuh, R.; and Bill, R.: Recent Manufacturing Advances for Spiral Bevel Gears. NASA TM-104479, 1991.

TABLE 6.4.1—DESIGN DATA AND MACHINE TOOL SETTINGS FOR  
SPIRAL BEVEL PINION UNDER STUDY

(a) Pinion design data

Number of teeth	
Pinion	12
Gear	36
Dedendum angle, deg	1.0
Addendum angle, deg	3.883
Pitch angle, deg	18.433
Shaft angle, deg	90.0
Mean spiral angle, deg	35.0
Face width, mm (in.)	25.4 (1.0)
Mean cone distance, mm (in.)	81.05 (3.191)
Inside radius of gear blank, mm (in.)	15.3 (0.6094)
Top land thickness, mm (in.)	2.032 (0.080)
Clearance, mm (in.)	0.762 (0.030)
Contact orientation, deg	70

(b) Generation machine settings

	Concave	Convex
Radius of cutter, $r$ , mm (in.)	73.687 (2.9011)	76.539 (3.0133)
Blade angle, $\psi$ , deg	159.0	26.0
Vector sum, $L_m$ , mm (in.)	0.7622 (0.03001)	0.1435 (0.0056)
Machine offset, $E_m$ , mm (in.)	0.07233 (0.0028)	1.4382 (0.05662)
Cradle to cutter distance, $s_1$ , mm (in.)	70.245 (2.7655)	74.410 (2.9295)
Cradle angle, $q$ , deg	60.4899	57.1823
Ratio of roll, $m_{cw}$	0.325169	0.315069
Initial cutter length, $u$ , mm (in.)	229 (9.0)	178 (7.0)
Initial cutter orientation, $\theta$ , deg	120.0	120.0
Initial cradle orientation, $\phi_c$ , deg	0.0	0.0

TABLE 6.4.2—ELLIPSE SIZE AND MAXIMUM CONTACT PRESSURE  
AS A FUNCTION OF ELLIPSE NUMBER AND CONTACTING

GEAR MESH SURFACE GEOMETRY

Ellipse number	Principal curvatures, mm				Curvature orientation, deg	Normal load, N	Ellipse half-lengths, mm		Maximum contact pressure, MPa
	Pinion		Gear				Major	Minor	
1	-85.6	12.2	119.1	73.2	-61.7	8 789	6.96	0.33	1777
2	-85.9	13.0	118.9	73.2	-61.0	8 826	6.93	.36	1737
3	-86.1	13.7	118.4	72.9	-60.4	8 863	6.91	.36	1702
4	-86.4	14.5	117.9	72.9	-59.7	17 803	8.69	.46	2103
5	-86.6	15.2	117.6	72.6	-59.1	17 883	8.69	.48	2066
6	-86.9	16.0	117.3	72.4	-58.4	17 966	8.66	.48	2033
7	-87.1	16.5	116.8	72.4	-57.7	18 051	8.64	.51	2003
8	-87.4	17.3	116.6	72.1	-57.0	18 138	8.61	.51	1975
9	-87.6	18.0	116.3	71.9	-56.4	18 228	8.59	.51	1949
10	-87.9	18.8	116.3	71.6	-55.7	18 320	8.59	.53	1926
11	-88.1	19.6	116.1	71.4	-55.1	18 415	8.56	.53	1905
12	-88.4	20.3	115.8	71.1	-54.4	18 513	8.53	.56	1885
13	-88.6	20.8	115.8	71.1	-53.8	9 306	6.76	.46	1482
14	-88.9	21.6	115.6	70.9	-53.1	9 357	6.76	.46	1469
15	-89.2	22.4	115.6	70.4	-52.5	9 409	6.73	.46	1457

TABLE 6.4.3—NUMBER OF GRID  
POINTS AND TOTAL HEAT

FLUX FOR MODEL

ELLIPSES

Ellipse number	Number of grid points within ellipse	Total heat flux of ellipse, W
1	24	260.3
2	25	144.0
3	27	36.1
4	42	168.3
5	41	414.3
6	41	644.0
7	45	860.9
8	47	1068.1
9	47	1257.7
10	47	1445.0
11	48	1621.9
12	50	1788.4
13	28	714.4
14	31	765.0
15	31	816.4

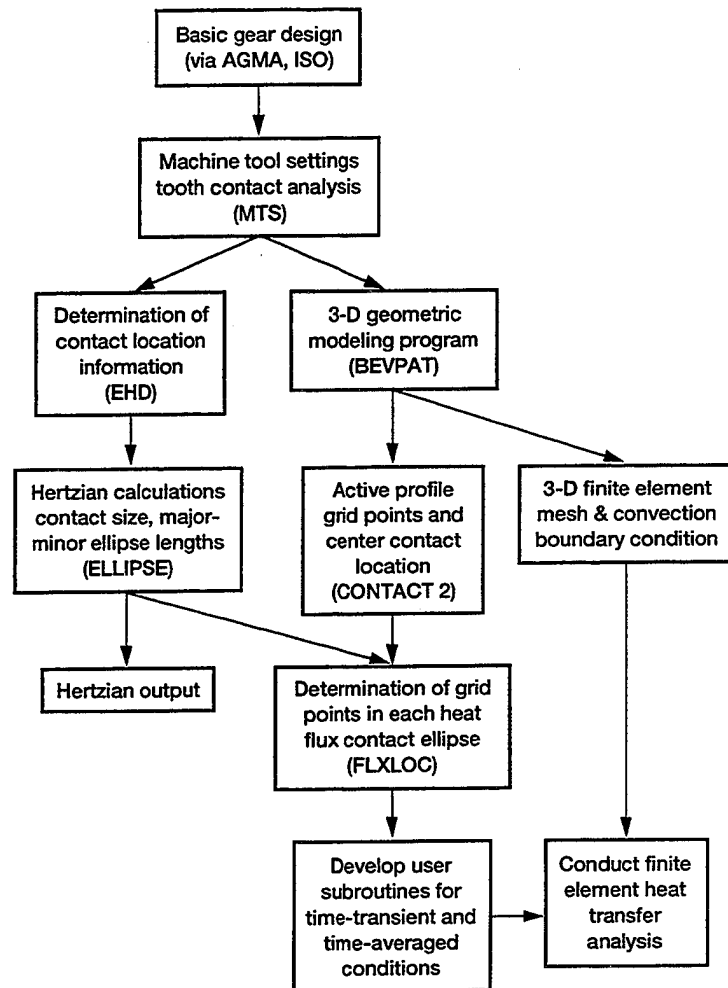


Figure 6.1.1.—Flow chart of analysis procedure for three-dimensional time transient or time-averaged heat transfer analysis.

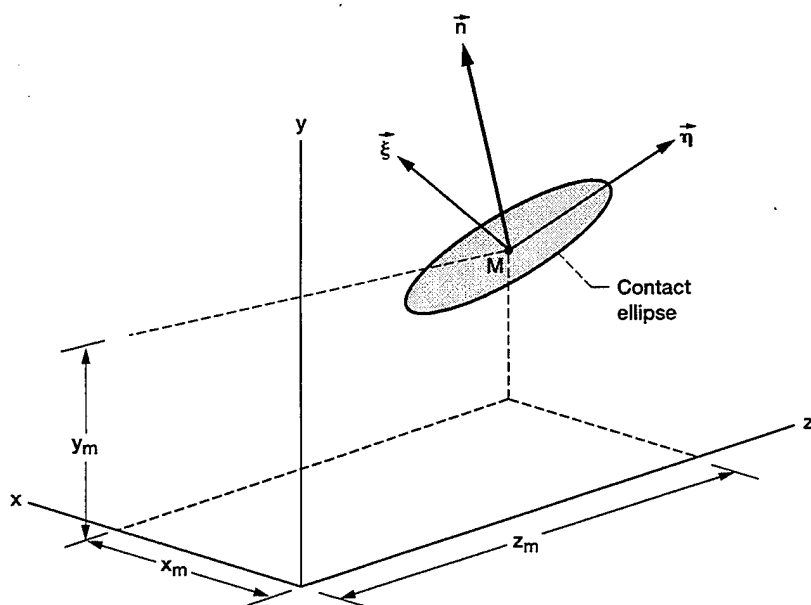


Figure 6.2.1.—Contact ellipse in three-dimensional space, coordinate system fixed to gear member under consideration.

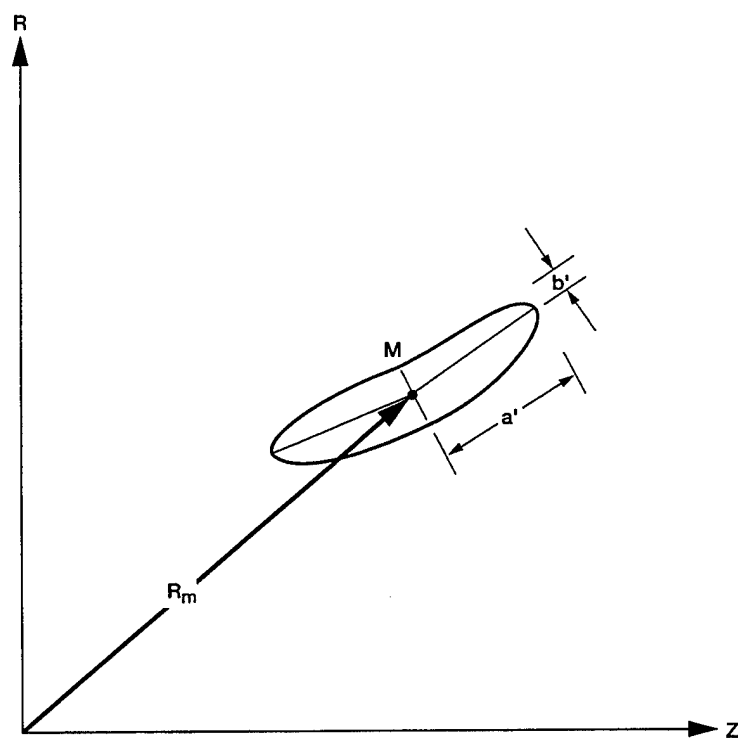


Figure 6.2.2.—Contact ellipse projection in radial-axial plane showing "bent" characteristic when projected.

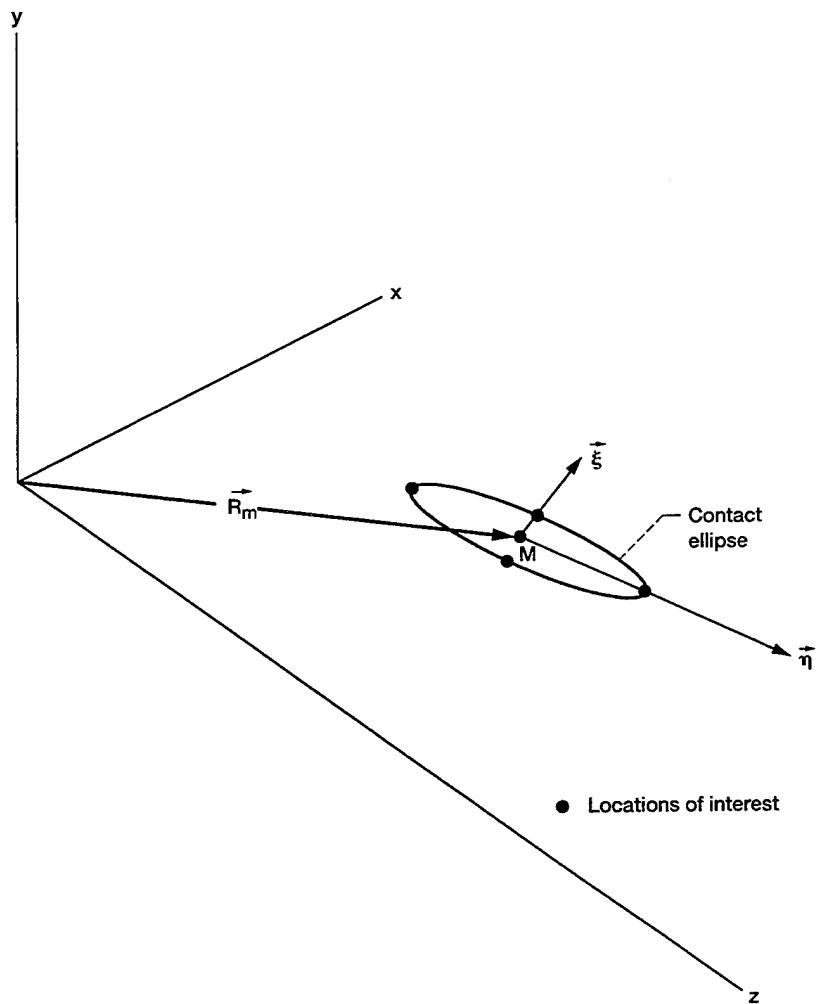
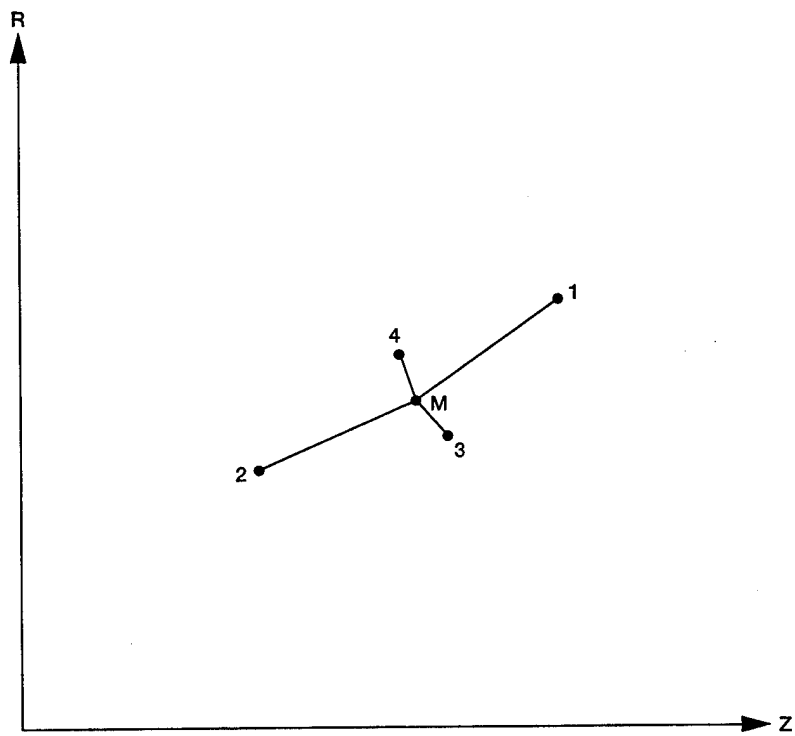


Figure 6.2.3.—Contact ellipse local coordinates with respect to gear fixed coordinates showing ellipse extreme locations of interest.



Points 1, 2: Major ellipse axis extremes  
 Points 3, 4: Minor ellipse axis extremes  
 Point M: Center of contact

Figure 6.2.4.—Ellipse extreme projections in radial-axial plane.

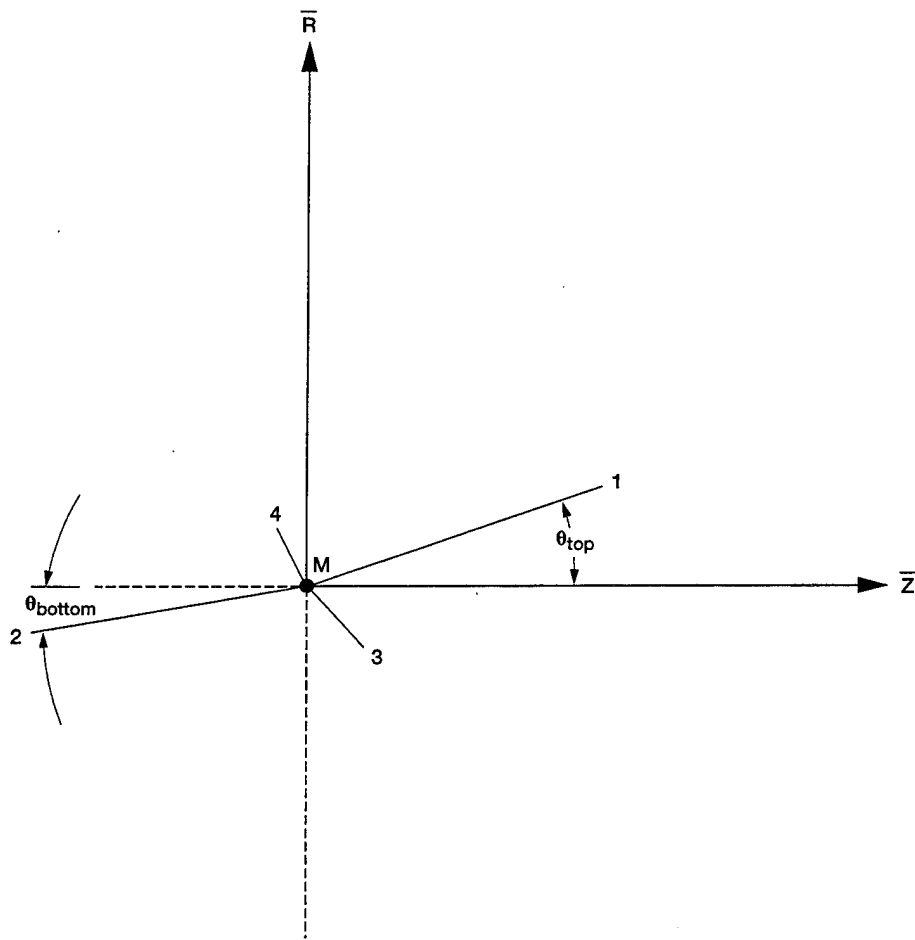


Figure 6.2.5.—Coordinate system that is centered at ellipse mean contact point.

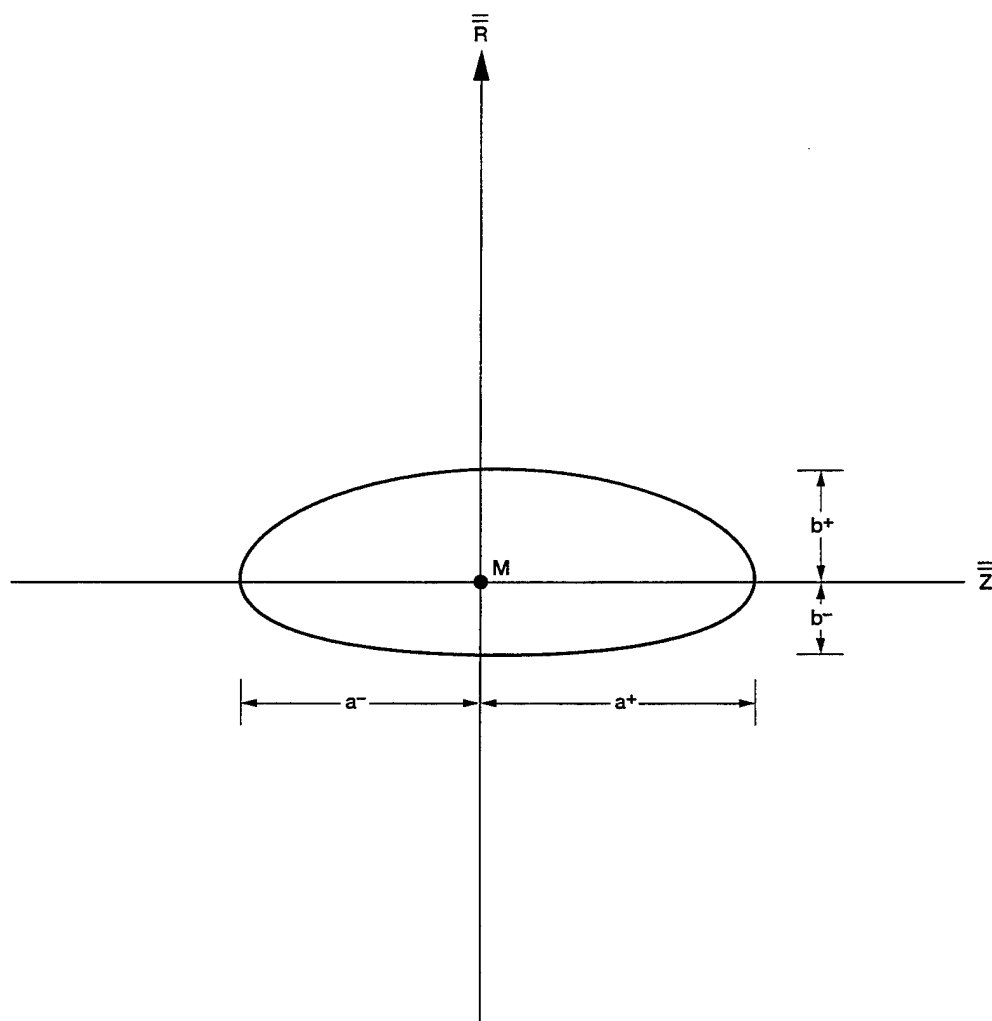


Figure 6.2.6.—Ellipse projections in localized coordinate system for determination of grid point (finite element model) status.

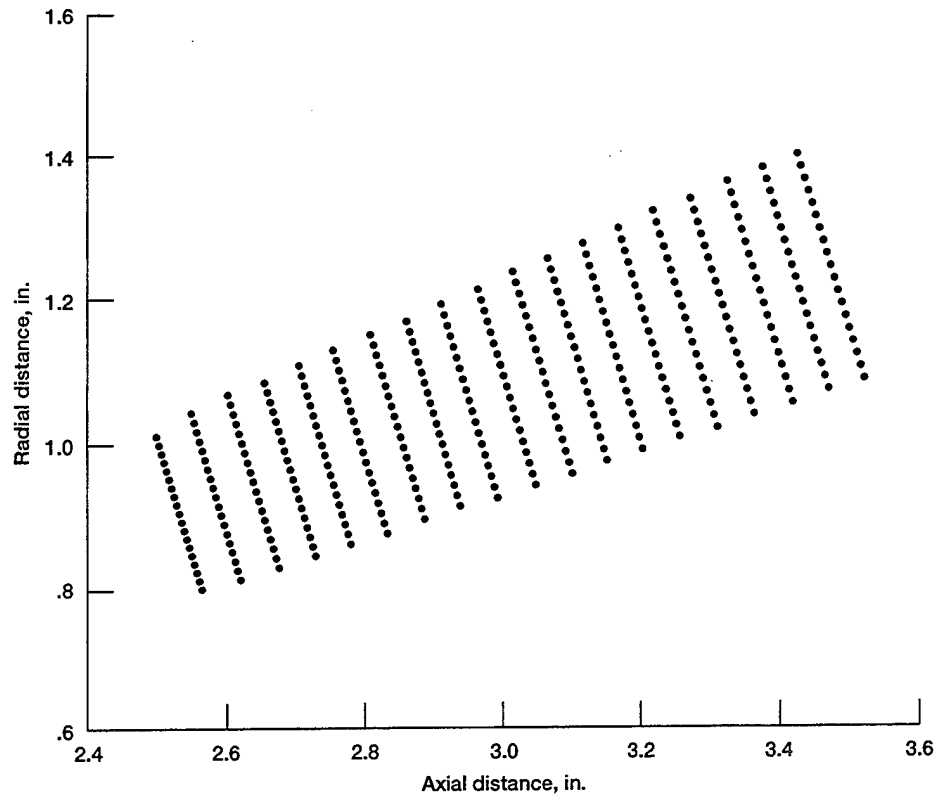


Figure 6.2.7.—Finite element grid points from active profile of model in radial-axial plane.

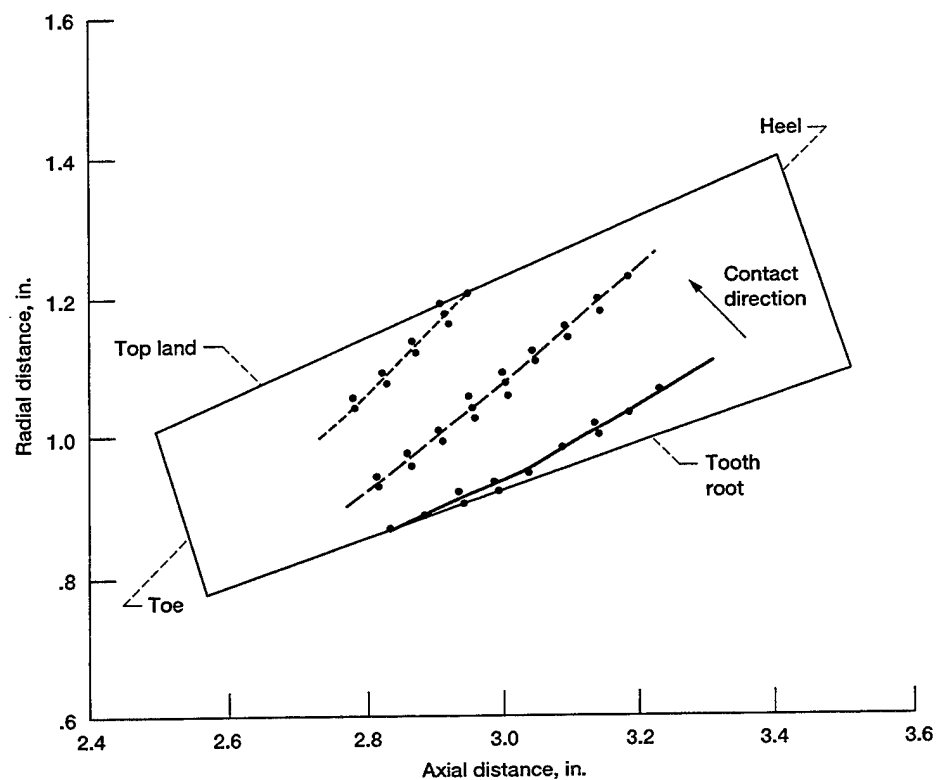


Figure 6.2.8.—Contact ellipse major axis projections and grid points found within projected ellipse boundaries for three ellipse positions.

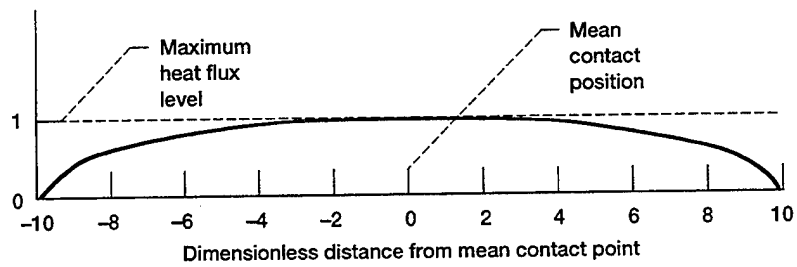


Figure 6.3.1.—Heat flux profile chosen for distribution to grid points.

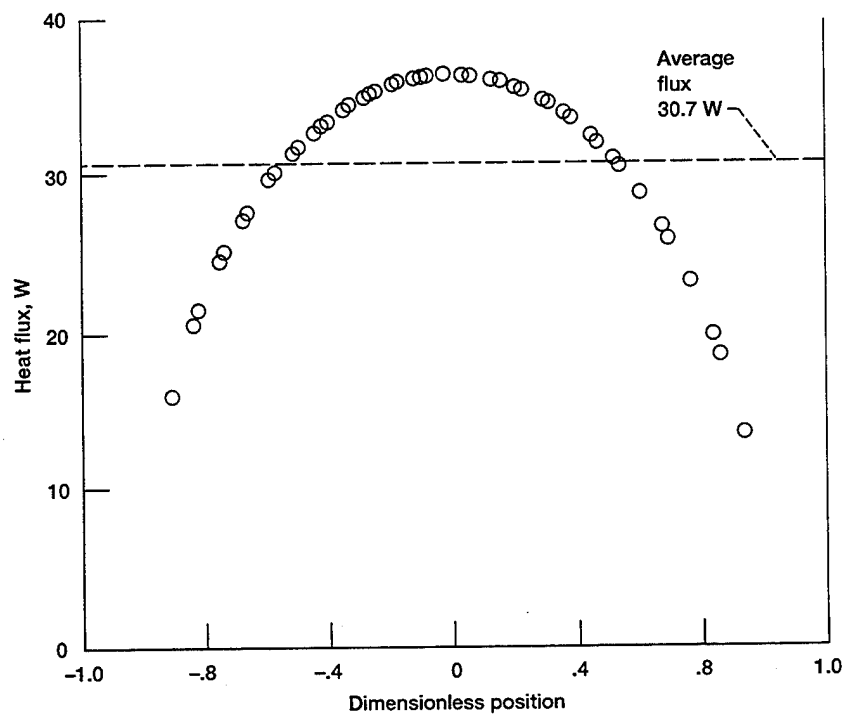


Figure 6.3.2.—Heat flux distribution based on 10:1 ratio for ellipse #10. This ellipse has 47 grid points within boundaries.

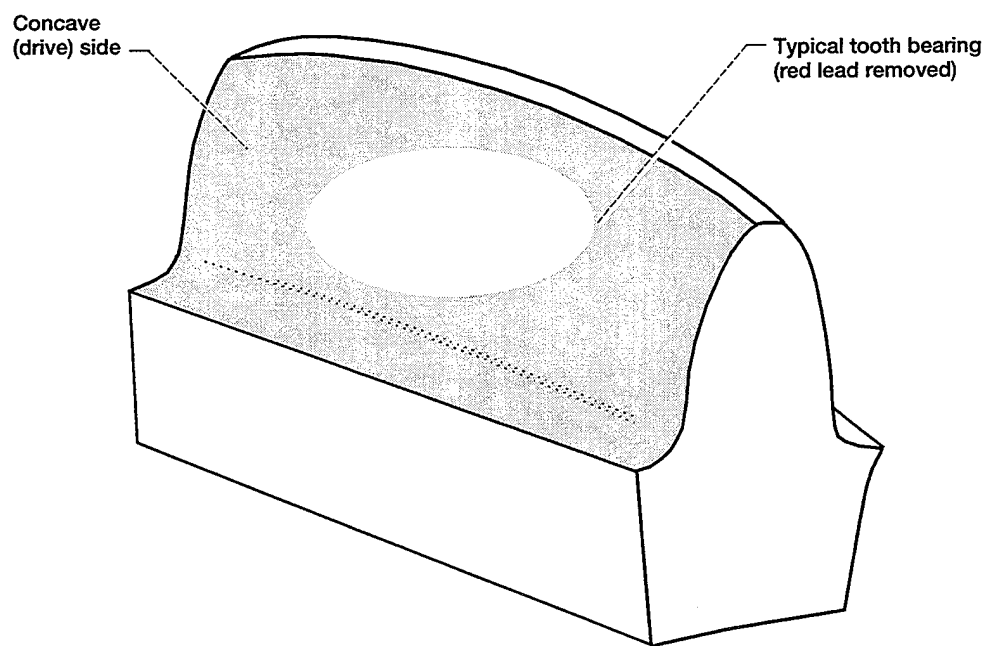


Figure 6.4.1.—Sketch of typical tooth contact pattern attained from test hardware used in this study for the pinion.

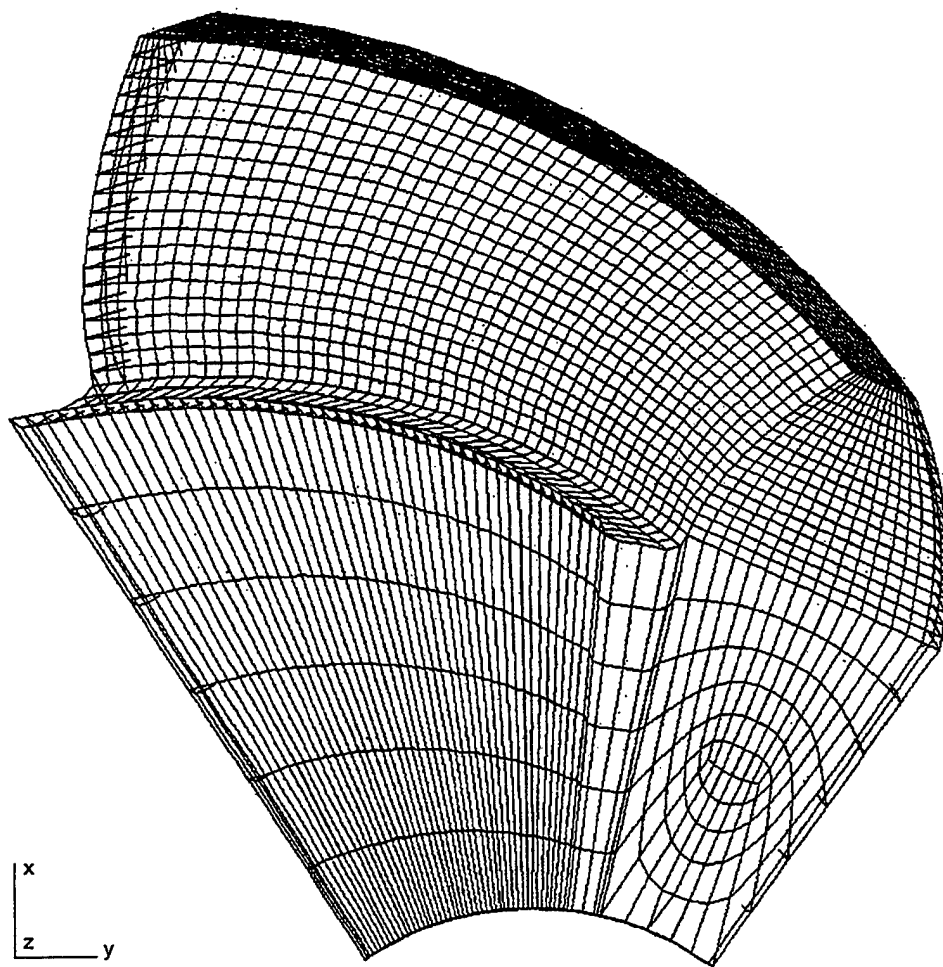


Figure 6.4.2.—Finite element model used for heat transfer study.

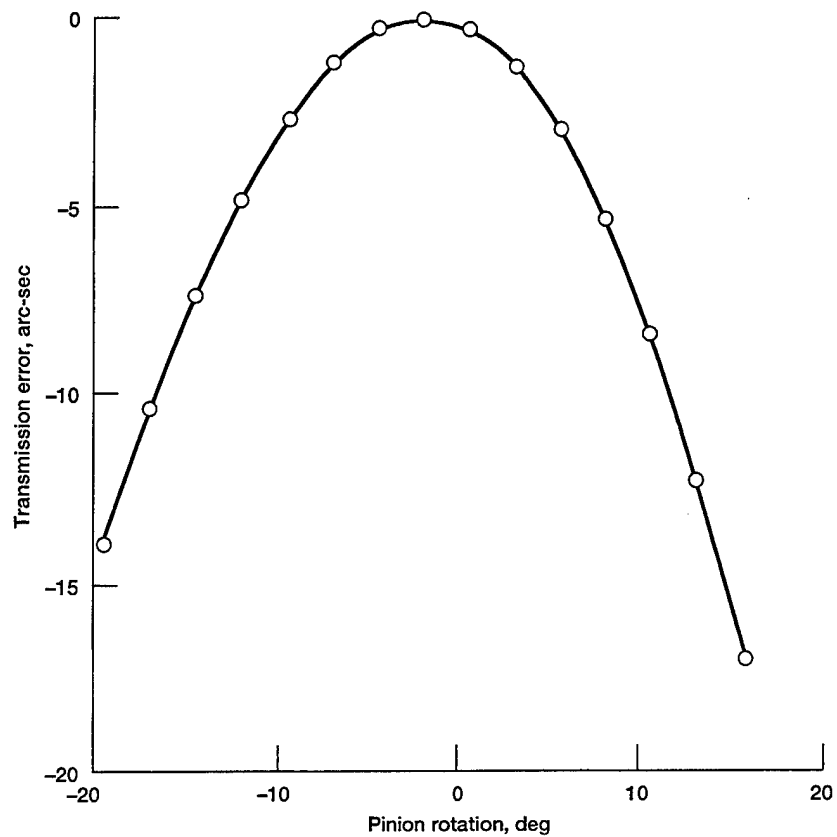


Figure 6.4.3.—Transmission error as a function of pinion rotation.

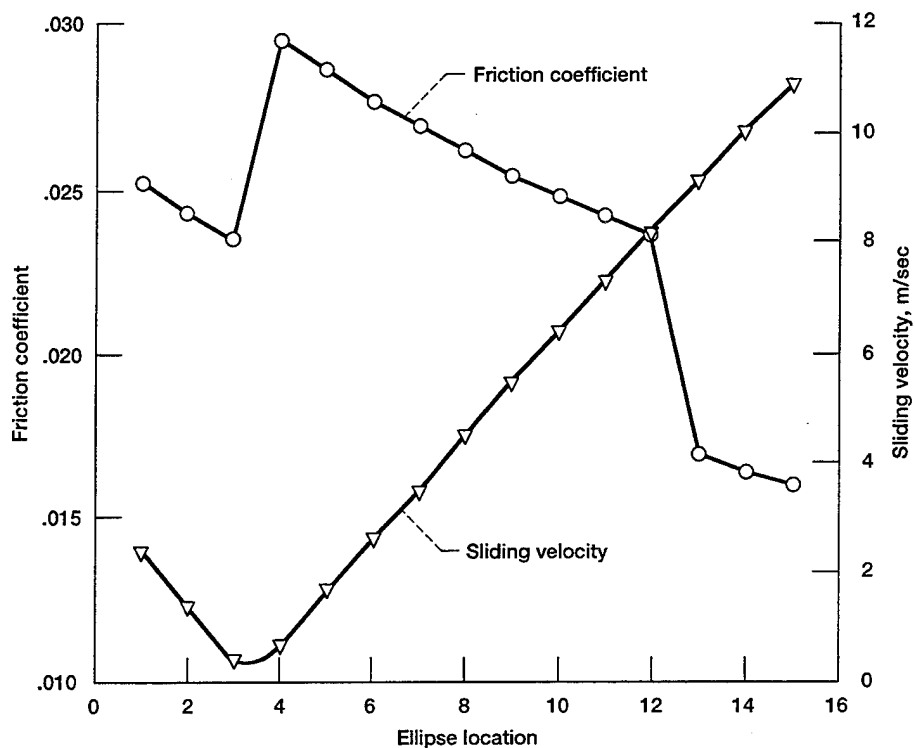


Figure 6.4.4.—Friction coefficient and sliding velocity as function of ellipse location.

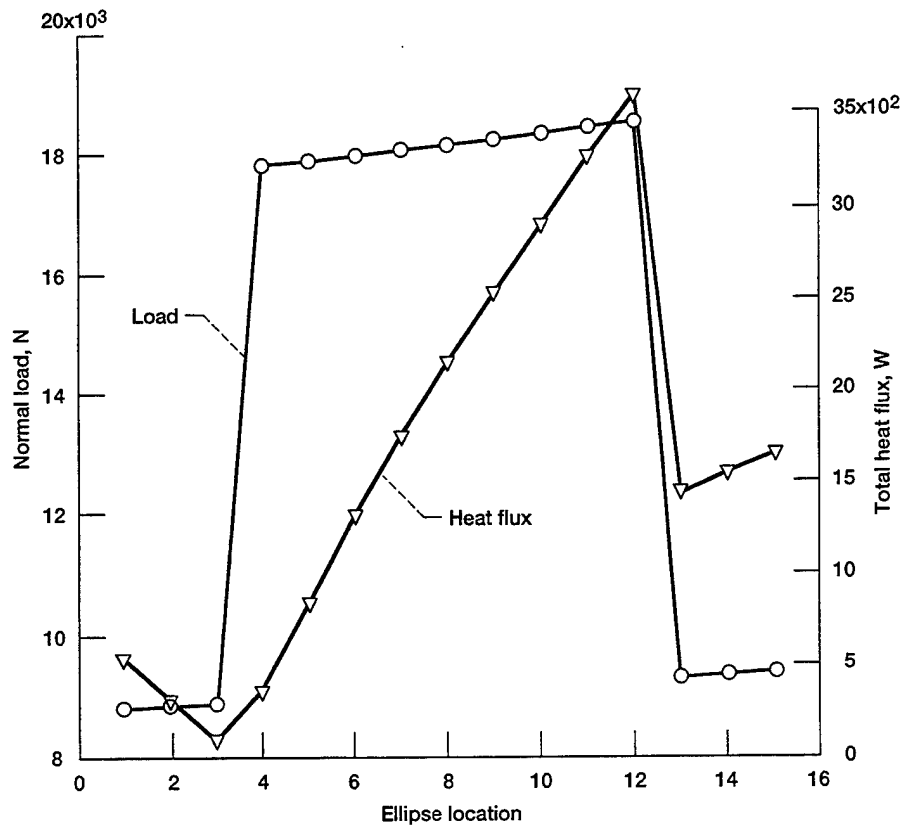


Figure 6.4.5.—Load and heat flux as a function of ellipse location.

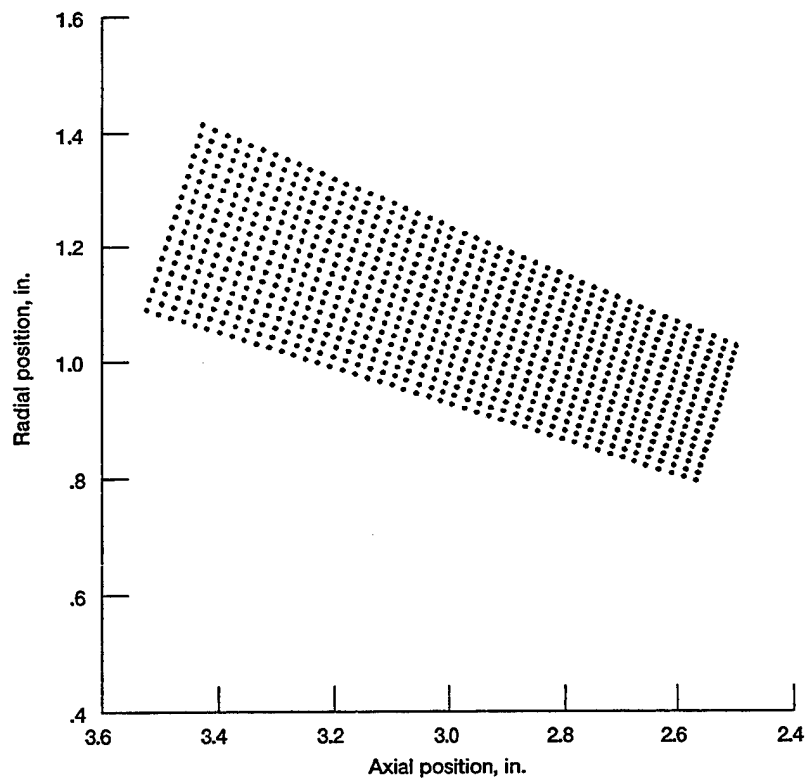


Figure 6.4.6.—Radial-axial plane of active profile grid points from the finite element model.

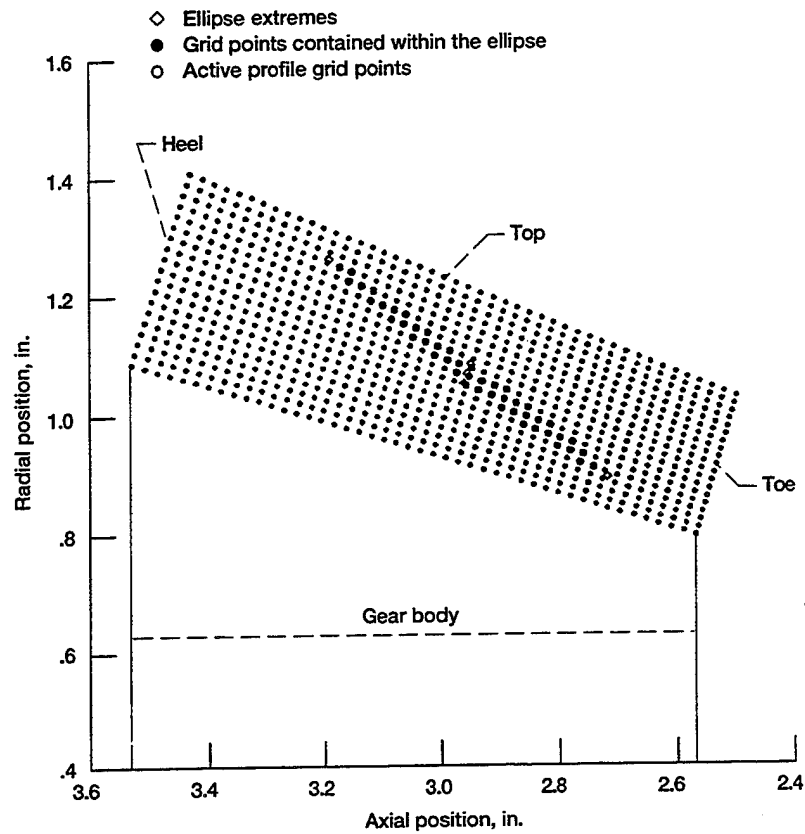


Figure 6.4.7.—Contact ellipse number 10 of 15, shown plotted on the entire active profile grid.

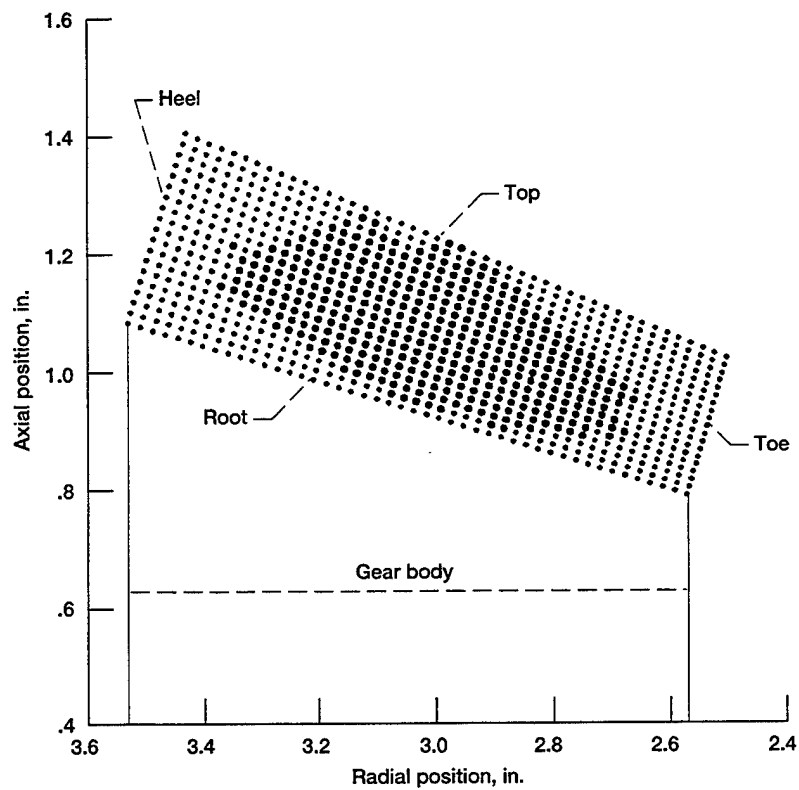


Figure 6.4.8.—Composite of all active profile grid points that have heat flux applied (darker symbols).

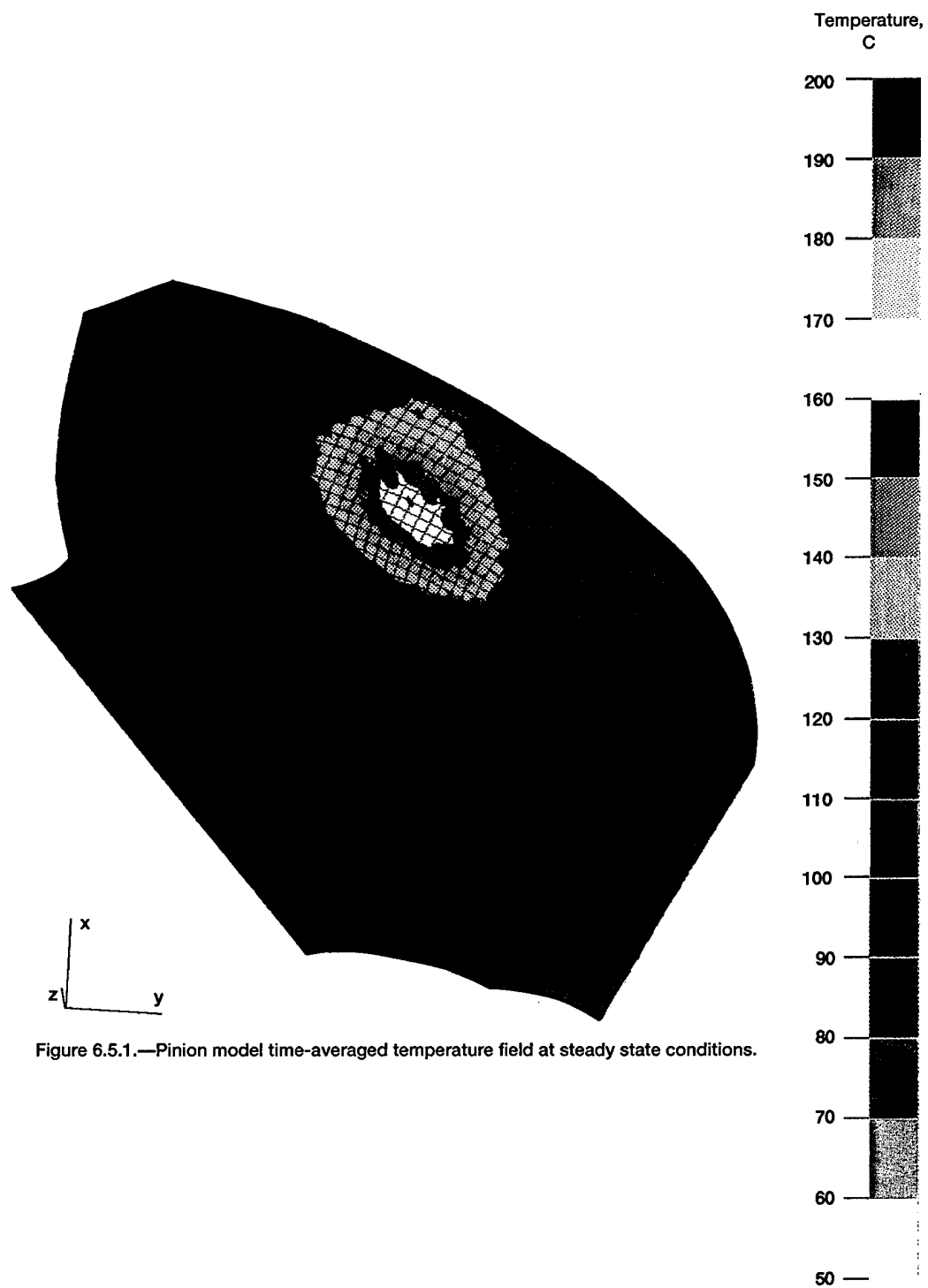


Figure 6.5.1.—Pinion model time-averaged temperature field at steady state conditions.

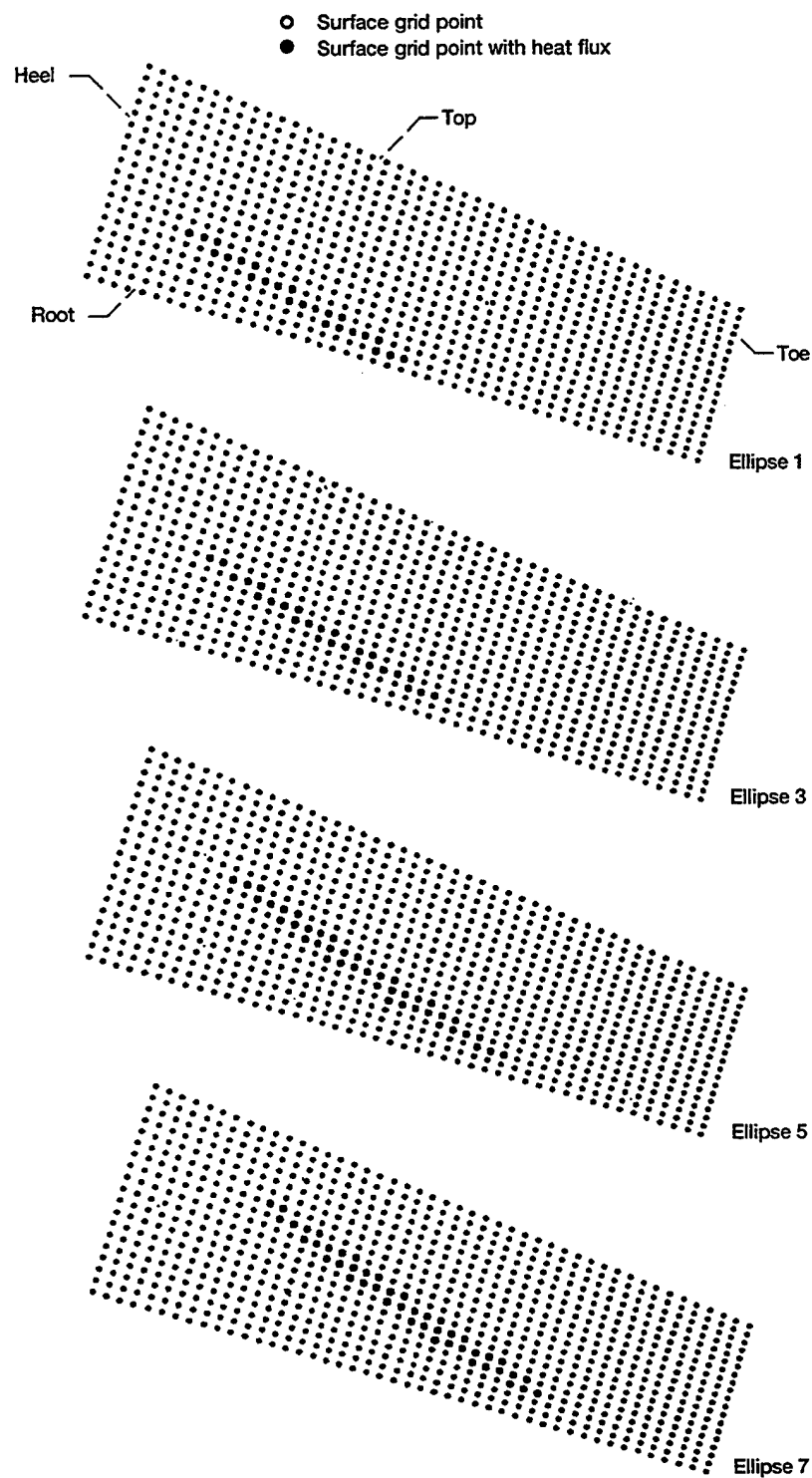


Figure 6.5.2a.—Pinion model showing contact locations for ellipses 1, 3, 5 and 7.

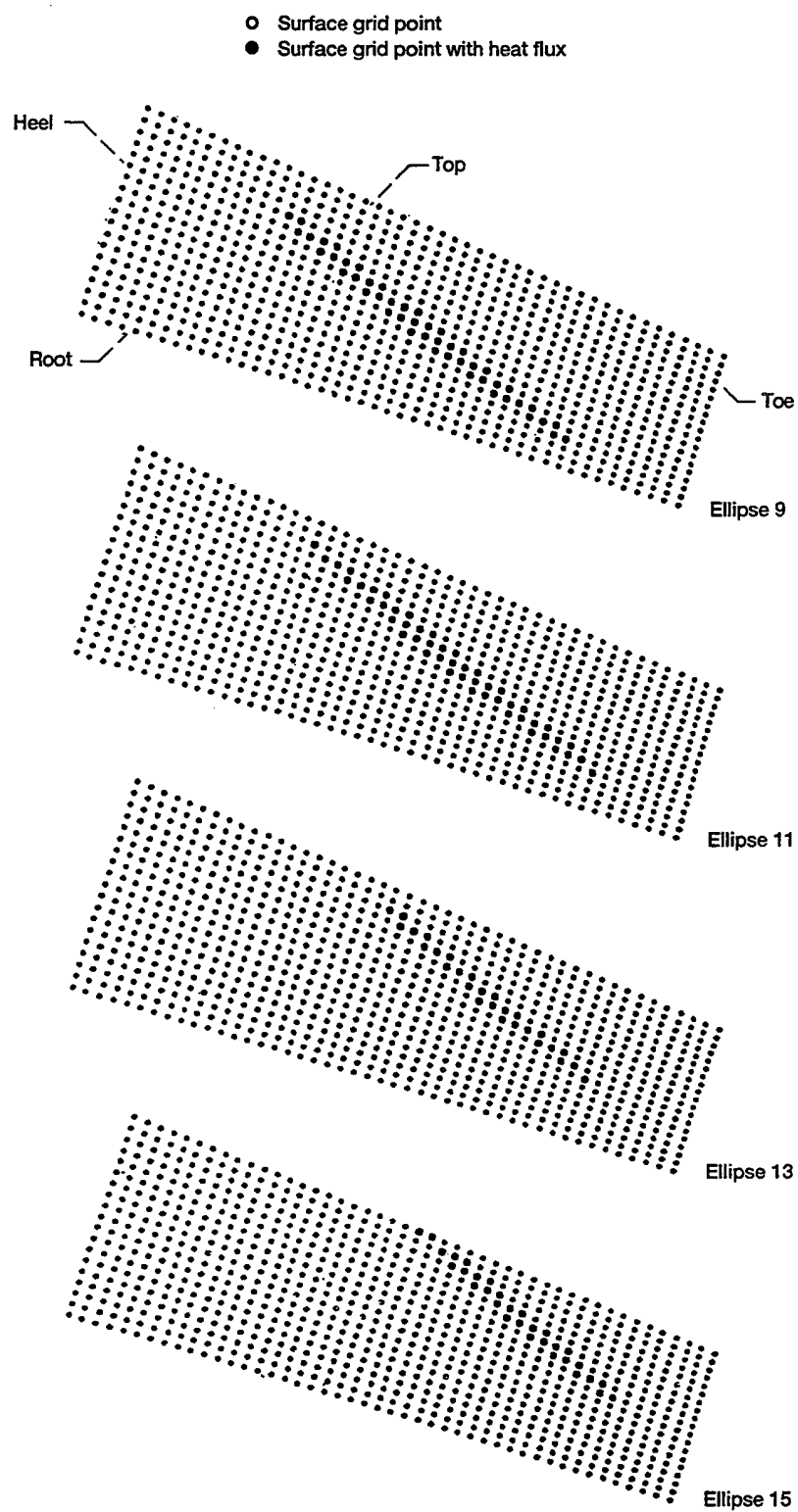


Figure 6.5.2b.—Pinion model showing contact locations for ellipses 9, 11, 13, and 15.

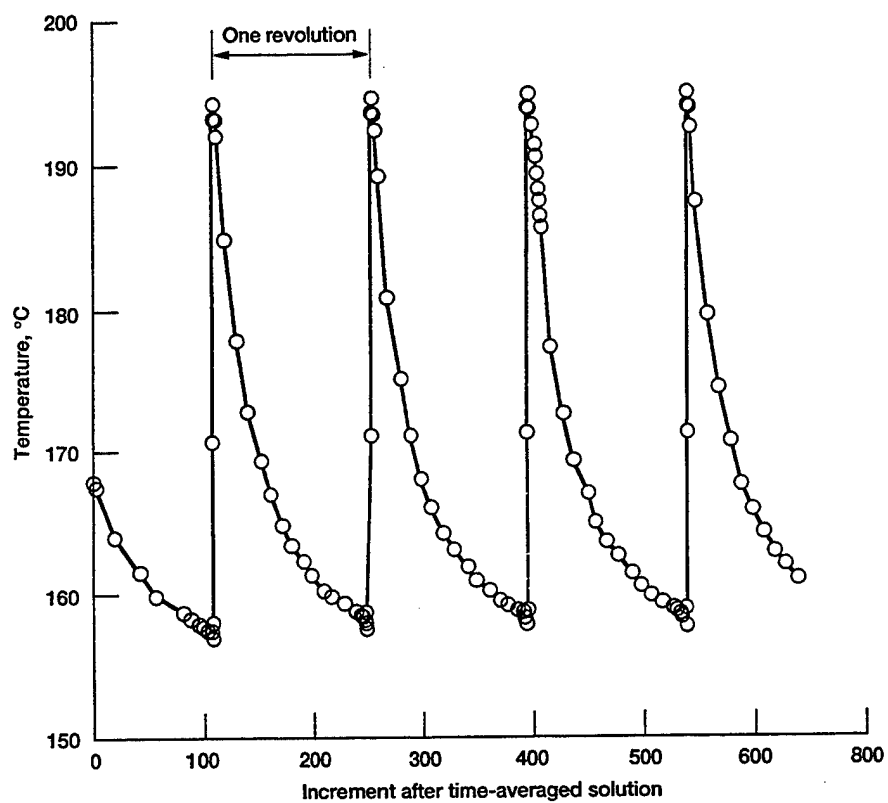
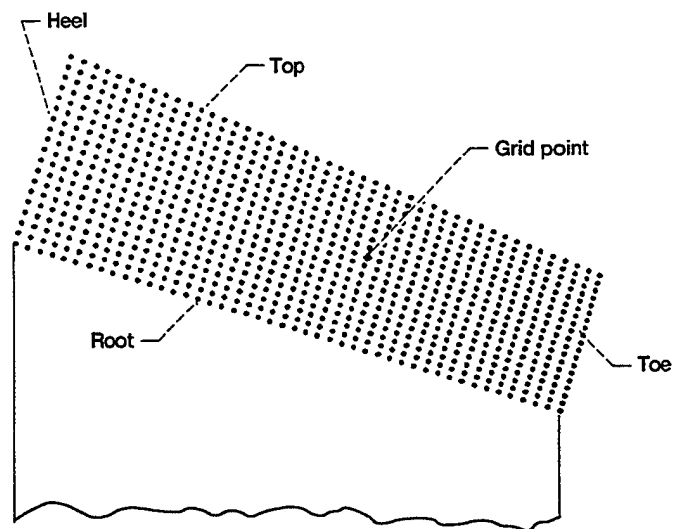


Figure 6.5.3.—Active profile grid point location and temperature transient.

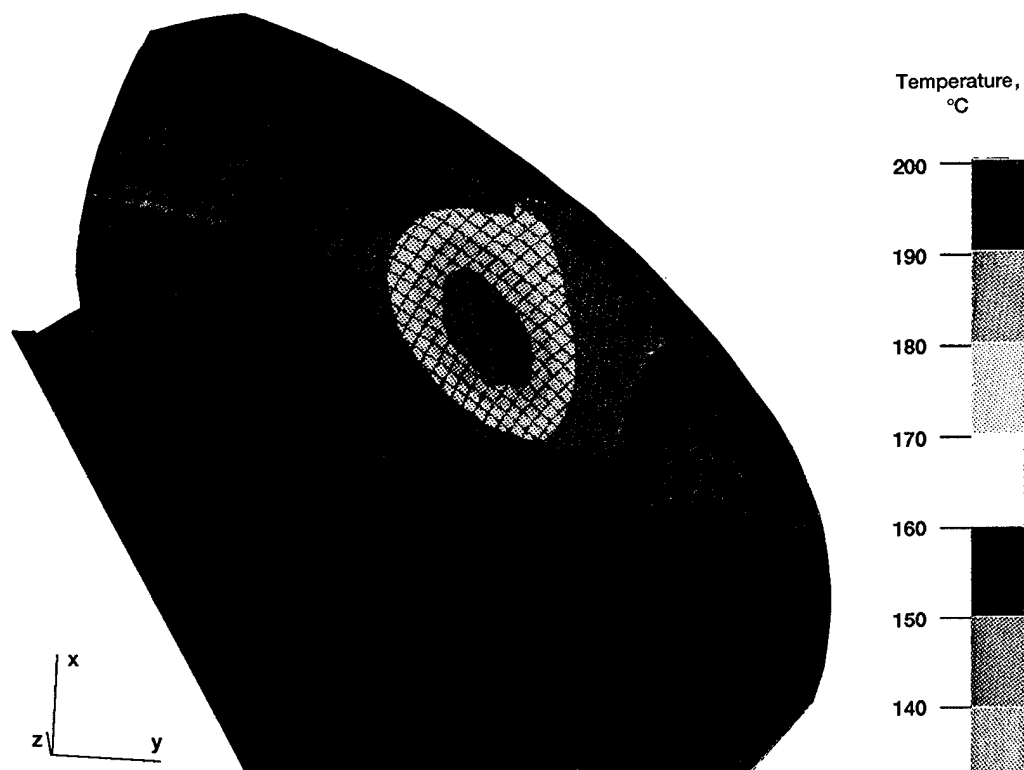


Figure 6.5.4.—Just before heat flux increments are applied to the model.

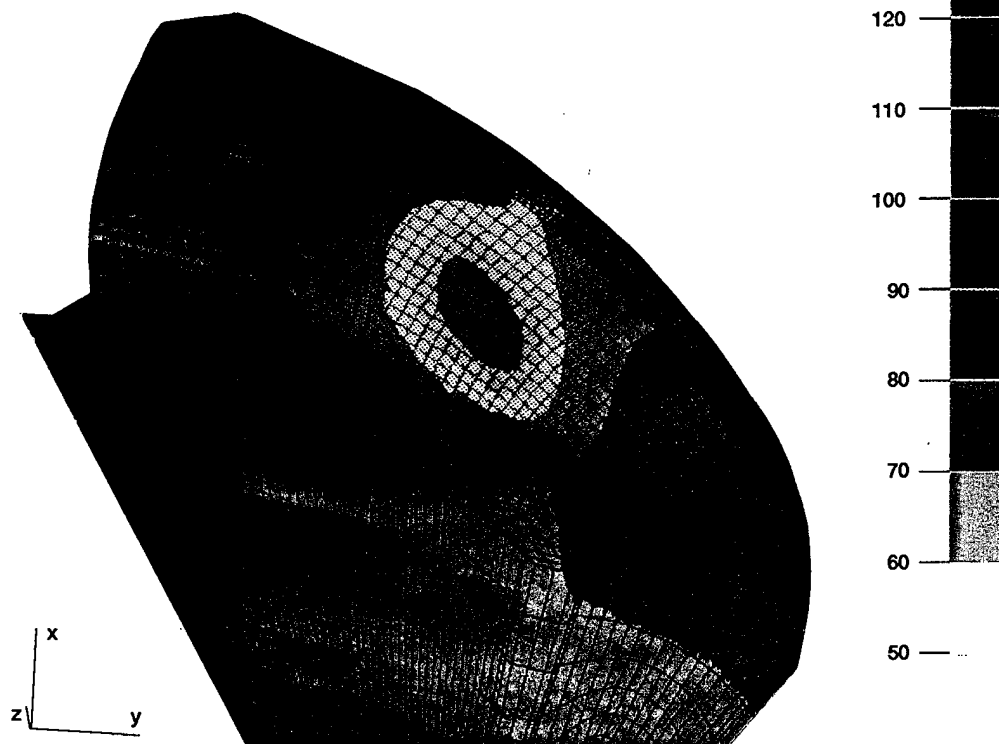


Figure 6.5.5.—Heat flux increment 5.



Figure 6.5.6.—Heat flux increment 10.

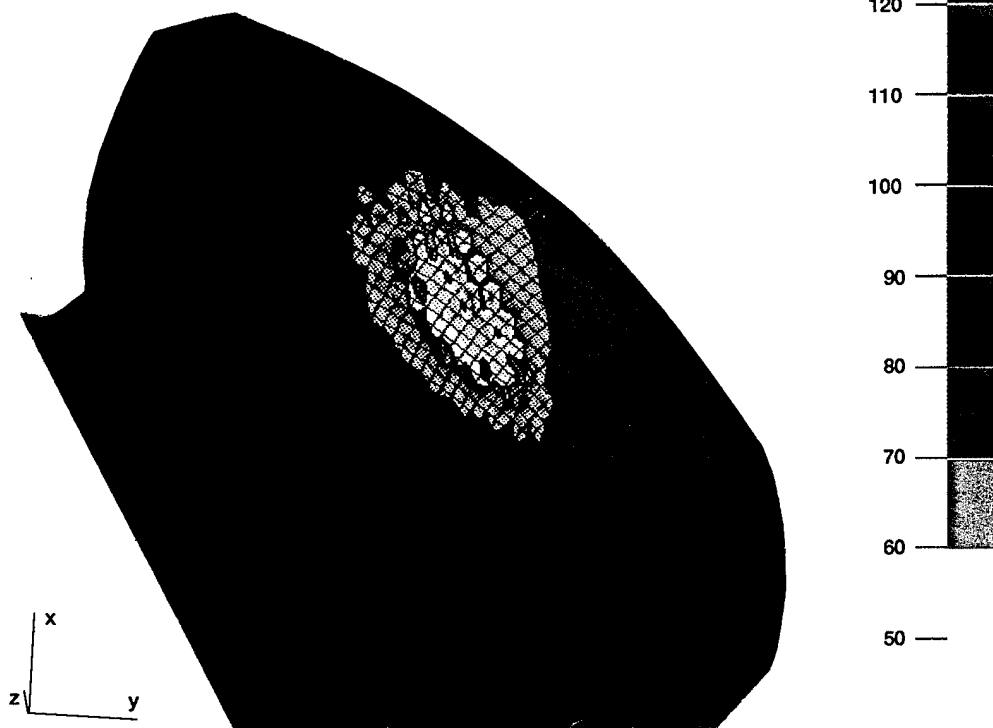


Figure 6.5.7.—Heat flux increment 13.

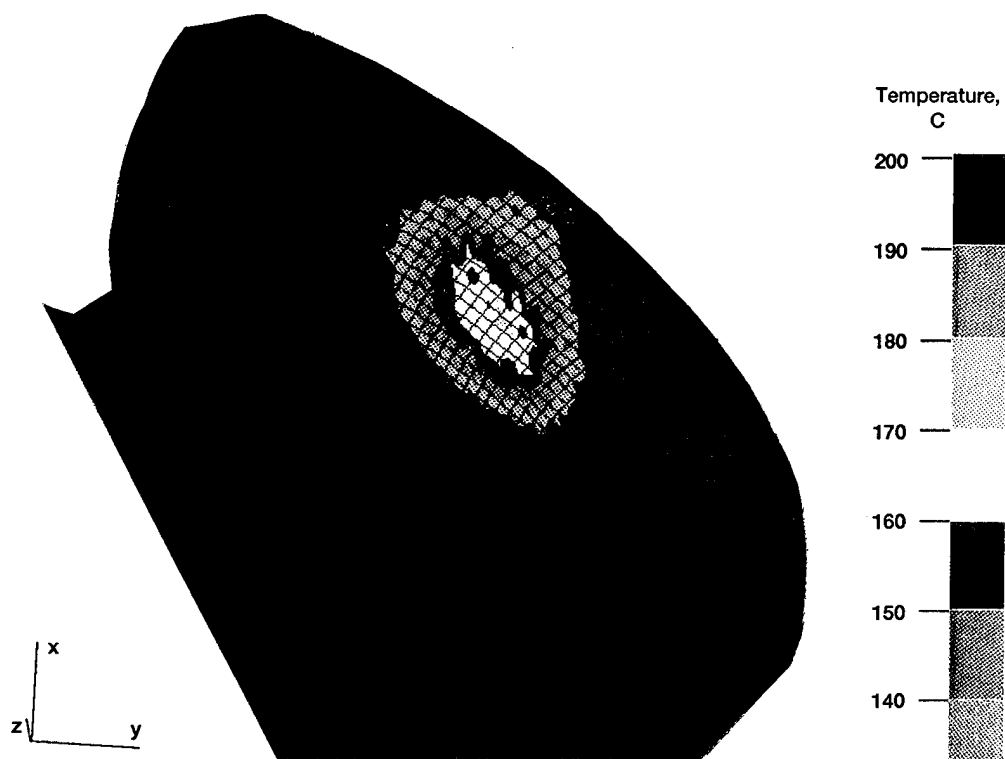


Figure 6.5.8.—Temperature field 70° rotation after the last heat flux.

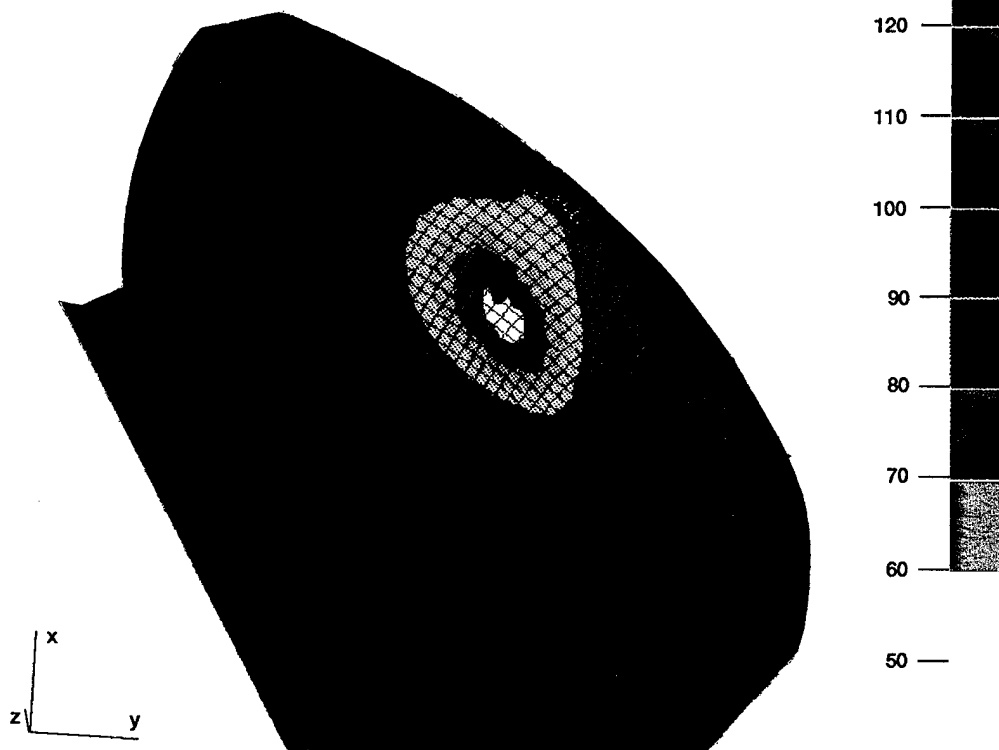


Figure 6.5.9.—Temperature field 195° rotation after the last heat flux.

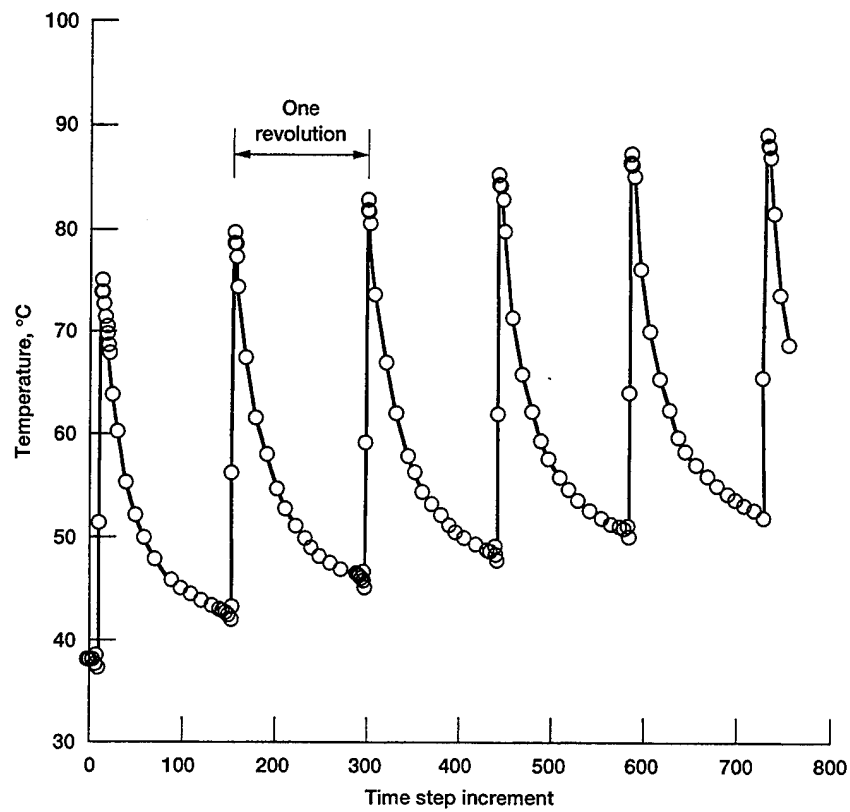


Figure 6.5.10.—Active profile grid point temperature from  $t = 0$  sec.

## CHAPTER 7: COMPARISON OF EXPERIMENTAL AND ANALYTICAL RESULTS

### 7.1 Introduction

In this chapter the experimental and analytical results are compared. This comparison serves as a check of some of the assumptions made and provides the opportunity to fine-tune the model.

A comparison of the time-averaged finite element analysis with the bulk thermocouple measurements is made. Also, the output from the analysis is compared with the infrared data relative to the rotational position where the measurement was made. The last comparison is of the flash temperature calculation with the results of other studies. Finally, some recommendations are made to improve experimental and analytical results.

### 7.2 Comparison of Measured and Calculated Results

Comparisons of the experimental and analytical results obtained in this study are now made. The bulk thermocouple pinion data (Chap. 3) are compared with the time-averaged finite element solution (Chap. 6). Then the infrared data are compared with the time- and position-varying analytical results.

**Time-Averaged Results:** The time-averaged results are used for comparison with the bulk thermocouple measurements. From the analysis, it was observed that the tooth extremities did not vary in temperature during the time-and-position boundary condition part of the solution. Only the active profile was affected by the rapidly moving heat flux. The boundary conditions at the full load and speed conditions were used to apply the necessary thermal boundary conditions with respect to heat transfer coefficients and the heat flux. If different speed and load conditions were desired, then the majority of the computer programs shown in Figure 6.1.1 would have to be rerun with the new speed and load conditions. Also, the estimation of the heat transfer coefficients would have to be recalculated.

The test position data that the time-averaged mode are compared with were for two of the positions from Figure 3.8.4. The data used for this purpose were when the fan jet was positioned at 90° before mesh on the gear and at the into-mesh position (positions 3 and 4, respectively, from Fig. 3.8.4). The oil inlet temperature was 38 °C (100 °F) for both experiments, and the jet pressures were 1.38 and 0.34 MPa (200 and 50 psi), respectively.

The time-averaged solution results produced with the boundary conditions described in Chapters 5 and 6, along with three other variations, were used for comparison. Modifications to the boundary conditions were with respect to heat transfer coefficients and ambient (air-oil mist) surrounding temperatures.

The comparison is shown in Figure 7.2.1. The data are plotted with respect to the bulk thermocouple location. The analytical results were found by viewing the three-dimensional surface temperature output. The symbols connected by lines are the experimental results. The range of analytical adjustments bracket the experimental results.

For the experimental data of lubricating into the mesh at 0.34 MPa (50 psi), the original boundary conditions, speed and load (as used in the Chap. 6 analysis), produced similar results except at the heel position. The temperatures at the other three locations were within 4 percent of each other. At the heel, the experimental value was 21 percent greater than the analytical result. This effect is attributed to the lubricant jet location. Other

results of Chapter 3, where the lubricating jet was positioned on the pinion, also exhibited a similar effect where the heel position was at a higher temperature than the toe or root bulk temperatures.

For the condition of lubricating the gear member 90° before mesh, two of the analytical variations produced similar results. When the experimental results are compared with these two analytical results, the root and heel locations indicated differences as high as 10 percent. The tooth top and toe locations for both analyses were within 1 percent of the experimentally measured temperature.

Therefore, the results using the different boundary condition assumptions for the heat transfer coefficient-ambient temperature conditions bracketed the two sets of experimental data with which they were compared. Further changes to the analysis boundary conditions could possibly improve the correlation further.

Comparisons with other bulk temperature measurements would require adjustments and possibly additions to the boundary conditions applied. One of the more difficult additions would be modeling the jet spraying directly on the gear being analyzed. Instead of having just a heat flux source, this case would create a heat flux sink and would have to be modeled as having a very high heat transfer coefficient to the surface while it passed beneath the lubricating jet. Then the heat transfer coefficient would change to some lesser value, which could be handled within the user subroutine as documented in Appendix C.

**Comparison of Time- and Position-Varying Analysis Results With Infrared Microscope Data:** The time- and position-varying analytical predictions are compared with the infrared microscope data obtained. These data serve to establish the temperature gradient across the tooth at a rotational distance away from the meshing location.

The results from the model of Chapter 6 are used. The analysis showed that when a heat flux passes over them, a substantial temperature change is experienced by the grid points on the active profile. The temperature field over the active profile varies during the entire revolution but it is repeatable. The analysis predicted a temperature gradient over the profile and gear body because the gear does not return to some common bulk temperature before the next meshing cycle. Therefore, there are temperature gradients that vary over the rotational position, and an infrared microscope can capture these changes as was documented in Chapter 3.

When the comparison is made in this section, the following must be kept in mind: the transient infrared measurement did not pass over the region of the tooth that would have the highest heat flux as predicted by the analysis, as can be seen by comparing Figure 3.9.5 with Figure 6.5.1. The infrared microscope was not located at the point where a maximum temperature of the surface would pass. However, the measurement serves as a verification of the analytical model and boundary conditions.

The time- and position-varying boundary conditions in this study were only applied to one case of the model contained in Chapter 6 because of the computer time required. Therefore, the effects of speed and load are not presented analytically because the most important case is when the conditions are the maximum for some given design.

The infrared microscope data used for the comparison were for a fan jet lubricating on the gear 90° before mesh. The oil inlet temperature was 38 °C (100 °F) and the jet pressure was 1.40 MPa (203 psi). The maximum voltage differential, adjusted for sapphire lens attenuation, was 0.115 V. The infrared data as taken during the experiment are shown in Figure 7.2.2.

Next, while obtaining the time- and position-varying results, the analytical data are viewed at a position that coincides with the location where the infrared measurement was made, at 48 increments, 2.5° rotation per increment, past the last heat flux increment due to meshing. Using the data from Figure 3.9.5, which indicate the

path traversed during the infrared measurements, locations are approximated on the three-dimensional temperature field data at the 120° out-of-mesh position. The analytical prediction at the position of interest and the infrared microscope path are shown in Figure 7.2.3. The infrared path is the same as that shown in Figure 3.9.5. The temperature predicted by traversing from the root to tooth tip and to the next tooth repeating the process is shown in Figure 7.2.4. The maximum temperature differential over this path is approximately 37 °C (67 °F).

Before a comparison can be made, however, the root temperature used as a reference surface temperature in Chapter 3 (to determine the infrared measured temperature) was adjusted to match the analytical value at this point. In Chapter 3 the results of Tables 3.9.1 and 3.9.2 assumed that the root temperature was the reference temperature. Based on Figure 7.2.3, in the root region the temperature was 95 °C (203 °F). Next, the temperature differential based on the adjusted voltage differential is found (see Fig. 7.2.5). The varying adjusted voltage differential was found for over 30 locations for a 30° rotation from the data as shown in Figure 7.2.2. The adjusted radiance was calculated (see Chapter 3) and then the temperature was calculated based on the varying radiance from the reference temperature at 95 °C (203 °F). The result of this procedure is shown in Figure 7.2.6.

Finally, the analytical prediction and the experimental results are plotted together in Figure 7.2.7. The analytical and experimental results show the same trends, but some of the extreme temperature excursions measured were not produced analytically. As was mentioned in Chapter 3, no apparent reasonable explanation for the dramatic temperature decrease seen just prior to the active profile tooth top corner position could be given. The sudden decrease at this point is attributed to the tooth top land corner affecting the signal measured by the infrared microscope. In the analysis the slight decrease predicted was much less than the measured value. From Figure 7.2.7, the maximum difference between the results was approximately 10 percent, excluding the region associated with the top corner of the test hardware coming into view of the infrared microscope. A comparison of temperatures at the point where the maximum heat flux would cross the surface (at approx 15° of rotation as shown in Fig. 7.2.7) and at the tooth top shows that the analytical and experimental values were within 5 percent of each other at both locations.

### 7.3 Comparison of Flash Temperature Calculation and Results of Other Studies

In this section, the results obtained from the analysis and experiment conducted herein are compared with the flash temperature approximation for this gear mesh as well as with other studies that have investigated this problem.

**Flash Temperature Calculation:** Based on the results of Appendix A, the varying flash temperature, or change in temperature from the nominal bulk value, was calculated to be approximately 189 °C (340 °F) for the speed and load conditions used in the finite element analysis section of the present study. Recalling from Chapter 6, Figure 6.5.3, the maximum temperature excursion based on the analysis at a particular grid point was 40 °C (72 °F). Other grid points close to the top edge of the analytical model had a maximum temperature change from their pre-heat flux condition that was in excess of 60 °C (108 °F). For the grid point that was followed for many revolutions (in Fig. 6.5.3), basically the same analytical temperature differential existed even when the model was started from ambient conditions or from  $t = 0$  seconds (see Fig. 6.5.10).

Within the analysis, many factors that could be modified would have an obvious effect on the maximum temperature change on the surface during one revolution. Flux or load distribution was assumed to be rather flat and elliptical with a ratio of 10:1. Therefore, only grid points at the extreme ellipse locations were penalized with reduced flux. Flux locations closer to the center of contact were only slightly higher than if an average was used for the entire ellipse.

The friction coefficient is another possible difference that can have a great effect on the heat flux and maximum temperature. From Coleman (Ref. [7.1]), friction coefficients varying from 0.02 to 0.1 would not be unexpected during meshing. In Chapter 5, from the curve fit of data taken for the friction coefficient of a synthetic lubricant currently in use in turbine engines and drive systems, the friction coefficient varied from about 0.016 to 0.03 for the case studied in Chapter 6. Obviously, if the heat flux was increased by a factor of 3 to 5, the predicted maximum temperature excursion should increase in nearly the same proportion. Also, in the calculation procedure of the Gleason Works (Ref. [7.2]), the friction coefficient is part of the geometry or X-factor calculated. Using this method, a different friction coefficient would affect the results in a similar manner.

**Comparison to Results of Other Studies:** A comparison of the present study on spiral bevel gears to other studies is presented. Experimental results for this type of gear were found in conjunction with helicopter transmission scoring tests using thermocouples (Ref. [7.3]) and in a study of temperature measurement using an infrared microscope (Ref. [7.4]).

The study of Ku (Ref. [7.3]) used thermocouple locations similar to those used on the bulk thermocoupled pinion shown and discussed in Chapter 3. From a limited number of tests, the same basic bulk temperature conclusions were found with the tooth top having the highest measured temperature when compared with other locations.

The experimental study of Wymer (Ref. [7.4]) was conducted on a helicopter tail rotor gearbox. The same rapidly varying temperature profile was found as in the study presented herein. The signal was not analyzed any further than to measure the voltage differential and relate the results to a maximum temperature rise above a bulk reference temperature obtained by a thermocouple buried near the toe on the active profile out of the contact zone. The bulk temperature increased linearly with power as was found in Chapter 3 of this study (see Fig. 3.8.3). The range of temperature fluctuation from the infrared microscope measurements was centered about that of the time-averaged mode of the instrument. The temperature change across the gear surface was about 20 °C (36 °F) for the condition of constant torque and varying speed. This temperature differential remained constant and did not change with speed as the load was held constant. A similar result was obtained by looking at the data of Table 3.9.1 where speed and load were varied. The reference and maximum temperatures changed, but the difference between minimum and maximum only varied from 29 to 40 °C (52 to 72 °F).

With respect to a comparison of the present analysis with any analytical work, the only known published work that considered a spiral bevel gear thermal analysis is that of Chao (Ref. [7.5]). Using their methodology produced a maximum temperature change across the surface of 40 °C (72 °F) during meshing by following the center of contact. These results agree with the range of temperature change found in the present study. A rapid increase in temperature at the beginning of the active profile position was shown in Reference [7.5] but was not predicted in the present analysis because at this location the heat flux input was low. The maximum nodal temperature increase due to the heat flux at the initial ellipse locations, as the pinion was going into mesh, was at most 5 °C (9 °F). A combination of load sharing and a relatively low sliding velocity at these locations resulted in low heat generation. As the contact moved to locations where the combination of high sliding velocity and single tooth contact occurred, temperatures increased over 40 °C (72 °F) in one time increment.

## 7.4 Recommendations

This section identifies some of the areas to be pursued to improve the experimental and analytical modeling reported in this study.

Needed for the experimental study are either thermocouples or thin-film gages that can be applied to the active profile to produce data using lubricants, speed, and loads applied for useful aerospace conditions. To

verify the analysis, surface temperature data during meshing would be useful. In this study, surface data from a remote rotational location were used to verify the behavior of the analytical model. It would be much better to have fixed-location instrumentation that could produce measurements at a high enough rate to detect the moving heat flux and to measure any temperature rise associated with it.

For the analytical part of the study, any improvements in the heat transfer coefficient description, heat flux distribution, and partitioning of the heat flux would provide the most realistic set of boundary conditions. Many of these considerations are based on a combination of structural and thermal behavior so that the proper load distribution is used. With the newly available three-dimensional contact capabilities that finite element programs are now making available, the combination of structural load location and path, including all tooth, shaft, and support structure stiffnesses, will soon be possible provided that there is enough computational power to handle these very large models.

## REFERENCES

- [7.1] Coleman, W.: A Scoring Formula for Bevel and Hypoid Gear Teeth. J. Lub. Technol., vol. 89, Apr. 1967, pp. 114-126.
- [7.2] Scoring Resistance of Bevel Gear Teeth. The Gleason Works, Rochester, NY, 1966.
- [7.3] Ku, P.; Staph, H.; and Carper, H: Gear Tooth Scoring Investigation. Report USAAMRDL TR-75-33, Southwest Research Institute, San Antonio, TX, July 1975.
- [7.4] Wymer, D.; and Macpherson, P: An Infra-Red Technique for Monitoring Gear Tooth Surface Temperatures. Research Paper RP 458, Imperial College, London, England, Jan. 1974.
- [7.5] Chao, H.; and Cheng, H.: A Computer Solution for the Dynamic Load, Lubricant Film Thickness and Surface Temperatures in Spiral Bevel Gears. NASA CR-4077, 1987.

Analysis condition	
○	Boundary conditions Chapter 6; $T_{AMB} = 38\text{ }^{\circ}\text{C}$ (100 $^{\circ}\text{F}$ )
●	Drive side $h = 3383\text{ W/m}^2 \cdot ^{\circ}\text{C}$ ; Rest the same
▽	Boundary conditions Chapter 6; $h \approx 0$ , top, heel, toe faces
▼	Boundary conditions Chapter 6; $T_{AMB} = 60\text{ }^{\circ}\text{C}$ (140 $^{\circ}\text{F}$ )
Experimental conditions	
□	Jet 90° before mesh on gear; 1.38 MPa (200 psi); 38 $^{\circ}\text{C}$ (100 $^{\circ}\text{F}$ ) oil inlet temperature
■	Jet into mesh; 0.34 MPa (50 psi); 38 $^{\circ}\text{C}$ (100 $^{\circ}\text{F}$ ) oil inlet temperature

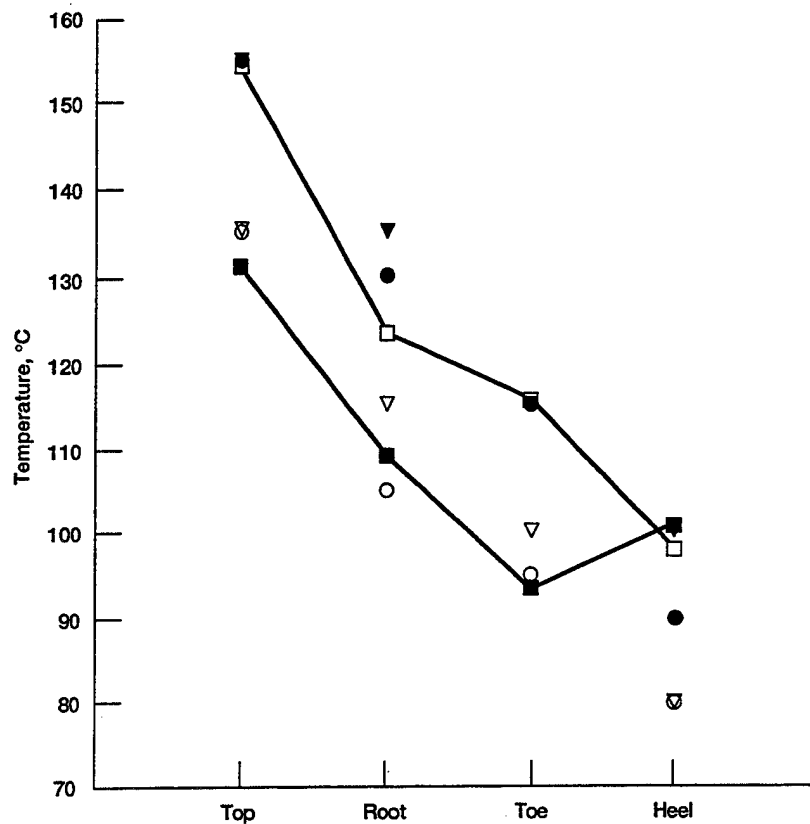


Figure 7.2.1.—Comparison of bulk measurements from thermocouples to time-averaged boundary condition analytical results.

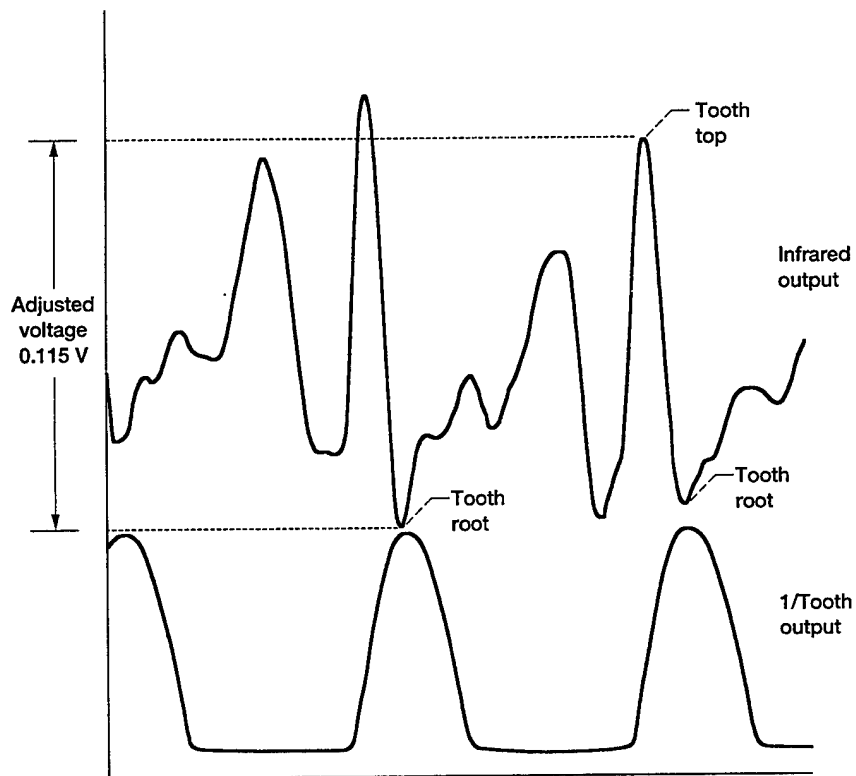


Figure 7.2.2.—Infrared data from jet location B; high flow as shown in Table 3.9.2.

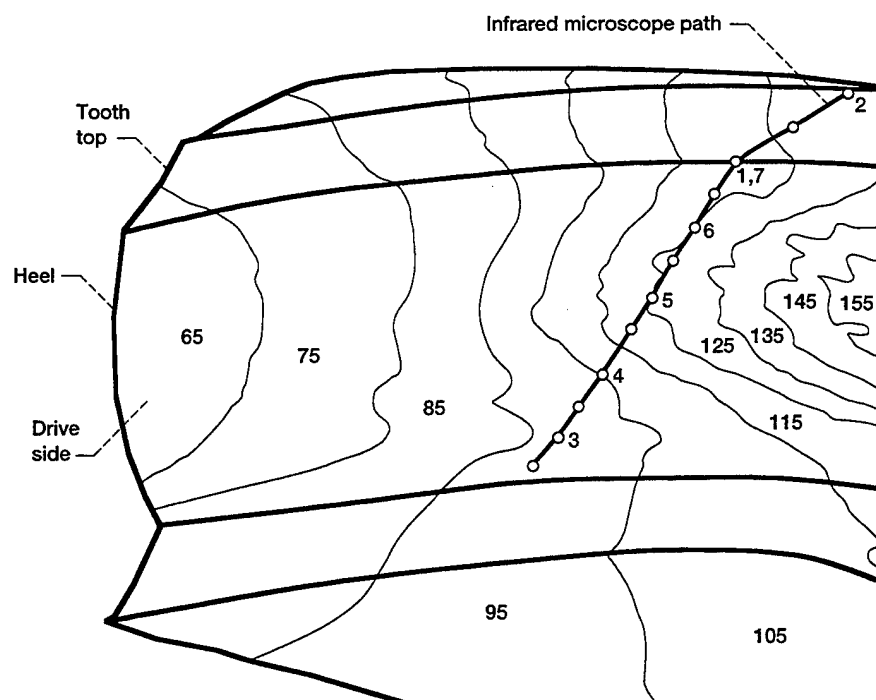


Figure 7.2.3.—Temperature field of pinion at 120° out-of-mesh position. Model is shown from approximately half the face width to the heel. Infrared path locations are numbered to relate to Figure 3.9.5. Temperature shown is in degrees centigrade.

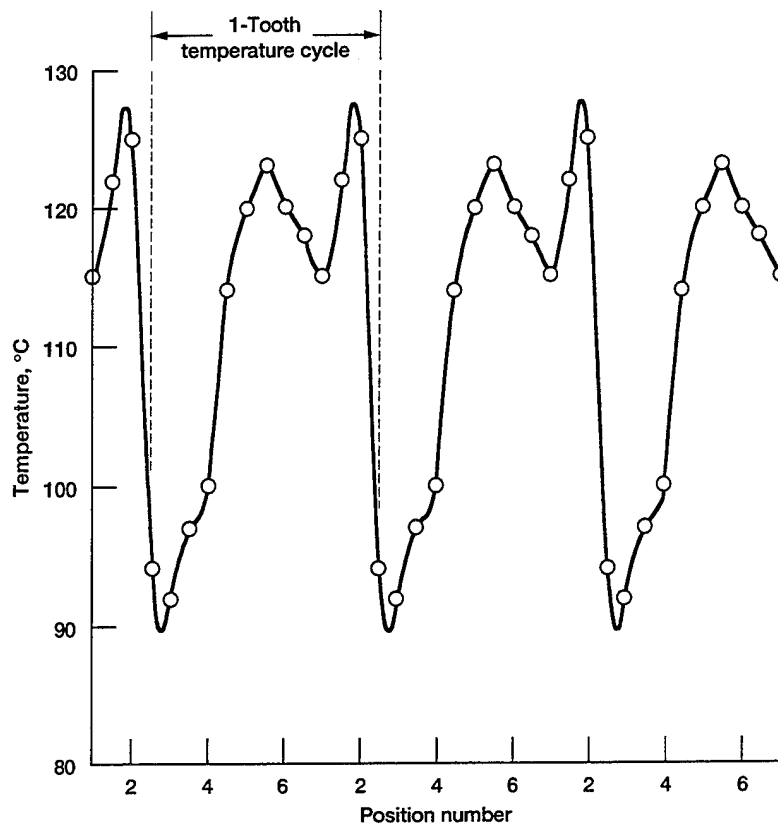


Figure 7.2.4.—Analytical prediction of temperature over an approximate region where the infrared microscope measurement was made.

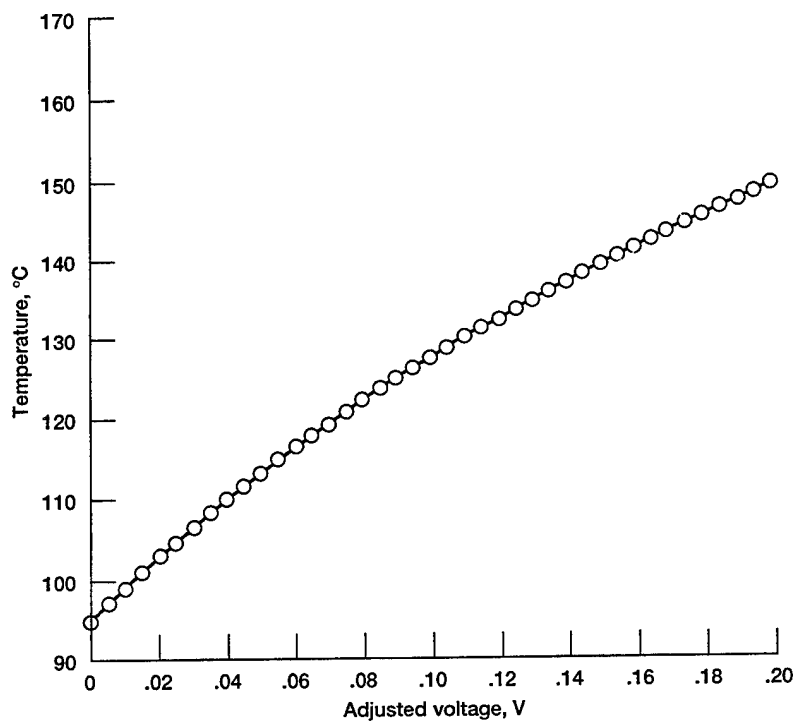


Figure 7.2.5.—Variation of temperature with adjusted infrared voltage using 95 °C (203 °F) as the reference temperature.

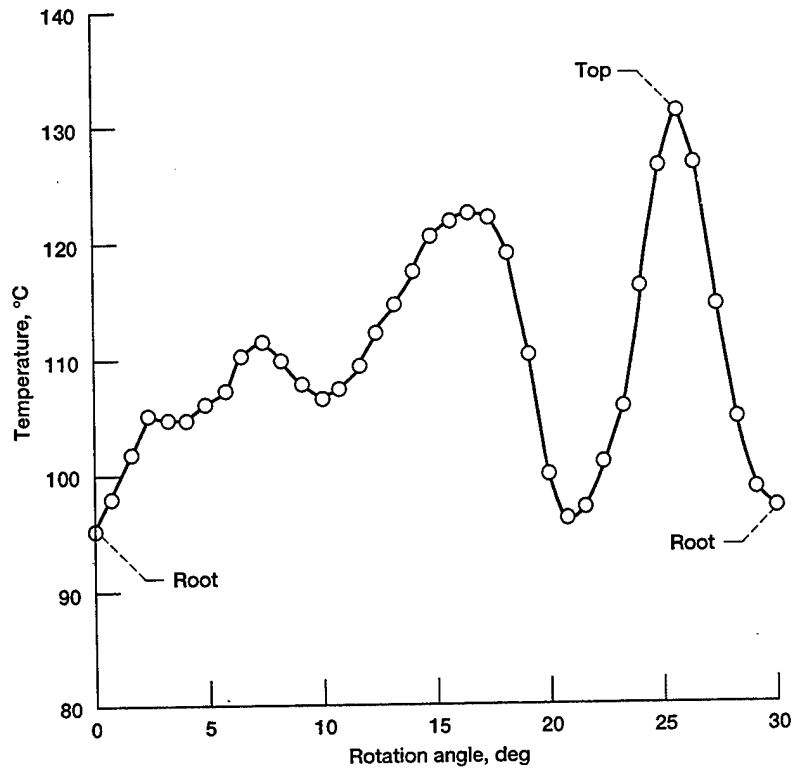


Figure 7.2.6.—Temperature variation of the entire infrared adjusted voltage using Figures 7.2.2 and 7.2.5.

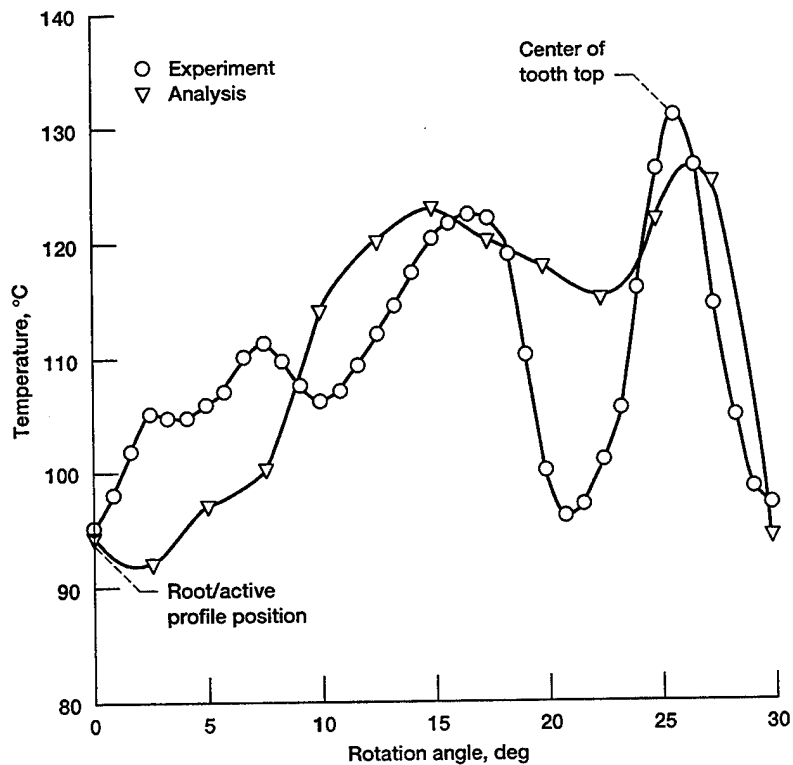


Figure 7.2.7.—Comparison of infrared microscope results with that predicted with the analysis that was developed.

## CHAPTER 8: CONCLUSIONS

An experimental and analytical study was conducted on the thermal behavior of spiral bevel gears. In a test facility, measurements were made on aerospace quality spiral bevel gears. A finite element-based thermal analysis procedure was also developed to produce a three-dimensional representation of the temperature field based on the heat generation produced during gear meshing.

The experiment utilized three different instrumented spiral bevel pinions. A bulk thermocouple pinion was used to collect data from four tooth locations and to interpret data taken with an infrared microscope. Two other pinions, one with thermocouples imbedded in the active profile and a second with thermocouples applied as thin films, were used to measure the rapid temperature rise during meshing. The bulk thermocouple pinion worked very well and permitted data to be taken at a wide variety of conditions. The thermocouple schemes used to measure the rapid temperature transients failed with only a minimal amount of data collected in one case and no useable data produced in the other.

The finite element method pursued in this study is an extension of an existing finite element structural analysis to produce a heat transfer finite element model. A simplified two-dimensional model was first used to develop an analysis methodology. One of the first and most troubling problems was the computer time required for a simple model using finite element analysis as compared with the same model solved with an explicit finite difference method. This problem with the finite element method was resolved using time-averaged boundary conditions with the capability of model restarts to continue the analysis with the time- and position-varying boundary conditions. Boundary condition variants between time averaged and time and position varying were contained within subroutines appended to the model finite element data. This permitted the time-averaged solution to be used as the initial conditions for the time- and position-varying solution. A three-dimensional, high-mesh-density model of a one-tooth sector was constructed.

The following general conclusions can be drawn:

1. An experimental study was conducted to investigate the thermal behavior of a spiral bevel pinion by using a thermocoupled pinion and varying the speed, load, lubricant pressure and temperature, jet type, and jet location. Jet location and load had the greatest effect on the pinion bulk temperatures. Increasing the oil inlet temperature or reducing the lubricant flow rate or pressure had a milder effect on temperature change.
2. Active profile thermocouples were used in an attempt to measure surface temperatures resulting from the heat flux passing over the instrumentation. Unfortunately, one instrumentation scheme using thermocouples electrodischarge-machined in the active profile failed because of scoring. The machining process obviously disrupted the profile enough to cause scoring on the instrumented teeth. The distortion due to the machining process was enough to have metal-to-metal contact when the full conditions were imposed and the net result was a dramatic increase in heat generation that led to the surface failure from scoring. If there had been some other parametric reason for scoring, all teeth would have experienced the same failure.

The other instrumentation scheme used thin-film thermocouples and failed because of interaction with the other gear member. A relatively light load and low speed virtually removed the thermocouples where the contact between the meshing bodies took place. Either a hard overcoat layer or thinner thermocouples must be applied to the measurement surface to make this measurement using typical aerospace lubricants.

3. A procedure was developed to extend a gear geometry modeling method to conduct a three-dimensional heat transfer analysis. A three-dimensional Hertzian contact analysis of the meshing surfaces was developed to determine the contact ellipse size and heat flux location. This was accomplished by using center contact point

curvatures and orientations of the meshing gears. Surface grid points contained within each contact ellipse were determined. Ellipse and grid point heat flux locations changed as the gears rolled through mesh.

4. The heat flux value to be applied to individual contacting ellipses was determined by using the relative sliding velocity between the gears, the coefficient of friction based on an empirical data curve fit, and the load based on an assumed load sharing. Heat transfer coefficients for the three-dimensional sector model were determined using values for a flat plate, rotating disk, or an estimation where empirical results were not available. These conditions were then applied to the model. Either the time-averaged or time- and position-varying boundary conditions were appended to the overall model data by user subroutines.

5. Results from the bulk thermocoupled pinion were compared with the time-averaged solution. The analytical solution demonstrated a minimal change at the bulk thermocouple locations during the application of the time- and position-varying solution. Therefore, the time-averaged conditions at the bulk thermocouple locations could be compared directly. Two experimental tests having conditions close to the boundary conditions assumed on the model were compared. Results were within 4 percent of each other at the top, root, and toe bulk thermocouple locations. The one major difference between the analysis and the experimental results for this situation was at the heel bulk thermocouple location; here, the temperature difference was as high as 21 percent. This discrepancy can be overcome by a modeling change at the heel position to reflect the connection to the rest of the facility shafting.

By varying the heat transfer coefficient or ambient conditions, the predicted values bracketed the experimental results used for comparison. The analysis predicted the same trend found in almost all experiments: the hottest to coolest bulk regions at the measurement locations were top, root, toe, and heel, respectively.

6. A comparison of the time-varying infrared measurement with the analytical prediction using time- and position-varying boundary conditions was made. The analysis was compared at the same position with respect to the rotational location from the mesh and the measurement location across the tooth at that position. The maximum difference between the two results was less than 10 percent excluding a region where the infrared microscope output is affected by the top corner edge of the tooth passing into view.

7. The results from an infrared microscope were also compared with the bulk thermocouple data. The infrared microscope temperature differential and the tooth thermocouple temperature difference between the tooth root and top locations were within 7 percent of each other.

8. The results from the analytical and experimental studies reported herein were compared with those of other available studies. The standard design calculation of flash temperature far exceeded the temperature differentials found from the analysis. The large discrepancy found between the results could be attributed to such factors as friction coefficient. Other available analytical results predicted about the same range of temperature differential over the meshing profile as found in the study conducted herein.

Experimental results from the thermocoupled pinion and infrared microscope produced the same trends as found in a limited number of tests reported in the open literature.

## APPENDIX A—CURRENT FLASH TEMPERATURE CALCULATION

The procedure to calculate the flash temperature using the current methodology is presented. This calculation is accomplished by using two different techniques. First, the method using the calculation procedure documented in Chapter 2 is applied (Refs. [A.1] and [A.2]). Second, the X-value from the Gleason summary sheet for the spiral bevel gear design used in the present study is presented.

For the evaluation of flash temperature, the minimum amount of data required to perform the calculation procedure is shown in Table A.1. The equations for the maximum temperature and flash temperature are given as (Ref. [A.1])

$$T_f = T_i + \Delta T_G \quad (A.1)$$

where

- $T_f$  critical temperature of calculated scoring index, °F
- $T_i$  gear blank temperature just before going into mesh, °F
- $\Delta T_G$  maximum calculated temperature rise (flash temperature), °F

where

$$\Delta T_G = \frac{G}{C_1} \sqrt{c_p} k_t^{0.75} \left( \frac{50}{50 - s} \right) P_d^{0.6875} n_p^{0.3125} \left( \frac{T_{ps}}{T_p} \right)^{1/3} \quad (A.2)$$

where

- $G$  geometry factor
- $C_1$  thermal constant for gear material
- $C_p$  elastic coefficient  $C_p = \sqrt{\frac{3E}{4\pi(1 - \nu^2)}}$  ; if both materials are the same,  $C_p = 2800$  for steel gear material where  $E = 30 \times 10^6$  psi (modulus of elasticity) and  $\nu = 0.3$  (Poisson's ratio)
- $K_t$  load factor, lb
- $s$  surface finish,  $\mu$ in.
- $P_d$  transverse diametral pitch, 1/in.
- $n_p$  pinion speed, rpm
- $T_{ps}$  operating torque, in.·lb
- $T_p$  maximum pinion torque, in.·lb,

$$K_t = \frac{T_p L_o L_m}{L_v F} \quad (A.3)$$

where  $L_o, L_m, L_v$  are overload, load distribution, and dynamic factors (here assumed to be equal to 1 for high-quality gearing), and  $F$  is the face width in inches.

First the geometry factor must be found. Because the Gleason Works (Ref. [A.1]) did not contain the pressure angle of the gear set used, the chart for 25° pressure angle, 35° spiral angle, and 90° shaft angle is used. This chart is shown in Figure 2.3.1. Using the numbers of teeth for the pinion and gear results in the geometry factor being approximately 0.0073. For steel gears  $C_p = 2800$ , and  $C_1 = 41$ . Using values from Table A.1 and assuming that the  $L_o$ ,  $L_m$ , and  $L_v$  factors each equal 1 produces  $K_t = 3150$ . Substituting these values in Equation (A.2) produces a temperature change of  $\Delta T_G = 304^\circ\text{F}$ .

From the Gleason summary sheet for this design, the geometry factor was given as 0.008047. Therefore, the flash temperature would have been higher ( $\Delta T_G = 335^\circ\text{F}$ ) than the amount calculated using the chart for the slightly different pressure angle.

Using the X-factor from the Gleason summary sheet is now described. For the design under consideration, the X-value was given as 0.559. The temperature change  $\Delta T_x$  is calculated from the following equation (Ref. [A.1]):

$$\Delta T_x = X \sqrt{\frac{T_p L_o L_m}{L_b}} \left( \frac{20}{50 - s} \right) n_p^{0.3125} \left( \frac{T_{pa}}{T_p} \right)^{1/3} \quad (\text{A.4})$$

where  $T_{pa}$  is given by

$$T_{pa} = \frac{30\,000}{Q_p}; \quad T_{pa} = \left( \frac{250\,000}{Z_p} \right)^2 \quad (\text{A.5})$$

where  $Q_p$  is the pinion strength factor and  $Z_p$  is the pinion durability factor. The smaller calculated value for  $T_{pa}$  is used in Equation (A.4). In this case  $T_p$  equals  $T_{pa}$ , or the maximum torque equals the operating torque. From the summary sheet,  $Q_p$  is 12.401,  $Z_p$  is 5118, and  $T_{pa}$  is 2386. Substituting these values into Equation (A.4) produces the temperature rise  $\Delta T_x$  of  $343^\circ\text{F}$ .

Therefore, using either the method from charts or the gear summary gave similar results. The most useful part of this analysis is that a comparison of different designs and the different operating conditions of the same design can be made quickly. From the  $\Delta T$  value, the gear blank temperature just prior to meshing must be added to produce the maximum temperature expected (Eq. (A.1)).

## REFERENCES

- [A.1] Scoring Resistance of Bevel Gear Teeth. The Gleason Works, Rochester, NY, 1966.
- [A.2] Drago, R.: Fundamentals of Gear Design. Butterworth Publishers, Stoneham, MA, 1988.

TABLE A.1—PARAMETERS USED FOR FLASH

## TEMPERATURE CALCULATION

Number of teeth, pinion, gear .....	12, 36
Diametral pitch, in. <sup>-1</sup> .....	5.141
Face width, in. ....	1.0
Angle, deg	
Shaft .....	90
Pressure .....	22.5
Spiral .....	35
AGMA class .....	12
Transmitted power, hp .....	720
Pinion speed, rpm .....	14 400
Surface finish, $\mu$ in. ....	10

## APPENDIX B—SOLID MODEL GENERATION DESCRIPTION

The output from a program developed by Handschuh (Ref. [B.1]) is used to define the three-dimensional model from a geometric modeling package (Ref. [B.2]). A one-tooth sector is developed for the pinion. The model includes the tooth body, axial body, and fillet root region. The model used in the study of Chapter 6 had a fillet radius equal to the clearance; therefore, there is a flat region connecting the fillet radius from the concave side to the fillet radius of the convex side of the adjacent tooth. In theory, a complete three-dimensional model could be produced by rotating the one-tooth model an appropriate amount to the next tooth position. This process is then repeated until all teeth are geometrically constructed. A model of the entire gear with a moderate amount of mesh density would be impossible to run, even on today's super computers, because of the calculation space limitations. The output from the program of Reference [B.1] is now described.

**(1) Set the view of the model to look from the toe to the heel down the axis of rotation:**

```
SET,LINES,0
SET,LABELS,OFF
VIEW
1
0,180,90
```

**(2) Output the 10-by-10 mesh of the active profile grid points on the concave side:**

```
GRID, 1,, 0.771470/ 0.191343/ 2.569924
GRID, 2,, 0.795022/ 0.202851/ 2.562148
      *
      *
      *
GRID, 99,, 1.296054/ -0.448119/ 3.440090
GRID, 100,, 1.339687/ -0.430413/ 3.429237
```

**(3) Output the 10-by-10 mesh of the coast profile grid points on the convex side:**

```
GRID, 101,, 0.636857/ 0.475595/ 2.569924
      *
      *
      *
GRID, 200,, 1.365255/ -0.340728/ 3.429237
```

**(4) Connect the tooth base grid points from the concave to the convex side:**

```
LINE, 1,ST,, 1, 101
      *
      *
      *
LINE, 10,ST,, 91, 191
```

(5) Connect the concave side grid points to the convex side grid points to make a two-dimensional surface (PATCH):

```
PATCH, 1,QUAD,, 1/ 2/102/101
PATCH, 2,QUAD,, 2/ 3/103/102
      *
      *
      *
PATCH, 90,QUAD,, 99/100/200/199
```

(6) Connect the patches to form three-dimensional regions of the gear tooth body (HYPERPATCHES):

```
HPAT, 1,2P,, 1, 10
HPAT, 2,2P,, 2, 11
      *
      *
      *
HPAT, 81,2P,, 81, 90
```

(7) Generate a three-dimensional gear body under the tooth starting from the toe and going to the heel:

```
GRID, 201,, 0.339707/ 0.084255/ 2.569924
LINE, 11,ARC,0/0/0/0/1.0/ 22.8222, 201
      *
      *
      *
GRID, 219,,0.312335/ -0.157946/ 3.526907
LINE, 20,ARC,0/0/0/0/1.0 24.4238, 219
PATCH, 91,2L,, 1, 11
PATCH, 92,2L,, 2, 12
      *
      *
      *
PATCH, 100,2L,, 10, 20
HPAT, 82,2P,, 91, 92
HPAT, 83,2P,, 92, 93
      *
      *
      *
HPAT, 90,2P,, 99, 100
```

(8) Now, generate the fillet radius region on the concave side of the tooth:

```
LINE, 21,ARC, 0.7763/ 0.1707/0/ 0.7763/ 0.1707/1.0/ 88.471, 1
LINE, 22,ARC,0/0/0/0/1.0/ -1.529, 201
      *
      *
      *
LINE, 39,ARC, 0.9585/-0.5085/0/ 0.9585/-0.5805/1.0/ 88.880, 91
```

```

LINE, 40,ARC,0/0/0/0/1.0/ -1.120, 219
PATCH, 101,2L,, 21, 22
PATCH, 102,2L,, 23, 24
*
*
*
PATCH, 110,2L,, 39, 40
HPAT, 91,2P,, 101, 102
HPAT, 92,2P,, 102, 103
*
*
*
HPAT, 99,2P,, 109, 110

```

**(9) Generate the flat region between the concave and convex side fillet radii between adjacent teeth:**

```

LINE, 41,ARC,0/0/0/0/1/ -4.119, 221
LINE, 42,ARC,0/0/0/0/1/ -4.119, 222
*
*
*
LINE, 60,ARC,0/0/0/0/1/ -3.336, 240
PATCH, 111,2L,, 41, 42
PATCH, 112,2L,, 43, 44
*
*
*
PATCH, 120,2L,, 59, 60
HPAT, 100,2P,, 111, 112
HPAT, 101,2P,, 112, 113
*
*
*
HPAT, 108,2P,, 119, 120

```

**(10) Generate the fillet radius region on the convex side fillet for the adjacent tooth:**

```

GRID, 261,, 0.789332/ 0.093448/ 2.569924
LINE, 61,ARC, 0.7866/ 0.1145/0/ 0.7866/ 0.1145/1.0/ -88.471,261
LINE, 62,ARC,0/0/0/0/1/ -1.529, 242
*
*
*
GRID, 288, 0.916070/ -0.581393/ 3.526907
LINE, 79,ARC, 0.9273/-0.5634/0/ 0.9273/-0.5634/1.0/ -88.880,288
LINE, 80,ARC,0/0/0/0/1 -1.120, 260
PATCH, 121,2L,, 61, 62
PATCH, 122,2L,, 63, 64
*
*

```

```

      *
PATCH, 130,2L,, 79, 80
HPAT, 109,2P,, 121, 122
HPAT, 110,2P,, 122, 123
      *
      *
      *
HPAT, 117,2P,, 129, 130

```

The model hyperpatches generated from this procedure are shown in Figure B.1.

## FINITE ELEMENT MESH GENERATION AND HEAT TRANSFER BOUNDARY CONDITIONS

At this point, the data set just generated is read into the three-dimensional modeling program described by PDA Engineering (Ref. [B.2]). Next, the model is meshed, equivalenced, and bandwidth reduced; material properties are then added and boundary conditions applied.

### (1) Provide finite element mesh for the example used in Chapter 6:

```

MESH,H1T81,HEX/8/1,NUM,2/16/2/16/5
MESH,H82T90,HEX/8/1,NUM,6/5/6/16/6
MESH,H91T99,HEX/8/1,NUM,6/2/6/2/5
MESH,H100T108,HEX/8/1,NUM,6/2/6/2/5
MESH,H109T117,HEX/8/1,NUM,6/2/6/2/5

```

This meshing procedure produced 20 250 elements and 22 586 grid points. The finite element model generated based on the meshing commands given above is shown in Figure 6.4.2.

### (2) Equivalence redundant grid points generated and optimize the bandwidth of the model:

```

EQUIVALENCE, TOLERANCE=0.005, TOPOLOGICAL
EQUIVALENCE, TOLERANCE=0.005, GEOMETRICAL
OPTIMIZE, BANDWIDTH, CUTHILL-MCKEE

```

### (3) Input material properties and assign them to all the hyperpatches of the model:

```

PMAT,1,ISO,30E6,,0.3,7801.,,,,,,43.25,3689873.
PFEG,H1T117,HEX/8/1,1

```

### (4) Apply a temperature boundary condition to all nodes of the active profile (concave side) to permit user subroutine access:

```

DFEG,H1T81,TEMP/N,38.0,1,FACE1

```

**(5) Apply the rest of the heat transfer coefficient boundary conditions to all exposed faces of the three-dimensional model:**

Concave side (active profile):

DFEG,H1T81,CONV,4450.,1,FACE1

Tooth top between concave and convex sides of tooth:

DFEG,H9/18/27/36/45/54/63/72/81,CONV,50.,2,FACE4

Convex side (coast profile):

DFEG,H1T81,CONV,50.,3,FACE2

Tooth body face at the toe:

DFEG,H1T9,CONV,160.,4,FACE6

Shaft body face at the toe:

DFEG,H82/109,CONV,160.,5,FACE5

DFEG,H91/100,CONV,160.,6,FACE6

Shaft body face at the heel:

DFEG,H90/117,CONV,160.,7,FACE6

DFEG,H99/108,CONV,160.,8,FACE5

Tooth body face at the heel:

DFEG,H73T81,CONV,160.,9,FACE5

Fillet root region between the concave and convex sides:

DFEG,H91T117,CONV,50.,10,FACE3

Axial section on the concave side of the model:

DFEG,H109T117,CONV,0.001,11,FACE1

Axial section on the convex side of the model:

DFEG,H82T90,CONV,0.01,12,FACE2

Inside diameter of the shaft body:

DFEG,H82T117,CONV,0.001,13,FACE4

At this point, a conversion routine is run to output the bulk data necessary to specify the model and the associated heat transfer boundary conditions. To investigate the temperature excursions during the meshing process, user subroutines are appended to this bulk data to control the heat flux and heat transfer coefficients depending on either the time-averaged solution or the time- and position-varying boundary conditions.

## REFERENCES

- [B.1] Handschuh, R.; and Litvin, F.: A Method for Determining Spiral Bevel Gear Tooth Geometry for Finite Element Analysis. NASA TP-3096, 1991.
- [B.2] PDA Engineering. PATRAN Plus, Release 2.5, Costa Mesa, CA, 1990.

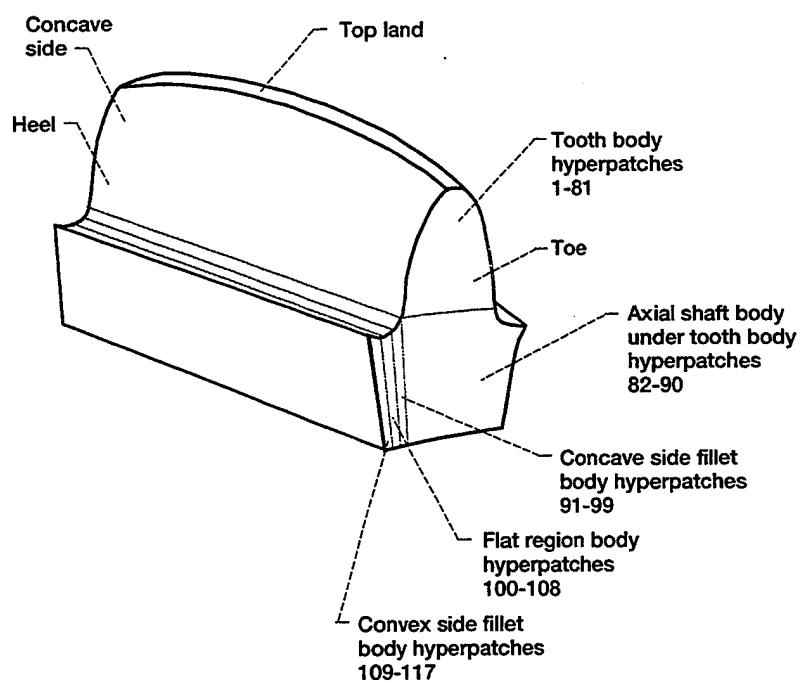


Figure B.1.—Three-dimensional solid model hyperpatch designation.

## APPENDIX C—USER SUBROUTINES

The user subroutines required to conduct the finite element analysis using the time-averaged and time- and position-varying boundary conditions are described. Only one set of user subroutines is used with the bulk data at a given computation time. In the study reported herein, the time-averaged boundary condition user subroutines are employed first. This permits the solution to reach steady state with a minimum of required computation time. Then the time- and position-varying user subroutine is employed. The program used to conduct the finite element analysis (Ref. [C.1]) allowed model restarts; therefore, the user subroutines are switched from the time averaged to time and position varying. The program is then run for enough increments to get the solution to repeat.

An explanation and the construction of each of these two different user subroutines to conduct the analysis are presented.

### Time-Averaged Boundary Condition User Subroutine

```
C This subroutine uses the time-averaged heat
C fluxes for all the active surface grids that
C have heat fluxes. This procedure was performed by
C summing the heat flux for each grid point for
C all the heat flux positions. The total flux was
C then assigned to a particular node. The FORCDT
C call from the bulk data deck will then check each
C active grid point node to see if any heat is
C applied. Flux applied to a grid point is in
C watts.
C
C
C      SUBROUTINE FORCDT(X1,X2,X3,F,T,TIME,DTIME,NDEG,
C      *NODE,X4,XORD,NCRD,IACFLG,INC)
C
C      DIMENSION F(1),T(1),XORD(3)
C
C      DIMENSION FLNODE(10000),NNODE(10000)
C
C      NSREV=NUMBER OF TIME STEPS PER REVOLUTION
C      NFLUX=NUMBER OF HEAT FLUXES APPLIED
C      NNODE(I)=NODE NUMBER I ON THE ACTIVE PROFILE WITH
C      A HEAT FLUX APPLIED
C      FLNODE(I)=FLUX VALUE OF GRID POINT I
C      F(1)=FLUX VALUE PASSED FROM THE USER SUBROUTINE
C      TO THE ANALYSIS
C
C      DATA FOR CALCULATION
C
C      DATA NSREV,NFLUX/144,402/
C
C      DATA (NNODE(I),I=1,10000)
C      */
C      *2999, 3003, 3491, 3492, 3493, 3494, 3981, 3982,
```

```

      *
      *
      *
*17817,18149,
* 9598*0/
C
  DATA (FLNODE(I),I=1,10000)
  */
  * 1.61, 6.97, 2.50, 0.41, 3.53, 8.48, 5.84, 2.97,
      *
      *
      *
  * 5.42, 6.34,
  * 9598*0.0/
C
  RNSTEP=DFLOAT(NSREV)

C
C CHECK FOR ACTIVE PROFILE HEAT FLUX LOCATIONS
C
  DO 10 I=1,NFLUX
    IF(NODE.EQ.NNONE(I))F(1)=FLNODE(I)/RNSTEP
    IF(NODE.EQ.NNODE(I))GO TO 20
10  CONTINUE
C
  F(1)=0.0
C
20  CONTINUE
    RETURN
    END
C
C HEAT TRANSFER FILM COEFFICIENT SUBROUTINE
C
  SUBROUTINE FILM(H,TINF,TS,N,TIME)
C
  H=1.0
C
  RETURN
  END

```

This is the entire time-averaged user subroutine that would be required to successfully execute the time-averaged boundary conditions. Note that the user subroutine is called each time step. Each active profile grid point is checked in the user subroutine to see if there is a flux applied by comparing each active grid point to the actual flux grid points. If a grid point is not found in the user subroutine list, its heat flux value is set equal to zero. Note that the FILM subroutine basically serves no purpose in this part of the solution.

#### Time- and Position-Varying Boundary Condition User Subroutine

```

C
C Time- and position-varying user subroutine follows. Grid
C point numbers and flux amounts must be organized.

```

```

C Also, the actual time must be tracked to know when
C a certain ellipse is in effect, for example.
C
C     SUBROUTINE FORCDT(X1,X2,X3,F,T,TIME,DTIME,NDEG,
C     *NODE,X4,XORD,NCRD,IACFLG,INC)
C
C     DIMENSION F(1),T(1),XORD(3)
C
C     DIMENSION FL(100,1000),NNODE(100,1000),NFLUX(100)
C
C     N2=NUMBER OF CONTACT ELLIPSES
C     DT=TRANSIENT TIME STEP LENGTH
C     NSREV=NUMBER OF TIME STEPS PER REVOLUTION
C     FL(I,J)=FLUX VALUE OF ELLISPE I, GRID POINT J
C     NNODE(I,J)=GRID POINT NUMBER OF ELLIPSE I,GRID
C     POINT J
C     NFLUX(I)=NUMBER OF GRID POINTS IN ELLIPSE I
C
C     DATA N2,DT,NSREV/15,2.8935E-5,144/
C
C     DATA (FL( 1,I),I=1, 1000)
C     */
C     * 6.97, 8.48, 9.60, 9.81,10.65,11.30,11.81,11.91,
C       *
C       *
C       *
C     * 976*0.0/
C
C     FLUX VALUES FOR THE NEXT 14 ELLIPSES FOLLOWS
C
C     DATA (NNODE( 1,I),I=1, 1000)
C     */
C     * 3003, 3494, 3985, 3986, 4477, 4968, 5459, 5460,
C       *
C       *
C       *
C     * 976*0/
C
C     GRID POINT NUMBERS FOR THE NEXT 14 ELLIPSES
C     FOLLOWS
C
C     DATA (NFLUX(I),I=1,100)
C     */
C     * 24, 25, 27, 42, 41, 41, 45, 47, 47, 47,
C     * 48, 50, 28, 31, 31,
C     * 85*0/
C
C     CHECK TO SEE WHAT INCREMENT OF THE REVOLUTION
C     THE TOTAL ELAPSED TIME OF THE MODEL IS ON.
C     VARIABLE "IC" KEEPS TRACK OF WHICH TIME INCREMENT

```

```

C THE SOLUTION IS CURRENTLY SOLVING.
C
C   RNSTEP=TIME/DT
C
C   RCHECK=(TIME+0.01*DT)/DT
C
C   NSTEP=IFIX(RNSTEP)
C
C   NCHECK=IFIX(RCHECK)
C
C   IF(NCHECK.NE.NSTEP)NSTEP=NCHECK
C
C   NS=NSTEP/NSREV
C
C   IC=NSTEP-NS*NSREV
C
C   IF(IC.LE.N2)GO TO 100
C
C   F(1)=0.0
C
C   GO TO 20
C
C 100 CONTINUE
C
C CHECK FOR GRIDS IN THE ACTIVE PROFILE THAT HAVE
C A HEAT FLUX APPLIED
C
C   JF=NFLUX(IC)
C   DO 10 J=1,JF
C   IF(NODE.EQ.NNODE(IC,J))F(1)=FL(IC,J)
C   IF(NODE.EQ.NNODE(IC,J))WRITE(6,25)IC,NODE,F(1)
25  FORMAT(1X,'IC=',I5,1X,'NODE=',I5,1X,'F(1)=' ,F10.3)
C   IF(NODE.EQ.NNODE(IC,J))GO TO 20
10  CONTINUE
C   F(1)=0.0
20  CONTINUE
C
C   RETURN
C   END
C
C SUBROUTINE FOR FILM COEFFICIENTS
C
C   SUBROUTINE FILM(H,TINF,TS,N,TIME)
C
C   DATA N2,DT,NSREV/15,2.8935E-5,144/
C
C   RNSTEP=TIME/DT
C
C   RCHECK=(TIME+0.01*DT)/DT
C
C   NSTEP=IFIX(RNSTEP)

```

```

C      NCHECK=IFIX(RCHECK)
C
C      IF(NCHECK.NE.NSTEP)NSTEP=NCHECK
C
C      NS=NSTEP/NSREV
C
C      IC=NSTEP-NS*NSREV
C
C      IF(IC.LE.N2)GO TO 100
C
C      GO TO 20
C
C 100 CONTINUE
C
C      H=0.0
C
C      GO TO 30
C
C 20 CONTINUE
C
C      H=1.0
C
C 30 CONTINUE
C
C      RETURN
C      END

```

Obviously this user subroutine is more involved than that of the time-averaged solution. With respect to going through mesh, elapsed time and the position of the tooth in question are checked. The time step length in the bulk data deck and the user subroutine must be the same. One complication is that each heat flux ellipse has different grid points contained within its boundaries as well as a flux value that changes from grid point to grid point within a given ellipse. Therefore, for each time step each of the active grid points is checked to see if it lies within a given ellipse. If the grid point does not have a gear flux for that increment, the flux is set to zero. This is repeated each time step for each active profile grid point. When the time step increment is not part of the meshing cycle, all active profile grid points have a zero heat flux. Also, in this user subroutine, the same timekeeping is conducted in the FILM subroutine. When the pinion is meshing with the gear, the heat transfer coefficients for all surfaces are set to zero; when the tooth moves out of mesh, they then resume their assigned values.

If the numerical model were to include a position-varying heat transfer coefficient, such as the lubricant jet spraying directly on the pinion or on the gear being modeled, the FILM subroutine would be the place to modify the heat transfer coefficient value. The coefficient could be dramatically increased to numerically describe the quenching effect of the jet. In the present study reported herein, the jet was assumed to be impinging on the other gear member and convection only resulted from the air-oil mist contained in the test section.

The construction of the user subroutines, with respect to the participating grid points and their assigned heat flux values, is done by a computer program so that the user is spared a tedious and time-consuming task. A shell user subroutine is merged with the output from the appropriate computer program (see Chapter 6) to construct the user subroutine for a particular model and the imposed boundary conditions. This process must be repeated for the time-averaged and then the time- and position-varying boundary conditions.

The bulk data deck only requires that the time step size be changed to continue the model solution from the time-averaged to the time- and position-varying phases of the solution sequence. Restarts permit the model to be rotated for the desired number of revolutions until the solution stabilizes and the bounds of the time-varying temperature are repeatable.

## REFERENCE

[C.1] MARC Finite Element Program. Rev. J.4-1. MARC Analysis Research Corporation, Palo Alto, CA, 1990.

# REPORT DOCUMENTATION PAGE

OMB No. 0704-0188

Public reporting burden for this collection of information is estimated to average 1 hour per response, including the time for reviewing instructions, searching existing data sources, gathering and maintaining the data needed, and completing and reviewing the collection of information. Send comments regarding this burden estimate or any other aspect of this collection of information, including suggestions for reducing this burden, to Washington Headquarters Services, Directorate for Information Operations and Reports, 1215 Jefferson Davis Highway, Suite 1204, Arlington, VA 22202-4302, and to the Office of Management and Budget, Paperwork Reduction Project (0704-0188), Washington, DC 20503.

1. AGENCY USE ONLY (Leave blank)		2. REPORT DATE January 1995		3. REPORT TYPE AND DATES COVERED Technical Memorandum	
4. TITLE AND SUBTITLE  Thermal Behavior of Spiral Bevel Gears				5. FUNDING NUMBERS  WU-505-62-10 1L162211A47A	
6. AUTHOR(S)  Robert F. Handschuh					
7. PERFORMING ORGANIZATION NAME(S) AND ADDRESS(ES) NASA Lewis Research Center Cleveland, Ohio 44135-3191 and Vehicle Propulsion Directorate U.S. Army Research Laboratory Cleveland, Ohio 44135-3191				8. PERFORMING ORGANIZATION REPORT NUMBER  E-7584	
9. SPONSORING/MONITORING AGENCY NAME(S) AND ADDRESS(ES) National Aeronautics and Space Administration Washington, D.C. 20546-0001 and U.S. Army Research Laboratory Adelphi, Maryland 20783-1145				10. SPONSORING/MONITORING AGENCY REPORT NUMBER  NASA TM-106518 ARL-TR-403	
11. SUPPLEMENTARY NOTES This report was submitted as a dissertation in partial fulfillment of the requirements for the degree Doctor of Philosophy to Case Western Reserve University, Cleveland, Ohio, August 1993. Responsible person, Robert F. Handschuh, organization code 2730, (216) 433-3969.					
12a. DISTRIBUTION/AVAILABILITY STATEMENT  Unclassified - Unlimited Subject Category 37				12b. DISTRIBUTION CODE	
13. ABSTRACT (Maximum 200 words)  An experimental and analytical study of the thermal behavior of spiral bevel gears is presented. Experimental data were taken using thermocoupled test hardware and an infrared microscope. Many operational parameters were varied to investigate their effects on the thermal behavior. The data taken were also used to validate the boundary conditions applied to the analytical model. A finite element-based solution sequence was developed. The three-dimensional model was developed based on the manufacturing process for these gears. Contact between the meshing gears was found using tooth contact analysis to describe the location, curvatures, orientations, and surface velocities. This information was then used in a three-dimensional Hertzian contact analysis to predict contact ellipse size and maximum pressure. From these results, an estimate of the heat flux magnitude and the location on the finite element model was made. The finite element model used time-averaged boundary conditions to permit the solution to attain steady state in a computationally efficient manner. Then time- and position-varying boundary conditions were applied to the model to analyze the cyclic heating and cooling due to the gears meshing and transferring heat to the surroundings, respectively. The model was run in this mode until the temperature behavior stabilized. The transient flash temperature on the surface was therefore described. The analysis can be used to predict the overall expected thermal behavior of spiral bevel gears. The experimental and analytical results were compared for this study and also with a limited number of other studies. The experimental and analytical results attained in the current study were basically within 10 percent of each other for the cases compared. The experimental comparison was for bulk thermocouple locations and data taken with an infrared microscope. The results of a limited number of other studies were compared with those obtained herein and predicted the same basic behavior.					
14. SUBJECT TERMS  Gears; Heat transfer; Gear teeth; Lubrication				15. NUMBER OF PAGES 195	
				16. PRICE CODE A09	
17. SECURITY CLASSIFICATION OF REPORT Unclassified	18. SECURITY CLASSIFICATION OF THIS PAGE Unclassified	19. SECURITY CLASSIFICATION OF ABSTRACT Unclassified	20. LIMITATION OF ABSTRACT		